The Development of an Antagonistic SMA Actuation Technology for the Active Cancellation of Human Tremor

by

Anupam Pathak

A dissertation submitted in partial fulfillment
of the requirements for the degree of
Doctor of Philosophy
(Mechanical Engineering)
in the University of Michigan
2010

Doctoral Committee:

Associate Professor Diann Erbschloe Brei, Co-Chair
Assistant Research Scientist Jonathan E. Luntz, Co-Chair
Associate Professor Brent Gillespie
Associate Professor John A. Shaw

Acknowledgements

I am sincerely grateful for my advisor, Diann Brei, who has offered her guidance and support through my graduate school career and enabled me to complete this dissertation. Diann's mentorship helped to foster my creativity both as a researcher and engineer, and she has always encouraged me to pursue new ideas and opportunities. I have felt, among the rest of her students, a part of an extended family, which is something I have always appreciated. Jon Luntz, my co-advisor, has also played a key part in my work. I have been fortunate to experience his passion for technical knowledge almost every day, and he has always encouraged me to have the confidence to learn new topics, no matter how difficult they seem. My committee members, John Shaw and Brent Gillespie have offered significant guidance in this process, for which I am thankful. Several portions of this dissertation could not have been accomplished without John Shaw's help and the use of his experimental facilities.

My excellent science and math instructors in the past have collectively influenced my pursuit of this dissertation through their guidance, and encouragement for personal development. My Berkeley professors have all challenged me to learn, pursue research, and attempt to solve the many social issues we experience today. I particularly want to thank Benson Tongue my research advisor at Berkeley for his generous mentorship and support, both past and present. His instruction helped me immensely, and his comedy has taught me to enjoy life and stay optimistic.

I'd like to thank all of my friends all across the world for their support and camaraderie, and I want to give a special thanks to the participants in the China EAPSI

program for their interest and discussion regarding my research. My lab mates (past and present) -- Paul Alexander, Jarod Kelly, Jim Otten, Monica Toma, Nathan Wilmot, Brian Barnes, John Redmond, Julianna Abel, Brent Utter, Won Hee Kim, Shishira, and Poorna Mane -- have all supported me along the way, and I have always enjoyed sharing our common interests in creativity and invention.

Most importantly, I must acknowledge my family. I'm thankful for my girlfriend Karolina who has supported me through this entire process, and served as an inspiration through her love for learning, and her artistic creativity. She has been a wonderful influence in my life. My two sisters, Smita and Shalini, who I love very much, have always been proud and supportive of my endeavors and I am so lucky to have them. My brilliant parents have been and continue to be role models that I aspire to. Both my Mom and Dad have always offered unconditional love and support that has enabled me to take risks in life and pursue areas I'm passionate about.

Table of Contents

List of Figures

List of Tables

Abstract

The Development of an Antagonistic SMA Actuation Technology for the Active Cancellation of Human Tremor

by

Anupam Pathak

Co-Chairs: Diann Erbschloe Brei and Jonathan E. Luntz

Human Tremor is an unintentional bodily motion that affects muscle control among both healthy individuals and those with movement disorders, occasionally to severe detriment. While assistive devices avoid the risk of side effects from pharmacological or surgical treatments, most devices are impractical for daily use due to limitations inherent in conventional actuators. The goal of this research is to address these limitations by developing an antagonistic Shape Memory Alloy (SMA) actuation technology, enabling a new class of active tremor cancellation devices. This is accomplished through the construction of a model and body of empirical support that provides the necessary design insight and predictive power for an antagonistic actuator that ensures stable amplitude and high frequency motion with low power draw.

Actuation frequency and power draw were improved while balancing their competing effects through the development of: 1) a method that accurately measures the convective coefficient of SMA to enhance actuator design, 2) a growth process for carbon nanotube cooling fins to enhance cooling in a fixed medium, and 3) an

understanding of the antagonistic architecture to produce increased frequency in a controllable manner. To enable applications requiring predictability for positioning and complex control, a thermodynamic model for antagonistic SMA was derived to account for inertial, slack, boiling, friction, and convective effects. Using the model, a series of simulation studies provided design insight on the effect of operating environment, driving signal, and environmental conditions so that the generic actuation system can be utilized in a wide variety of applications beyond tremor cancellation. If high forces are required in such applications, stability issues can arise, which were addressed in experimental shakedown research that broadens the high-stress SMA design space. The technology enabled by this dissertation was demonstrated in a working Active Cancellation of Tremor (ACT) prototype that produced 71% RMS cancellation of human tremor. The cancellation results show significant improvement over the current state of the art by providing intuitive, lightweight, compact hand-held tremor cancellation that is a promising solution to numerous assistive applications in medical, military, and manufacturing sectors.

Chapter 1: Introduction

Human tremor is a persistent physiological condition that is present to some degree in all people. While tremor is typically benign, in operations requiring fine muscle control such as microsurgery, precision manufacturing, or military targeting, it can severely affect performance. Additionally in over 10 million people in the US, a significantly amplified form of human tremor manifests as an abnormal motion disorder called Essential Tremor. In many such cases, the significant difficulty that tremor causes in daily functioning—tasks as simple as eating and drinking—impairs quality of life and can lead to social isolation.

Unfortunately, current pharmacological treatments have varying success in abating the condition, and surgical procedures are invasive, costly, and present the risk of harmful side-effects. In response to this problem, physically assistive technologies approach tremor mitigation in three ways: isolation, suppression, and active cancellation. While tremor isolation and suppression have found uses in telerobotic systems and in actively damped input devices, they are limited in mobility and are unacceptable for daily use due to their bulk, weight, high cost, and issues with user acceptance. Hand-held active cancellation, however, provides an attractive solution due to its potential for intuitive operation, portability, low weight, and overall user comfort.

While active cancellation is promising, it has not been fully realized since it creates strict packaging, stroke, weight, and frequency limitations on the actuator. Conventional technologies have difficulty meeting these restrictions due to issues with

scalability, leading to excess weight and bulk. Most smart materials have difficulty in output stroke and fragility, though Shape Memory Alloys (SMAs) present an appealing solution due to the material's extremely high energy density, robustness, low weight, and compact nature. By configuring SMA wires in an antagonistic architecture, an extremely small actuator can be developed that is capable of producing high-speed cyclic motion profiles (ideal for tremor cancellation). The antagonistic architecture is also able to offer a greater range of control than traditional single-wire spring- or load-reset architectures.

While antagonistic SMA presents a viable solution, several fundamental research issues exist that must be resolved before the technology can be fully utilized. Stability in output amplitude, for example, is a significant challenge since SMA is known to exhibit degradation in recovered motion above certain stress levels. Actuation frequency is another research issue, as little understanding and engineering data exist to properly specify coolants that produce a required frequency response without creating excess power draw. Predictability and design insight are also currently lacking for antagonistic SMA, and there is a strong need for a physically-based model that is capable of assisting in actuator and controller design.

Thus, the goal of this dissertation is to enable a new class of human tremor cancellation by developing a model and experimental based technological understanding of antagonistic SMA actuators. By bringing to bear the necessary predictability, controllability and design insight on the design process, the competing goals of the antagonistic actuator can be managed to produce stable high amplitude output in a compact hand-held package while improving frequency with minimal power draw.

1.1 Tremor

Tremor is defined as an unintentional muscle movement in the human body which is rhythmic and oscillatory in nature. It is found both in healthy individuals and among those suffering from neurological movement disorders. The effects of tremor can be severe. For healthy people working in sectors needing fine muscle control such as microsurgery, precision manufacturing, or military targeting, even small tremors can cause catastrophic effects (e.g., injury to a patient during surgery). For individuals suffering from neurological disorders, the extent of tremor is much greater and can be debilitating, causing loss of ability to function in lifestyles or occupations held prior to disease onset. This section provides a brief definition of the different forms of tremor and their causes along with the current modes of treatment. This research will focus on both normal physiological tremor and essential tremor for which assistive devices are a possible form of treatment. A review of the current approaches taken to reduce these forms of tremor is provided to aid in identifying the technological need for this dissertation (discussed in Section 1.3).

1.1.1 Tremor Classifications

There are many classifications and causes of tremor, i.e. see (Sagma 2003), but the most debilitating class is an interference of activated muscle movement (this is found both in healthy and impaired individuals). These types of tremors, called *action* tremors, occur in three forms: *postural*, *isometric*, and *kinetic* (Table 1.1). *Postural* tremor occurs in unsupported limbs, and can be noticed when a subject extends their arms outward from the body (Evidente 2000). *Isometric* tremor is noticed during contraction against stationary objects (such as firmly grasping a cup), and *Intention* tremor occurs during voluntary targeted motions such as finger-to-nose testing. *Intention* tremor has a distinct characteristic of increasing in amplitude while a patient

is engaged in target-directed motion (Evidente 2000).

Causes of action tremor vary, but the two most common are classified as *physiological* and *essential* tremors. *Physiological* tremor is found in all normal persons (Sagma 2003), and often is exacerbated by exhaustion, emotional distress, or certain body positions that offer no musculature support (Joyce and Rack 1974). *Essential* tremor, on the other hand, is an abnormal movement disorder, and is the most common one worldwide (Zesiewicz and Hauser 2001) with estimates as high as 4% among persons older than 65 years (Thanvi, et al. 2006). True prevalence of essential tremor may be much higher (up to 50%) since most people with mild forms are unaware of it (Sagma 2003). Neurological disorders such as Parkinson's disease and Cerebellar lesions (damage to the Cerebellar region of the brain) may also cause action tremor, though they are less common than essential tremor (in the case of Parkinson's Disease, 20 times less common) (Sagma 2003).

1.1.2 Tremor Motion Characteristics

Tremor is characterized as a periodic motion (Shahani and Young 1976) that is rhythmical and sinusoidal in nature (Figure 1.1). Because the human body is a mechanical structure with internal damping and elasticity, the frequency of this

Table 1.1. Summary of three types of action tremor. Postural tremor is the most common form. (Sagma 2003)

Action Tremor Type	Frequency (Hz)	Amplitude	Occurrence	Examples
Postural	Medium to High (4-12)	Increases with voluntary movement	Limb maintains position against gravity	Physiological tremor; essential tremor; metabolic disturbance; drug or alcohol withdrawal
Intention / Kinetic	Medium (<5)	Increases with targeted movement	Movements of the limb (targeted for Intention)	Cerebellar Lesion
Isometric	Medium (<5)	Variable	Contraction against stationary objects	Grasping a heavy object in one hand

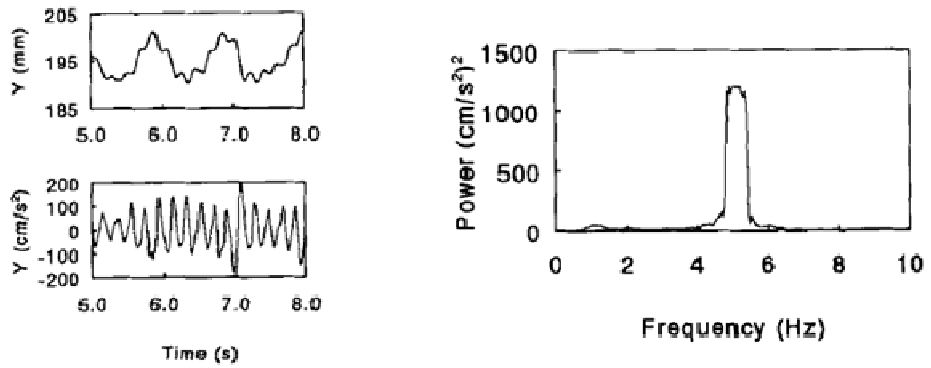

(a) Position and Velocity Signals **(b) FFT of Power**

Figure 1.1. Form of Essential Tremor in the Wrist. Accelerometer reading of a patient's hand shows a tremor of 5 Hz with 1 Hz intended motion. The velocity data shows the tremor's sinusoidal nature (Elble, et al. 1996).

periodic motion is highly dependent on the body part from which the tremor is measured (Table 1.2). For example, tremor associated with the eye can be as high as 35-40 Hz (Bengi and Thomas 1973). Elbow tremor (impacting precision of forearm motions) is much lower, occurring in the range of 3-5 Hz (Fox and Randall 1970). Even lower frequencies have been reported from irregularities of subtetanic motor unit firings (slow nerve firings that do not produce continuous motion). This motion was first suggested by (Schäfer 1886) and were later confirmed in several studies (Allum, et al. 1978; Dietz, et al. 1976; Marshall and Walsh 1956). It has been reported that these motor unit firings produce fluctuations in force and displacement confined to the 0-4 Hz frequency range due to the low-pass filtering properties of skeletal and musculature structure. For healthy individuals, these irregular movements may dominate the motions associated with physiological tremor (Stephens and Taylor 1974; Sutton and Sykes 1967). Rifle aiming is one example where these irregular motions cause barrel "wobble", which was identified to be in the 1-5 Hz range by the National Small Arms Center (NSAC 2007).

Table 1.2. Typical Tremor or Tremor Frequencies in the Body.(Bengi and Thomas 1973; Elble and Randall 1978; Fox and Randall 1970; Higgins and Stultz 1953; NSAC 2007; Paul S. Slack and Ma 2007)

Bodily Region	Tremor Frequency (Hz)	Est. Amplitude
Ocular (Eye)	35-40	1.2 min arc
Wrist	8-12	7 mm
Elbow	3-5	1-5 mm
Body (standing position)	1.5	~ 2 mm

Tremor amplitude is quite variable as well, and depends on both the type of tremor involved and additional factors like muscle fatigue and other psychological conditions. Despite this variability, a strong inverse relationship has generally been reported between amplitude and frequency for normal physiological tremor. In studies conducted by (Elble and Randall 1978), amplitude for wrist tremor was interpolated using a logarithmic function with amplitude of approximately 7 mm at 4 Hz, decaying to 0 mm above 10 Hz (Elble 1986; Elble 1995). Calzetti et. al. (Calzetti, et al. 1987) reported a similar trend with patients suffering from essential tremor. People experiencing the largest amplitudes of motion (10 mm) were moving at frequencies below 4 Hz, while the smallest amplitudes (~ 0.15-1 mm) occurred at frequencies of 7 to 10 Hz (Calzetti, et al. 1987). Physiological tremor amplitude is also a function of muscle fatigue, according to a recent study of a population of trained surgeons (Paul S. Slack and Ma 2007). In these tests, professional surgeons were monitored before and after lengthy surgeries, and tremor amplitudes in general increased after the procedures, with amplitudes ranging from ~1 mm to 5 mm (Paul S. Slack and Ma 2007).

1.1.3 Treatments for Essential Tremor

Active tremor in the form of movement disorders such as essential tremor, Parkinson's Disease (Forssberg, et al. 2000; Teravainen and Calne 1980) and other neurological disorders (e.g. cerebral lesions) may cause significant disability, especially when the tremors become large in amplitude. While rehabilitation is possible

for some forms of stroke (Volpe, et al. 2002), it is limited for patients experiencing conditions such as essential tremor. Individuals who have tremor typically suffer in daily operations and often have difficulty holding a cup or glass without spilling, applying make-up, and eating (Evidente 2000). Those who have occupations requiring fine muscle control and movement (e.g. artists, surgeons, musicians, drafters) often are forced to quit their professions (Evidente 2000). Currently, there are three approaches being made to reduce these debilitating effects – pharmacological treatments, surgery, and assistive devices.

1.1.3.1 Pharmacological Treatments

Pharmacologic treatments exist to help alleviate some of the symptoms associated with movement disorders, but at this time they are unable to slow or stop disease progression. For Parkinson's Disease, medications that produce Dopamine (e.g. Lovodopa) have shown success in alleviating tremor symptoms (NPF 2009), while essential tremor is commonly treated with Beta blockers (Evidente 2000). Currently, there is no established pharmacological treatment for cerebral lesion, and many medications have shown only mixed success (Anouti and Koller 1995). While many patients do benefit from drug treatments, side-effects can be severe – Dyskineasias (abnormal movements) is a common side effect of medications for Parkinson's Disease, such as the case with Lovodopa, and some individuals may additionally experience confusion, hallucinations and psychosis (NPF 2009). Beta blockers used for essential tremor also pose problems because they mask signs of hypoglycemia and may cause significant memory loss and confusion in the elderly (Evidente 2000).

1.1.3.2 Surgical Treatments

For patients who are resistant to drug treatment or have severely disabling tremor, pharmacologic solutions alone are often inadequate (Anouti and Koller 1995; Evidente

2000). In these cases surgical treatments such as thalamotomy and thalamic deep brain stimulation have been shown to be effective, though side effects such as dysphasia, dysarthria, disequilibrium, weakness, sensory loss, and memory decline are still present (Evidente 2000). While these side-effects are temporary for deep brain stimulation, they are irreversible for thalamotomy. Potential risks during the actual thalamotomy surgery are considerable, with the most serious danger caused by bleeding in the brain, causing a stroke. The effects of stroke can be mild or more severe, causing permanent weakness, intellectual impairment, or death (NPF 2009).

1.1.3.3 Assistive Devices

For many patients, the tremor is untreatable or the risks involved from surgery or side-effects from medication are too great. For these individuals, the treatment approach has been to suppress tremor using external physical means. For human-computer interaction, several digital filtering algorithms have been researched to filter tremor noise from a computer input device, including a pen (Riviere, et al. 2003) and a computer mouse developed by IBM R&D (Levine and Schappert 2005). Unfortunately, the effects of tremor often extend beyond computer interaction and in those cases cannot be abated by software,, without the help of additional hardware. The MIT damped joystick, for example, was designed to aid in the control of an electronic wheelchair by physically forcing the person's tremor to cease through a grounded force-feedback system (Hendriks, et al. 1991). A commercially available "Neat Eater" (Figure 1.2) is another device aimed to aid in controlling tremor for eating (Michaelis 1988). This is a passive, physically grounded device that the user can manipulate to control feeding motions. In this device, tremor is reduced through viscous dampers acting directly on the user's arm and rigidly supported against a table or other heavy object. While physically grounded systems like the Neater Eater are effective in

reducing tremor, a major drawback of such systems is that they require a heavy inertial mass to actuate against, making them cumbersome and restricted in mobility.

In response to the inconvenience of stationary grounded systems, recent developments have been made to develop more versatile devices. The DRIFT project (later termed WOTAS), for example, focused on creating a wearable prosthetic for upper-limb suppression (Heath, et al. 2003), which was designed to counteract tremor through the application of actively controlled forces. Similar work in wearable tremor suppression systems has been conducted in the use of magnetorheological (MR) fluids, which change viscosity depending on the type of fluid and the magnetic field applied (Manto, et al. 2003; Rosen, et al. 1995). DC motors have also been utilized in wearable prosthetics, and are similarly used to physically force an individual's tremor to cease (Rocon, et al. 2005). While prosthetics are indeed capable of tremor suppression, they do have design challenges. For passive or damped systems, one of the main drawbacks is that the dissipative force is also resistant to the patient's voluntary motion (Rocon, et al. 2003). This has the effect of restricting intended motion and making the device

Figure 1.2. Neater Eater. A passive device used to stabilize tremors encountered during eating (NeaterSolutions 2009).

awkward and obtrusive to the user. Another significant complication arises in user comfort since significant forces are applied to the muscle affected by tremor and these forces need to be supported by another part of the body, which may cause pain (Manto, et al. 2003). Because these forces need support, these prosthetics require extra structure and can become bulky (see Figure 1.3b).

1.1.4 Mitigation of Physiological Tremor

Unlike movement disorders, normal physiological tremor is typically thought to be benign (Sagma 2003), yet there are several situations when precise motions are necessary (e.g. surgery, micro-assembly, military targeting, etc.) where the damaging effects of tremor can be magnified. In such cases, the individual's tremor cannot be chemically or neurologically corrected since the unwanted motion is simply normal muscle behavior. This presents a challenging problem since potential solutions are limited to external stabilization devices which must be suitably designed to meet the demanding specifications of various occupational conditions. This is a new area of

(a) DC Motor Actuators (b) WOTAS Project

Figure 1.3. Wearable Orthoses for the suppression of human tremor. Sensors detect tremor from the user and force the limb to stop moving (Rocon, et al. 2007; Rocon, et al. 2005).

development and some promising devices are starting to emerge from the medical, manufacturing and military sectors, although they still have several hurdles to overcome.

1.1.4.1 Medical Sector

In the medical sector, any occupation requiring precise positioning or orientating of objects is susceptible to physiological tremor. One example of particular concern is the imprecision caused by operator tremor during microsurgery, which in the past has only been suppressed by arm or wrist rests (Patkin 1977). More recent technological advances, however, have allowed much greater precision through the use of tremor filtering and motion scaling in telerobotic systems (Cao and Rogers 2007). However, because these systems are costly and eliminate patient interaction, there is an increasing trend towards the development of hand-held stabilization systems. One example of such an approach is the "steady hand" robot, where the surgeon and robot manipulate the same tool together (Taylor, et al. 1999) to allow for doctor-patient interaction, but it is still relatively large and bulky.

To address the size issue, the Micron (Figure 1.4) was developed as a hand-held surgical tool employing active cancellation to reject unwanted tremor from an operator while still allowing intended motions (Ang 2004; Ang, et al. 2005; Riviere, et al. 2003). Improvements have been made to the Micron to decrease cost and weight since there is a need for the system to feel like regular passive instruments, however further improvement is difficult due to its use of piezoelectric stacks, which are inherently heavy, expensive, and fragile. For these reasons, the Micron is still significantly larger and heavier than most surgical tools that are much thinner and less massive (most weigh less than 50 g, while the Micron weighs 100 g). In addition, the piezoelectric material used in the Micron offers very little tip displacement, limiting the tool's

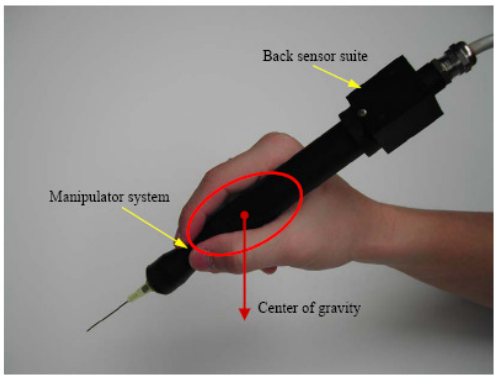

Figure 1.4. Micron Surgical Tool. This 170 g device was designed to produce a tip displacement of 200 micrometers to reduce tremor during microsurgery (Ang, et al. 2005).

usefulness to specialized eye surgeries only; typical surgeon hand tremor amplitude is much larger, ranging from 1 and ~5 mm (Paul S. Slack and Ma 2007). Due to the inherent limitations of the Micron's piezoelectric actuator, stabilizing these tremors (an order of magnitude above its current capabilities) is impossible with the tool's given size. Thus, there is a clear need for a suitable actuation system capable of stabilizing these more general tremors of larger magnitude. Such a system would not only improve the quality of the surgeon's work, but would also have impact on the time required to complete surgical procedures. This would both reduce the patient's time under anesthesia, and reduce the overall complexity of lengthy surgery which has been shown to correlate to a patient's risk of post-operative complications (Sharoky 2005).

1.1.4.2 Manufacturing Sector

Like the medical field, the precision manufacturing industry is also showing a growing need for new hand-held tools featuring tremor isolation. One example lies in photonics assembly, which typically involves macro-scale devices but requires positioning accuracy on the order of tens to hundreds of nanometers (Voyles and Hulst 2005). In this industry, assembly operations cannot be automated since current machines lack the adaptability that a human operator has at the sub-micron scale. For

instance, slight changes in temperature can cause significant geometric deformations, and non-linearities due to friction and backlash are highly unpredictable (Voyles and Hulst 2005). Attachment means such as UV epoxies, solder, and weldments are volatile at these small scales (Kallmayer, et al. 1995; Kallmayer, et al. 1996), and thus require a human operator. As a consequence, most devices are currently being assembled manually under extremely tedious conditions, that are made worse by hand tremor and lack of fine motor control (Tolbert 2002). Hand-held tools that are capable of assisting in tremor cancellation are currently unavailable, but could significantly reduce assembly times that are currently on the order of hours as compared to minutes for electronic devices of similar complexity (Voyles and Hulst 2005).

1.1.4.3 Military Sector

In the military, human tremor affects many operations including range-finding and overall rifle marksmanship. This is typically combined with additional physiological factors, including rapid breathing and heartbeat, due to the extreme stresses encountered during combat. Traditionally, the military has addressed this problem through extensive training, though this is a costly and time consuming process with varying degrees of effectiveness. In actual combat situations, even for the best trained and talented shooters, it is often difficult to perform the fundamentals inherent in good marksmanship techniques, which include assuming and maintaining a steady position, aiming, controlling breathing and executing a proper trigger squeeze (Army 1994; Army 2003). It has been estimated that physiological responses (such as muscle tremor and increased breathing rate) during combat conditions raise the levels of shooter-induced disturbances by at least an order of magnitude higher and interfere with the soldier's ability to keep the rifle aimed on target (Army 2003; Nersessian 2001). Overall, this results in a decrease in soldier survivability, and an increased risk

of civilian casualties especially because today's combat occurs in increasingly urban environments.

Several approaches have been made in the past to counteract the harmful effects caused by soldier tremor. One technique called the Inertial-Reticle System (IRS) was developed at the Army Research Laboratory and employs a video screen to sight the target using an artificial optical grid (Von Wahlde, et al. 1996). Using inertial rate sensors in three axes of rotation to track the rifle motion, the system would automatically fire once the target is aligned with the barrel. The weapon itself is not stabilized in this system, though the effects of user tremor are compensated. While the IRS has potential for increasing aiming accuracy, it is an extremely bulky system (lacking portability) and requires the use of expensive view-finding electronics.

As a result, more recent projects have focused on designing the weapon to be self-stabilizing through an active suspension. Intelligent Automation Inc. for example has worked on developing piezoelectric actuators for barrel stabilization as part of an SBIR program (IntelligentAutomation 2009). The INertially Stabilized Rifle (INSTAR) similarly used piezoceramics with regenerative electronics to cancel tremor in 1 degree of freedom (Bharti and Frecker 2004; Brei, et al. 2003; Lindner, et al. 2002). The INSTAR was successfully demonstrated on the benchtop to reduce human tremor. However, the device was not actually fielded because of robustness concerns with the piezoelectric approach since the actuator was too fragile to withstand heavy shocks likely to occur during combat. Despite these limitations, the INSTAR demonstrated a proof of concept for active tremor cancellation in a weapon system, and with a more rugged, actuation solution, a fieldable system may be possible.

Overall, abnormal human tremor can have a strong negative impact on people's quality of life and occupational performance. Even normal tremor can significantly

interfere with precise hand operations such as those required during surgery or manufacturing. While there are pharmacological and surgical treatments for people suffering from tremor disorders, they may produce dangerous side-effects and are limited in their effectiveness. As an alternative to these treatments, and for normal physiological tremor, assistive devices have significant promise in positively affecting the lives of many people.

1.2 Classification of Tremor Reduction Approaches

Because there is a significant need for assistive systems, several existing approaches have been developed, ranging from large telerobotic systems to small precision instruments. This section surveys these existing technologies and groups them into three main categories: *isolation, suppression*, and *cancellation*.

1.2.1 Isolation

Tremor isolation generally approaches the problem by separating the user from the interacting object or operation. For example, tele-robotic surgery is a form of tremor isolation since motion input is passed through a computer (to filter the human's tremor signal), which then controls robotic manipulators that are in contact with sensitive areas. In these systems actual isolation is achieved through software filtering, and motion is translated to a stable input for a robotic system (Sung and Gill 2001). The key benefits of tremor isolation include the ability to perform motion scaling and the ability, through software, to make moving objects such as a beating heart to appear still to the surgeon (Talamini and Hanly 2005). Tele-robotic surgery is an active area of research and is being studied for use in a variety of scenarios; for a full review, see (Cleary and Nguyen 2002). Intuitive Surgical, Inc. has even successfully commercialized the tele-robotic DaVinci System (Ballantyne and Moll 2003), achieving FDA approval.

While these systems show significant potential, they do possess several drawbacks:

they are expensive, obtrusive, and difficult for many to adapt to. The initial capital cost of a tele-robotic surgical system, for example, can range from one million to several million dollars (Saraf 2006) making it currently prohibitive in most areas other than large research institutes. Additionally, the size of the entire surgical system tends to be extremely large, filling an entire room (Cleary and Nguyen 2002). This poses a significant practicality issue for individuals needing assistance in daily activity. Removing human interaction is also often undesirable – for example many surgeons dislike tele-robotic systems because they do not provide the same feedback (visual, psychological, haptic, etc.) one would receive from direct contact (Saraf 2006). Certain operations in the manufacturing sector, particularly micro-assembly, are unsuitable for tele-robotics because micro-scale environments are highly unpredictable and require a person's ability to adapt in multiple degrees-of-freedom.

1.2.2 Suppression

Tremor suppression, unlike isolation, actually forces a person's tremor to cease by applying a force and displacement to the affected limb. Sensors are used to detect the user's tremor, and controlled forces are applied to the limb from a large stationary object, such as the ground or a large table. The MIT force-feedback joystick (Hendriks, et al. 1991) is a system that utilizes tremor suppression by actuating against a heavy wheelchair to stop the user from shaking and assist in overall control. The Neater Eater (NeaterSolutions 2009) likewise achieves grounding from a large table, to which the device is anchored in order to assist people with disabilities during eating. To achieve a degree of portability, tremor suppression can also be implemented into wearable braces where the bulk of the user's body is utilized for grounding. The DRIFTS project (Figure 1.3b) consists of a wearable prosthetic that achieves this by sensing the user's tremor and applying a computed amplitude of force to counteract its effect. A similar wearable

exoskeleton (Rocon, et al. 2005) was studied for feasibility that utilized a set of DC motors to force the user's tremor to cease.

For several situations, tremor suppression can be a convenient, cost-effective solution. However, for portable hand-held systems, the required exoskeleton (Heath, et al. 2003; Rocon, et al. 2007) can make the overall structure undesirably cumbersome and heavy. Additionally, the amount of force required to stop the patient's tremor is high, making user discomfort a serious issue as was mentioned by Manto et al. 2003. Another issue with tremor suppression prosthetics (especially those using damping) is that they typically do not distinguish between unintended and intentional motions, which makes any intentional motions awkward and difficult (Rocon, et al. 2003). Thus, for hand-held systems, there is a need for an alternative approach that provides comfortable, intuitive operation in a compact lightweight system.

1.2.3 Active Cancellation

Active cancellation is a third category for tremor reduction that shows promise in solving these issues. In this approach, the user's tremor is allowed to exist but its effects are cancelled through a device that is placed between the user and object requiring stabilization. The active device functions by detecting the user's tremor and actuating the stabilized object opposite to the disturbance, resulting in a net zero inertial displacement. The Micron surgical tool (Choi and Riviere 2005) is one example of an active cancellation device used in surgical operations where the user's tremor is cancelled with a piezoelectric stack. The INSTAR (Brei, et al. 2003) similarly uses piezoelectrics to achieve active cancellation for rifle barrels. Another commercially successful use of active cancellation lies in Image Stabilization (IS) where many high-end cameras use electromagnetic or piezoceramic actuators to move the image sensor or lens to compensate for hand tremor (Sidman 2006).

While the active cancellation approach is useful in several applications, it does have some limitations. A primary issue lies in its implementation, since for hand-held systems the actuator must be capable of producing large strokes at the required frequencies, yet remain lightweight and compact. The actuator must also be robust enough to withstand the rigors of daily use, and its power consumption must be minimized to allow for a small, self-contained battery.

1.2.4 Summary and Downselection

Of the three approaches, active cancellation is the most promising for daily use for human tremor based upon several metrics listed in Table 1.3. Since the user's tremor is allowed to exist, there is no risk of discomfort or pain during operation (as experienced in tremor suppressing applications). Active cancellation systems can be highly portable and versatile for daily activities, which is infeasible for most tremor isolation systems. This is primarily due to the low force/displacement and structural requirements that allow for smaller, lightweight, and low-cost actuators. Self-contained packaging is also

Table 1.3. Comparison of the different technological approaches for tremor reduction. Active cancellation provides the most desirable solution for hand-held systems.

	Spec.	Isolation	Suppression	Active Cancellation
System Size (Volume)	Small (<18 cm^3)	Large (fits in room)	Medium, must be grounded to stationary object	**Small**, fits inside/around stabilized device
System Weight	Small (50g)	Very High	Medium	Medium (currently)
Cost	Low (<$100)	High, several million dollars for tele-robotic systems	Medium, less than one thousand dollars	Medium, less than one thousand dollars
Convenience	High	Low – obtrusive	Medium	**High**
Complexity	Low	High	Low	**Low**
User Acceptance / Comfort	High	Low -- Difficult to use at first, non-intuitive	Low -- Can cause pain and discomfort	**High** – Intuitive, devices used as they normally would be

feasible in active cancellation systems through the use of modern sensors and microcontrollers. Finally, active cancellation provides significant potential for intuitive use with almost no learning curve, allowing for greater user acceptance.

However, a suitable hand-held active cancellation technology has not yet been fully realized due to several main constraints. Table 1.4 provides a summary of the overall system needs for the medical/manufacturing, rehabilitation, and military sectors. To have the greatest impact across these areas, the tremor reduction system must be capable of generating large amplitude motions (1-5 mm), for low frequency (<4 Hz) elbow and full-body tremors (Elble 1986; Elble 1995; NSAC 2007). These tremors typically produce the most motion and are selected as a target of this dissertation's work. To cancel these disturbances, the system must be capable of sensing the user's tremor, distinguishing intended from unintended motion, and filtering out the disturbance. This can be achieved either through programmed or mechanical means where a predictable, controllable motion output is required to counteract the tremor's effect. For ease of use and versatility, the overall size of the system must be capable of being scaled to hand-held implements, on the order of 18 cm^3 (Choi and Riviere 2005) with a weight approaching 50 grams. This form-factor allows the system to be portable and applicable to a variety of hand tools. Additionally, cost must be low (less than $100) to reach individuals seeking assistance in daily life. For mobile systems, a battery power supply may be required, which must have a run-time that is greater than one hour (which makes minimal power draw a desired trait). For most applications, it is desirable that the entire device be self-contained in a rugged form-factor with the sensors and battery packaged inside.

Table 1.4. Actuation needs for tremor cancellation across multiple sectors. Conventional actuators typically cannot meet these challenging requirements. (Choi and Riviere 2005; Pathak, et al. 2007; Paul S. Slack and Ma 2007; Sagma 2003)

	Medical/Manufacturing	Prosthetics / Rehab.	Military
Frequency (Hz)	0-12	< 0-12	0-3
Amplitude (mm)	~0.02-5	~1-5 (may be larger)	~4
Volume (cm^3)	18	20-30	41
RMS Reduction	> 50%	>50%	>50%
Weight (g)	50	<100	<350
Ruggedness	Low	High	High
Battery Life	>1 hr	>1 hr	>1 hr
Cost	Medium (~$1K-10K)	Low (~$100)	Medium (~1K)

The extent of tremor cancellation is another requirement that must be considered when designing an effective product for daily use. Current deep brain stimulation (DBS) treatments use a Root Mean Square (RMS) amplitude reduction as a method of calculating tremor reduction (Putzke, et al. 2004). The RMS of the patient's tremor with the DBS device on is subtracted from the baseline RMS with the device off. This difference is divided by the baseline RMS to produce a percent reduction. In the study conducted by Putzke, et. al. 2004, it was shown in a study of 52 individuals treated by DBS that the average RMS tremor amplitude was reduced by approximately 50%, producing significant improvement in quality of life. On a 5-point qualitative chart, the average tremor was reduced from a score of 4 to 1, where 4 is described as "severe/disabling" and 0 represents no functional disability. Thus, to produce similar results, a 50% RMS reduction in human tremor was chosen as an additional design goal. By meeting this level of assistance, significant improvements in quality of life should be expected, and a viable alternative to conventional treatment methods such as DBS would be produced.

1.3 Actuator Selection for Active Cancellation

While active cancellation is a promising technological approach to tremor mitigation, its implementation in a hand-held compact system is a challenge due to strict actuation requirements. In general, the actuator must be capable of producing

relatively large amplitudes at human tremor frequencies in a lightweight, compact package (Table 1.3). In addition, it must be predictable, controllable, and capable of running at relatively low powers for battery operation. With these requirements in mind, this section delivers a comprehensive review of both conventional and unconventional actuation technologies to identify a potential actuator solution.

1.3.1 Conventional Actuation vs. Smart Material Actuation

While conventional off the shelf technologies such as electrical, hydraulic, and pneumatic systems offer attractive solutions to many large-scale applications, they typically suffer in performance when scaled down to the size needed for hand-held systems. The stress-strain comparison of actuation technologies (Figure 1.5), for example, shows that both solenoid and moving coil transducers, while capable of providing high strains (~ 50%, Figure 1.5), suffer in actuation stress (over three orders of magnitude less than smart materials), significantly reducing their specific work. In the chart, Figure 1.5, Hydraulic and Pneumatic systems provide the highest specific energy though they require large infrastructure (compressors and fittings) that are not accounted for in the calculation. Thus, to produce the same amount of work as smart materials (such as Shape Memory Alloys), the conventional actuator must increase in weight by almost three orders of magnitude (Figure 1.5), which is highly undesirable for handheld systems. Figure 1.6 further illustrates that smart materials can produce significantly greater amounts of work per unit volume than conventional actuators. Piezoelectrics, Magnetostrictors, and Shape Memory Alloys are all capable of producing nearly two orders of magnitude greater power at the same operating efficiency as pneumatic or moving coil systems. This additionally shows that smart materials can produce the same amount of work as conventional actuators, but in volumes that are roughly two orders of magnitude less (Figure 1.6), thus allowing for

the actuator to be embedded in highly compact spaces that are required for hand-held systems. Actuator weight is another critical metric in which smart materials outperform conventional technologies (Figure 1.7) at or below 100 grams. This is primarily due to the difficulty in miniaturization of electro-mechanical components, and the unavoidable reduction of magnetic flux density in small motors (Ikuta 1990).

This effect is apparent when considering a the tremor cancellation application for moderate amplitude. To illustrate this point a relatively small stabilized object can be considered requiring 3.5 N force, with a displacement of 7 mm. A compact electro-magnetic solution can be found in a voice coil linear actuator manufactured by H2W Technologies. This moving coil actuator is capable of providing a 7.1 mm stroke with 3.6 N continuous force output, and takes the form of a cylinder that is 53 mm long and 36 mm in diameter (H2WTechnologies 2009). The total weight of the system is 369 g, assuming that there is no bearing system (H2WTechnologies 2009). This weight is large for a hand-held tool to be used in every-day use, and can be expected to double for additional degrees of freedom due to the requirement of additional permanent magnets and moving coils.

A commercially available SMA actuator can also be built for the tremor cancellation application using the Flexinol wire supplied by Dynalloy, Inc. According to specifications, a 6 mil diameter wire is capable of operating under the 3.5 N requirement (Dynalloy 2009), and assuming a conservative operating strain of 3%, a length of 233 mm is required, which can be packaged through spooling or wrapping within the voice coil packaging (Redmond, et al. 2008). Assuming a density of 6.45 g/cm^3 (Dynalloy 2009) the total mass of the SMA wire is only 27 mg, which is over 10,000 times smaller than the voice coil actuator. Even with the use of coolant such as mineral oil (to improve frequency), the overall size and weight of the SMA actuator can

be designed to be considerably less than the voice coil, and would not considerably increase with additional degrees of freedom.

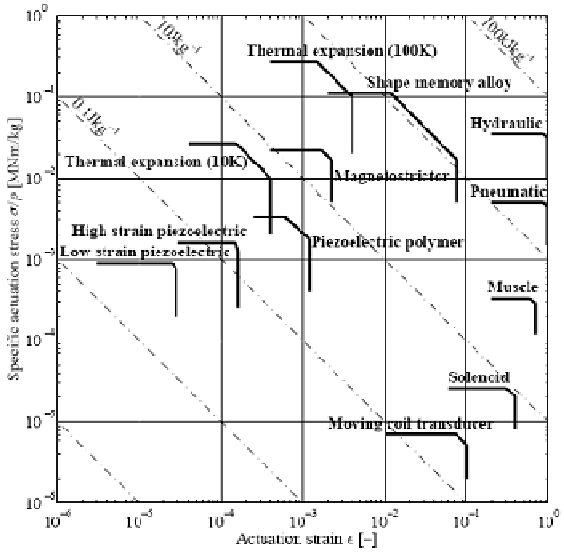

Figure 1.5. Stress-strain properties of both smart material and conventional actuators. Of all smart materials, Shape Memory Alloys provide the highest specific energy (Huber, et al. 1997).

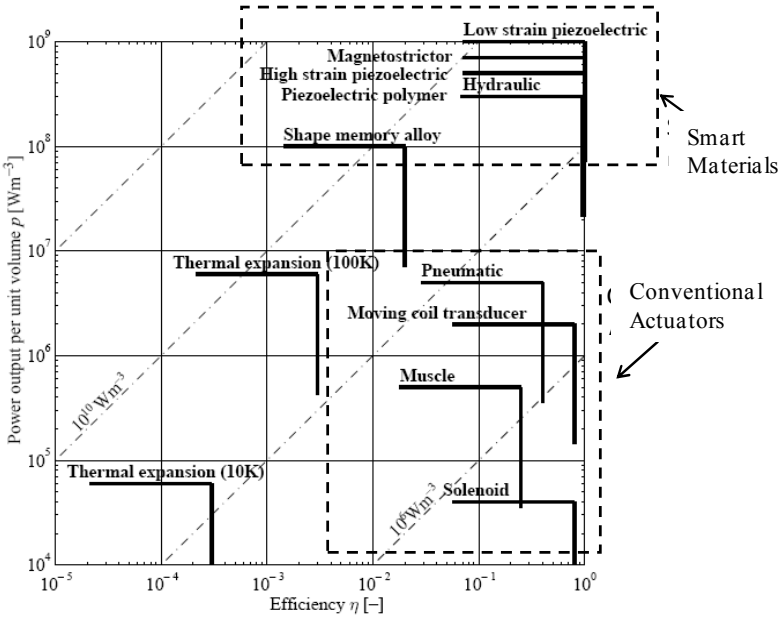

Figure 1.6. Power Density vs. efficiency of conventional technologies. Smart materials provide the greatest power output for a given operating efficiency **(Huber, et al. 1997).**

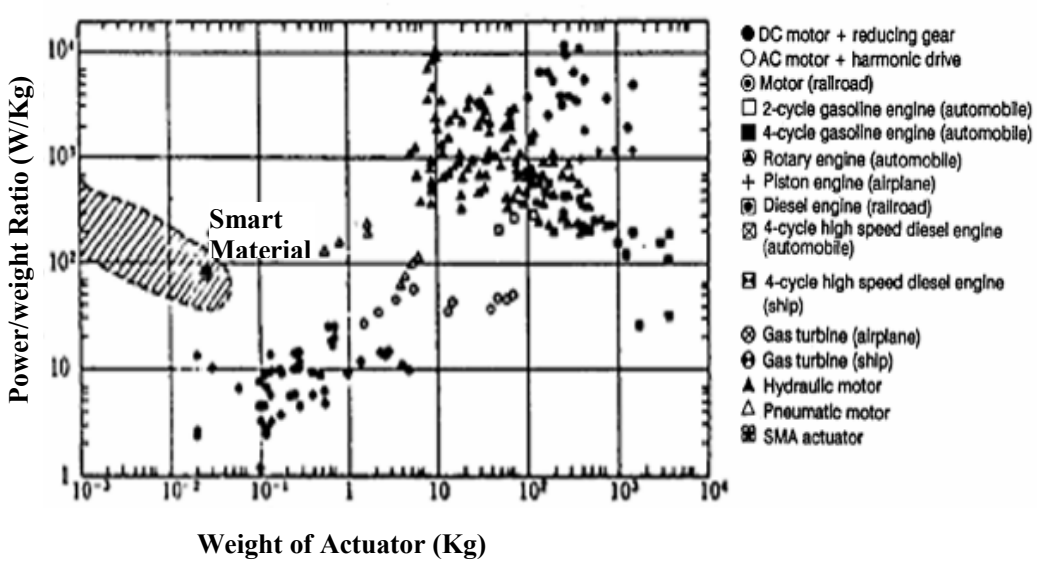

Figure 1.7. Power/weight ratio vs. actuator weight of actuation technologies. Smart materials operate at a unique region of low weight and moderate power (Ikuta 1990).

While the increased power requirements of the SMA wires do increase the overall battery weight of the hand-held system, the overall weight savings with the battery/actuator combination are superior. To show this, it is assumed that the energy required to drive the SMA actuator is due to the latent heat of transformation, 24.2 kJ/kg (Dynalloy, 2009), and convective heat transfer. The power lost due to convection is calculated assuming a 23 °C ambient mineral oil coolant with convective coefficient assumed of 1000 W/m^{2}K, and average wire surface temperature of 50 ºC. Thus, using these metrics the same 6 mil diameter, 233 mm long SMA wire operating at 3 Hz, is estimated to require 6 Watts of power. For a 1 hour run-time, a lithium ion battery of 37.5 grams would be required, assuming a battery energy density of 160 Wh/Kg (Vincent 2000). The voice-coil, on the other hand, consumes 0.7 W of power (H2WTechnologies 2009) and thus requires only 4.5 grams of batter weight. However, the combined actuator/battery system would equal 373.5 grams, which is nearly 10 times greater than the combined actuator/battery weight of the SMA actuator (38.53

grams). In fact, assuming 100 grams are used for the mineral oil coolant (which at 0.8 g/cc produces an ample 125cc), the SMA battery/actuation system is still lighter than the voice coil system for run-times of less than 7.3 hours. This run-time is ample for most daily activities, and the battery of the hand-held device can easily be charged between these periods of use. For longer periods of continuous run-time a connected power source can be used in versions that aim to maintain the lightweight and compact benefit of the SMA actuator.

1.3.2 Smart Materials

Due to their advantages over conventional systems, smart materials present a promising solution for a lightweight, compact, and simple actuator in a new class of hand-held active cancellation systems. Four smart material actuation types (magnetostrictors, electrostrictors, piezoelectrics, and shape memory alloys) were selected as potential candidates due to their capability of delivering high forces and displacements while satisfying frequency requirements. The following sections present each actuation technology in detail including the mechanism of actuation, technology benefits, and drawbacks. A general summary and comparison is provided in Table 1.5.

1.3.2.1 Magnetostrictors

Magnetostrictors are materials typically consisting of alloys of iron and rare earth elements such as terbium and dysprosium, which generate strains in response to an externally applied magnetic field (Cullity and Graham 2008). The work density of this material (work output per unit volume) typically lies in the range of 18-90 KJ/m^3 (Lagoudas 2008) and the output strain typically saturates at 60 microstrain for pure elements such as Cobalt. By alloying multiple elements, “giant” magnetostriction can be accomplished, and one alloy, Terfenol-D, can produce strains of up to 0.1% (Clark 1980) and is most commonly used in engineering applications such as in ultrasonic

transduction and vibration control of heavy structures (Dapino, et al. 2000). The response speed of magnetostrictors, can be fast, from 10-30 KHz, (Lagoudas 2008) because the mechanical response is due to the rapid molecular response from an applied magnetic field. However, the material is inherently nonlinear and exhibits significant hysteresis, making it difficult to control (Banks, et al. 1997). Another disadvantage with magnetostrictors is their need for a controlled magnetic field to produce actuation. This requirement essentially cancels out any benefits gained from the material's high specific work because additional volume and weight must be used in a packaged field-generating device. The low actuation stroke of the material is another issue since complicated leveraging would be needed to produce sufficient motion for tremor cancellation. In addition, overall cost is high, and the material is brittle and fragile. For these reasons, the material is unsuitable for any hand-held systems requiring a small and cost-effective actuator capable of producing large stroke.

1.3.2.2 Electrostrictors

Electrostrictors function like magnetostrictors except they require an electric field to produce mechanical actuation. This phenomenon is due to the presence of small electric domains that are randomly oriented throughout the material. When an external electric field is applied, these domains rotate and produce a bulk strain. Unlike piezoelectrics, these domains are isotropic in the absence of an electric field and are not poled (Sundar and Newnham 1992). The work density (up to 200 KJ/m^3) achievable by electrostrictors is relatively high when compared to magnetostrictives and piezoelectrics indicating that the material can produce larger stresses, 60-180 MPa, (Lagoudas 2008) over similar operating strains (Table 1.5). The material also has a low hysteresis (<1%) in a limited temperature range (Uchino 1992), though despite this reduced hysteresis, electrostrictives are highly non-linear, exhibiting a roughly

Table 1.5. Comparison of viable smart material linear actuation technologies. Shape memory alloys have the highest work densities and strain.

	SMA	Magnetostrictive materials	Electrostrictive Materials	Piezoelectric
Work Density	2– 18 MJ/m^3 [1]	18-90 kJ/m^3 [1]	42-200 kJ/m^3 [1]	7-60 kJ/m^3 [1]
Actuating Strains	2-6% [1]	0.05-0.09% [1]	0.06-0.1% [1]	0.06-0.2% [1]
Specific Work	0.7-3 kJ/kg [2]	4-7 J/kg [2]	8-20 J/kg [2]	1-3.5 J/kg [2]
Hysteresis	High [3]	High [4]	Low [5]	High [5]
Frequency	0.1-20 Hz [1]	10 Hz-30 kHz [1]	10 Hz-1 kHz [1]	10 Hz-1 MHz [1]

[1] (Lagoudas 2008); [2] (Huber, et al. 1997);
[3] (Banks, et al. 1997); [4] (Tan and Baras 2004)
[5] (Uchino 1992);

quadratic relationship between voltage and displacement (Banks, et al. 1997; Hu, et al. 2004). Another drawback is their high electrical capacitance, which is up to five times as high as piezoelectrics. This significantly increases the required driving currents at dynamic operation. Additionally, the fact that they produce very small strains makes their applicability to stabilizing actuators difficult.

1.3.2.3 Piezoelectrics

Like electrostrictors, piezoelectrics are capable of producing a net mechanical strain from an externally applied electric field. This is accomplished through the deformation of aligned domains within the material (Arnau 2008). Achievable strains are in the range of 0.06-0.2%, though the work density is typically lower than magnetostrictives or electrostrictives (on the order of 7-60 KJ/m^3) due to lower actuation stresses in the range of 10-30 MPa (Lagoudas 2008). However, piezoelectrics have many additional advantages over electrostrictors. For example, they operate over a wide range of frequencies (10 Hz to 1 MHz), allowing for their use in motors (linear or rotary) where a highly rapid microscopic piezoelectric motion can be translated to smooth macroscopic output motion (Hemsel and Wallaschek 2000). Piezoelectrics also exhibit approximately linear behavior in the first order (Chopra 2002), and have

relative temperature insensitivity (Banks, et al. 1997). Due to their electrical nature, they have a very fast response time, as opposed to servomechanisms that suffer from lag (Banks, et al. 1997).

Because of all these favorable qualities, piezoelectric actuators have been developed for hand-held stabilizers including the INSTAR and Micron surgical tool, discussed in Section 1.2.3. In the INSTAR project, piezoelectric actuators with regenerative electronics were chosen and developed for a 1 degree of freedom rifle stabilization platform (Lindner, et al. 2002). These piezoelectric actuators were semi-successful. They demonstrated the necessary performance of ±400 μm resulting in a point-of-aim displacement of ±1.5 m at 400 m range, and the regenerative electronics increased battery life from ~1000 to ~8000 shots, assuming a standard 9v battery and a 2 second per shot run-time. However, the actuator was too large to fit into the stock (22 by 28 by 128 mm) and was heavy (500g). In addition, even if manufactured in bulk the cost of the actuator, regardless of piezoelectric form (ceramic or single crystal), was expensive. Most importantly, there were strong concerns about incorporating this into a "real" fielded system due to the fragility of piezoelectrics and their sensitivity to environmental conditions, especially in water, considering the high voltages employed (±200 V). Due to these concerns, implementing piezoelectrics in hand-held cancellation systems can be a significant challenge, motivating the search for an alternative smart material.

1.3.2.4 Shape Memory Alloys

Shape Memory Alloys (SMAs) offer an attractive solution to the problems encountered with piezoceramics due to their low cost, high work density, and ability to withstand shock. The work density of SMAs are the highest of the materials compared, ranging from 2-18 MJ/m^3 (Lagoudas 2008). This is due to their high actuation strains

(of 2-6%), which is orders of magnitude greater than other smart materials such as piezoelectrics and magnetostrictors (Table 1.5). The specific work of SMA (work per unit mass) is also high, ranging from 0.7-3 KJ/Kg, showing the greatest promise for use as a lightweight actuator. Because of these properties, and the fact that the material is available in wire-form, several packaging techniques can be employed such as spooling (Redmond, et al. 2008), or bio-mimicry – e.g. as human tendons – (De Laurentis and Mavroidis 2002) to enable actuator's use in a wide variety of form factors. Due to an outer oxide layer, SMA's are also chemically resistive to the environment (Rondelli 1996), and are commonly being sought for implantations within the human body (Shabalovskaya 1996). The cost of SMA is comparatively low in wire form. When compared to piezoceramic stacks on a work-normalized basis, SMA wire is capable of producing work at a cost of approximately 5.80 $/J (Dynalloy 2009). This is three orders of magnitude less than that of the piezoelectric stack, which has an increased production cost of approximately 5,600 $/J (Piezomechanick 2009). Despite its many merits, SMAs have several challenges including their slow frequency response (0.1-20 Hz), which is primarily dictated on the heat transfer rate to/from the material (Lagoudas 2008). SMAs are also non-linear and hysteretic, which creates problems in predictability and control. By addressing these challenges to manage its limitations, however, the benefits of SMA can be exploited to create a lightweight, compact solution for tremor cancellation. Thus, the material was therefore selected for further investigation.

1.4 Shape Memory Alloy Background

Due to its high stroke, low cost, and high work density, SMA is appealing for its application in hand-held tremor cancellation devices. To use the material in an application, however, it is necessary to understand the details of its function and

address the material's shortcomings. To introduce the material, a brief history of its discovery and development is outlined in the following section along with a discussion of the atomic mechanisms behind the shape memory effect and pseudoelasticity. Applications (across several different sectors) utilizing these unique properties of shape memory alloys are presented. A survey of the material's known issues and research areas is also presented, to give context for this dissertation's research.

1.4.1 History of Shape Memory Alloys

The shape memory effect was first observed in 1932 by Swedish researcher Arne Ölander who observed the shape change abilities in gold-cadmium alloy (Au-Cd), noting its ability to create macroscopic strains (Ölander 1932). In 1950, L.C. Chang and T.A. Read studied this phenomenon in Au-Cd at the microscopic level, using x-rays to measure the changes in internal crystal structure. These researchers noted the effects of stress, and temperature on the diffusionless phase transformations responsible for the material's shape memory effect and superelasticity (Chang and Read 1951). Broad applications of shape memory alloys, however, were not found until the material and manufacturing advances discovered at the Naval Ordinance Laboratory (NOL). These developments were sparked in 1959, when William J. Buehler was investigating equiatomic nickel-titanium compositions (which he named NiTiNOL -- **Ni**ckel **Ti**tanium **N**aval **O**rdinance **L**aboratory) for use in the nose-cones of reentry vehicles. Initially Buehler noticed some distinct changes in acoustic damping properties of the material, as a Ni-Ti bar when dropped would ring like a bell when hot, but would only produce a dull "thud" when cool indicating curious damping properties (Kauffman and Mayo 1997). In 1961 Buehler produced a small strip of Nitinol to demonstrate the material's fatigue resistance during a laboratory meeting. It was in this meeting that Dr. David S. Muzzey, who was present at the meeting, applied heat from his pipe lighter

causing the material to stretch outward, demonstrating the shape memory effect (Kauffman and Mayo 1997).

Following this essentially accidental discovery, Dr. Frederick E. Wang joined Buehler's group and helped further material developments. Initially, progress of finding applications for Nitinol was slow due to manufacturing problems, expense, and difficulty in obtaining consistent performance between batches (Kauffman and Mayo 1997). However, Buehler and Wang continued to work on the material, studying the effects of composition (e.g. 55-Nitinol, 60-Nitinol), manufacturability issues, and possible applications (Buehler and Wang 1968). Wang, an expert on crystallography, also studied the mechanism behind this shape change, in an effort to understand the overall crystal lattice of Ni-Ti and the displacive movement of atoms during phase transition (Wang, et al. 1965). Eventually this work paid off, and the team was able to eliminate major manufacturing issues (Buehler and Wang 1968; Kauffman and Mayo 1997). After the discovery period of the 1960's, extensive research has been conducted to clarify some of the subtleties with the material including its phase diagram, precipitates resulting from heat-treatments, and the R-phase transformation. An extensive summary of the current state of metallurgical understanding can be found in the recent publication by Otsuka and Ren 2005.

1.4.2 Shape Memory Phenomena

The primary reason for the unusual behavior observed in shape memory alloys is due to its diffusionless phase transformations. While changing shape, the material's crystal structure is also changing from a Martensite phase (B19' for NiTi) to a high temperature Austenite phase (B2 for NiTi) (Otsuka and Ren 2005), which is "programmed" in the material through an annealing process (Bhattacharya 2003). Because of its low degree of symmetry, the crystal structure of the Martensite phase can

exist in several symmetrically related variants that are energetically equivalent. Under zero stress, these variants tend to form self-accommodating arrangements called twinned Martensite, which produce no macroscopic strain. If stress is applied the variants re-orient in a single direction producing De-twinned Martensite and causing a net deformation (Shaw 2002). Because the crystal structure is both stress and temperature dependent, it can be manipulated to produce two useful phenomena: The Shape Memory Effect and Pseudoelasticity.

1.4.2.1 Shape Memory Effect

The Shape Memory Effect (SME) describes the low-temperature deformation of the material and subsequent recovery upon heating. In Figure 1.8 this is illustrated

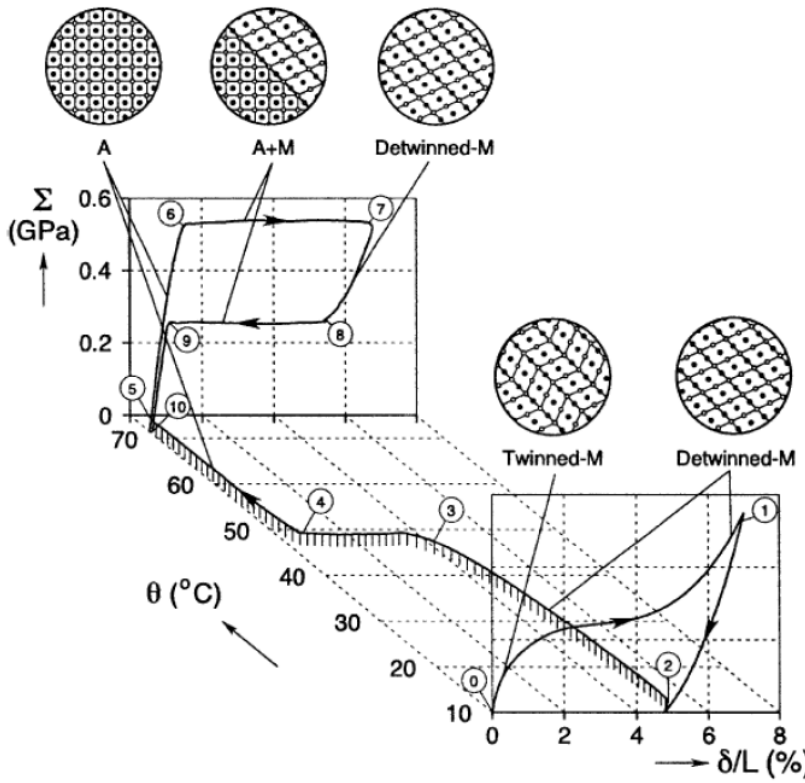

Figure 1.8. Transformation from the Austenite to Martensite phase, in two temperature regions. The shape memory effect occurs when deformation is recovered upon heating (Shaw 2002)

beginning at point ⓪, where the material is cooled below its Martensite finish temperature, M_f (which can be adjusted by slightly altering alloy composition), thus producing randomly oriented twinned Martensite. The material is mechanically loaded between points ⓪ and ①, causing a number of the randomly oriented twinned variants to align and producing a macroscopic deformation that remains after unloading to point ②. When the material is heated to point ③, a reverse transformation from Martensite to Austenite occurs, leading to a complete shape recovery to point ④. Because the phase transformation characteristics of the material are reversible, this cycle can be continuously repeated (by cooling to point ⓪).

1.4.2.2 Pseudoelasticity

Pseudoelasticity (or superelasticity) is a unique property of SMA where deformations are recovered after unloading when the material is held above the Austenite finish (A_f) temperature. Figure 1.8 illustrates this effect, beginning at point ⑤ with the wire heated under zero load. Upon loading, the Austenite structure is deformed under its modulus of elasticity until point ⑥ is reached where an initial Martensite nucleation occurs. This nucleation event typically occurs at a slightly raised stress above the Martensite transformation plateau that is dependent on the loading rate and heat transfer to the environment (Iadicola and Shaw 2004). The continued loading from ⑥ to ⑦ occurs at a relatively constant stress at this plateau as the internal phase of the material is transforming directly from Austenite to stress-induced de-twinned Martensite. At point ⑦, loading is removed and the stress-strain path descends to point ⑧ where the Austenite nucleation event occurs (at a stress below the reverse transformation plateau). At point ⑨ the reverse transformation is completed, producing 100% Austenite, and completely unloading the material returns the curve to its starting point (point ⑩). It is important to note that the stress of the Martensite and Austenite

"plateaus" (i.e. between points ⑥-⑦ and ⑧-⑨) are highly dependent on the temperature of the wire (Dye 1990).

1.4.3 Applications

Since their discovery, there have been many applications utilizing both the pseudoelastic properties and the shape memory effect of SMAs in various architectural configurations. These applications utilize the material either as an actuator (controlled heating), a reactive device (responding to environmental temperature changes), or a super-elastic metal. Many clever inventions have taken advantage of these uses, which currently span the military, aerospace, medical, and consumer market sectors.

1.4.3.1 Military and Aerospace

The first successful use of Nitinol employed the shape memory effect to create a reactive "shrink-to-fit" pipe coupler. This device was developed by Raychem Corporation in 1969 to join hydraulic lines on the F-14 Jet Fighter. This coupler was composed of a Nitinol alloy with a low transition temperature (below -120^{o} C) with its Austenite shape formed to the final deployed coupling dimensions (Kauffman and Mayo 1997). Before fitting the coupler, it was first cooled in a liquid nitrogen bath and radially expanded (deformed) so that upon warming to room temperature the coupler shrinks producing a desirable compression fit. SMAs have also been successfully used in space applications. The Frangibolt release device (Busch, et al. 1992) is one example that uses SMA that is gradually heated to sever mechanical connections that would otherwise be released with pyrotechnic mechanisms introducing unwanted shock. It was estimated that until 1984, 14% of space missions experienced failure due this shock causing missions to be aborted in some cases (Godard, et al. 2003).

Several research programs have also studied SMA for use in aerospace applications. The Smart Wing program is one example that investigated the use of

SMA tendons to actuate hingeless ailerons. In addition, SMA torque tubes were employed to achieve wing twisting(Pitt, et al. 2001). The Smart Aircraft and Marine Propulsion System demonstration (SAMPSON) project demonstrated the use of SMA to tailor the inlet geometry of various propulsion systems including that used for the F-15 (Sanders, et al. 2004). A similar concept was recently used by Boeing, Inc. in the development of active "chevrons" along the trailing edge of exhaust nozzles to optimize the trade-off between noise mitigation and engine performance during flight (Mabe, et al. 2006). Flight testing has been conducted with these devices showing positive results, and development for commercialization is continuing (Hartl and Lagoudas 2007).

1.4.3.2 Medical Field

In the medical field, Nitinol has found several different applications due to its biocompatibility. One of the most widespread uses has been the development of stents (Figure 1.9) where pseudoelastic SMA is used to support weak or blocked arteries and airways (Tsugawa, et al. 1997). The field of cardiovascular surgery has also benefited from SMA, where various surgical tools such as graspers (Duerig, et al. 1999) have been developed. The Simon vena cava filter (Figure 1.9) is another medical device that deploys once inside the body and functions as a filter for large embolized blood clots. These clots present a serious risk if they reach the heart or lungs, so they are trapped by the lower legs of the apparatus and dissolved over time. To keep the device in its Martensite phase, it is mechanically deformed by constraining it within a sheath. Once the device is in position, the sheath is removed and the device deploys. The material's pseudoelasticity has also been utilized in the design of endo-surgical tools (Figure 1.9) where SMA components allow for distal steering and deployment (MemryCorporation 2009). Additionally, pseudoelastic SMA in wire form has found applications in

orthodontics due to their ability to exert a nearly constant force over large strains. Some eyeglasses use SMA as well, allowing the metallic structure to recover what normally would be severe and damaging distortions (Figure 1.9).

1.4.3.3 Consumer Market

Shape memory alloys have also found applications in the general consumer market. For example, in the household consumer market, anti-scalding devices have been developed for water faucets and shower heads to shut off the flow of water should its temperature go beyond a certain limit (Kauffman and Mayo 1997). Other simple inventions using SMA include automatically lowering deep fryers (Falcioni 1992), thermally activated clothing for firefighters that produce an air gap when heated (Congalton 1999), and the widespread use of pseudoelastic cell phone antennas (Kauffman and Mayo 1997). Recently, the automotive industry has also taken interest in the material. Active air dams (McKnight, et al. 2009), for example, have been developed at GM, which employ SMA actuators to change the vehicle's aerodynamics and ground clearance depending on the speed of the car. SMA actuated louvers have

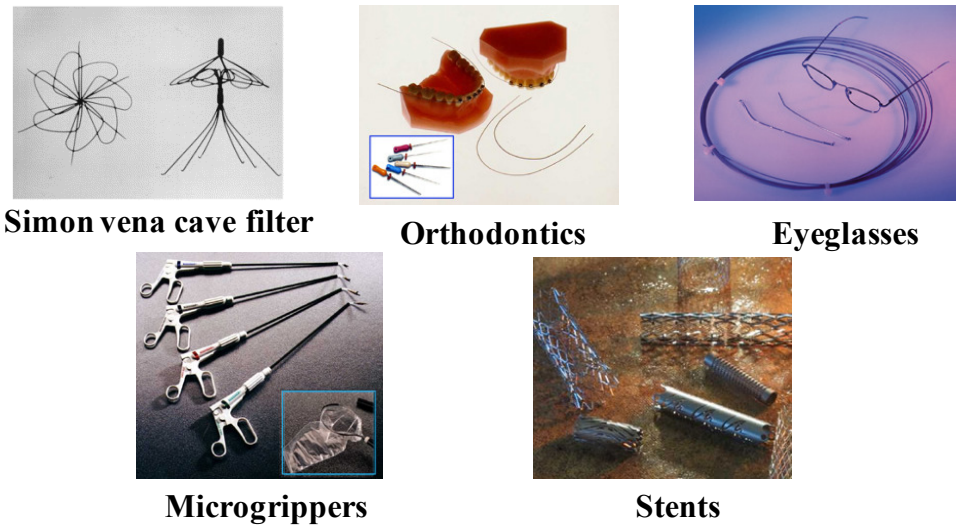

Figure 1.9. Examples of SMA biomedical applications. Most current applications utilize the shape memory effect. (MemryCorporation 2009)

also been developed to reduce cooling airflow in the engine, which will decrease engine warm-up times and decrease drag at high speed (Browne, et al. 2008).

1.4.4 Antagonistic Architecture

When building an actuator that utilizes the Shape Memory Effect, a practical means must be designed to apply a mechanical load while the material is cooling and allow for cyclic motion. This can be achieved using three methods: spring-reset, load-reset (e.g. due to gravity), and antagonistic actuation (Figure 1.10). Unlike spring- and load-reset architectures, antagonistic actuation employs two opposing SMA wires to parallel the antagonistic nature of biological muscles and produce cyclic motion. This is achieved by alternately heating one wire while the opposing wire is cooled.

For many applications, spring-reset and antagonistic mechanisms often have an advantage in packaging over other architectural solutions. Load-reset architectures are more limited in use as they require a large mass, are difficult to package, and are restricted in zero-gravity environments such as in outer space (Reynaerts and Brussel 1998). Traditional spring- and load- reset configurations also suffer from drawbacks in actuation speed when compared to antagonistic actuators since they solely rely on cooling for the return cycle (Ditman, et al. 1996). Additionally, they are difficult to control through the SMA's hysteresis (Song, et al. 2003) and provide only a 1-way work output which is asymmetrical and difficult to implement for vibration cancellation applications. For the cancellation of human tremor, antagonistic actuation is the most suitable configuration (Table 1.6) because it offers a greater range of controllability and higher frequencies (Ditman, et al. 1996). Because both directions are actuated by the SMA wires, uniform controllable cyclic motion can be produced with a custom heating input signal to match the inverse of human tremor (which also often approximates a uniformly cyclic motion). Higher frequencies are also possible as the

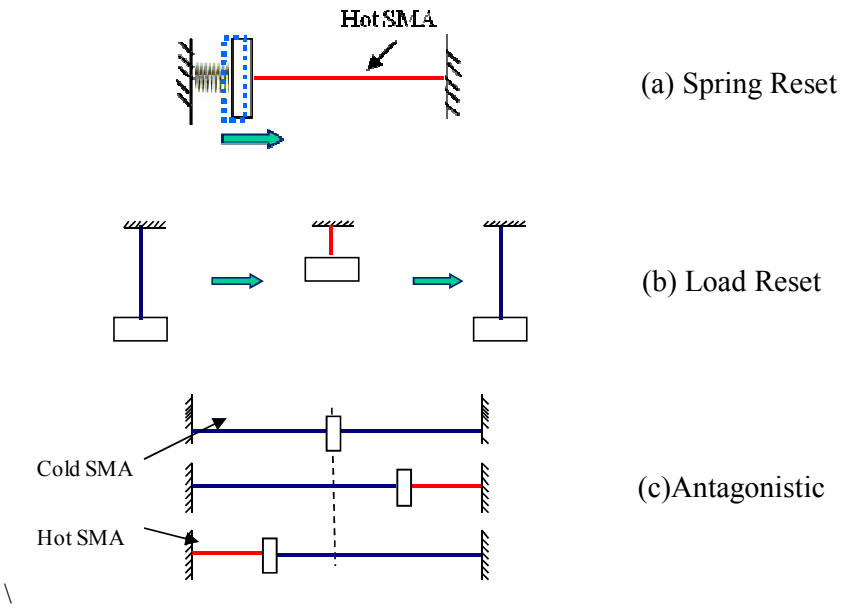

Figure 1.10. Typical Actuation Schemes. Antagonistic actuation provides greater range of control and can be run at higher frequencies than other methods.

wires can be actuated while their opposing pair is still cooling (Ditman, et al. 1996), though care must be taken to prevent over-stressing both wires.

Because of these benefits, antagonistic actuation has been widely used in a variety of applications. For example, antagonistic SMA wires have been developed to mimic tendons in prostheses for human assistance (De Laurentis and Mavroidis 2002; Pfeiffer, et al. 1999). Several applications in position control were developed including an adaptive control surface for an aircraft wing (Maclean, et al. 1997) and a rotor blade tracking system (Singh, et al. 2003). The reciprocal motion of the actuator was also proven to be beneficial in the control of automotive mirrors (Williams and Elahinia 2006) and in micromanipulation (Bellouard, et al. 1998; Kohl, et al. 2002; Zhang, et al. 2001).

While these applications demonstrate the actuator's benefits, several challenges in the implementation of antagonistic SMA exist and have not been completely resolved. Actuation frequency and power draw, for example are difficult to accurately balance, and only basic estimates are made to guide coolant selection (Huang 2002). However,

Table 1.6. SMA Architecture Comparison for Human Tremor Cancellation. The antagonistic configuration presents the most desirable solution.

	Spring Reset	Load Reset	Antagonistic
Packaging	**high**	low	medium
Ease of Control	no	no	**yes**
Low Weight	**yes**	no	**yes**
2-Way Work Output	no	no	**yes**
Frequency Improvement	no	no	**yes**

with accurate cooling data, actuator designs can be significantly improved to meet frequency requirements yet minimize the actuator's overall power draw.

In addition, predictability remains an issue for the actuator. Currently many material models exist for the single SMA wires such as empirical approaches by (Tanaka 1986), (Liang and Rogers 1990) and (Brinson 1993). Recent thermodynamic models have also been developed to describe device physics. These include work developed by Achenbach and Müller 1985 (extended by Seelecke and Müller 2004) and Shaw 2002. However, modeling of the antagonistic actuator is currently sparse with only a small number existing that are limited in capability. For example, the models developed by Ditman, et al. 1996 and Singh et. al 2003, are application-specific and rely on empirical correlations that require a large number of experiments to calibrate. Their empirical nature also does little to introduce a full insight of the physical behavior of the actuator. Additionally, the first-order model developed by Grant and Hayward 2000, is limited in applicability as it greatly simplifies the antagonistic architecture as a spring whose stiffness depends on heating input (Grant and Hayward 2000; Grant 1999). This simplified model is useful in control, but greatly simplifies the actuator and does not provide an understanding of its physical behavior.

Issues of controllability arise with antagonistic actuators that have typically been resolved with ad-hoc (e.g. PID) and heuristic approaches. While these controllers have produced relatively accurate and precise motion tracking capabilities (Moallem and

Tabrizi 2009; Teh and Featherstone 2008), they are extensively tuned on-line leading to higher development costs. In addition, during the product's life these simple controllers have a risk of performance degradation as most do not compensate for changing operating conditions such as varying ambient temperature or decreasing battery charge.

1.4.5 Research Issues

While antagonistic actuation shows significant promise for use in hand-held tremor cancellation, several challenges and gaps in understanding must be addressed both at the material and architecture level before it can be widely used. These research issues can be categorized into three main concerns: cyclic repeatability, speed, and prediction; each is discussed in further detail.

1.4.5.1 Cyclic Repeatability

When cycled under load (either thermally or mechanically), SMA has been shown to exhibit softening or shakedown, reducing the amount of recoverable strain as the actuator is cycled. This effect has raised concerns about the material's predictable reliability over a device's lifetime, prompting recent investigations of this phenomenon. For example, shakedown has been experimentally tested (Figure 1.11) by heating and cooling the SMA under load (Erbstoeszer, et al. 2000; Lagoudas, et al. 2000), and by mechanically cycling the wire in its super-elastic state (Iadicola and Shaw 2002; Miyazaki, et al. 1998). Under thermal cycling with constant load, recent studies have shown that in many situations the loss in strain approaches a steady-state as the number of cycles increases to infinity (Erbstoeszer, et al. 2000). This effect is used in several applications, where the material is stabilized by shaking it down under a load that is higher than the device load to ensure that no additional loss in motion will occur over the actuator's lifetime (Barnes, et al. 2005; Pathak, et al. 2007).

While a stabilizing effect has been noted in all of these studies, a predictive model is

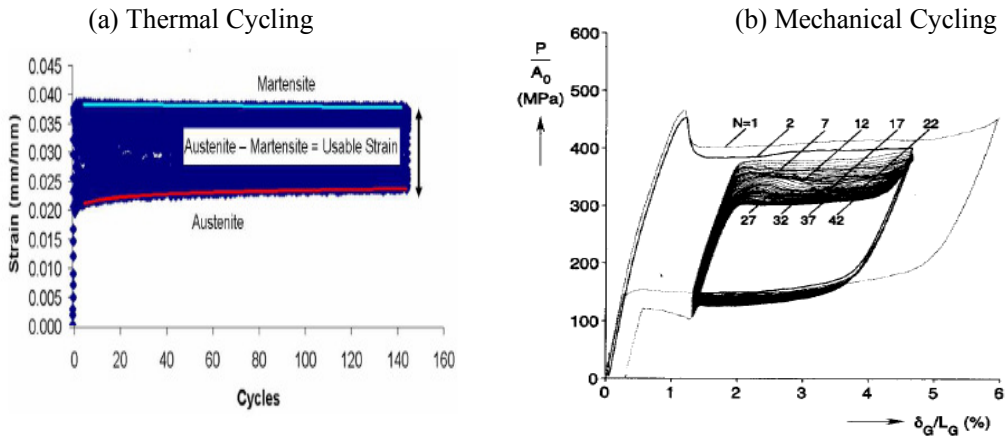

Figure 1.11. Example data from thermal and mechanical shakedown. Loss in recovered motion initially occurs and in some cases can stabilize (Shaw 2002). Thermal cycling performed at 480 MPA (Barnes 2005).

lacking since its exact mechanism is not fully understood. Preliminary work by Melton and Mercier (1979) and Miyazaki et. al (1998), hypothesize that the successive reorientation of Martensite can lead to an accumulation of defects that can act as obstacles to reverse (Martensite to Austenite) transformation. In addition, it is suggested that slip deformations are responsible for generating a stress field that increases the amount of residual Martensite visually observed using optical microscopy after the SMA specimen is unloaded (Miyazaki, et al. 1998). The amount of residual Martensite was reported to increase with the number of mechanical cycles, correlating to the successive loss in strain (Miyazaki, et al. 1986). The amount of permanent strain is also reported to be dependent on the amount of stress applied to the material (Iadicola and Shaw 2002), and annealing temperature (Lagoudas, et al. 2003). Because of these complexities, predictive modeling of the shakedown process has not been established making the process difficult to understand and account for. However, a first empirical step towards characterizing the process would prove to greatly improve shakedown procedures and the design of SMA actuators. Such an empirical model would also lay an important foundation towards a physically-based analytical model of the shakedown process.

1.4.5.2 Actuation Frequency

Achieving high cyclic speeds poses another fundamental challenge when implementing antagonistic SMA actuators. While one-way actuation is fast, with response times on the order of milliseconds, and can be achieved through ohmic heating at a high current (Qiu, et al. 2000), high frequency cyclic actuation is challenging because there is no simple mechanism to extract heat from the bulk material. However, recent developments in alternative cooling methods have enabled SMA's to be used in dynamic applications. Water-cooling of thin SMA wires, for example, was used in the development of a high-bandwidth tactile display allowing responses of up to 40 Hz (Wellman, et al. 1998). Thin film SMA's have also recently been developed for use in micro-systems and have estimated response speeds of up to 100 Hz (Krulevitch, et al. 1996). While decreasing the bulk volume of the material and increasing its surface area (i.e. using wires or thin films) is very effective at increasing heat transfer, it also reduces the amount of usable work. External heat pumps such as peltier coolers (Bhattacharyya, et al. 1995; Shahin, et al. 1994) have been proposed to enhance cooling without sacrificing stress/strain performance, though these systems add unwanted power consumption and bulk to the system. New methods, therefore, are still needed to enhance the cyclic speed of SMA without changing the cooling environment or sacrificing the material's overall benefits of being small and lightweight.

An additional aspect that must be understood is the effect of increasing actuation frequency (and convective heat transfer) on power consumption. Because a significant amount of heat is lost to the environment, the energy required for joule heating and passive cooling is significantly greater than the work output (Salzbrenner 1984). This is due to the fact that, during each cycle, the material must be heated to its transformation temperature and heated through its transformation enthalpy. Studies have measured the

work efficiency to be only 4% of the ideal Carnot efficiency when using a working fluid for heating (Salzbrenner 1984). When operating at high frequencies in a passively cooled environment, this efficiency is further challenged due to the additional heat losses from convection. Operating the material in a medium with high convective properties (e.g. to increase frequency response), for example, can reduce work efficiencies several-fold (Potapov and Da Silva 2000). Thus, it is extremely important to properly select the actuator's cooling environment to just meet frequency specifications, avoid any overcooling of the actuator, and minimize the power draw.

Unfortunately this is currently difficult to accomplish since the required data on the convective properties of SMA is challenging to obtain. This is due to the fact that accurate surface temperature measurements of the thin SMA wires are difficult to obtain since thermocouples can be invasive and detach under the transformation motion. Thermal imaging cameras can be employed to obtain surface temperature measurements, though there are challenges focusing on extremely thin wires and measurements cannot be taken in media other than air. A new measurement methodology capable of obtaining the convective coefficients of SMA wires of any diameter in a variety of cooling media is therefore needed and would provide useful data that can quantify the frequency/power tradeoff and power draw for SMA actuators.

1.4.5.3 Prediction and Control

Even under stable operation (i.e. after being shaken down), the behavior of antagonistic SMA actuation is difficult to predict or even control. This is primarily due to the material's hysteresis and non-linearity, and the fact that motion is heavily dependent on stress, input current, resistivity, and environmental conditions (Shaw 2002). Efforts have been made to predict the behavior of the material (typically actuators in single-wire form) through numerous models. Early SMA models primarily

focused on the empirical approaches such as those by (Tanaka 1986) and (Liang and Rogers 1990) that for the first time describe the phase fraction of Martensite as an internal variable. Superelasticity was added to these models by (Brinson 1993) where Martensite phase fractions were decomposed into two variants (twinned and detwinned), yet still the empirical cosine relationship for their evolution was retained. These empirical approaches are useful for their simplicity, though they are largely untested for arbitrary stress, strain, and temperature paths and have only been calibrated for a select number of special experiments.

To provide more physical insight and understanding, thermomechanical modeling has been revisited for 1-D applications. Ivshin and Pence 1994, for example, developed a model based on equilibrium thermodynamics, and another model using concepts of statistical thermodynamics was developed by Achenbach and Müller 1985, which was extended by Seelecke and Müller 2004. Recent thermodynamic modeling developed by Shaw 2002 has also shown promise in understanding SMA physics including spatially varying effects such as propagating phase transformation fronts and localized heat transfer. Reductions of this model were further demonstrated by Shaw and Churchill 2009, demonstrating an analytical solution for a single wire SMA actuator for use in design.

While these models show significant promise for use in predicting actuator behavior and building design intuition, they have not been applied to antagonistic SMA actuators. It is therefore currently necessary to re-formulate a thermodynamic model for the antagonistic architecture where two SMA wires are coupled through a mathematical relationship describing force and displacement compatibility. Additional relationships unique to an antagonistic actuator must also be mathematically developed, including conditions where the wires induce boiling, or become slack and support zero force. A

reduced, relatively simple model that accounts for these conditions and is capable of capturing general system behavior would be very useful to aid in enhancing the overall controllability, establishing design insight, and achieving predictability of antagonistic SMA actuators.

1.5 Research Goals and Objectives

The goal of this research is develop an antagonistic SMA actuation technology that is capable of enabling a new class of active human tremor cancellation. This is accomplished through the construction of a model and body of empirical support that provides the necessary design insight and predictive power for an antagonistic actuator that ensures stable amplitude and high frequency motion with low power draw. The specific objectives to achieve this are to:

- develop an empirical model of shakedown in SMA wire and demonstrate its use in design for long-term cyclic stability in output amplitude,
- develop a methodology to characterize conventional cooling techniques and establish non-conventional cooling methods to assist in improving the actuating frequency of SMA while minimizing power consumption,
- derive and verify a thermo-mechanical representation of antagonistic SMA to enhance overall predictability and understand the various design tradeoffs affecting frequency, power draw, and packaging for a generic antagonistic actuator , and
- demonstrate the scientific foundation of antagonistic actuation technology as an enabler of a new class of tremor cancellation.

1.6 Research Approach

To accomplish the stated objectives, the study of antagonistic SMA for tremor cancellation is divided into four major studies: 1) The Study of Shakedown in the

Quasi-Static Design of the SMA Stabilizing Handgrip, 2) Investigations of Convective Heat Transfer from SMA, 3) Transient Thermodynamic Modeling and Experimental Validation of an Antagonistic SMA Actuation Actuator, and 4) The Dynamic Design of the Active Cancellation of Tremor (ACT) Case Study.

1.6.1 The Study of Shakedown in the Quasi-Static Design of the SMA Stabilizing Handgrip

To develop an understanding of the shakedown process in the context of actuator design, Chapter 2 establishes an empirical model for shakedown. This model was applied to a graphical design process for the stable-amplitude quasi-static operation of the antagonistic actuator of a **SMA S**tabilizing **H**andgrip (SMASH). The SMASH served as a preliminary case study of an active tremor cancellation system that was designed to stabilize tremor in two DOF for the M16 rifle. Because the shakedown process for the antagonistic actuator in the SMASH required knowledge of the operating force/displacement requirements, a dynamic model was derived and solved to provide these specifications. Predicted operating forces were calculated based on these specifications and an empirical graphical model was derived that accounted for SMA material curves and system load lines. Knowing the operating forces, a procedure to shake down the SMA wires was developed and an empirical model utilizing two exponential decay terms was presented and utilized to predict any remaining motion degradation over the actuator's lifetime. This procedure and empirical model is useful in any actuator requiring stable operation under high amounts of stress. Using the formulated shakedown process, an antagonistic SMA actuator was developed for a SMASH proof-of-concept prototype that was validated to give quasi-static motion performance with negligible amplitude degradation. Initial studies in the dynamic domain of a SMASH, particularly the open-loop cancellation of single-frequency

disturbances, confirmed potential for closed-loop tremor cancellation. By deriving an empirical model capable of predicting shakedown, a wide range of SMA actuators can be designed with predictable, stable output in stroke over their lifetime.

1.6.2 Investigations of Convective Heat Transfer from SMA

Since experimental data is limited for the convective coefficient of SMA wires in various cooling media (and optimal coolant selection is challenging), Chapter 3 presents a novel methodology to measure these values for various SMA wire geometries in different cooling environments (air, mineral oil, water, thermal grease). This general method is useful for obtaining the convective coefficient in any medium and any scale (including the microscale) where conventional methods can fail. Empirical correlations were formulated and fit to the measured data, which provide continuous functions that can be adapted in thermodynamic models.

In addition to conventional methods, additional studies focused on the feasibility of a new cooling enhancement that utilizes vertically aligned carbon nanotubes (CNTs) acting as micron-scale cooling fins. These cooling fins were intended to increase the effective surface area of the SMA wire, thus improving an actuator's operating frequency without requiring a potentially undesirable change in its environmental conditions. Using a Plasma Enhanced Chemical Vapor Deposition (PECVD) method, the CNTs were shown to have successfully grown directly on the SMA. An experimental procedure was developed to compare the CNT treated wire with bare wire, to show an effect of increased convection. This validated effect can be used in many situations where changes on cooling medium or flow rate are not desirable, yet an increase in cooling is required. Through the study of conventional and unconventional cooling, this dissertation advances the current data, measurement techniques, and cooling methods to balance the frequency and power draw of SMA actuators.

1.6.3 Transient Thermodynamic Modeling and Experimental Validation of the Antagonistic SMA Actuation Architecture

Using the measured convective coefficients in Chapter 3, a general thermodynamic modeling framework is developed in Chapter 4 for the antagonistic SMA actuator to enhance its overall predictability and to provide an understanding of its inherent design tradeoffs. The model consists of two coupled one-dimensional wire elements (based on a reduced version of the model developed by Chang 2006) that each contains two internal martensitic variables. These variables, along with temperature and displacement, evolve in the model with respect to time depending on active electrical heating and passive environmental cooling inputs. Due to its nature, the presented model is thermodynamically admissible (unlike some current antagonistic models) and captures several key elements such as the wires becoming slack, friction, boiling, and changing convective properties. To demonstrate its accuracy and to identify regions of limitation, the transient model was experimentally verified through dynamic tests of a physical actuator for a variety of conditions including frequency, duty cycle, amplitude, and wire diameter. Additional design studies of the model were conducted to provide insight into the effects of the actuator's key variables including mechanical advantage, cooling medium, ambient temperature, duty cycle, and wire length/diameter. The results of these studies can be directly used to guide actuator designs, and the model itself can be utilized to conduct design optimization or controller tuning simulations.

1.6.4 Dynamic Design of the Active Cancellation of Tremor System

To demonstrate and validate this dissertation's development of antagonistic SMA for use in human tremor cancellation, a medical case-study is investigated in Chapter 5. The Active Cancellation of Tremor (ACT) system was intended to be used to enhance quality of life by assisting individuals suffering from essential tremor in their daily activities (e.g. eating, drinking, using tools, etc.). The device senses the user's

disturbance and moves the stabilized object, such as a spoon, opposite to the direction of the disturbance, with an overall cancellation goal of 50% RMS (as defined in Section 1.2.4). Using the framework developed in this dissertation, the antagonistic actuator and controller in the ACT system were modeled and their design variables were studied in detailed design space mappings. From these mappings important tradeoffs were discovered relating wire geometry, controller gain, and convective media to power consumption and cancellation performance. By balancing these tradeoffs using a design optimization routine, a suitable design was discovered that was used in the fabrication of a physical prototype. This proof-of-concept ACT prototype was tested for a variety of single-frequency disturbances as well as a full human tremor signal showing significant cancellation. Though several steps from commercial readiness, the ACT prototype demonstrated feasibility for a lightweight, handheld stabilization system that can be used to enhance the quality of life for the millions of people currently suffering from essential tremor. The ACT also served to demonstrate the general class of hand-held active tremor cancellation that was enabled by the technological developments of this dissertation.

1.7 Contributions

This thesis develops a technological understanding of antagonistic SMA actuators to facilitate the development of hand-held active cancellation devices for the mitigation of human tremor. These devices have great potential to enhance human performance in military, medical, and occupational/manufacturing sectors. Additionally, such systems can play a role in aiding the quality of life for those suffering from neurological disorders. While assistive devices exist to reduce the effects of human tremor, there has been little success in the creation of a cost-effective, lightweight, compact hand-held system employing an active cancellation technology. The primary technological barrier

prohibiting this class of tremor cancellation is the actuator, which typically suffers from weight, size, volume, cost, fragility and power issues. The use of SMA configured in an antagonistic actuator has been identified in this dissertation as a promising approach; however, there are several issues that must be resolved (namely stability, frequency, power, and predictability) before it can be adopted for use in human tremor cancellation. Initial work solves the stability issue through shakedown experiments and empirical modeling, which is illustrated in a graphical quasi-static design process. This process can be used to design a variety of actuators operating at high loads to ensure repeatable cyclic operation with negligible amplitude degradation. Challenges regarding the material's frequency are addressed through the development of a methodology of measuring the convective coefficient of an SMA sample. This methodology is applied to a variety of scenarios to measure the convective coefficient of SMA wire to its diameter and surrounding environment. This data can be directly applied to various thermodynamic models to improve overall predictability in output motion and to provide an understanding of the relationship between actuation frequency and power consumption. To investigate further methods that improve actuation frequency, work was conducted to investigate the use of carbon nanotubes as microscale cooling fins. These fins are intended to increase the effective surface area of the SMA, increasing its cooling speed without changing its surrounding environment. The actuator's predictability issues are solved through the development of a thermodynamic model that is experimentally validated and can be utilized to conduct various design studies. The model is capable of assisting design through accurate predictions in performance, and can be used to study and design controllers off-line. To demonstrate the antagonistic actuation technology, the ACT (Active Cancellation of Tremor) case study is designed and specified based on the results of model-based

studies. These studies provide valuable insight on the effect of the actuator's design with respect to power consumption and closed-loop tremor cancellation. Experimental validation of the ACT device itself is also conducted, showing significant tremor cancellation and the potential for future versions to positively affect the lives of individuals affected by essential tremor. These results demonstrate significant potential for similar systems to reach military, manufacturing, and biomedical applications that are currently unattainable using conventional actuation technologies

Chapter 2: The Study of Shakedown in the Design of the SMA Stabilizing Handgrip

When placed in combat situations, external stresses on a soldier produce many unwanted physiological disturbances including elevated heartbeat, breathing, and muscle tremors or wobble, that interfere with aiming accuracy. In non-combat situations the US Army estimates have quantified shooter tremor through the arm and shoulder to contribute to approximately 20% of total error (Wellman et. al, 1997). In combat situations the tremor magnitude is thought to increase at least an order of magnitude or higher (Broden 1999, US Army 2003), drastically increasing the potential of civilian injury and reducing soldier survivability. To address this issue, a compact **SMA S**tabilizing **H**andgrip (SMASH) for the M16 rifle was investigated. The SMASH (Figure 2.1) is intended to be a self-contained unit capable of sensing the user's tremor, and moving a two degrees-of-freedom actuator to counter its effect while retaining tracking motion.

The operation of the SMASH system is analogous to image stabilizing systems utilized in small handheld video cameras. During SMASH operation, inertial rate gyro sensors located in the handgrip are used to detect the effects of shooter-induced disturbances on rifle. The real-time controller processes these sensor signals and generates actuator commands to stabilize the rifle barrel. Inherent in the controller is an algorithm that separates the target tracking motion, which is left unaffected, and the tremor motion. This is analogous to image stabilizing systems that reject higher

frequency hand disturbances from the line of sight but do not affect the lower frequency pan/tilt pointing commands. As in image stabilization systems, the net effect is to steady the rifle point of aim, action and barrel for improved shot accuracy. This is accomplished with a two Degree of Freedom (DOF) suspension system controlled by opposing high energy density shape memory alloy (SMA) actuators that move the barrel in the azimuth and elevation directions.

As with all hand-held active tremor cancellation systems, the SMASH must be capable of producing large displacements in an extremely small package. While SMA is capable of meeting this need, its use as an actuator in situations requiring high force outputs is complicated to implement, such as the case with the SMASH. This is due to the material's degradation in recoverable strain, which occurs when there is a large amount of operating stress (e.g. above approximately 200 MPa for Flexinol wire, Dynalloy 2009). While degradation in amplitude can be circumvented by lowering the operating stress through the use of leverage or larger wire diameters, it cannot always be avoided. For example, the strict packaging constraints of the SMASH are unable to accommodate a lever, and the wire diameter is restricted to smaller sizes to ensure fast cooling for the frequency requirement (0-3 Hz). In such situations shakedown is unavoidable, and must be accounted for in the actuator's design. Unfortunately, this is challenging since there is no clear design methodology in existence and the shakedown process itself is not well understood and difficult to predict. Therefore, to account for motion degradation during the lifetime of the SMASH (and any other SMA actuator operating at high stress) it is crucial to develop a capability to predict its behavior over a known number of actuation cycles at a given load, and apply this information to actuator design.

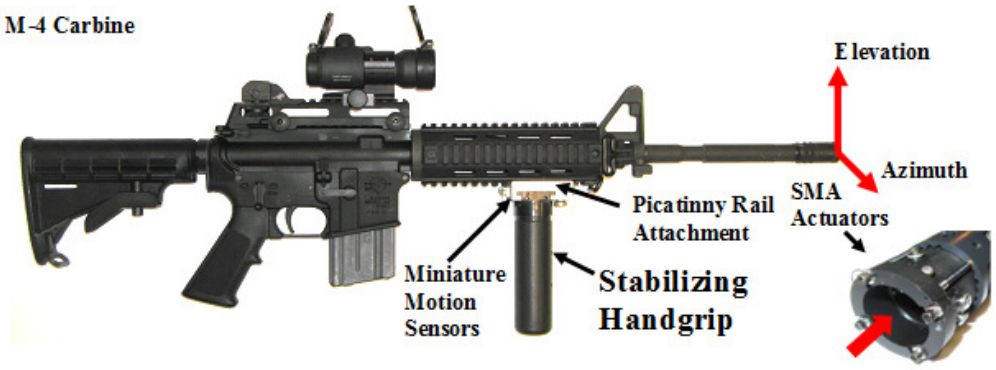

Figure 2.1. Stabilizing Handgrip System Concept.

This chapter addresses this need in the context of designing the antagonistic actuator for the SMASH for quasi-static specification, which is shown through dynamic modeling to bound the requirements over the frequency range of interest (0-3 Hz). Thus, for this quasi-static case, an iterative empirical graphical design process is detailed where, initially, system loads for the SMASH are estimated through experimental characterization of a preliminary prototype. Based upon these loads, a regimen to shake down the SMA wire is defined and an empirical model is developed to quantify the amount of degradation expected in the actuator's lifetime. Using the stabilized wire, the SMASH is validated to operate without degradation, and preliminary studies in the dynamic regime are presented, demonstrating open-loop cancellation. These studies serve to illustrate key challenges with the SMA actuator, namely power consumption, frequency response, and predictability, which are addressed in the following chapters (Chapters 3-5).

2.1 Dynamic Weapons Modeling

When designing for stable output amplitude (reducing shakedown), it is essential to understand the force/displacement requirements of the actuator. In the case of the SMASH, these were unknown and had to be calculated through a dynamic model. The generic small arms system model is formulated from two key components a) a human

interface model based upon research conducted for power tool design accounting for both shoulder and arm input disturbances, and b) an active stabilization interface model accounting for the system stiffness and actuator forces/displacements. Since no data to date is available on the actual input disturbances from the arm and shoulder human interfaces, a method is supplied to estimate them from shooting range variability data that is available. Based upon this model, a process is described for generating the actuation specifications for an active stabilization system as a function of frequency given the derived human disturbance inputs. As examples, two distinct case studies are provided: the M24 sniper weapon which has the active stabilizer between the stock and barrel (with only the barrel being stabilized) and the M16 assault rifle which has the actuator placed at the location of the hand to stabilize the entire rifle. Each system is investigated relative to the human interaction including the effect of shooter-disturbance frequency, disturbance location (shoulder vs. arm), and system parameters (stiffness, barrel rotation). The present small arms model provides a means for defining the actuation specifications, and also gives insight into the inherent system sensitivities allowing for better active stabilization design.

2.1.1 Generic Weapons Model

A wide range of actively stabilized weapon systems can be abstracted to the form shown in Figure 2.2. The relevant nomenclature, units and parameter values for two case studies (the M24 used in prior INSTAR work and the M16) is given in Table 2.1. In the system model, the butt of the stock of mass M_s is braced against the shoulder at point **A** and pivots with rotational inertia I_s about that point by an angle θ_s relative to horizontal. The supporting hand is located at a distance L_{arm} from the shoulder. The barrel of mass M_b pivots with rotational inertia $I_{b,p}$ by an angle θ_s relative to horizontal about a fixed point **B** on the stock at a distance L_B from the shoulder.

A spring of stiffness k_2 between the barrel and stock located at a distance C_s from the pivot supports the barrel. The stock's center of mass is located at a distance L_{cm} from the shoulder and the barrel's center of mass is located at a distance C_{cm} from the pivot. To stabilize the barrel, the actuator platform acts with a force F_p between the stock and barrel at a distance C_a from the pivot. To hold the barrel down against the actuator, the spring is preloaded with a force F_o. The resulting model is established with disturbance inputs x_s (shoulder) and x_a (arm), actuation input F_p with two degrees of freedom, θ_s (stock elevation) and θ_b (barrel elevation). In addition, to maintain a linear model form, the spring preload F_o is treated as an additional input, although it is assumed to remain constant.

Motions of both the shoulder and the arm introduce disturbances into the system, and are defined to be in the range of 0 to 3 Hz (Nersessian 2001) – and may be due to the low-frequency irregular muscle firings discussed in Section 1.1.2. For this model, it is assumed that the trigger hand of the operator does not interact significantly with the rifle compared to the arm and shoulder. It is assumed that any shoulder motions such as

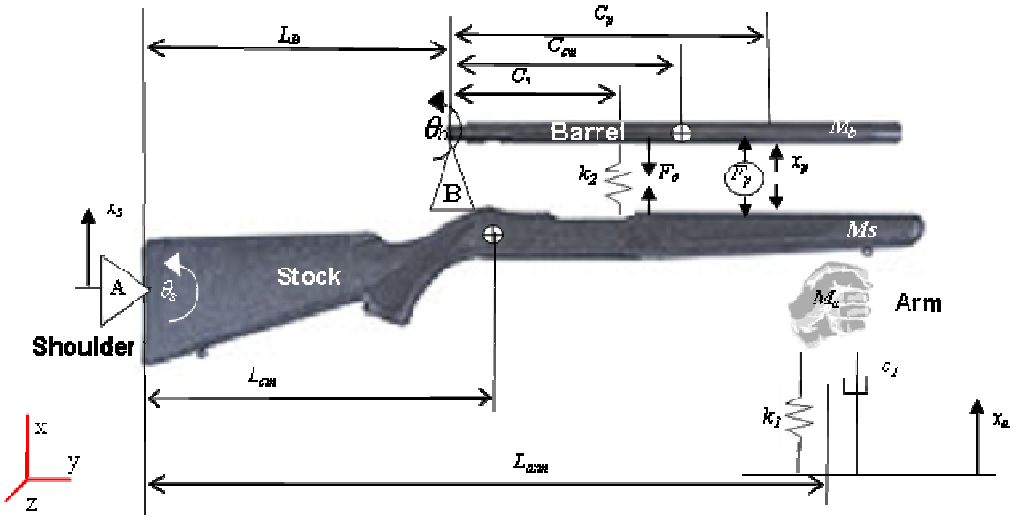

Figure 2.2. Generic Model. A schematic of a generic hand-arm system, applicable to a variety of systems.

Table 2.1. Nomenclature used in the system modeling and parameter values used in the M16 and M24 case studies.

Symbol	Description	Units	M24	M16
L_B	Distance from origin to pivot point **B**	m	0.51	0.00
L_{arm}	Distance from origin to arm	m	0.71	0.62
L_{cm}	Distance from origin to center of mass of the stock	m	0.27	0.27
C_s	Distance from pivot to spring	m	0.10	0.62
C_p	Distance from pivot to platform actuator	m	0.20	0.62
C_{cm}	Distance from pivot to center of mass of barrel.	m	0.13	0.50
M_a	Mass of arm	kg	0.2	0.2
M_s	Mass of stock	kg	1.71	0.00
I_s	Moment of inertia of stock (and arm) about pivot **A**	kg m^2	0.32	0.07
M_b	Mass of barrel	kg	1.75	4.31
$I_{b,B}$	Moment of inertia of barrel about pivot **B**	kg m^2	0.14	1.30
k_2	Active stabilization spring constant (between stock and barrel)	N/mm	225	4.31
k_1	Spring constant for arm	kN/m	4.71	4.71
c_{arm}	Damping constant for arm	N-s/m	65.7	65.7
F_p	Force from stabilizing actuator	N	variable solved for	
x_p	Displacement of stabilizing actuator	mm	"	
θ_b	Angular pitch of the barrel	Rad	"	
θ_s	Angular pitch of the stock	Rad	"	
x_a	Shoulder disturbance input	m	"	
x_s	Shoulder disturbance input	m	"	

those induced by breathing and heartbeat are unaffected by the motions of the rifle (i.e. the body is much more massive than the rifle). Therefore, the shoulder disturbance is modeled as a base disturbance x_s of the shoulder point **A**. While in reality the stock rolls against the soft material of the shoulder at this point, contact between the stock and the shoulder is assumed to be a pure pivot.

The arm, on the other hand, has comparable mass to the rifle, and arm motions both affect the motion of the rifle and are affected by it. Following an established method for modeling the dynamic response of an arm trying to stabilize a vertical handgrip in the use of power tools (for both elevation and azimuth directions) (Reynolds and Keith 1977; Reynolds and Soedel 1972), the musculature dynamics are modeled by attaching the arm mass M_a through a spring of stiffness k_1 and a damper with damping constant C_{arm} to a movable point x_a representing the desired holding position of the arm. External forces acting on the arm cause it to deviate from this position according to the

mass-spring-damper dynamics. Apart from necessary adjustments in the stock and barrel moments of inertia I_s and $I_{b,B}$ and values for the human arm, k_1 and C_{arm} the overall system model is identical in both azimuth and elevation motions, so only the elevation case is given.

2.1.1.1 System of Equations

Assuming small angles (barrel disturbances are on the order of milliradians), the equations of motion for the system are formulated using Newton's second law applied to the rotational inertias for elevation or azimuth direction of the stock and barrel, I_s about the shoulder pivot **A** and I_b about the barrel pivot **B**. In the vertical direction, the rifle stock experiences a downward force due to gravitational acceleration g that is countered by a pre-compression force of the actuator spring. This force is the result of the spring's compression an initial distance x_{po} from its free length l_{spring}. The force exerted by the platform, F_p, works to counter the disturbances caused by the user's shoulder and arm. Summing the moments on the stock about the shoulder pivot **B** in the elevation direction yields,

$$I_s \ddot{\theta}_s = -M_s L_{cm} \ddot{x}_s - F_p (C_p + L_B) + \frac{(C_s + L_B)}{C_p} C_s k_2 (x_{p,o} + x_p - l_{spring})$$
$$- k_1 L_{arm} (x_s + L_{arm}\theta_s - x_a) - L_{arm} c_1 (\dot{x}_s + L_{arm}\dot{\theta}_s - \dot{x}_a) + L_B F_{r,tot} - L_B N \quad . \quad \textbf{(2.1)}$$

N is the normal force acting to support the weight of the barrel in the static condition and is equal to $M_b g$. $F_{r,tot}$ is the total reaction force from the pivot point, and can be separated into steady-state static ($F_{r,ss}$) and transient dynamic ($F_{r,trans}$) components calculated from a vertical force balance on the barrel,

$$F_{r,ss} + F_{r,trans} = F_p - \frac{k_2 C_s}{C_p}(x_{p,o} + x_p - l_{spring}) - M_b(\ddot{x}_s + (L_B \ddot{\theta}_s) + (C_{cm} \ddot{\theta}_b)) - M_b g \,. \quad \textbf{(2.2)}$$

by balancing moments on the barrel about the pivot point **B,** the rotation of the barrel is

defined as

$$I_{b,B}\ddot{\theta}_b = -M_b C_{cm}(\ddot{x}_s + L_B\ddot{\theta}_s) + F_p C_p + \frac{k_2 C_s^2}{C_p}(x_{p,o} - x_p - l_{spring}) - C_{cm} M_b g \quad . \tag{2.3}$$

To simplify these equations, the effect of gravity in the elevation direction is canceled using a static analysis. Assuming the spring k_2 has an initial length l_{spring} and an initial compression x_{po}, the moment balance for the barrel about pivot point **B** under steady-state conditions

$$k_2 C_s (x_{p,o} - l_{spring}) = C_{cm} M_b g + F_o C_s \quad . \tag{2.4}$$

The initial compression of the spring both supports the moment due to gravity and provides an additional preload (if required by the system). Similarly, the vertical force balance on the barrel under steady-state conditions becomes

$$k_2 (x_{p,o} - l_{spring}) = -M_b g - F_o - F_{r,ss} \quad , \tag{2.5}$$

and the moment balance about the stock under static conditions is

$$k_2 (C_s + L_B)(x_{p,o} - l_{spring}) = L_B M_b g + F_o (C_s + L_B) \quad . \tag{2.6}$$

Because gravity is canceled by spring pre-compression, both terms for gravity and the pre-compressed distance for the spring no longer appear in the system equations. Without these two terms, the equations become applicable to the azimuth case as well. The original equations of motion (2.1-2.3) represent a system with two degrees of freedom, namely the angular rotation of the stock θ_s and barrel θ_b. The coordinates of interest however are the actuator's displacement x_p and the barrel rotation θ_b (the displacement requirement is solved to produce zero barrel rotation). Therefore, a change of coordinates is performed to eliminate θ_s and express it in terms of x_p,

$$\theta_s = \theta_b - \frac{x_p}{C_p} \quad . \tag{2.7}$$

Changing the form of the system to apply to azimuth as well as elevation directions by the substitution of the static equations (2.4-2.6), and applying the change of coordinates (Equation 2.7) to the original equations of motion (2.1-2.3) the final system model is derived in matrix form resulting in a linear second order, two degree of freedom vibrational system

$$M\begin{bmatrix} \ddot{x}_p \\ \ddot{\theta}_b \end{bmatrix} + C\begin{bmatrix} \dot{x}_p \\ \dot{\theta}_b \end{bmatrix} + K\begin{bmatrix} x_p \\ \theta_b \end{bmatrix} = G_s + G_a + HF_p + DF_o \tag{2.8}$$

where the mass matrix M is

$$M = \begin{bmatrix} -\dfrac{I_s + L_B^2 M_b}{C_p} & I_s + L_B M_b (L_B + C_{cm}) \\ -\dfrac{M_b C_{cm} L_B}{C_p} & I_{b,p} + M_b C_{cm} L_B \end{bmatrix}. \tag{2.9}$$

the damping matrix C is

$$C = \begin{bmatrix} -\dfrac{C_{arm} L_{arm}^2}{C_p} & C_{arm} L_{arm}^2 \\ 0 & 0 \end{bmatrix}. \tag{2.10}$$

and the stiffness matrix K is

$$K = \begin{bmatrix} -\left(\dfrac{C_s^2 k_2 + k_1 L_{arm}^2}{C_p}\right) & k_1 L_{arm}^2 \\ \dfrac{k_2 C_s^2}{C_p} & 0 \end{bmatrix}. \tag{2.11}$$

The matrix describing the generated shoulder motion G_s consists of the moments caused by the disturbance motion x_s,

$$G_s = \begin{bmatrix} (-M_s L_{cm} - L_B M_b)\ddot{x}_s - L_{arm} C_{arm} \dot{x}_s - k_1 L_{arm} x_s \\ (-M_b C_{cm})\ddot{x}_s \end{bmatrix}. \tag{2.12}$$

and the matrix for the generated arm motion G_a consists of the moments caused by the arm disturbance x_a,

$$G_a = \begin{bmatrix} L_{arm} C_{arm} \dot{x}_a + k_1 L_{arm} x_a \\ 0 \end{bmatrix}. \quad \textbf{(2.13)}$$

Lastly, the H matrix contains the moment arms over which the actuator acts,

$$H = \begin{bmatrix} -C_p \\ C_p \end{bmatrix}. \quad \textbf{(2.14)}$$

and the D matrix represents the moment arms for the spring preload F_o,

$$D = \begin{bmatrix} C_s \\ -C_s \end{bmatrix}. \quad \textbf{(2.15)}$$

The resulting set of two linear differential equations (Equation 2.8) describes the elevation and azimuth dynamics of the rifle system in a form suitable for analytical solution.

2.1.1.2 Estimating Human Disturbances

The human shoulder and arm input disturbances, (x_a and, x_s), are necessary to define the actuation force and displacement specifications F_a and x_p. For a weapon system, these disturbances may be estimated from military field data for shooting variability at a given distance (Weaver 1990). The general model (Equation 2.8) is adapted to represent a non-stabilized system by assuming infinite actuator spring (k_2) stiffness, thus effectively making a rigid connection. Actuation, F_a is set to zero and human disturbances of the shoulder x_s or the arm x_a are independently back-solved to produce the known target distribution. Because the system model is linear, the shoulder and arm disturbance can be solved separately since the output of the model is the sum of each individual result. Linearity allows each disturbance input and the corresponding barrel response to be decomposed into sinusoids (at the same particular frequency w) which

can be represented by functions of the form

$$x(t) = \mathrm{Re}(\bar{x}e^{iwt}) \tag{2.16}$$

where $\bar{x}$ is a complex number whose magnitude and phase reflect the amplitude and phase of the function. From this point on, the extraction of the real component of this complex form Re(•) and the functional dependence on time are assumed and omitted for brevity. The system response of the rifle model is thus represented as $\theta = \bar{\theta}e^{iwt}$ where the complex vector $\theta=[x_p\ \theta_b]^T$ holds both amplitude and phase of the two system degrees of freedom, the platform actuator displacement and barrel angular motion. Thus, the matrix form of the system model (Equation 2.8) written in complex form is:

$$\bar{A}\bar{\theta}e^{iwt} = [\bar{G}_s\bar{x}_2 + \bar{G}_a\bar{x}_a + H\bar{F}_a]e^{iwt} + DF_o \tag{2.17}$$

where the system matrix $\bar{A} = -w^2M + iwC + K$. The shoulder disturbance matrix G_s becomes the complex coefficient matrix $\bar{G}_s$,

$$\bar{G}_s = \begin{bmatrix} (M_1L_{cm} + L_pM_2)w^2 - L_{arm}C_{arm}\,iw - k_1L_{arm} \\ (M_2C_{cm})w^2 \end{bmatrix}. \tag{2.18}$$

and similarly for arm disturbances,

$$\bar{G}_a = \begin{bmatrix} L_{arm}C_{arm}iw + k_1L_{arm} \\ 0 \end{bmatrix}. \tag{2.19}$$

The closed-form of the required disturbance for the shoulder or arm to produce a given barrel motion θ_b is

$$\bar{x} = \frac{\bar{\theta}}{B\bar{A}^{-1}\bar{G}} \tag{2.20}$$

where the magnitude of $\bar{\theta}$ is the amplitude of the known angular disturbance of the

barrel (obtained from shooting data), and B is the selection matrix [0 1] since only the barrel motion is of interest. Thus, given a specification on the acceptable barrel motion $\bar{\theta}$, the required disturbance (Equation 2.20) allows the estimation of the amplitude of either the arm disturbance $\overline{x_a}$ or the shoulder disturbance $\overline{x_s}$ which produces that motion. Selection of which disturbance is accomplished by choosing the complex matrix $\bar{G}$ to be either $\overline{G_a}$ (Equation 2.13) for the arm or $\overline{G_s}$ (Equation 2.12) for the shoulder.

2.1.1.3 Generation of Actuator Requirements

The derived models coupled with the defined arm and shoulder disturbances ($\overline{x_a}$, $\overline{x_s}$) as input sets the stage to determine the actuation force and displacement requirements, F_p and x_p, necessary to cancel the human disturbances. This is accomplished by setting the barrel to be perfectly stabilized (i.e. $\overline{\theta_b} = 0$) by making $\bar{\theta}$ in the assumed complex solution for Equation 2.17 $\bar{\theta} = [\overline{x_s}\ 0]^T$. The spring preload is solved separately and added to the actuator requirement for each disturbance. The actuator requirements to cancel the disturbances (arm and shoulder) are computed individually to gain insight of each impact. In reality, the entire measured shooting error is due to each disturbance. To represent the effect of this combination, the requirements for the two disturbances can be combined using the convex combination

$$\alpha R_s + (1-\alpha) R_a = R_{tot} \qquad \textbf{(2.21)}$$

where α is a proportionality constant selected between the interval [0,1], R_s is the shoulder requirement, R_a is the arm requirement, and R_{tot} is the total requirement. Since the total requirement varies linearly between the individual requirements as α varies from 0 to 1, the "worst case scenario" occurs when α is adjusted to create 100% of the

disturbance requiring the highest force and displacements. Thus, the greater force or displacement specification due solely to either a shoulder or arm disturbance safely bounds all other possible combinations of disturbances.

Considering either disturbance input on the right hand side of the complex form of the system equations (Equation 2.17) individually, and setting the preload to zero, the actuator force F_p can be brought to the left hand side, and the system of two complex variable equations and two unknowns becomes

$$\begin{bmatrix} \overline{A}_{1,1} & -H_1 \\ \overline{A}_{2,1} & -H_2 \end{bmatrix} \begin{bmatrix} \overline{x}_p \\ \overline{F}_p \end{bmatrix} = \overline{G}\overline{x} \tag{2.22}$$

from which the contribution of the disturbance to the required actuator displacement $\overline{x_p}$ and force $\overline{F_a}$ can be solved. The subscripts under A represent the row and column of the matrix A and the subscript under H represents the row of vector H.

The contribution due to the static spring preload F_o can be computed similarly by setting the frequency w to zero along with the disturbance inputs and barrel motion. Adding this contribution to the complex magnitude of the contribution due to the disturbance yields the total maximum force $x_{p,max}$ and displacement $F_{a,max}$ required by the actuator. For a given spring preload F_o and disturbance x (and its corresponding matrix G), the specification is

$$\begin{bmatrix} x_{p,\max} \\ F_{a,\max} \end{bmatrix} = \left| \begin{bmatrix} \overline{A}_{1,1} & -H_1 \\ \overline{A}_{2,1} & -H_2 \end{bmatrix}^{-1} \overline{G}\overline{x} \right| + \begin{bmatrix} K_{1,1} & -H_1 \\ K_{2,1} & -H_2 \end{bmatrix} DF_o \,. \tag{2.23}$$

2.1.2 Weapon System Case Studies

To demonstrate the model's application, it was employed for two distinct cases: The M24 sniper rifle used in the INSTAR work (Barnes, et al. 2005; Brei, et al. 2003) and the M16 rifle. For each case, the human arm mass, compliance, and damping were

incorporated to define the necessary actuation specifications required to cancel the shoulder and arm disturbances in the dynamic region. In the course of these simulations, the interplay between the human, weapon and active stabilization was explored including the effect of shooter-disturbance frequency, disturbance source (shoulder vs. arm), and system parameters (stiffness and barrel rotation).

2.1.2.1 M24 Sniper Rifle

The M24 sniper rifle was studied because it represents the model in its most general case: independent stock and barrel masses, and a suspension spring with preload occurring at a different location from the actuator. The system is solved with the parameters for the elevation direction given in Table 2.1. The arm values M_a, C_{arm}, and k_1, were determined from studies of the human arm (Reynolds and Soedel 1972). The active suspension spring constant k_2 was taken from INSTAR specifications (Brei, et al. 2003). All other parameters were directly measured from the rifle. The full system model (Equation 2.8), including the human arm dynamics, was used with each human disturbance, shoulder x_s and arm x_a, introduced individually to ascertain their impact on the system response and actuation requirements.

2.1.2.1.1 Human Disturbance Estimation

Due to a lack of physical subject data, human input disturbances x_s and x_a were estimated from Equation 20 to produce a targeting error of ± 1.88 mrad of the rifle barrel pivot point (Barnes, et al. 2005). The solution for the required shoulder input disturbance as a function of frequency (Figure 2.3) remains almost steady at the static value of 1.3 mm. This is due to the fact that the base shoulder excitation acts directly on the rifle with the actuator being rigid and the arm compliance minimally affecting overall motion. On the other hand, the arm input decreases over the frequency range to

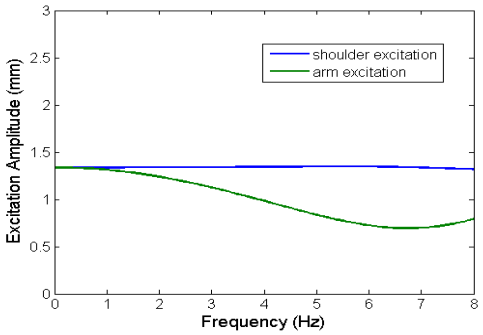

Figure 2.3. M24 Disturbances. Required disturbance inputs to excite the sniper rifle barrel 1.88 mrad for both arm and shoulder vibration.

a minimum of 0.7 mm at 6.8 Hz, which is the arm model resonance point. The excitation of the arm resonance coupled with the rifle inertia makes it easier to move the rifle at those frequencies, where base excitations of the arm amplify through the resonant dynamics.

2.1.2.1.2 Actuator Requirements

Using the methodology defined in Section 2.1.1.3, the model was run for the M24 rifle to produce actuator requirements (Figure 2.4) considering each disturbance (arm and shoulder) individually. In the frequency range of 0-3 Hz, the actuator force requirement for the arm disturbance dominates the shoulder disturbance, but the displacement requirements for both remain nearly identical. Since the rifle stock has a greater mass than the arm, its resonance is at a lower frequency and is consequently easier to move, producing a lower force requirement. Because of this effect, the specifications calculated for the arm bounds any other possible combination of shoulder/arm disturbances (Section 2.2.1.3). Note that this may have some impact on shooter training when using an actively stabilized rifle. For example, the shooter can concentrate on reducing tremor in their arm more than in their shoulder since the actuator has an easier time canceling shoulder disturbances. Since the modeled spring in the arm is much less stiff than the suspension spring, the addition of human arm

dynamics creates a resonance at 6.1 Hz for the shoulder and 5.6 Hz for the arm making it easier for the actuator to move the entire system near these frequencies (Figure 2.4). The static case of the system solution (0 Hz) is the same for both the arm and shoulder. The force of 43.8 N establishes a bound in the frequency range of 0 to 7.0 Hz, and the displacement of 382 μm in the frequency range of 0 to 7.7 Hz. These values agree exactly with the actuation specifications used in the INSTAR (Brei, et al. 2003). Thus, in a conservative design where the stabilizer must act at multiple frequencies, the actuator specification for a M24 active stabilizer can be set to the static values of 43.5 N for force and 382 μm for displacement independent of the disturbance source.

2.1.2.2 M16 Assault Rifle

The model was also exercised for the M16 rifle to gain an understanding of the tremor cancellation requirements for the SMASH. From a modeling perspective, the M16 represents a kinematically different case than the M24 because the stock and barrel are rigidly attached, and the actuator is held directly by the arm (Figure 2.5). Because of this effect, little inertia is attached to the arm, and the effects of the system dynamics on the actuator become more significant. For the M24, the stock mass

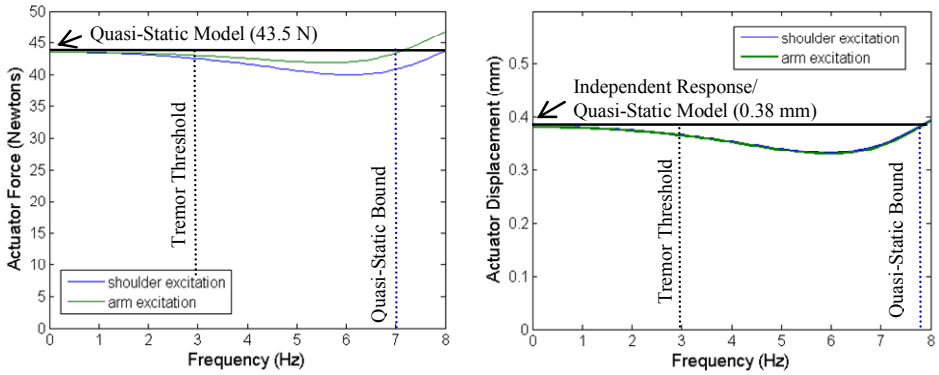

(a) Force (b) Displacement

Figure 2.4. M24 Actuator Requirements. Force and displacements required to stabilize the sniper rifle barrel for both shoulder and arm disturbances.

contributed to absorbing the disturbances; whereas in the M16, the actuator is required to do more work.

To model the M16, the stock and barrel are lumped together into M_b (the barrel), and the separate stock mass M_s is set to zero (effectively, the handgrip becomes the stock). The pivot point is brought over to the shoulder by setting its distance from the stock L_B to zero. L_{arm}, the distance from the stock to the arm grip, and C_s and C_a, the distances from the pivot point to the actuator and return spring, are all assigned a value l_p (Figure 2.5). Parameters used to fit the model to this new system in the elevation direction are listed in Table 2.1. Values for the mass of the arm M_a, damping constant C_{arm}, and stiffness k_1 were all taken from Reynolds and Soedel 1972. All other physical parameters of the rifle were directly measured. The human interactions x_s and x_a are included in the system (Equation 2.8) along with the compliance and damping present from a human arm support.

2.1.2.2.1 Human Disturbance Estimates

As with the M24, the human input disturbances x_s and x_a were estimated from Equation 2.20 assuming a targeting error of ± 3 mrad of the rifle barrel pivot point, determined through triangulization

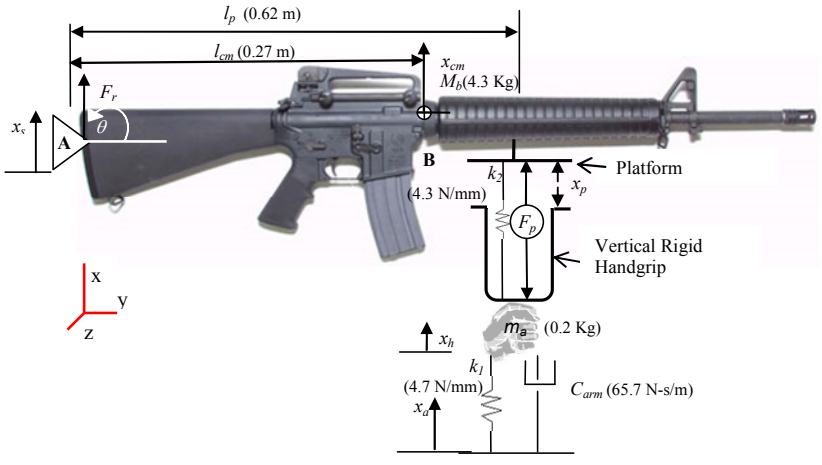

Figure 2.5. Dynamic M16 Weapons Model. Model is reduced version of general hand-arm system.

$$\tan^{-1}\left(\frac{s}{D}\right). \tag{2.24}$$

with the target distribution s set to ± 0.75 m (three standard silhouettes) and the shooting distance D set to 250 m according to military data (Weaver 1990). The resulting input human disturbances are shown in Figure 2.6. As with the M24, the shoulder excitation of 1.87 mm is nearly constant because shoulder directly displaces the rifle inertia. The arm excitation amplitude, on the other hand, is not constant, and decreases to a local minimum of 0.82 mm at 5.4 Hz, which occurs due to a system resonance between the rifle inertia and the arm compliance. This is a 56% deviation from the quasi-static arm excitation, indicating the significance of the system dynamics.

2.1.2.2.2 Actuator Requirements

The effect of human interface with the M16 is more pronounced than the M24 due to the change in mass attached to the arm (the mass of the stock is set to zero). This brings system resonance to lower frequencies with minima in force requirements of 1.3 N at 4.1 Hz for the shoulder and 3.7 N at 5.4 Hz for the arm. In addition, the difference in actuator force requirements between arm and shoulder disturbances is more distinct

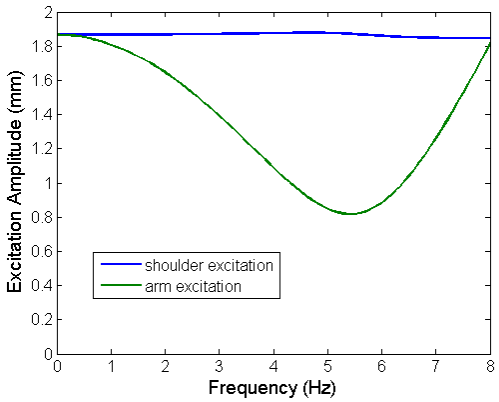

Figure 2.6. M16 Disturbance Estimates. Disturbances for the M16 for both arm and shoulder required to excite the rifle barrel at an amplitude of 3 mrad.

than in the M24, emphasizing the benefit of training a soldier. For example, a soldier should seek rigid arm support to suppress its disturbances, which in Figure 2.7a dominate shoulder disturbance requirements over 0 to 3 Hz. For the M16, the quasi-static requirements of 1.9 mm and 8 N provide an upper bound for the displacement requirements until 7.9 Hz. Forcing is bounded until 5.8 Hz for the shoulder and 7.9 Hz for the arm. Over the frequency range of interest (0 to 3 Hz), the quasi-static force and displacement requirements significantly over-specify the actuator (see Figure 2.7). These large variances are in contrast to the M24 which varied less due to its spring-dominated dynamics (Figure 2.4). Two explanations for this relative difference from quasi-static exist: a) the M16's actuator is less stiff, which brings its resonance to lower frequencies, and b) the M16's actuator has only the mass of the arm to displace during stabilization, where the M24 has the additional inertia of the stock to help reduce the force requirements for stabilization (this is particularly dominant at higher frequencies).

2.1.3 M16 Stabilizing Handgrip Specifications

Because they serve as an upper bound to overall actuator requirements, the quasi-static actuator specifications of 8 N and +/- 1.9 mm were chosen. Additionally,

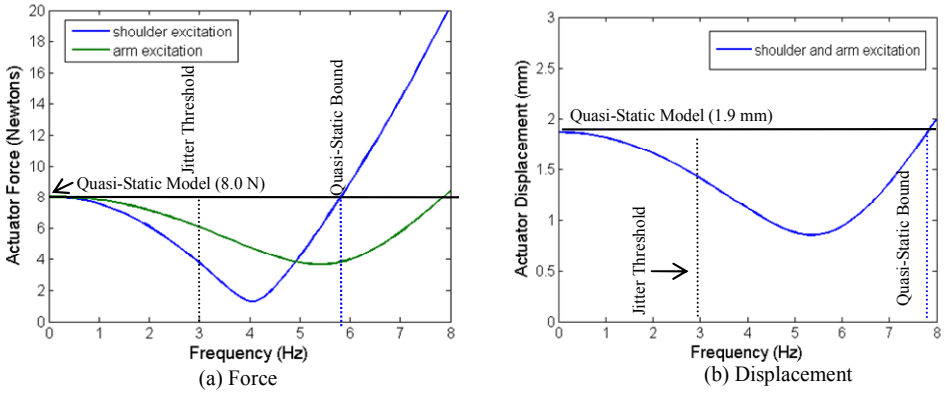

Figure 2.7. Force and Displacement Results for Stabilization Requirements for the M16.

through guidance received during collaboration with U.S. Army personnel several supplementary key customer needs were identified in the stabilizing handgrip as summarized in Table 2.2. As with other hand-held systems studied in this dissertation (See Chapter 5) the Army identified a benefit from a modular and self-contained system. The handgrip was required to be adaptable to a variety of weapon systems including the M16 rifle. Such a device was required to be capable of withstanding harsh environmental conditions and shock typically encountered during combat scenarios. Total weight was specified to be below 350 grams and cost less than $450. Under no-power mode, the stabilizer was to act as a neutral, unmoving attachment and should be stiff enough so as not to interfere with normal targeting. The general space requirement was based on a standard issue handgrip available on the market, and power was assumed to be delivered from a battery packaged within this volume.

2.2 Stacked Platform Design

To achieve stabilization in the elevation and azimuth direction, the SMASH platform was designed to produce motion in two degrees of freedom using a decoupled stage (termed the Stacked Platform) that allowed for easier control. Linear sliding stages were designed to move in the elevation and azimuth directions, and the motions

Table 2.2. Stabilizing Handgrip Specifications.

Feature	Specification
Handgrip Size	
Height cm (in)	10.0 (3.94)
Diameter cm (in)	2.29 (0.90)
Max Force N (lb)	8 (1.8)
Max Displacement mm (in)	2 (0.08)
Operating Temperature ^{o}C (^{o}F)	-40 - 60 (-40 – 140)
Weight g (lb)	350 (1.1)
Environment	Sealable
Cost (US Dollars)	<$450
Other	Simple Reparability
	Ease of Assembly
	Mass Producible
	Attaches to Rail System
	Rigid when powered off

of the two stages were combined through an additional set of sliding joints to an output stage. The overall structure (Figure 2.8) fits inside a handgrip, while maintaining a hollow interior for a battery and electronics. This hollow interior was made possible by packaging the SMA wires along the circumference of the cylinder, and illustrates the overall benefit of employing SMA over conventional actuation such as voice coils or motors. To provide stiffness in the elevation direction and support the weight of the rifle, a coil compression spring rests on a dowel press fit to the azimuth stage. For characterization within this section, two forms of packaging the SMA wire are explored: spooling around the pegs to make a smaller length handgrip and straight, unwrapped wire achieved via a telescoping extendable structure that increased the overall length of the handgrip.

2.2.1 Architecture and Operation

Both the azimuth and the elevation stages are actuated antagonistically, with two pairs of SMA wires acting in opposite directions. This configuration was selected to

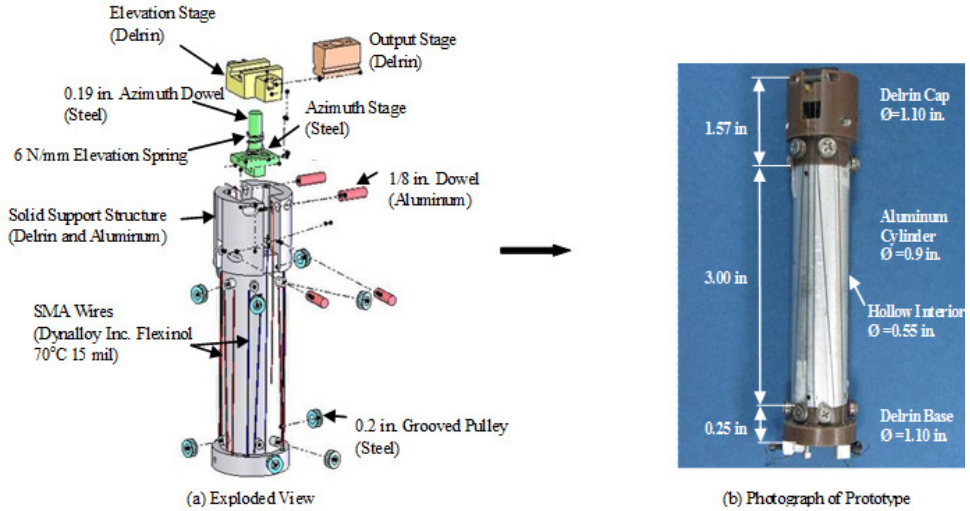

Figure 2.8. SMASH Platform Architecture. Exploded and collapsed views of the direct drive actuator. Elevation and Azimuth motions are coupled to the connection to the M16 rifle.

assist in overall controllability since both the forward and return stroke can be actively shaped through input heating profiles. The stacked platform actuator (Figure 2.9) produces motion when one of its antagonistic wires is heated, which both forces the stage to the required direction of travel and stretches the opposing cool wire producing de-twinned variants in its Martensite phase. For example, the azimuth stage (Figure 2.9a) is moved leftward against friction by heating the left wire and allowing the right wire to cool. This effectively deforms the right wire, which is then ready to actuate and move the stage to the right. The elevation direction (Figure 2.9b) is similarly actuated upward by running current through the wires responsible for moving the stage against spring forces. The upward motion also deforms the cool wires, which are in turn heated to move the stage down, stretching the upward wires, and completing the work cycle.

2.2.2 Loading Theory

The operational theory behind the stacked platform's operation is summarized in Figure 2.10, where the blue lines represent the system load lines including the force effects of de-twinning the opposing cool wire ($F_{m,l}$ for the left Martensite wire and $F_{m,r}$ for the right), combined with either the additional friction forces for azimuth ($F_{friction}$),

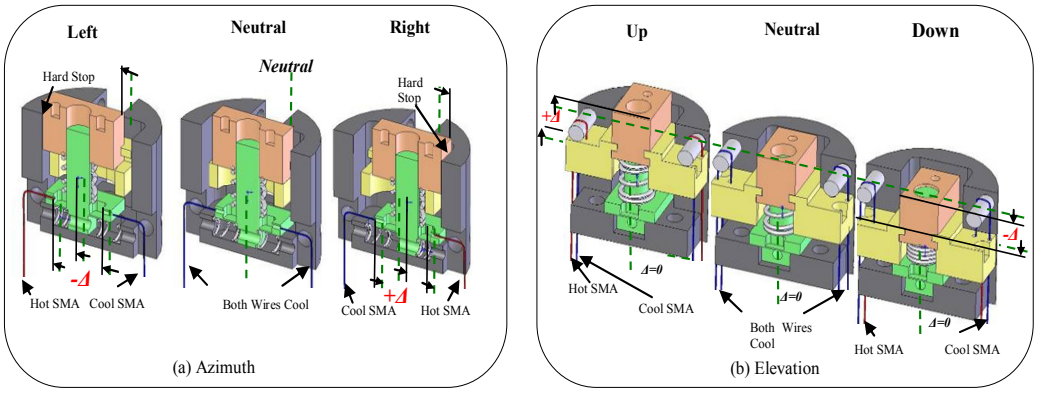

Figure 2.9. Azimuth and Elevation Motion. Stages are actuated by antagonistic SMA wires that are electro-resistively heated to produce motion in the required direction of travel.

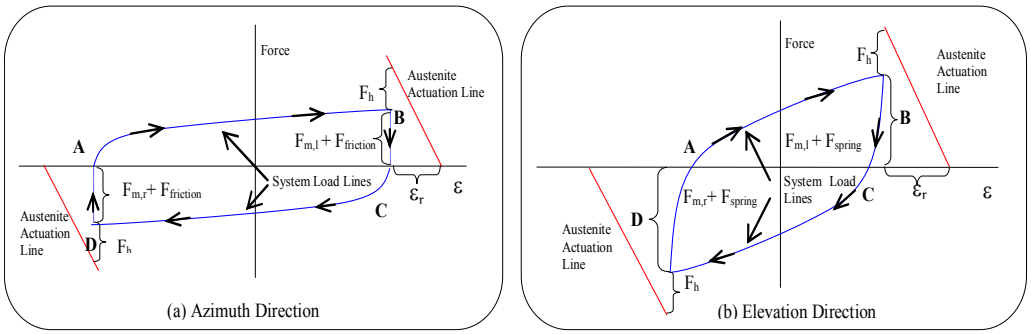

Figure 2.10. System theory for azimuth and elevation directions of operation. SMA martensitic force, azimuth friction, and elevation spring stiffness all contribute to the system load lines.

or the spring stiffness for elevation (F_{spring}). The red lines represent the actuation lines which are the SMA wires in Austenite form. Operation in the azimuth direction, beginning with the slider moved to the left side, begins at point **A** (Figure 2.10a). As the actuating right wire is heated, the slider is moved towards the right hard stop, point **B**, exerting a force F_h (the difference between the Austenite curve and the system load line) against the stop. The actuator load line is offset from this hard stop an amount ε_r, which corresponds to the additional strain the wire is capable of producing under zero load. For the device to produce full motion, the Austenite curve must at least intersect the system load line at point **B** (F_h must be greater or equal than zero).

As the actuating wire is cooled, the operating curve follows the path between points **B** and **C**, where the slider is kept in the right position due to friction. Heating the left wire causes the slider to move leftward, and the path between **C** and **D** is followed. Finally, in cooling, the curve between **D** and **A** is traced and the cycle is completed. The elevation direction (Figure 2.10b) is identical to the azimuth, with the only difference being the elevation spring stiffness (F_{spring}) replacing the azimuth friction ($F_{friction}$) in the load lines. Because of this change, the unloading between points **B** and **C**, and **D** and **A** is not vertical, as the spring contributes to deforming the cooled actuating wire in twinned Martensite form.

2.3 Quasi-Static Design Methodology

Because SMA demonstrates shakedown and its material properties change according to cycling conditions (Erbstoeszer, et al. 2000; Lagoudas, et al. 2000), it is not possible to obtain the operating system or the actuation load lines directly from the manufacturer. While, it is possible to stabilize the material through a shakedown procedure (Erbstoeszer, et al. 2000), the loading requirements are themselves a function of the operating system load lines. Thus, the initial step in the design process (Figure 2.11) is to determine an approximate range for the system loads, labeled as Step 1. These loads are used to shake down the SMA wire (Step 2), and in Step 3 the appropriate wire length is selected using the measured shake down strains and an empirical model. After installing the wire in the actuation system, the post-shakedown load lines are measured to verify that the operating loads are below the selected shakedown level (Step 4). If the loads are greater, the shakedown process is repeated. However, if they are less, the design process is deemed successful and the actuator is

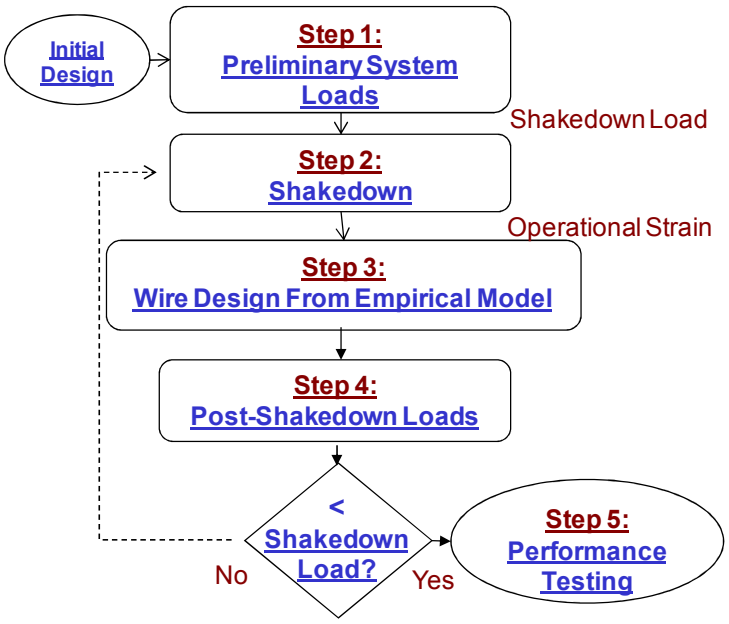

Figure 2.11. System theory for azimuth and elevation directions of operation. SMA martensitic force, azimuth friction, and elevation spring stiffness all contribute to the system load lines.

passed to performance testing in Step 5. This experimental design procedure is demonstrated in context of the SMASH prototype that was built for the M16 case study.

2.3.1 Stabilizing Handgrip Prototype

A preliminary prototype for the experimental design process was designed and built based upon the specifications for the M16 outlined in Table 2.2. The elevation spring stiffness was set to 6 N/mm such that the rifle would act as a neutral, unmoving attachment with the device in its de-activated state. The stages were designed to travel the required displacement of ± 2 mm from the neutral position (total of 4 mm) in the elevation and azimuth directions to stabilize the M16 rifle. Since the design process is iterative and an exact SMA wire length was not possible to initially define, flexibility for the packaged wire length was built into the system. If extra wire length was needed, the SMA could wrap around 0.2 inch diameter pulleys installed on the perimeter of the base, and if even more length were needed the base of the device was designed to telescope outward. Because the system loading behavior, recoverable strain, and consequent SMA wire length were all unknown, it was necessary to develop a procedure to specify the material requirements. This was accomplished by measuring the system loads without the wire and adding them to the Martensite loading plateau of the pre-shakedown SMA wire. Using a factor of 1.5 above these loads, the SMA wire was then shaken down, installed in the device, and verified to produce the required motion.

The final prototype and dimensions are detailed in Figure 2.8b. Most of the components in the device assembly were hand machined. The azimuth stage was fabricated from steel with the vertical azimuth dowel press-fit in the base. The elevation, output stages, and solid support structure were machined from Delrin due to its high strength and machinability. The pulleys were lathed from steel and were held in

place by screws threaded into the support structure. The elevation spring was obtained off-the-shelf from Century Spring, Inc and the 70º C Flexinol SMA wire was supplied by Dynalloy Inc. The wire diameter was initially set at 15 mil, which was verified as being sufficient for the required actuation forces.

2.3.2 Initial System Load Lines

Because the shakedown process requires an estimate of the operating load lines, it was necessary to estimate the force requirements before-hand. These were difficult to predict because the anticipated forces due to azimuth friction, elevation spring stiffness, and the de-twinning of the inactivated SMA wire were all unknown. Therefore tests were performed to separate and measure the friction and stiffness loads without the SMA wire installed. Separate material curves were also obtained for the SMA wires both in Austenite and (twinned) Martensite phases.

2.3.2.1 Experimental Setup and Procedure

The test apparatus used to characterize the effects of the azimuth friction and the elevation spring is illustrated in Figure 2.12. A probe threaded to a Cooper Instruments DFI 2555 force transducer was designed to contact and push the elevation and azimuth platforms at the wire contact points (simulating actuation), with the displacement recorded by a Microtrak 7000 Laser Displacement Sensor. Signals from both the force and displacement readouts were fed into a National Instruments NI USB-6009 Data Acquisition Card, read by a PC running LabView for storage and further analysis. A DC Voltage supply was connected to the handgrip device to heat selected SMA wires. A collection of weights was used as a varying load on the handgrip's output stage. Because the system was designed to be decoupled, stiffness studies were conducted separately for each direction, with the handgrip device oriented vertically in the vice for the azimuth direction (Figure 2.13a) and horizontally for the elevation direction (Figure

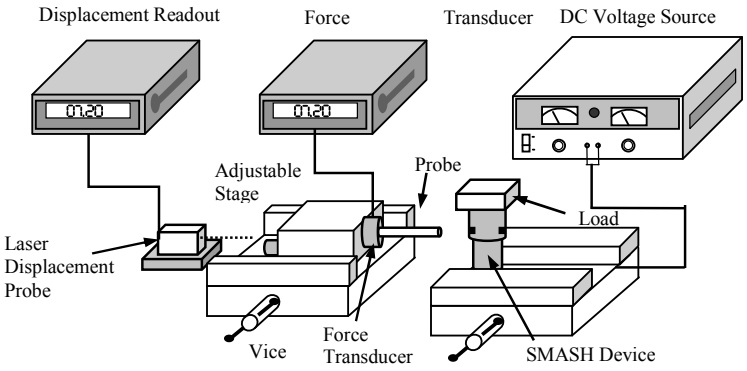

Figure 2.12. Schematic of Test Apparatus. Data was recorded using LabView computer software.

2.13b). In trials for each direction the force probe was dialed towards the stage, pushing it all the way through its range of motion to the hard stop.

2.3.2.2 Initial Azimuth Load Lines

The initial friction tests for the azimuth direction were obtained for motions in the left and right directions (Figure 2.15a). Force was defined as positive in the left direction (resisting motion to the right) and negative in the right direction. In each test, the force increased sharply in magnitude as motion was initiated to overcome friction and reached a flat plateau to remain relatively constant through the remainder of the motion. An average of these force plateaus for varying normal loads is shown in Figure 2.15b. In the figure, there is initially a clear increase in the required force with increasing normal load where, for example, the required force for rightward motion is increased by 79% from 5.03 to 9.02 N as the normal load was increased by 76% from 1.29 to 2.27 Kg. At the higher normal load there is less of a distinction. For example, there is only a 5.4% increase in required rightward force from 9.02 to 9.51 N for a 44% increase in load from 2.27 to 3.28 Kg. In addition, there is a consistently lower force requirement for motion in the left direction (negative displacement) by an average of 15%. This effect is attributed to imperfections in machining both the steel azimuth slider and the Delrin support structure and could be corrected by switching to higher

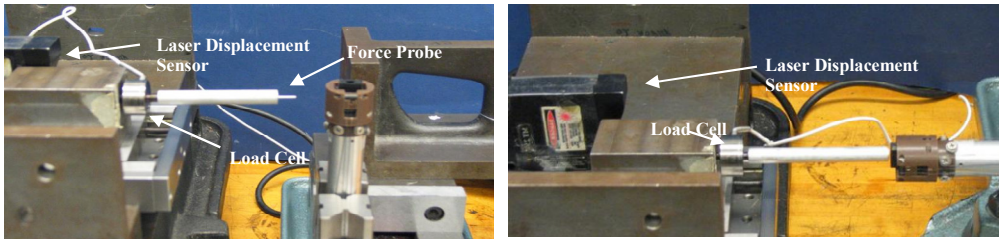

(a) Azimuth Direction (b) Elevation Direction

Figure 2.13. Experimental setup for elevation and azimuth testing. Force-displacement data is obtained in both the azimuth and elevation directions using a laser displacement sensor and load cell.

precision machining equipment. Because the data is non-linear, a traditional linear friction model cannot be fit. However, the forces are bounded below 10 N for all loads below the 3.28 Kg level which simulates the rifle load.

2.3.2.3 Initial Elevation Load Lines

Since the elevation stage does not support significant normal forces under standard operation, it was assumed that these friction effects were negligible. The force profile for the elevation stage with no wire is plotted in Figure 2.14. Because only spring effects are present in this case, the relationship is linear, initially moving off the hard stop and then increasing with a steady slope of 5.8 N/mm which is very close to the designed stiffness of 6 N/mm. This stiffness along with the spring preload of 16.7 N was designed so that with no wires installed, the rifle weight would compress the stage

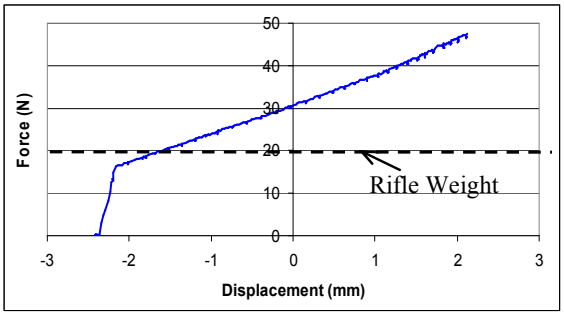

Figure 2.14. Elevation Wire Effects. Spring stiffness and martensitic force profiles for the elevation stage.

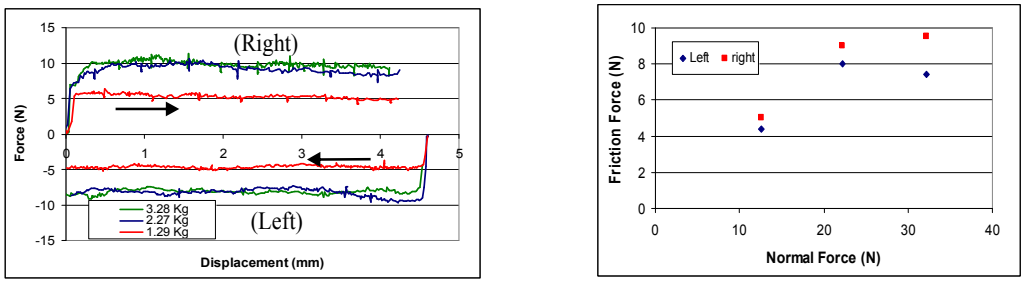

(a) Load Lines

(b) Average Friction Force vs. Normal Force

Figure 2.15. Frictional Forces for the Azimuth Direction. Force-Displacement curves under varying normal forces were obtained for both the left and right azimuth directions.

close to the neutral position (Figure 2.14). This was done to keep the slider in the neutral position under zero power, and reduce the average power consumption when stabilizing disturbances around this neutral position.

2.3.2.4 Pre-Shakedown SMA Load Lines

The final variable that required measurement was the force needed to de-twin SMA in its Martensite form. To measure this force level, a 10 inch long, 15 mil diameter SMA wire was fixed at one end with a mechanical crimp that was attached to a Cooper Instruments DFI 2555 load cell fixed to a movable stage (Figure 2.16 and Figure 2.17). Displacement was measured by an LVDT driven by an Omega LDX-3A Transducer Conditioner. Signals from both the force and displacement readouts were fed into a National Instruments NI USB-6009 Data Acquisition Card, read by a PC running LabView. The wire was first heated by a Kepco ATE 55-20DMG power supply to its Austenite form and the stage was slowly loaded to a weight of 65 N while recording force and strain. The wire was then cooled at the Austenite free length and then the stage was again loaded recording the loading curve required to de-twin the twinned Martensite to 3.5%. Figure 2.18 shows the collected data for both Austenite and Martensite states. The Austenite stiffness is linear and increases at a slope of 7.9 kN/strain while the Martensite displays a plateau that remains relatively flat as the wire is strained to 3.5%. Since the wires in the device are designed to strain at a maximum of

3.5% (as a safety factor against permanent plastic deformation of the wire), the maximum martensitic force was measured at this point to be 15 N.

2.3.3 Post-Shakedown SMA Load Lines

Because the SMA wires were to be installed in an actual device and the load lines measured, the material had to first be shaken down to reduce motion degradation during operation. This was performed by cycling the wire under a constant load that was a factor of safety above the estimated system loads. The estimated azimuth system load was obtained by adding the bounded friction forces of 10 N to the 15 N required to de-twin the SMA Martensite phase resulting in a total of 25 N. In the elevation direction, because two wires actuate each direction, the martensitic force is accounted for twice (30 N) and then added to the spring force (15 N) yielding an overall requirement of 45 N for both wires (22.5 N for each wire). Following Erbstoeszer, et al. 2000, the SMA wire was shaken down at approximately 1.5 times the maximum estimated load of 25 N (40 N shakedown load).

2.3.3.1 Shakedown Experimental Setup and Procedure

Using the same apparatus as the one used for the SMA load lines (Figure 2.17) the SMA was cycled under a constant load of 40N (350 MPa) with a power supply that was programmed to alternately heat the wire in air with 1.5 amps of current for 7 seconds and shut off power for 25 seconds to allow the wire to cool. Since the 40 N load is well

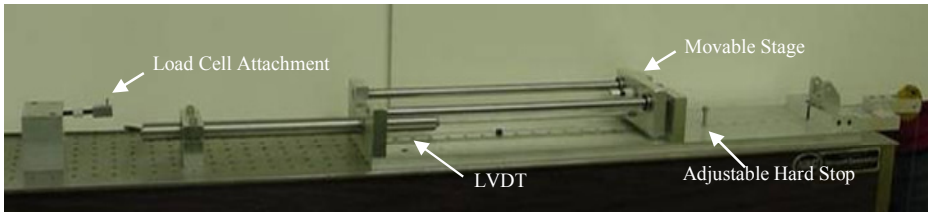

Figure 2.16. Material loading and Apparatus. A side-view photograph of the experimental setup used for wire shakedown.

above the approximately 9 N (79 MPa) Martensite plateau of the wire, a removable hard stop was set at a known strain of 3.5% from the Austenite length to prevent the wire from overstraining and to actuate at the design strain for the SMASH. Thus, the wire cycled from a strained Martensite length fixed by this hard stop, to a contracted Austenite length.

2.3.3.2 SMA Shakedown Results and Empirical Modeling

The SMA wire was cycled under the load of 40N over approximately 400 cycles. Data collected for the first wire is shown in Figure 2.19, where the contracted Austenite length decreases over the first 200 cycles, and begins to level off approaching a stable, steady-state contracted length. The behavior exhibited in Figure 2.19 is similar to the thermal cycling mechanisms reported by Barnes et. al. 2005 and Erbstoeszer et. al. 2000, and can also be correlated to the shift encountered in pseudoelastic cycling (Miyazaki, et al. 1998). This zero load shift is theorized to be formed by a combination of slip deformation and the accumulation of residual Martensite, observed optically by Miyazaki et al. (Miyazaki, et al. 1998).

An empirical model was fit to the curve in Figure 2.19 by applying a curve fit with two exponentially decaying constants plus a constant,

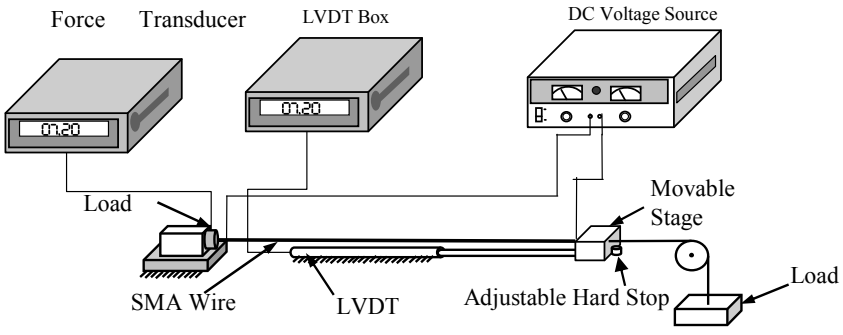

Figure 2.17. Schematic for Material Loading and Shakedown Test Apparatus. Data was collected by LabView Software.

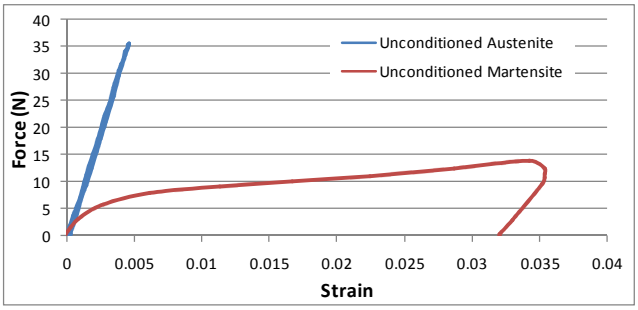

Figure 2.18. Material Properties of Pre-Shakedown SMA. Austenite and Martensite loading curves.

$$[\varepsilon] = ae^{(-bN)} + ce^{(-dN)} + \varepsilon_f \,. \tag{2.24}$$

where ε is the strain in the material, N is the number of cycles, and ε_f, is the amount of strain expected as the cycles are taken to infinity. The experimental data and the model fit are plotted in Figure 2.19, and it was found that the fit followed the data remarkably well (0.99 R-value) and predicted a steady-state strain difference (defined as motion relative to the hard stop divided by the unloaded Austenite wire length) of 2.5% at infinite cycles. Thus, assuming no rate constants appear at higher cycles, the predicted

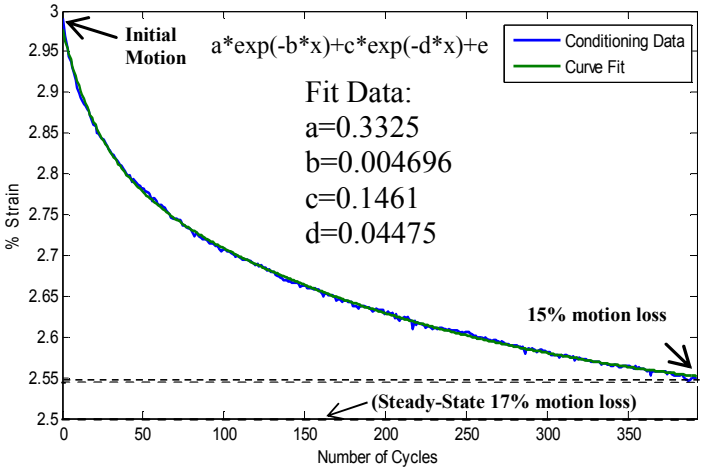

Figure 2.19. Shakedown Data with Fitted Curves. Data for elevation and azimuth wires are plotted along with their respective curve fits and predicted steady-state values.

shakedown after 400 cycles is reduced to only 2% (from 17%) of the actuator's motion recovery.

2.3.3.3 Post-Shakedown Material Characterization

To experimentally verify the expected shift in Austenite zero and to measure SMA material properties after cycling, the wire was characterized using the shakedown test apparatus (Figure 2.17). The Austenite force-deflection curves were first measured by keeping the wire heated under a constant current and applying a load below the 40 N used during shakedown. The Martensite force-deflection curves were similarly obtained by heating the wire, allowing it to cool, and applying incrementally increasing loads below 40 N until the wire was stretched to the hard stop. The results (Figure 2.20) show that the shakedown of the wire shifted the Austenite zero by 0.5%, which correlates to the strain shift in Figure 2.19. The results also slightly increased wire stiffness to 8.5 kN (75 GPa)/strain which was 7% greater than the stiffness of 7.9 kN (69 GPa)/strain before shakedown. Linear extrapolations of the Austenite lines (Figure 2.20), when intersected with the 40N force level and subtracted from the hard stop closely match the 3% and 2.55% strain produced by the SMA before and after shakedown (Figure 2.19) confirming the mode of operation.

2.3.3.4 SMASH SMA Length Selection

The results of the shakedown process and material characterization were utilized to determine the appropriate wire length for the SMASH. Because the force of 40N used during shakedown represents an upper bound for the actuator, the steady-state strain under this load of 2.5% (Figure 2.19) was used to calculate that 16 cm (6.3 in) of wire was required to produce 4 mm of displacement. Thus, the SMASH with its base extended can produce the required motion without spooling the wire but the wire must be fully transformed for each cycle potentially limiting the stroke at high speeds where

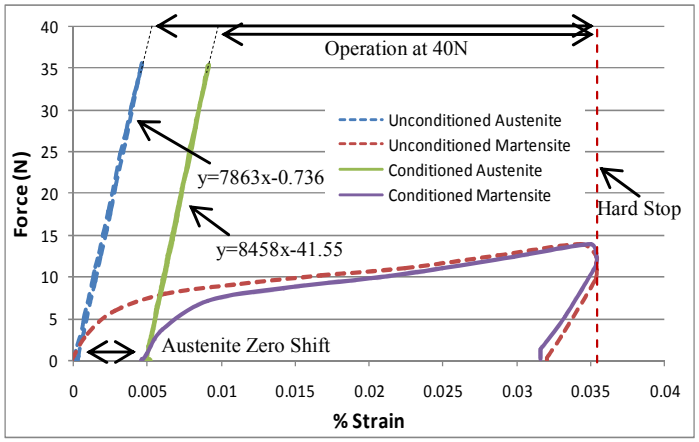

Figure 2.20. Material Characterization. Wires were tested before and after shakedown.

heat transfer rates become an issue. Spooling the wire, on the other hand, packages more wire in the same handgrip height, allowing the potential for partial transformation during high speed operation. Thus, roughly twice the required length (33 cm of 70º C, 15 mil diameter wire) was spooled in the device to determine the feasibility of spooling and the potential losses that may be encountered.

2.4 Platform Characterization

After following the experimental design procedure, the shaken down SMA wires (33 cm) were installed in the fabricated SMASH prototype which was then tested for the M16 case study. These tests were conducted under both quasi-static and dynamic regimes to ensure full actuator authority under the required frequencies. Cancellation tests of simulated tremor were also conducted using an actual M16 rifle. Performance results from these studies are detailed in the following sections.

2.4.1 Quasi-Static Platform Performance

To ensure that the SMASH was capable of producing full motion under the quasi-static specification, experiments were conducted to verify the system response and actuator output in both elevation and azimuth directions. Since the SMA behavior

changes after shakedown, the operational graphs were re-generated using the same experimental setup shown in Figure 2.13. The SMASH prototype was also tested in an experimental set up that simulated the rifle loading for the M16 case study for overall performance. Motion performance for both output directions was recorded using this setup and was analyzed to ensure both that full motion was generated and that cyclic actuation at the rifle mass of 3.3 kg produced after approximately 10 cycles no further degradation in performance due to shakedown. In the dynamic studies (Section 2.4.2) the actuator is shown to produce full motion after thousands of cycles.

2.4.1.1 Azimuth Testing with Shaken Down Wire

In the azimuth direction, the system load lines were obtained with the antagonistic wire beginning in twinned Martensite and Austenite (at the same initial strain). By monitoring the applied loads during the experiment, care was taken when obtaining the Austenite curves to ensure that the system was not loaded beyond the level used for shakedown, as the wire could be damaged. The system Austenite and Martensite loading lines including azimuth friction from a simulated rifle mass of 3.3 Kg are shown in Figure 2.21 for both directions. Because of the forcing sign convention the two Martensite system curves form a "box" as the system moves to the left, stretching the right-pulling wire (positive loading), and then moves to the right, stretching the left-pulling wire (negative loading). In Figure 2.21 the system Martensite curves correspond to the system load lines in Figure 2.10 with the force levels slowly increasing to a maximum of 26 N for each direction. This is very close to the predicted load level of 25 N (10 N from sliding friction and 15 N from the Martensite plateau), with the difference being caused by unaccounted losses such as those encountered during wire spooling.

The shaken down right and left Austenite curves shown in Figure 2.21 were taken

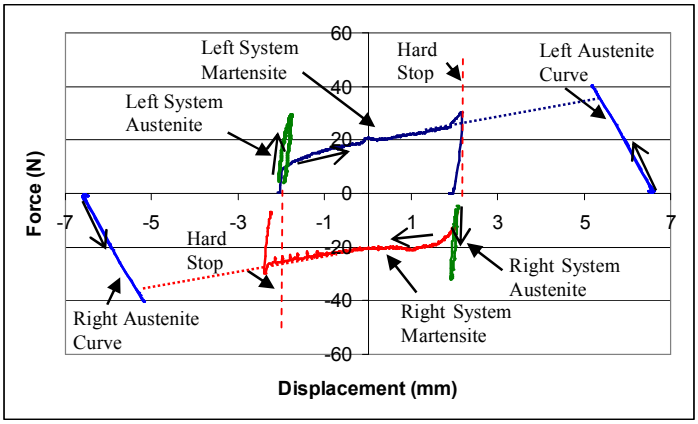

Figure 2.21. Azimuth System Curves. Shaken down unpackaged Austenite curves are added as reference.

directly from the material characterization test (Figure 2.20). The 6.5 mm shift from the neutral position was calculated from the knowledge that each antagonistic wire was strained 3.5% from each opposing hard stop. Since 304 mm of wire was used for each side, the Austenite zero would exist at 3.5% of this length, or 10.6 mm from each hard stop (6.5 mm from the neutral position). These curves represent the force-deflection characteristics of each wire acting as an actuator, rather than as part of the system. Therefore, for example, the intersection of the left Austenite curve with the extrapolated (shown by the dashed line) left system Martensite curve represents the motion that the device can generate in the left direction if the actuated wire were packaged straight, without bending over a pulley. Because losses exist in the spooled packaging, this intersection provides an upper bound prediction on the motion generated by the device.

2.4.1.2 Elevation Testing with Shaken Down Wire

The experimental procedure was repeated for the elevation direction and the results were compared with those obtained during the stiffness testing with no wire. According to the results (Figure 2.22) the system load line increases to a maximum that is 47 N higher than the amount caused by the elevation spring stiffness. Since there are two

actuating wires for each direction in the elevation stage, 30 N of this force is used for detwinning. The remaining 17 N (8.5 N for each wire) is attributed to unaccounted losses such as from spooling. The overall force requirement for each wire, however, is 30 N which is still safely below the 40 N of load used for wire shakedown.

2.4.2 Device Motion Performance

To confirm that the quasi-static motion meets the displacement requirements of 4 mm and that the material shakedown was indeed reduced, performance tests were conducted. In these test the platform was loaded with a simulated rifle mass of 3.3 Kg and the displacement was measured with a Microtrak 7000 Laser Displacement Sensor (Figure 2.23 and Figure 2.24) both in the azimuth and elevation directions. Motion was achieved by resistively heating SMA wires via a DC power supply under approximately 1 amp of current and cooling through natural convection in air. The cycle was repeated for ten cycles.

2.4.2.1 Test Results

The measured displacement profiles (Figure 2.23) indicate that for the azimuth direction the device was capable of exceeding the specification of 4 mm by an extra millimeter (5 mm total displacement, reaching the hard stops). In addition, the peaks in

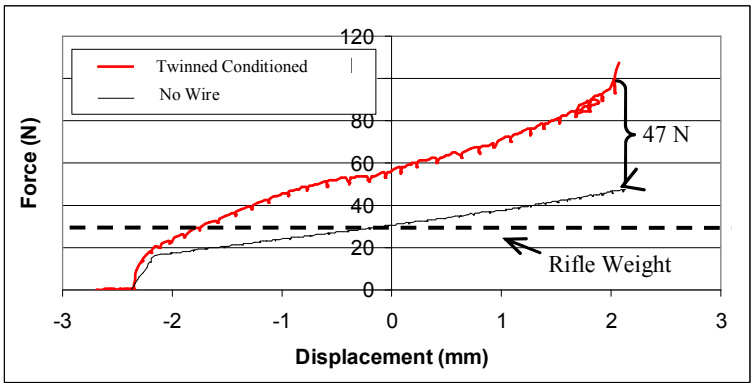

Figure 2.22. Elevation System Curves. System curves for no wire and shaken down Martensite are plotted.

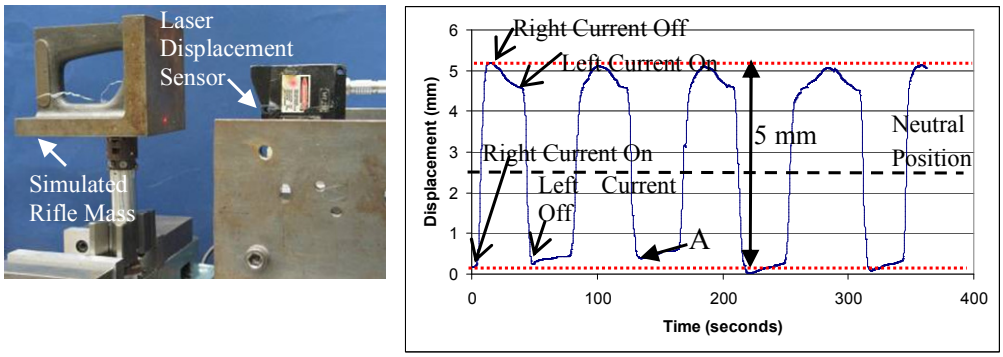

(a) Azimuth Setup

(b) Azimuth Motion Profile

Figure 2.23. Azimuth Motion Testing. Experimental setup to test azimuth actuator authority

the displacement profile show no noticeable downward trend in output motion indicating that the wire was properly stabilized and was operating below the shakedown load level. Apart from Point A where the wire was not completely heated, the motion was consistent at its maximum and minimum points. A final feature worth clarifying in Figure 2.24 is the dip in the displacement profile after the left or right current shutoff. This dip is simply caused by the wire relaxing under compliance of the hard stop when it is cooled by natural convection. This indicates that the wire not only brings the platform up to the hard stop, but pulls against it with significant force. The overall displacement in the elevation direction (Figure 2.24) also exceeded the 4 mm specification by 0.6 mm (4.6 mm total) and there was no noticeable degradation in the overall motion, indicating that the shakedown was also successful.

2.4.2.2 Spooling Effects

While the specified motion of 4 mm was exceeded in both directions using spooled wire, it was hypothesized that bending the SMA around the pulley created losses which when added to frictional losses from the pulley required extra actuation force. While the intent of spooling the SMA wire is to package additional wire in the device to produce extra motion (Redmond, et al. 2008; Redmond, et al. 2009), experiments were conducted to determine whether this actually was the case. To test this, a set length of

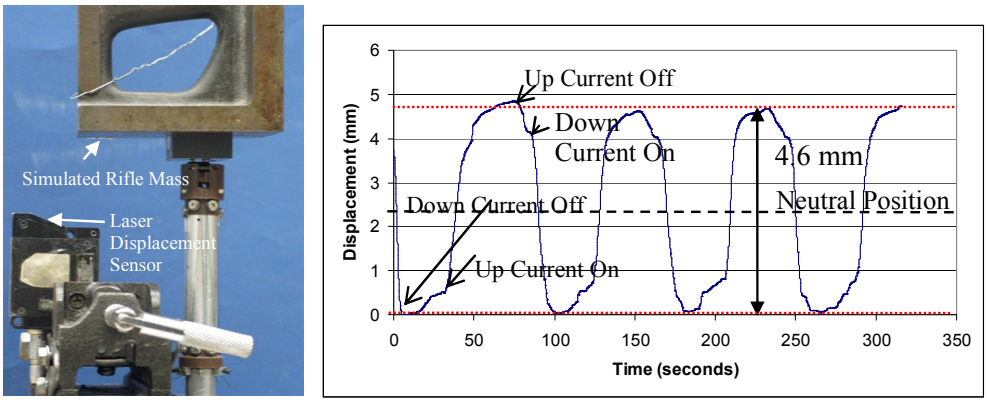

Figure 2.24. Elevation Motion Testing. Experimental setup to test actuation authority in the elevation direction.

12 cm (4.75 in) 15 mil diameter SMA wire was installed in the device both spooled and unspooled. To accommodate this length while spooling the wire, the overall height of the handgrip was reduced from 13.7 cm (5.4 in) to 6.6 cm (2.6 in).

Figure 2.25 shows the resulting displacement profiles. A maximum displacement of 4.3 mm was produced by the unspooled length of wire, while the spooled length produced a maximum of 1.8 mm. The spooled wire encountered significant losses, producing only 40% of the motion created by the unspooled length of wire. To further examine the mechanism for this loss in motion, an experiment was conducted to monitor both the strain and absolute motion at different locations in the spooled wire during actuation. This was achieved by marking six locations (two at each straight length of wire) and photographing the device before and after actuation. Absolute motion and relative strain was then computed by noting the pixels between marks. As seen in Figure 2.26, the SMA strain decreases from 4% to 2% after passing the first spool, and only 1.5% after passing the second. It should be noted that some of this strain in the last segment was used in taking up slack in the wire around the pulley and the amount of strain actually contributing to moving the output stage is anticipated to be even less than 1.5%. Possible causes for this loss in motion are friction and bending of

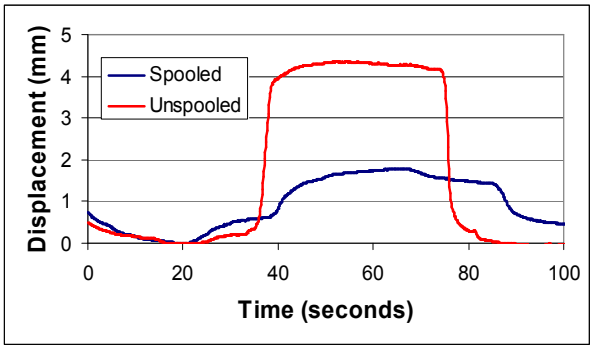

Figure 2.25. Output motion for spooled and unspooled SMA wires of the same length.

the wire about a small 5 mm radius. Because of these losses, care must be taken when choosing to spool SMA wire and to ensure that the application's motion requirements are satisfied with respect to space constraints. Since the additional wire length allowed by spooling more than makes up for the lost motion, the SMASH device still benefits from spooling, especially at smaller wire diameters. However, the greater voltage requirement and additional cooling load created by the additional packaged wire reduced the attractiveness of spooling in the final design, and thus straight wires were used with a longer handgrip height of 13.7 cm.

2.4.3 Dynamic Performance: Motion and Power Draw

Using the straight wires, initial dynamic tests of the SMASH were conducted to ensure that the displacement specification of 4 mm was met through the tremor

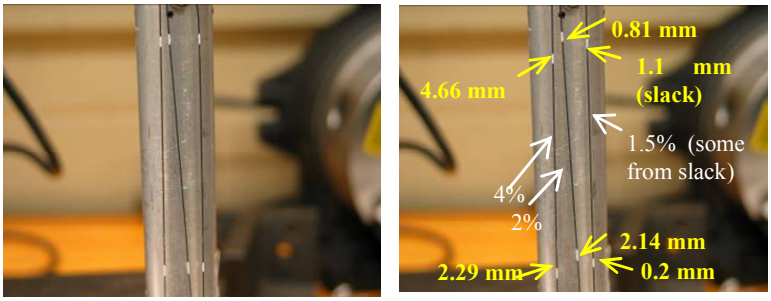

(a) Un-Actuated (b) Actuated

Figure 2.26. Monitored strain and displacement at different locations in the spooled wire after actuation. Significant losses occur after spooling.

frequency range of 0-3 Hz. The device was placed under a rigid beam (to simulate the 3.3 Kg load from the rifle) that was pivoted at one end, and the frequency response was obtained by setting the duty cycle to a nominal level of 17% and varying the frequency. The 15 mil SMA wires were submerged in water to improve cooling performance. For each frequency level, current was slowly increased (up to 1.5 amps) until the maximum displacement ceased to increase.

This maximum displacement was recorded and is plotted in Figure 2.27. Overall both elevation and azimuth directions matched the 4 mm specification throughout the frequency range. Only at the peak frequency of 3 Hz, did a very small amount of motion loss appear (0.3 mm for elevation and azimuth), though this could be eliminated with thinner wires or improved cooling. However, this was deemed unnecessary since most studies have indicated that the peak tremor frequencies reside around 1-1.5 Hz, for which motion specifications were satisfied in both the elevation and azimuth directions.

The power consumption (obtained by measuring the input current and voltage), is displayed in Figure 2.28 and shows that raising the driving frequency significantly increases the power consumption by as much as 60% between 1 and 3 Hz. Amplifying the output displacement also requires more power as the material is required to fully transform. At 1 Hz, for example, the power requirement increases approximately 2.4

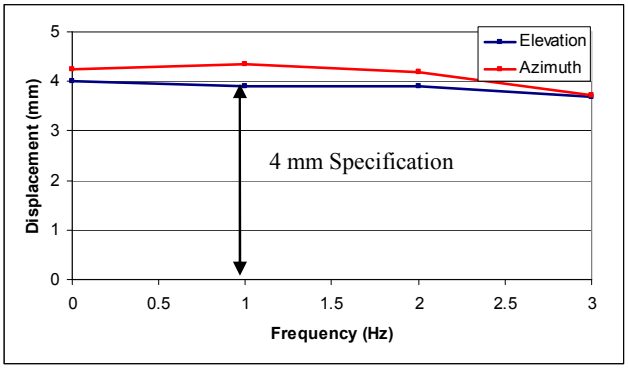

Figure 2.27. Frequency response of Nitinol 55, 10 mil, 70C wire.

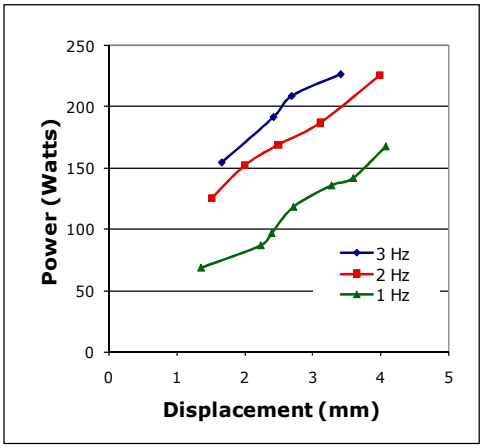

Figure 2.28. Power Consumption for Dynamic Cycling in Water. Results are for the elevation direction using 10 mil SMA wires.

times between 1 and 4 mm. In this test, the overall power draw is significant, and is in no sense optimized. To improve power draw in future designs, there is therefore a need for an accurate device model where design variables such as cooling medium, wire diameter, and length can be tuned to ensure a minimal power draw that is suitable for self-contained battery operated systems. This issue is studied and resolved in Chapters 3 and 4 of this dissertation.

2.4.4 Feasibility Studies for Cancellation of Motion Disturbances

With the SMASH's actuation capabilities shown to exceed specification both in the quasi-static and dynamic domains with insignificant shakedown, efforts were directed on showing feasibility for human tremor cancellation. Preliminary tests on a human subject were conducted to quantify a dominant tremor frequency and amplitude. Using these values, a dynamic shaker was used to excite an M-16 rifle at the dominant tremor frequency as well as higher frequencies within the frequency range of interest (2 and 3 Hz). With the SMASH placed between the shaker disturbance and barrel, studies were conducted to demonstrate open-loop cancellation at all of the tested frequencies.

2.4.4.1 Initial Tremor Tests

Initial tremor tests were conducted at Techno-Sciences, Inc. on a human subject who was instructed to hold a rifle steady while a laser displacement sensor measured barrel motion (Figure 2.29). Figure 2.30 shows the measured signal and its corresponding Fast Fourier Transform (FFT) peaks after applying a 0.1 Hz high pass filter. There is a significant peak near 1 Hz, and a large portion of the disturbance occurs at or below this frequency. This is consistent with tests done separately at the Picatinny Arsenal, with the frequency peak stated at 1.5 Hz (NSAC 2007). In addition, all FFT peaks occur below the 3 Hz range, and decline at higher frequencies, confirming the design specification of 0-3 Hz. In this test, the frequency of 1 Hz, at a peak-peak amplitude of 2 mm was concluded to be the dominant form of tremor.

2.4.4.1.1 Experimental Setup for Cancellation

Cancellation performance was measured at the tested tremor frequency of 1 Hz and at higher frequencies of interest (2 and 3 Hz) using the experimental setup shown in Figure 2.31 and Figure 2.32. The end of the M16 rifle was held by a clamp, which was attached to a pivot to allow rotations in the elevation direction. The SMASH was fitted to a rail adaptor, and was attached to the M16 rail system at the position shown. Water was used as a coolant for the SMA wires, and was filled in an aluminum cooling sleeve designed and fabricated to fit around the SMASH. The bottom of this cooling sleeve

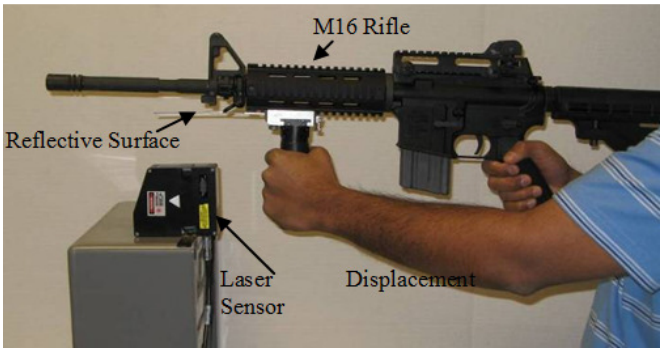

Figure 2.29. Experimental Setup for initial tremor testing.

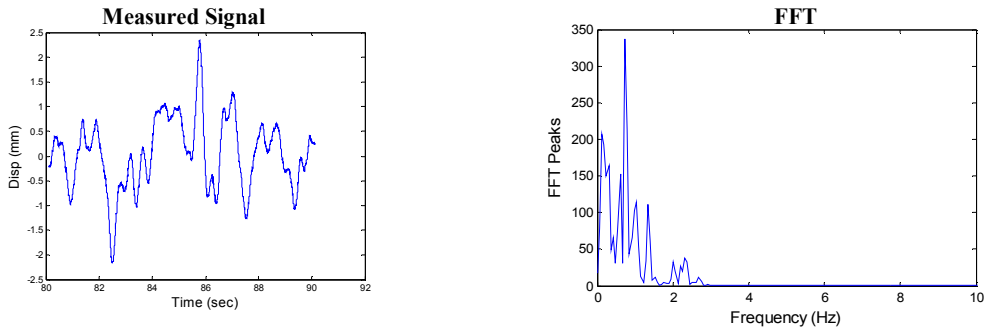

Figure 2.30. Position data and FFT of aiming disturbance after 0.1 Hz high pass filter.

was bolted to a LabWorks 139-40 Electrodynamic Shaker System, which was powered by an external amplifier. Barrel displacement was measured directly by a MicroTrak Laser Displacement sensor, and was recorded by an oscilloscope. The SMA wires in the SMASH were activated by a current pulse operating from a fixed voltage of 20 V with a duty cycle specified in a LabView program. The analog signals from this program were converted to a Pulse Width Modulated (PWM) signal through an Object-Oriented Programmable Integrated Circuit (OOPIC), and this signal was sent to a pair of MosFETs that functioned as switches for the PWM signal. Using a LabVIEW program, several different analog signals were used to drive the SMA wires. For the single-frequency studies, square waves of 18% duty cycle were used that had a peak current output of approximately 1.2 amps. Several smoothing functions were also employed that used the same peak output current but varied the transient shape of the current profile.

The experiment was run by setting the shaker to produce a sinusoidal disturbance, with the resulting barrel displacement recorded by the oscilloscope. The SMASH was then activated, and the phase and current amplitude signals sent to the SMASH were manually tuned until the best cancellation was measured. The experiment was repeated for several different input current profiles at 1, 2, and 3 Hz. The effects of each were recorded and are analyzed in the following section.

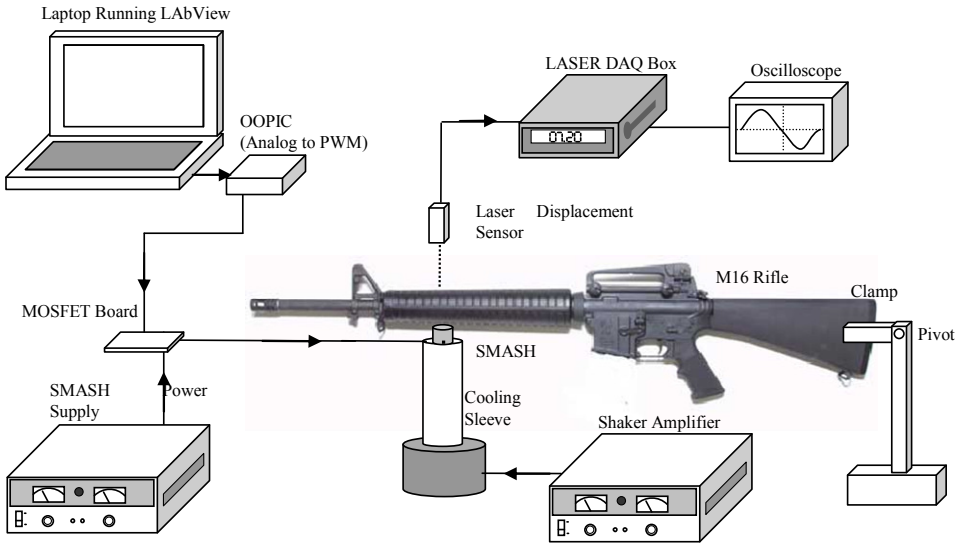

Figure 2.31. Experimental setup for the stabilization experiments. Shaker table simulates user disturbances acting through the arm and handgrip to the rifle barrel.

2.4.4.2 Cancellation Trials

The SMASH cancellation experiments were initially conducted with an 18% duty cycle square wave signal to maximize cooling time by heating the wires over a short period for each cycle. While this approach is favorable for high frequency operation, the output was not smooth compared to the disturbance sinusoid. Therefore, to further

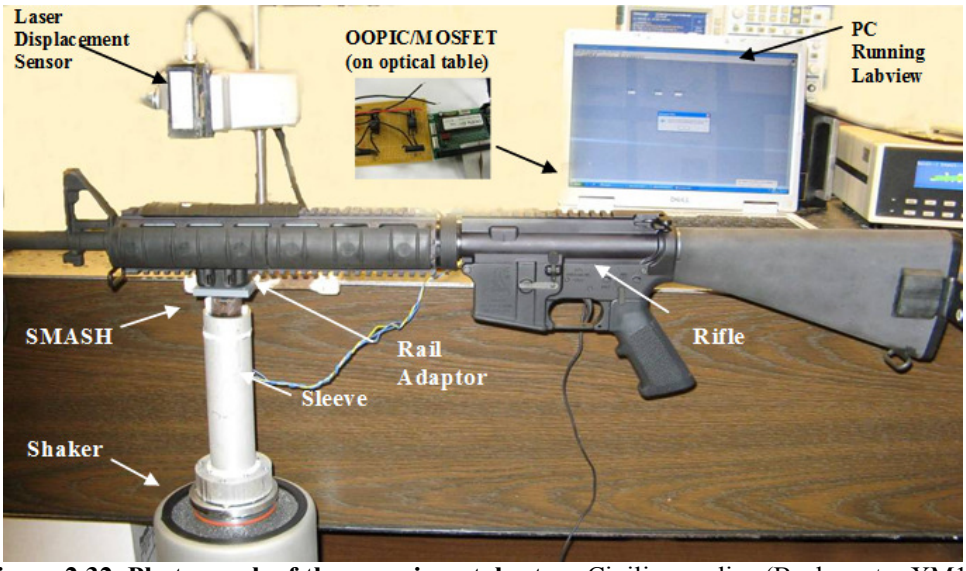

Figure 2.32. Photograph of the experimental setup. Civilian replica (Bushmaster XM15 E2S Rifle) was used in the actual tests.

improve stabilization, several different smoothing functions were tested to fit the SMASH actuation to the inverse of the sinusoidal shaker disturbance. Due to the highly non-linear behavior of SMA, it was difficult to predict the current input to produce such a shape, so this was done empirically in the absence of a predictive thermodynamic model for the actuator (which is developed in Chapter 4 due to this need). Based on observations of the resulting cancellation behavior of the sinusoid, two initial function shapes were developed -- a ramp, and a preheat waveform – and these two shapes were scaled and tested for the frequencies of interest.

2.4.4.2.1 Square Wave Input

The experimental results from the initial square wave trials at 1, 2, and 3 Hz are shown in Figure 2.33. The four traces in these plots are from 1) the shaker disturbance only, 2) the SMASH actuation only, 3) the sum of the shaker and SMASH signals, and 4) the cancelled motion (shaker and SMASH both activated). Significant reduction in motion was measured for all three frequencies, and the results are summarized in Table 2.3. Due to the mismatch in shape (but not amplitude) between the disturbance motion and the SMASH motion, the resulting error was made up of sparse, relatively narrow peaks. The RMS cancellation was consequently more significant than peak-to-peak cancellation (up to 70% for 2 Hz vs. 62% peak-peak). This is a positive result since RMS is a better measurement for overall reduction in aiming error than peak-to-peak since it represents the likelihood of shooting on target.

For all three frequencies tested, the sum of the disturbance and the measured SMASH motion (measured individually) almost exactly corresponded to the cancelled motion in Figure 2.33. This indicated that the system was linear and that if the disturbance profile is known, it could be cancelled by approximating its inverse with the stabilizing actuator. As a consequence, the stabilization data represents the overall

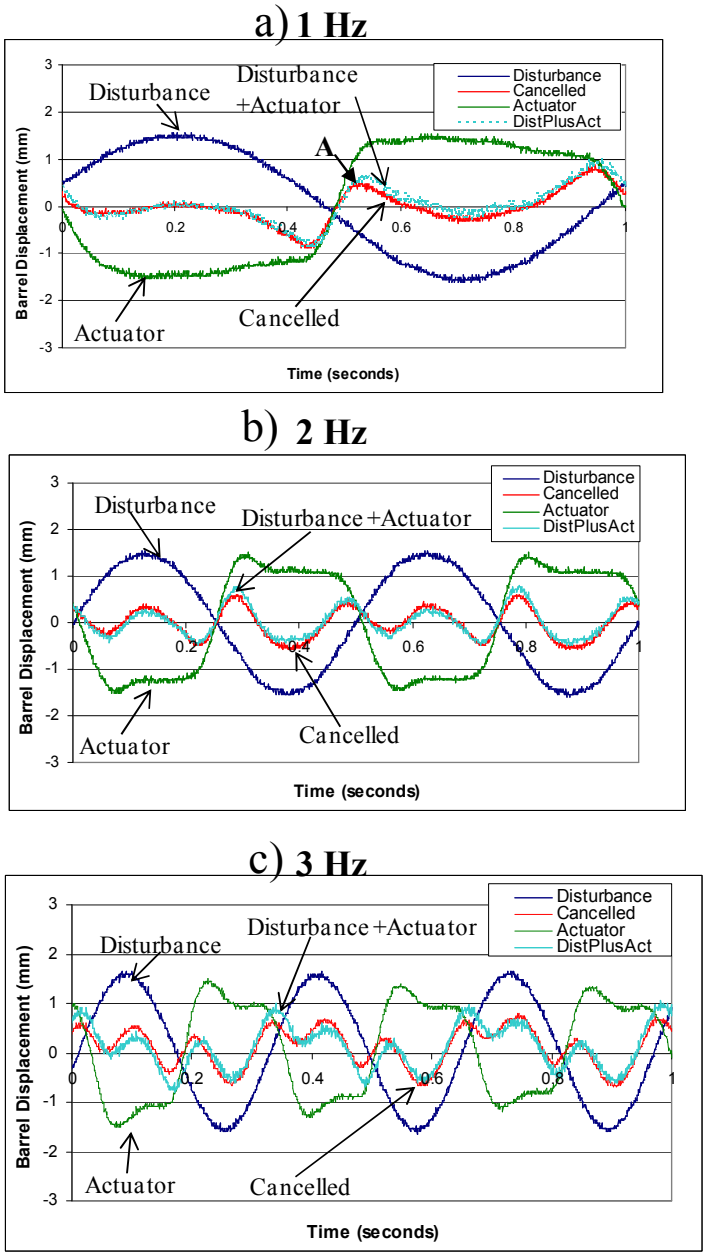

Figure 2.33. Initial cancellation results for 1, 2, and 3 Hz. In all three cases system linearity exists, and the additive result of the disturbance and actuator nets the measured cancellation.

error of the SMASH's ability to approximate the inverse of the sinusoidal input disturbance. Peaks in the plot, such as point **A** in Figure 2.33 indicate a jerk in the cancellation, which is due to the fact that the SMASH was transitioning much faster than the sinusoid leading to position error.

Table 2.3. Cancellation data for rifle stabilization experiments at 1 to 3 Hz for a 20% duty cycle square wave.

Frequency (Hz)	Disturbance (mm)		Cancellation (mm)		% Reduction	
	Amplitude	RMS	Amplitude	RMS	Peak-Peak	RMS
1	3.2	1.1	1.8	0.3	44 %	68 %
2	3.1	1.1	1.2	0.3	62 %	70 %
3	3.3	1.1	1.9	0.4	43 %	63 %

2.4.4.2.2 Smoothing Functions

To eliminate cancellation error, and to improve overall stabilization, current input functions were altered to help smooth the SMASH actuator and approximate a sinusoid more closely. Duty cycle was significantly increased (to 48% at 1 Hz) to produce a lower but more gradual input. The current profile was also modified to produce a gradual rather than step input that was previously using a square wave. After testing several inputs including modified square waves and sinusoids, two basic shapes were selected and applied to disturbances at 1-3 Hz: a ramp, and a ramp with preheat (Figure 2.34). The ramp was used to slow the initial motion and reduce overall jerk by gradually heating the wire to the Austenite finish temperature . The pre-heat profile, on the other hand, heated the wire faster to the Austenite start temperature, but then reduced the

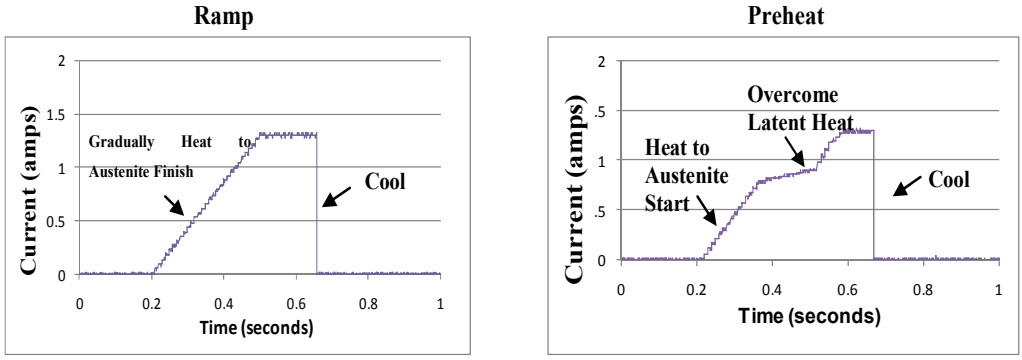

Figure 2.34. Ramp and Preheat current profiles used to smooth output profile.

heating while overcoming the latent heat of transformation. This was designed to produce even more of a gradual transition, and a final increase in current was produced to ensure full transformation of the wire.

1 Hz

Significant disturbance reduction was recorded at 1 Hz for both the ramp and ramp with preheat current profiles. The results (Figure 2.35a and b) show that the SMASH was able to approximate a sinusoid and cancel 68% and 75% of the peak to peak motion

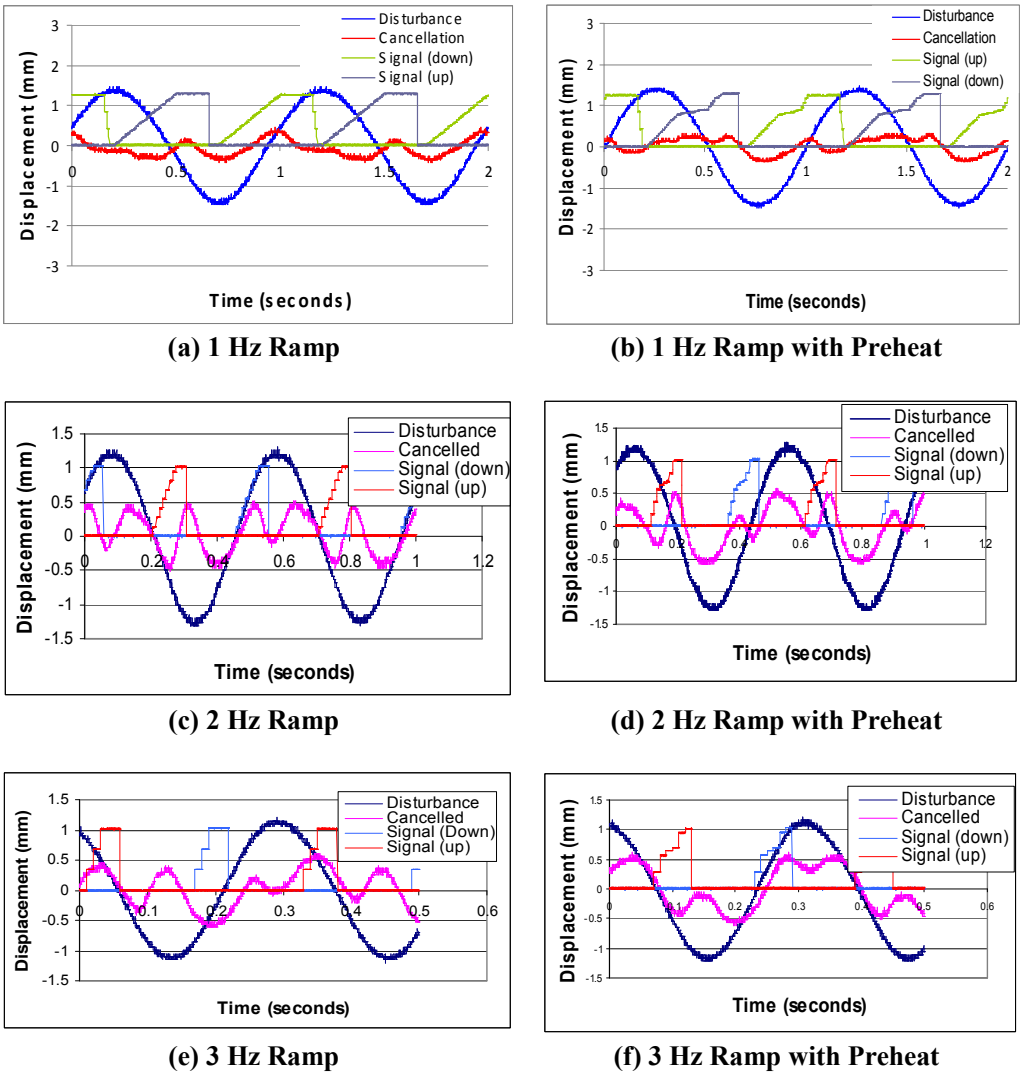

(a) 1 Hz Ramp **(b) 1 Hz Ramp with Preheat**

(c) 2 Hz Ramp **(d) 2 Hz Ramp with Preheat**

(e) 3 Hz Ramp **(f) 3 Hz Ramp with Preheat**

Figure 2.35. Open-Loop Cancellation Data. using Ramp and preheat smoothing functions are used for the input current profiles.

for the two trials. RMS motion was much greater (95% and 97%) indicating that the average barrel deviation was almost completely eliminated. While in open-loop, this RMS cancellation exceeds the 50% goal set in Section 1.2.4, and shows significant potential for successful closed-loop performance.

2 and 3 Hz

At the higher frequencies of 2 and 3 Hz (Figure 2.35c-f), it was more difficult to apply a higher duty cycle because there simply was insufficient time to cool the wires fully. For example, if the same duty cycle of 48% was used for the higher frequencies, a noticeable decay in motion would occur since the wires were only partially transforming back to Martensite and were remaining warm. Therefore, lower duty cycles of 20% were used, allowing full transformation but limited the smoothing effects of the current profiles, producing similar motion as square wave inputs.

While significant reduction in motion was measured (up to 67% RMS for 2 Hz and 58% RMS for 3 Hz), these were less than that achieved at 1 Hz because of the lower duty cycles used. This difference in cancellation is due to a physical limitation of the SMA under the conditions tested, and could be alleviated by improving the heat transfer such as by changing the cooling medium or reducing the wire diameter. In Chapters 3 and 4 of this dissertation, cooling and actuator design studies are accomplished to aid an achieving greater performance at these higher frequencies.

2.4.4.3 Smoothing Summary

Overall, significant reduction in barrel disturbance was recorded for all three frequencies (Table 2.4, Figure 2.36). However, at the higher frequencies of 2 and 3 Hz, the RMS cancellation is reduced when compared to 1 Hz. As discussed, the decrease in cancellation at higher frequencies is caused by the limitations in cooling, since the SMASH could not be slowly and smoothly heated at these fast cycle times. These

Table 2.4. Cancellation data for rifle stabilization for different smoothing functions.

Input Function	Disturbance (mm)		Cancellation (mm)		% Reduction	
	Amplitude	RMS	Amplitude	RMS	Peak-Peak	RMS
1 Hz						
Ramp	2.9	0.95	0.9	0.05	**68 %**	**95 %**
Ramp with Preheat	3.0	1.0	0.7	0.03	**75 %**	**97 %**
2 Hz						
Ramp	2.6	0.87	1.0	0.29	61 %	67 %
Ramp with Preheat	2.6	0.87	1.2	0.30	54 %	66 %
3 Hz						
Ramp	2.4	0.72	1.2	0.21	49 %	56 %
Ramp with Preheat	2.4	0.76	1.2	0.37	49 %	51 %

effects can be countered with improvements in the cooling system (studied in Chapter 3), but it should also be noted that the tremor tests in this and prior studies (NSAC 2007) indicate that the primary frequencies are closer to the 1 Hz region, so it is beneficial that the SMASH gives excellent performance at these lower frequencies. The empirically derived ramp and preheat current profiles produced significant improvements in cancellation at 1 Hz, indicating that a predictive thermodynamic representation of the antagonistic SMA actuator would be beneficial to further improve performance. Such a model (developed in Chapter 4), combined with information on the cooling properties of the SMA wire (Chapter 3) would be instrumental in ensuring the proper design of the actuator and closed-loop controller for future hand-held active tremor cancellation systems. Such a system is demonstrated in a second closed-loop case study in Chapter 5.

2.5 Conclusions

To ensure stable amplitude output of an antagonistic SMA actuator operating at high stress, this chapter develops an empirical understanding of shakedown that is applied to a design process for quasi-static operation of the SMASH. Because the required operating forces and displacements are critical to the stabilization of the

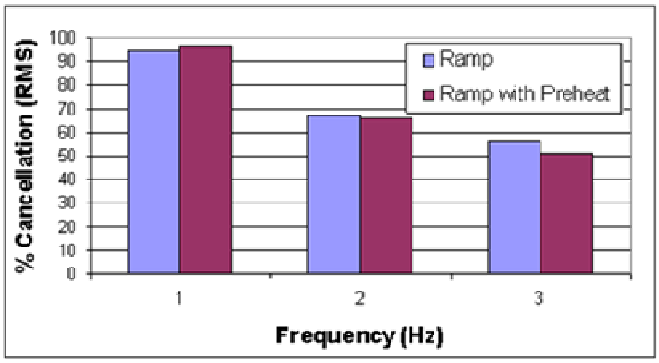

Figure 2.36. RMS cancellation data for the three frequencies tested.

actuator, a dynamic model was developed and applied to the M16 rifle. The quasi-static requirements for both the force and displacement (8 N and 2mm) were shown to dominate the dynamic tremor range of 0-3 Hz, and were therefore used to specify the antagonistic actuator's design. By developing a simple model of the actuator's loading path, the amount of force required to overcome the opposing wire, friction, and internal stiffness were taken into account. The wires were shaken down in an experimental apparatus under a load of 40 N, which was factor above the graphically estimated wire loading requirements of 25 N. By stabilizing the wire at this higher load, further degradation at the lower actuation loads were not intended to occur (Erbstoeszer, et al. 2000). Shakedown curves fit very well (0.99 R-value) to an empirical fit that consisted of two exponential decay terms plus a constant. This empirical fit was extrapolated to predict only 2% decay in motion over the lifetime of the installed post-shakedown wires.

Test results with the shaken down wires proved that the quasi-static specifications of 4mm in the azimuth and elevation directions were met and that repeatable motion with no measurable degradation in amplitude was produced. To investigate the potential for compact packaging, additional feasibility studies for wire spooling were conducted. Significant losses were found to occur after wrapping around the first

pulley, and when comparing spooled and un-spooled wires of the same length, a 60% decrease in motion was measured. As a result, careful consideration is required when choosing to spool SMA wire. For the SMASH application, the handgrip height was not a serious design driver (though operating voltage and cooling load were), and thus an un-spooled configuration was selected.

In addition to the quasi-static tests, preliminary dynamic tests were conducted to demonstrate the actuator's feasibility in meeting motion specifications under the frequency range of interest of 0-3 Hz. In these tests, only 0.3 mm loss was observed at the upper frequency limit. Overall power draw, however, was noticed to be sub-optimal (up to 225 watts at 3 Hz), and was likely due to excess cooling and wire length. While the amount of power draw is a significant issue, it can be corrected through an understanding of the actuator's convective properties, which is studied in detail in (Chapter 3). Feasibility for tremor cancellation was investigated in a series of open-loop tests. These cancellation tests were conducted at 1, 2, and 3 Hz, and revealed that the system was linear. Thus, by producing a perfect inverse of the known disturbance (i.e. the dominant sinusoidal decomposition of a human tremor signal) a zero net motion would be produced. To demonstrate this hypothesis, the three empirically derived heating profiles (square, ramp, and preheat) were tested to approximate this inverse for a 1 Hz 2 mm peak-peak sinusoidal disturbance, and almost total stabilization (97% RMS) was demonstrated. While produced in open-loop, this result exceeds the 50% RMS goal defined in Section 1.2.4 for significantly improving the quality of life for individuals affected by tremor. This promising result in open-loop shows potential for meeting the RMS cancellation goal under closed-loop control. To accomplish this with a minimal power draw, however, accurate cooling data is required along with an accurate, predictive actuator model. To achieve this, Chapter 4 derives

and experimentally validates the necessary thermodynamic modeling framework for the antagonistic actuator. This work, combined with the cooling data in Chapter 3 serves to extend the demonstrated potential of the SMASH and solve its fundamental issues in predictability and power draw. In doing so, the work on the SMASH can be extended to realize a new and general technology of hand-held active tremor cancellation.

Chapter 3: Investigations of Convective Heat Transfer from SMA Wires

As was demonstrated in Chapter 2, one of their fundamental challenges of SMA actuation resides in the balance of frequency and power consumption. For example, an actuator with under-specified cooling requirements can result in significant limitations in output frequency due to the use of large wire diameters or ambient media with low cooling properties. On the other hand, an actuator with over-specified cooling may produce insufficient force through the use of small diameter wires. Large amounts of power may also be required in this case due to the use of cooling media with excessively high convective properties (as was the case in Chapter 2 with the SMASH frequency studies). To balance these tradeoffs for portable hand-held human tremor cancellation systems, the frequency and power issues is addressed through a study of conventional and unconventional cooling techniques. For example, measurements of the convective coefficient of conventional cooling media can provide valuable information that can be used to predict the frequency and power draw of an actuator. Unfortunately, obtaining this data is challenging since accurate surface temperature measurements of thin SMA wires are required and cannot be obtained through traditional techniques. This is due to the fact that thermocouples are invasive and can detach (Churchill, et al. 2009), while IR cameras cannot focus on the thin wire and do not work in certain media other than air, such as thermal grease (Electrophysics 2008). To resolve this problem, the first section of this chapter introduces a non-invasive technique to calculate the convective coefficient for SMA by employing the material's

temperature-induced transformation strain to estimate its surface temperature. This method was used to indirectly measure the convective coefficient across a range of commonly utilized SMA wire diameters and ambient media where traditional methods are limited. Empirical correlations are formulated to fit the collected data that can be used directly in material models to optimize the design of SMA actuators for increased frequency performance with a minimized power draw.

In some applications, the output frequency of an SMA actuator cannot be increased through changes in wire diameter or cooling media. For example, the wires may be restricted in size to satisfy a force requirement, and introducing a different cooling medium such as water or thermal grease may be expensive of impractical. The introduction of flow (e.g. from a fan) may also introduce unwanted power draw and system complexity. Thus, to address the cooling issues that arise when conventional techniques cannot be used, this chapter investigates an unconventional surface treatment method capable of increasing the effective surface area of the SMA wires. In this study, the growth of vertically aligned carbon nanotube (CNT) cooling fins is investigated and their enhanced cooling effects are characterized. By extending this feasibility study, future applications are likely to benefit from further increases in cooling speeds through the use of higher CNT densities and longer lengths. Such performance increases will serve to enhance and inform the design process when creating compact antagonistic actuators for tremor cancellation, capable of operating at the high frequencies with minimal power draw.

3.1 Transformation Strain Based Method for Convective Heat Transfer Characterization of Shape Memory Alloy Wires

For many applications, conventional cooling techniques such as passive convection may be employed to meet power requirements and produce desired cooling speeds.

However, due to a lack of quantifiable data these techniques are typically implemented through trial and error, leading to sub-optimal performance. However, by accurately measuring the effects of heat transfer for various wire diameters and environmental fluids, accurate predictions in frequency and power draw can be made to improve these SMA actuators. Unfortunately, this is complicated since commonly used SMA wires are extremely thin (e.g. diameters below 20 mils) and measuring their surface temperatures to calculate the convective coefficients is challenging. With thicker samples of conventional materials, temperature measurements are usually achieved by mounting thermocouples directly on the surface. For example, experiments for long cylinders (Morgan 1975; Zukauskas, et al. 1985) have been accomplished using surface-mount thermocouples on large diameter samples, e.g. 28 mm (Sanitjai and Goldstein 2004), to monitor the cylinder surface temperature (T_s) for a fixed ambient temperature (T_a) and applied power P. Knowing the cylinder surface area A, Newton's law of cooling, neglecting radiation (Incropera and DeWitt 2001) due to relatively low surface temperatures,

$$P = hA(T_s - T_a), \tag{3.1}$$

is applied to solve for the convective coefficient h. This method is typically not possible with SMA because it is difficult to mount thermocouples to the smaller diameter wires and to keep them connected over the large strains (4-8%) of the SMA during temperature-induced transformation. In addition, thermocouples are also invasive since heat transfer occurs from the SMA sample to the thermocouple through its bonding agent reducing the measured surface temperature. This effect is enhanced for the smaller diameter SMA wires that are on the order of some of the smallest commercially available thermocouples (Omega 2009). Furthermore, the large electrical currents used to heat SMA wires, interfere with thermocouple measurements (Churchill, et al. 2009).

Applications using regular metallic wires, such as hot wire anemometers, overcome this size issue because it is possible to correlate temperature to changes in electrical resistivity of the material; but in SMA, the resistivity is non-monotonic with temperature and changes with cyclic history (Churchill and Shaw 2008; Nam, et al. 2002; Wu, et al. 2000). Direct surface temperature measurement using infrared cameras is often used for convective studies (Ay, et al. 2002; Churchill, et al. 2009), though this method is difficult for very thin SMA wire due to resolution limitations. Additionally, capturing thermal images is extremely difficult in environments other than air (e.g. thermal grease, oil, and water), (Electrophysics 2008).

The temperature measurement issue is further complicated since the convective coefficient is known to differ depending on surface properties (roughness, temperature) of a particular material (Bhattacharyya, et al. 2002), making the use of conventional materials such tungsten used in hot wire anemometers infeasible. For example, the convective heat transfer was shown to increase by 40% for laminar flow (70% for developing flow) when doubling the average surface roughness from 1 μm in a 0.62 mm diameter tube (Kandlikar, et al. 2003). This effect was predicted to be more pronounced for decreasing geometric sizes. Indeed, on the microscale a 25% increase in convection for just a 4% increase in relative roughness was predicted (Koo and Kleinstreuer 2005). Depending on the manufacturing process, the surface roughness of the SMA oxide layer can appreciably differ in the characterized ranges. For example, in a recent study, average roughness was shown to decrease from 0.8 to 0.2 μm through electrolytic polishing (Pohl, et al. 2004). Therefore, it is crucial that the convective coefficient is measured for a particular material of interest (especially for small geometries), as the use of another material has a high potential to introduce error. For general estimates of the convective coefficient, there are non-dimensionalized

empirical relationships in the literature (Morgan 1975; Zukauskas, et al. 1985) that may be scaled down to smaller SMA wire diameters – between 6 to 20 mils (0.15 to 0.51 mm). However, even at the larger diameters on which the models were based (28 mm), variations of up to 20% are typical (Incropera and DeWitt 2001). Such variances would produce the same amount of error in predicted cooling times (and thus actuation frequency), thus warranting a need for more accurate estimates.

To address these challenges, this section introduces a non-invasive technique, the *transformation strain based methodology*, to calculate the convective coefficient, h. The method takes advantage of the SMA's temperature-induced transformation strain to estimate the surface temperature T_s. This is achieved through the creation of a temperature-strain mapping, which is produced through experiments in an environmental chamber. With these mappings, Newton's law of cooling (Equation 3.1), is utilized to calculate the convective coefficient, h, by immersing an SMA wire of known surface area A (assumed not to change) in a temperature-controlled medium (fixed T_a), observing the steady-state power P applied to the wire, monitoring the motion recovery of the wire, and using the temperature-strain mappings to give T_s. This new experimental method can be applied to any size SMA wire in any ambient environment. To validate the method, experimental results were compared to those obtained from a standard IR camera for large diameter wires in air (the only region where IR measurements are possible). After this verification, further experiments were extended for a range of commonly used smaller diameter commercial wires in a variety of ambient environments where most standard measurement techniques do not apply: still air, flowing air (of varying flow rate), mineral oil, thermally conductive grease, and water. Empirical correlations based upon physical variables such as wire diameter, fluid properties, temperature, and flow rate were formulated by fitting correlations from

literature (Incropera and DeWitt 2001) and optimizing the free variables. These correlations provide continuous relationships to estimate convective coefficients within and beyond the tested regime, which can be used in predictive models of SMA actuators to assist in system design.

3.1.1 Transformation Strain to Temperature Correlation

To accurately calculate the convective coefficient, h, of SMA, the transformation strain method uses the Newton's law of cooling (Equation 3.1), but the surface temperature is not directly measured. Instead, the surface temperature is mapped to the midpoint of full strain recovery. A correlation between the mid-point transformation strain and the surface temperature for each wire sample is obtained through a series of very slow (quasi-static) heating cycles in an environmental chamber under near-zero loads. This correlation is used to estimate the surface temperature T_s in all the convective coefficient experiments in this dissertation.

To obtain the midpoint transformation temperatures for the SMA wires, each sample was heated in an Envirotronics FLX-300 environmental chamber while recording strain. For each test, a 7 inch sample of 70 ºC Flexinol (Dynalloy) SMA was installed in the test setup (Figure 3.1) with one end of the SMA connected to a very low friction sliding stage that moves when the SMA is heated, and the other end attached to an aluminum block fixed by a tensioning screw. The free Austenite reference length was set by heating the wire and adjusting the wire-tension through the tensioning screw until all slack was taken out. A residual tension remained in the wire to offset the very small friction in the linear ball bearing. The wire was then allowed to cool and was strained with the tensioning screw to a 4.5% elongation from its Austenite free length (Figure 3.1a). The ambient temperature inside the chamber was slowly increased (several minutes per degree near transition) to ensure proper mixing. The SMA

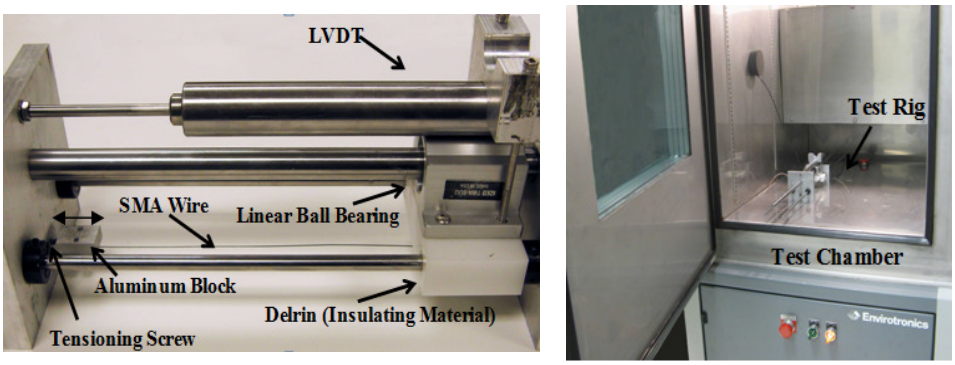

(a) Experimental Test Apparatus

(b) Apparatus in Environmental Chamber

Figure 3.1. Test apparatus for midpoint transformation temperature measurements. The temperature of a length of SMA wire is precisely controlled by slowly varying the temperature in the environmental chamber while its length is measured using an LVDT attached to a linear bearing.

contracted when the ambient temperature reached its transformation temperature, and full motion recovery occurred within 1º C for all wires. This displacement was measured with a LVDT sensor (monitored by an oscilloscope), and the midpoint transformation temperature was recorded when the slider position was half way between the 4.5% prestrain and the Austenite free reference length.

The procedure was repeated twice for each different wire diameter (ranging from 6 to 20 mils) and two separate spools of 10 mil SMA wire were also tested. It was assumed that due to these near-zero loads (and small reset loads) the wire's material properties did not change over many cycles (Churchill and Shaw 2008; Sun, et al. 2008). The measured midpoint transformation temperatures (Table 3.1) varied slightly for the different wire diameters, ranging from 57-63 ºC with an average deviation of 2.8% from the mean of 61.2 ºC. A higher deviation was observed spool to spool. For example, when 10 mil wires from two different spools were tested, their deviation from one another was 4.8%. However, testing different wire segments taken from the same spool produced constant and repeatable results within less than 1% error, which is within accuracy of the test chamber. Thus, the transformation temperature is not highly

Table 3.1. Measured Midpoint Transformation Temperatures. Temperatures were measured at a midpoint strain of 2.25% for 70 ºC Flexinol SMA wire under near-zero load and 4.5% initial strain.

Spool Number	Diameter (mils)	Midpoint Transformation Temperature T_s (^oC)	% Deviation from Average Midpoint Transformation Temperature
1	6	61	+1.2
2	8	59	-2.1
3	10	59	-2.1
4	10	62	+2.8
5	12	57	-5.5
6	15	61	+1.2
7	20	63	+4.5

dependent on wire diameter, but is sensitive to each spool of wire which has its own individual processing history. Therefore, to ensure accuracy in all further experiments, tests representing a particular SMA wire diameter were all performed from the same spool possessing consistent processing history.

3.1.2 Transformation Strain Based Experimental Method

The convective coefficient h can be indirectly calculated using Newton's cooling law (Equation 3.1) by 1) knowing the cross sectional area A and ambient Temperature T_a, 2) measuring the applied power with current and voltage probes and 3) correlating the measured midpoint transformation strain to estimate the surface temperature T_s. This methodology is useful for environments where traditional methods such as IR cameras cannot be utilized. For this experimental method, the SMA samples were tested under varying steady-state resistive heating in air (at various flow rates), still oil, thermally conductive grease, and still water. This combination of media and wire diameter selections were intended to span a wide range of cooling conditions. As validation the convective coefficient was measured using surface temperature readings with an IR camera for the only two feasible test conditions: 15 and 20 mil, in still air. Traditional empirical models (Incropera and DeWitt 2001) were used with free

parameters *C* and *m* optimized using a generalized reduced gradient (GRG) to provide a best fit to the data. These correlations provide a mathematical relationship to calculate the convective coefficient in a continuous form. This relationship is highly useful when creating material models such as the thermodynamic model for antagonistic SMA (developed in Chapter 4), and allows variables such as wire diameter to be interpolated between discrete points to explore a design space with ease.

3.1.2.1 Experimental Procedure

Each test was conducted with the same experimental apparatus used in the midpoint transformation temperature measurements; however, the wire was electro-resistively heated via a DC power supply (Figure 3.2) instead of an environmental chamber. Input power to the wire was computed from the applied voltage and current, which were measured with voltage and current probes connected to an oscilloscope. The apparatus was placed with the SMA in a horizontal configuration inside a leak-proof PVC box filled with the various environmental fluids and their ambient temperatures were measured by a type-K thermocouple placed inside the box. For the free convection in air tests, the PVC box was covered to ensure that stray air currents did not affect the

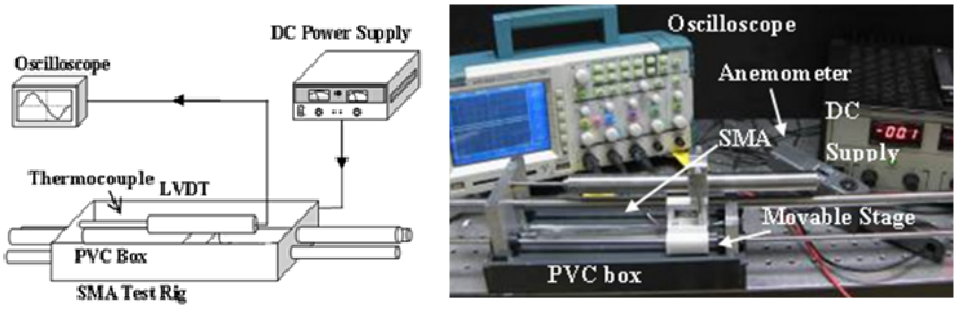

(a) Schematic of Experimental Setup **(b) Photograph of Experimental Setup**

Figure 3.2. Experimental test apparatus for h-value testing. Leak-proof PVC box is filled with various fluids tested and strain is monitored while applying electrical power, which is recorded at the midpoint transformation strain.

measurement. Forced convection in air was conducted outside the box, with an electrical fan whose proximity and speed were varied to produce a desired test flow rate that was measured by a hot wire anemometer at the middle of the wire segment.

Tests were conducted at flow rates of 150, 250, 450, and 625 ft/min. In all experiments, the input power was slowly increased and recorded when the half-way displacement between the 4.5% prestrain and the Austenite zero reference length was recorded by the LVDT. The recorded power along with the associated ambient temperature and midpoint transformation temperature (Table 3.1) were used in Equation 1, to predict the convective coefficient, *h*. For each wire diameter, the test was repeated for different media: air (free and forced), mineral oil, thermal grease, and distilled water (Figure 3.3).

3.1.2.2 Convection in Air

There exists a tradeoff between simplicity and performance for cooling in air. For free convection (cooling in still air), no additional complications are introduced to the system, though the convection heat transfer is low. To provide forced convection, flowing air may be introduced through a fan. While this often requires additional power draw and system complications, the resulting heat transfer improvements may be sufficient for a given application's speed and power requirements. This section studies both free and forced convection for SMA wires of varying diameter to provide a better understanding of the heat transfer effects under these regimes.

3.1.2.2.1 Free Convection in Air

In the experimental results for cooling in still air (Figure 3.3) a significant dependency on wire diameter is evident. Overall, the convective heat transfer coefficient decreases as the wire diameter is increased – for 6-mil wire, the *h*-value is 153 $W/m^2 K$, while the *h*-value for 20-mil wire is reduced by 44% to 68 $W/m^2 K$. At the

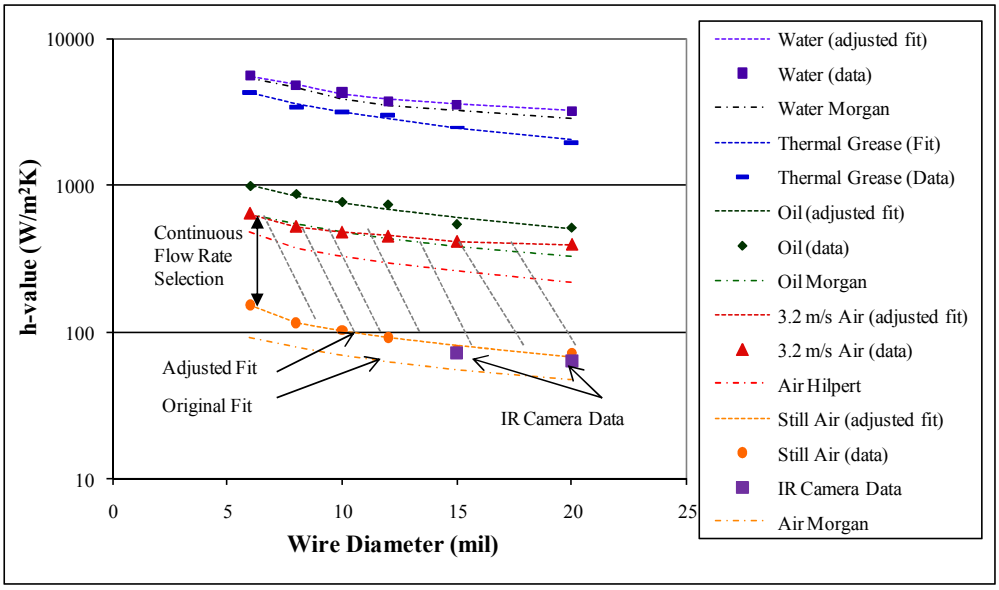

Figure 3.3. Convective Heat Transfer Coefficients in Different Media. The measured *h*-value for 70 ºC Flexinol SMA wire at its midpoint transformation temperature decreases with wire diameter and varies greatly with cooling medium. The empirical fits plotted with the data closely match the form of the functional dependence.

upper limit, the *h*-value for the collected data should theoretically approach zero at very large diameters. This is because a very large diameter cylinder restricts convective flow and the primary mechanism of heat transfer is through conduction across the fluid. At extremely small diameters the flow would not be resisted and the h-value would increase to a "free-flow" limit.

3.1.2.2.1.1 Validation

To validate these results and the general midpoint transformation temperature methodology to measure *h*, a second experiment was conducted using an infrared camera for surface temperature measurements (Ay, et al. 2002; Meinders, et al. 1998). Due to focus resolution limitations (~200 pixels/inch), the IR camera was used to validate measurements for the two largest diameters (15 and 20 mils) in still air since unpredictable inaccuracies would occur when measuring across any air-fluid interface. During testing, the SMA wires were clamped in a fixture (Figure 3.4), and heated with an electrical current while monitoring the surface temperature with an infrared imaging

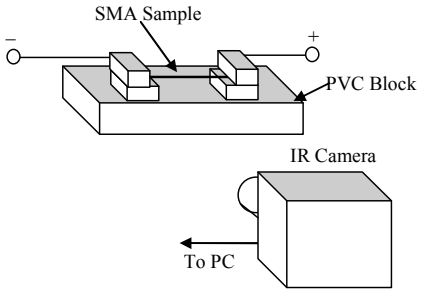

(a) Experimental Setup for IR Camera Testing

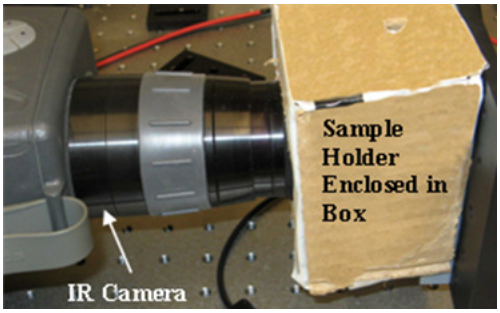

(a) Photograph of Testing in Progress

Figure 3.4. Experimental Test Apparatus for IR Testing. SMA sample was shrouded in a box to protect from stray air currents, and an IR camera measured surface temperature under steady-state joule heating.

system (FLIR ThermaCam SC1000) with a PtSi 256x256 detector array. During data collection, the SMA sample was shrouded in a box to protect from stray air currents and the applied current was increased in increments where the steady-state surface and ambient temperatures were recorded.

For the surface temperature readings, an emissivity for the 70 ºC Dynalloy wire of 0.76 was programmed in the camera. The emissivity was measured by applying a coating of known emissivity to a portion of the wire, heating the sample to a uniform temperature, and comparing readings from the coated and uncoated surfaces. Because the sample length was short (0.5 inches) and the contact resistance of a voltage probe invasive, the input power was calculated by multiplying the resistance by the square of the current. Wire resistivity was measured in both Martensite and Austenite states for both wire diameters, and the normalized values are listed in Table 3.2. For temperatures below the transformation temperatures listed in Table 3.1, the input power was computed using the Martensite resistivity, while Austenite resistivity was used for temperatures above. Because the resistivity during transformation is not monotonic and difficult to predict due to its dependence on prior cyclic history (Churchill and Shaw

2008), data was not collected in this temperature range. However, with the data above and below, interpolation could be performed through the transition range.

In Figure 3.3, the two additional data points are plotted for the IR camera measurements, showing excellent agreement. Using the IR camera, the convective coefficient for the 20 mil wire was calculated to be 67 W/m^2K which is only 1.5% from the measurement from the midpoint transformation temperature method. The 15 mil diameter produced a higher convective coefficient of 73 W/m^2K using the IR camera measurement, which is a 3% deviation. In Figure 3.5, the *h*-value measurements using the IR camera are plotted with respect to the wire's surface temperature, and it is evident that the convective coefficient did not vary with temperature in any measurable way. This is likely due to the fact that the properties of air affecting natural convection are not heavily temperature dependent (Incropera and DeWitt 2001). Therefore, the interpolation of the *h*-value from above and below wire transformation temperature is valid.

After gathering data for the convective heat transfer in air (assumed to produce the lowest *h*-values), a further calculation was performed to verify the decision to neglect radiation in Equation 1. This was performed by examining the ratio of power dissipation between radiation (assuming the Stefan-Boltzmann Law with emissivity of 0.76 as discussed earlier) and natural convection,

Table 3.2. Wire resistivity for the 70 ºC Flexinol SMA wires used in IR testing. Values were measured for Austenite and Martensite phases.

Diameter (mils)	Martensite Resistivity (ohms/m)	Austenite Resistivity (ohms/m)
15	8.67	7.68
20	5.31	4.53

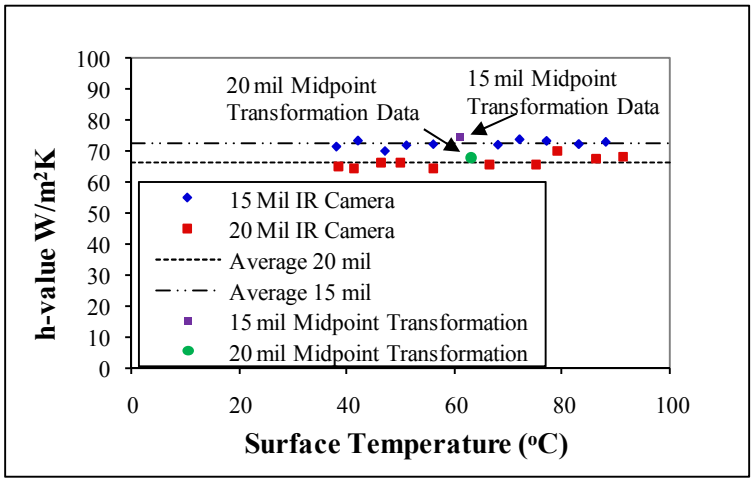

Figure 3.5. Convection coefficient for cooling in free air using IR Camera measurement. *h*-values are independent of temperature well above and below transformation and provide good agreement with midpoint transformation tests.

$$r = \frac{\varepsilon\sigma(T_s^4 - T_{amb}^4)}{h(T_s - T_{amb})}. \tag{3.2}$$

Assuming a mean cooling surface temperature T_s of 60 ºC (Table 3.1), convective coefficient h of 50 W/m^{2}K (lower bound to the data in Figure 3.4), and Stefan-Boltzmann constant σ as 5.6704E-8 W/m^{2}K^4 the ratio in this worst case was calculated to be only 0.09. For a mid-range case for h equal to 500 W/m^{2}K the ratio linearly decreases to only 0.009. This shows that convection is indeed dominant, and that neglecting heat transfer due to radiation is a valid assumption.

3.1.2.2.1.2 Empirical Correlation

For the set of data collected for free cooling in air (Figure 3.3), a continuous correlation was formulated to provide a continuous fit that can be used in predictive modeling of SMA. This equation was chosen to be based on Morgan's correlation for an isothermal horizontal cylinder (Morgan 1975) due to its commonality and relative simple form. In this empirical model, the non-dimensional Nusselt number (ratio of convection to conduction in the fluid) is approximated from

$$\overline{\mathrm{Nu}}_d = \frac{\bar{h}D}{k} = C\mathrm{Ra}_D{}^m, \tag{3.3}$$

where $\bar{h}$ is the average convective coefficient over the entire surface of the wire, D is the wire diameter in meters, k is the thermal conductivity of air (in unites of W/mK), and C, m are free variables. The Rayleigh number, Ra_D, for a cylindrical shape is defined as

$$\mathrm{Ra}_D = \frac{g\beta(T_s - T_a)D^3}{\upsilon\alpha}. \tag{3.4}$$

In Equation 3.4, g is the acceleration due to gravity, β is the thermal expansion coefficient of the fluid, T_s is the wire's surface temperature, T_a is the fluid's ambient temperature, v is the fluid's kinematic viscosity, and α is the thermal diffusivity. All fluid properties are evaluated at a film temperature estimated as the average of the surface temperature (the mean of 60 ºC, from Table 3.1) and the measured ambient temperature (23 ºC), and the values are listed in Table 3.4. Substituting the Rayleigh number, Equation 3.4, into the Nusselt number correlation, Equation 3.3, and solving for the convection coefficient allows,

$$\bar{h} = kC\left(\frac{g\beta(T_s - T_a)}{\upsilon\alpha}\right)^m D^{3m-1}. \tag{3.5}$$

This equation for the average convective coefficient yields additional mathematical insight towards the physical limits on diameter. If $3m$ is less than 1, which is true for all proposed fits (Table 3.4), h approaches zero for large D and infinity for small D. This is in accordance with the limitations of convection due to fluid flow discussed earlier. To optimize the empirical fit, values for C and m were adjusted using a generalized reduced gradient algorithm (GRG) that minimized the average fit error to the collected data to only 2.4%, which is significantly less than the average 33% error produced by the Morgan original correlation (Figure 3.3). These parameter values are listed in Table

3.3 for the two Rayleigh number regimes that the experimental conditions fell within. Figure 3.3 shows the empirical fit with the experimentally measured data points. In general, the trend is fit very well and the equation provides useful values that can be interpolated between two points or extrapolated to diameters that were not measured in the experimental study.

3.1.2.2.2 Forced Convection in Air

When subjected to forced convection, the *h* values for the SMA increased with flow rate but demonstrated a similar dependence on diameter as observed under free convection. For example, the results (Figure 3.6a and b) show that the convective coefficient decreases by 40% under a fixed flow rate of 625 ft/min when the wire diameter is increased from 6 to 20 mils. This change in *h* between different diameters also existed for other constant flow rates (see family of curves in Figure 3.6b), decreasing on average by 47% with average deviations of 3%. The family of curves in Figure 3.6a shows the increasing trend with increasing flow rates, and heat transfer is improved under forced convection by an average factor of 4.9 (with 8% average deviation) for all wire diameters under a flow rate of 625 ft/min.

3.1.2.2.2.1 Empirical Correlation

An equation of the form proposed by Hilpert (Hilpert 1933) for horizontal cylinders under forced convection was used as a basis for constructing a continuous correlation for its relative simplicity. In this correlation, the Nusselt number is related to the Reynolds number, Re_D, and Prandtl number, Pr, as

$$\overline{\mathrm{Nu}}_D = \frac{\overline{h}D}{k} = C\,\mathrm{Re}_D{}^m\,\mathrm{Pr}^{1/3} \qquad \textbf{(3.6)}$$

where *C* and *m* are correlation constants (Table 3.4) and *k* is the thermal conductivity. The Reynolds number is defined as

Table 3.3. Fit Parameters for Collected Cooling Data for 70 ºC Flexinol SMA wires. Parameters for fits based on those suggested by Morgan [11] for free cooling and Hilpert [21] for forced. Values based on experimental data are given for *C* and *m*, along with an additional free variable *R* for thermal grease.

Medium	Ra_D	*C*	*m*	*R*
Still Air	10^{-10}-10^{-2}	0.875	0.038	
	10^{-2}-10^{2}	1.477	0.142	
Moving Air	10^{-2}-10^{2}	1.235	0.377	
Mineral Oil	10^{-2}-10^{2}	1.600	0.137	
Thermal Grease		2.998	0.130	10.3
Water	10^{-2}-10^{2}	1.021	0.169	
	10^{2}-10^{4}	0.868	0.208	

$$\mathrm{Re}_D = \frac{uD}{\nu}, \tag{3.7}$$

where *u* is the flow rate, *D* is the wire diameter in meters, and *v* is the kinematic viscosity. As for free convection, all fluid properties (Table 3.4) were evaluated at an estimated mean film temperature of 42 ºC, which is an average of the wire's surface temperature, 60 ºC, and ambient temperature, 23 ºC . As for the free cooling correlation, the mathematical limits on wire diameter of Equation 3.4 match physical intuition. For values of *m* less than 1, the predicted *h* value approaches infinity at very small diameters and zero at very large diameters.

Using the GRG algorithm, values of *C* and *m* (Table 3.3) were optimized in

Table 3.4. Fluid Properties for Tested Media. Properties for air and water were taken from (McQuillan 2009), while oil was taken from (Incropera and DeWitt 2001). Thermal grease properties were not known other than the thermal conductivity, listed by the manufacturer (Omega 2009). All properties evaluated at film temperature of 42 °C.

Fluid	Kinematic Viscosity $\nu \cdot 10^5$ (m^2/s)	Thermal Conductivity *k* (W/mK)	Prandtl Number Pr	Thermal Diffusivity $\alpha \cdot 10^6$ (m^2/s)	Thermal Expansion Coefficient $\beta \cdot 10^3$ (1/K)
Air	1.71	0.027	0.712	24.0	3.18
Oil	160	0.143	0.002	0.082	0.70
Thermal Grease	Unknown	2.300	unknown	unknown	unknown
Water	0.06	0.634	4.00	0.157	0.390

Equation 3.4 to minimize the average fit error to 6.4% for the range of data, capturing the effects of both diameter and flow rate. Figure 3.6a displays these fits for the upper and lower bounding cases for wire diameter, and shows the adjusted fit over many wire diameters under and air flow rate of 625 ft/min. For most of the data points, the predicted error was small but the model did deviate by as much as 13% for the maximum airflow speed of 625 ft/min for the 20 mil wire, though this is still a significant improvement over 22% deviation from the unadjusted Hilpert correlation. This deviation may be due to a combination of the model's limitations in correlation and experimental error such as possible non-uniform airflow speeds. These variations may have occurred along the length of the wire (the flow sample was taken at the middle of the wire segment), or may have varied in time due to turbulence induced by the fan.

3.1.2.3 Free Convection in Mineral Oil

While increasing the air flow rate dramatically improves the convective heat transfer performance (Figure 3.6a), higher frequency applications may warrant a change in medium since producing very high air flow rates may become impractical due to fan size and power consumption. Mineral oil is an attractive alternative to air cooling due to its higher convective properties and very high electrical resistance (greater than 10^{10} ohms/m). To characterize mineral oil for its potential use in cooling SMA wires, experimental data was collected for technical grade light viscosity mineral oil obtained from McMaster-Carr, Inc. The cooling results in Figure 3.3 show a similar trend to other media with respect to wire diameter as an increase in diameter generally reduces the heat transfer coefficient. For example, the *h*-value is reduced by 49% from 6 to 20 mils, which is close to the 44% reduction reported for free convection in air. In addition, when compared to free convection in air, the *h*-value for all diameters in

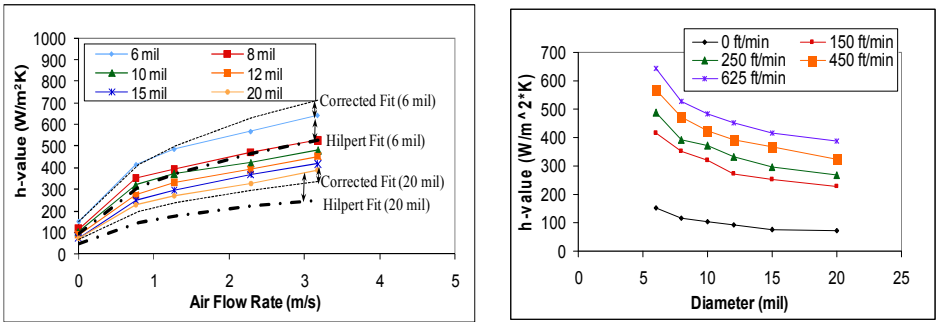

(a) Flow Rate **(b) Diameter**

Figure 3.6. Effect of Air Flow Rate on the Convective Coefficient for Varying 70 ºC Flexinol SMA wire Diameter. Experimental data and three empirical fits are shown for air at 22 ºC. *h*-values decrease with increasing wire diameter, and increase with a decaying amount for increasing air flow rates, spanning a wide range of *h*-values.

mineral oil was consistently higher (e.g. the convection coefficient increased by a factor of 6.5 for 6 mil., and 8.9 times for 20 mil).

For the data correlation, the exact properties of the particular mineral oil used were not known so values were estimated for general light-viscosity oil (Incropera and DeWitt 2001), and the numbers are provided in Table 3.2. A fit using these parameters was conducted with the GRG algorithm to determine values for *C* and *m* in the Hilpert correlation, Equation 3.3. Using the values provided in Table 3.4 for mineral oil, the average fit error was minimized to only 3.8% which is an improvement from the unadjusted average fit error of 36% (Figure 3.3). Overall, mineral oil provides a higher increment in performance than 625 ft/min air flow, and as an added benefit requires no additional power draw. This, however, comes with a price of packaging complexity as the mineral oil must be sealed around the SMA wires. Additionally, the viscous nature of mineral oil can be problematic and cumbersome for parts that need frequent servicing.

3.1.2.4 Effective Convection in Thermal Grease

To further improve the heat transfer from the SMA wire (beyond the performance of mineral oil) thermally conductive grease can be employed. Thermal grease is

typically used in the electronics industry, to improve the thermal contact between a chip and a heat sink (Kromann 1995). For applications involving SMA, it can be used in a similar fashion where the heated wire is immersed in the grease, which acts as a direct conduit to transfer heat to an ambient environment. The experimental data shown in Figure 3.3 represents the convective coefficient for various diameters of SMA immersed in OmegaTherm OT-201 thermally conductive silicon paste. The paste was selected due to its very high thermal conductivity, and also it's electrically insulating properties. Unlike the rest of the fluids tested in this chapter, the thermal grease is highly viscous and does not flow to produce free convection. Instead, the primary mode of heat transfer is conduction. For simplicity and to allow for comparison to the other media tested, this form of heat transfer is approximated as an effective convective coefficient *h*. The data in Figure 3.3 shows that the effective convection is still heavily dependent on wire diameter. For example, the *h*-value decreases by 55% between 6 and 20 mils which is on the same order as the decreases reported for air and mineral oil (44% and 49% respectively). The amplitude of the effective *h*-values calculated for thermal grease is also significantly higher than other mediums tested. For example, the effective convection at 6 mil wire diameters 4.3 times higher than the same wire in mineral oil, and 28 times than free-cooling in air.

A continuous fit to the collected data was again based on Morgan's free-convection equation (Equation 3.3), with the fluid properties lumped into an additional free-variable *R* (units of $s^2/m^4.K$) since they were unknown. By substituting Equation 3.4 into Equation 3.3 and grouping terms the average convective coefficient is expressed as

$$\overline{h} = Ck\left[gR(T_s - T_\infty)\right]^m D^{3m-1} \quad \textbf{(3.8)}$$

where the fluid properties are lumped into a single variable,

$$R = \left(\frac{\beta}{\upsilon \alpha} \right). \tag{3.9}$$

In the lumped correlation, Equation 3.8, the thermal conductivity k, was listed by the manufacturer to be 2.3 W/mK. Using the GRG optimization method, but allowing R to vary in addition to C and m, the average fit error was minimized to 3.1%. The values of the optimized free variables are listed in Table 3.3, and the resulting fit is plotted with the data in Figure 3.3. Because the grease was fitted to a fluid of lumped properties, the original Morgan correlation could not be calculated for comparison in this special case. When compared to mineral oil, thermal grease provides significantly higher cooling allowing for higher frequency responses for a given diameter, which is important for many applications. It is also easier to seal since it does not flow through small spaces. However, thermal grease does have some disadvantages over mineral oil. For example, it is significantly more viscous and is consequently even more difficult to work with. Thermal grease is also comparatively expensive and may become impractical when large quantities are needed.

3.1.2.5 Free Convection in Water

As long as the transition temperature for the SMA is below water's boiling point, water immersion is an effective yet simple, cooling method. For 70º C Flexinol wires, water provides a protective measure against overheating, since running excess current through the wires would cause the water to locally boil, dissipating the extra heat without damaging the wire. If the transition temperature of the wire is higher than the boiling temperature of pure water, ethylene glycol could be added to raise the fluid's boiling temperature, though this sacrifices some of the water's convective properties. Because the transition temperatures of the tested 70 ºC Flexinol SMA wires were below the boiling point of pure water, the medium was tested with no additives. Additionally, to ensure that the medium's electrical resistance was very high (and that the input

power measurements were accurate), technical grade distilled water from McMaster-Carr Inc was used for the experiments.

The cooling performance for distilled water was tested to be the highest among all media studied (Figure 3.3). When compared to the next highest tested medium, thermal grease, convective coefficients were approximately 1.3 times higher for 6 mil and 1.6 times higher for 20 mil wires. When compared to free cooling in air performance is dramatically increased 36.5 and 44.5 times for 6 and 20 mil wire diameters. The strong dependency on wire diameter is also present in the water cooling data, with a 43% reduction in the convective coefficient from 6 to 20 mils. The data for free cooling was used to create a fit based on Morgan's correlation (Equation 3.3), and all fluid properties were readily found in literature and are listed in Table 3.2. Values for C and m were slightly adjusted by the GRG algorithm (values listed in Table 3.3) to provide a continuous expression for the distilled water cooling with an average error of only 1.2%, which is an improvement over the unadjusted Morgan correlation's error of 8%.

3.1.2.6 Comparison of Cooling Media

The data collected using the transformation strain based method depended on environmental and geometric variations that produced a wide design space (spanning two orders of magnitude from ~100 W/m^2K to ~5000 W/m^2K). From this space an optimal combination of cooling medium and wire diameter can be selected based on a design's cooling requirements and power restrictions. As intuitively expected, increasing the wire diameter decreased the cooling performance for all cases (on average by 48% between 6 and 20 mil). The cooling medium also had a large effect as distilled water provided the highest h-value of all the tested media: between 3210 and 5590 W/m^2K for the diameter range tested, which was as much as 1.6 times higher than that of conductive grease, and as much as 44.5 times higher than free convection in air.

Though water provides a very high heat transfer and possesses a high heat capacity, the coolant is more difficult to manage in an application than thermal grease. This is due to the fact that water coolants require better sealing and special care for parts to resist corrosion. Thermally conductive grease, however, is significantly more expensive, has a greater density, (Table 3.5) and is difficult to spread evenly throughout a device. Despite these limitations, thermal grease does possess one key advantage over the other cooling media, which is its thermal conductivity (which is up to 115 times greater than air). Because of this property, heat build-up can be avoided by transferring it to an external heat exchanger such as cooling fins. Unlike water and thermal grease, oil provided an intermediate level of *h*-value, between 512 and 997 W/m^2K, which was up to 7.1 times more than still air, or up to 6.3 times less than water. Oil is inexpensive (Table 3.5), does not promote corrosion, but does require careful sealing similar to water. Still air provided a lower *h*-value, between 69 and 153 W/m^2K, but is much easier and cheaper to use in an application requiring no additional parts or installation. Due to its low heat capacity, air should be exchanged to prevent temperature build-up. This can be done through the introduction of forced air where *h*-values between 389 and 644 W/m^2K at a flow rate of 625 ft/min were produced, (up to 5.6 times more than still air), though this benefit comes with the cost of an external fan or other means to move the air. An extra advantage gained by using forced convection is the ability to make live adjustments of the *h*-value over a large range (by a factor of 1.7 in these tests), such that the balance between cyclic performance and power consumption can be adjusted in real-time.

While not included in this study due to the additional complexities involved, forced convection of other fluids (water, in particular due to its low viscosity) can also be used to increase and tailor in-situ the *h*-value, by potentially another order of magnitude as it

Table 3.5. Comparison of the Conventional Media Studied. Various factors in must be considered in addition to cooling performance when selecting a coolant. (EngineeringToolBox 2009; Incropera and DeWitt 2001; Omega 2009)

Medium	*h-value* (15 mil), W/m^2K	*Heat Capacity,* J/gK	*Thermal Conductivity*	*Density g/cc*	*Cost $/cc*	*Complexity*
Still Air	72	1.01	0.02	1E-3	0	Low
Moving Air (625 ft/min)	417	1.01	0.02	1E-3	0	Medium
Mineral Oil	541	1.67	0.15	0.8	0.03	High
Thermal Grease	2495	Unknown	2.31	2.5	0.83	High
Water	3574	4.18	0.58	1.0	0.001	High

did for air (Figure 3.3). While it is the case that the convective coefficient can be significantly altered by changing the cooling medium, there are situations where this change is undesirable. For example, the sealing issues when switching from air to liquid cooling may be unacceptable for certain applications. However, if the convective coefficient could be increased without changing to a different cooling medium such issues would be avoided. In the following section, a new method is investigated to achieve this effect by altering the surface properties of the SMA wire and increasing heat transfer to its environment.

3.2 Carbon Nanotube (CNT) Fins for the Enhanced Cooling of Shape Memory Alloy Wire

While changing the cooling environment can significantly increase the frequency of SMA actuators, many applications may be constrained to a single medium. For example, a compact device may require forced air cooling that is unachievable since a fan would require unwanted power consumption and create excess bulk. In this situation selecting other cooling media such as thermal grease or water would over-cool the actuator creating significant power losses during the heating cycle. If the effective surface area of the SMA wire were increased, however, simpler media such as air

cooling could be retained. In this section, a novel method to produce this effective surface area increase using nanostructures as cooling fins is investigated. This new method can be used to benefit applications that have strict weight and space requirements (such as miniature hand-held devices) that restrict the wire diameter and ambient medium yet require faster cooling times. Such circumstances parallel problems that currently exist in the field of high performance micro-electronics where recent research has focused on exploiting the superior thermal conductivity of carbon nanotubes (CNTs) for their use for heat dissipation (Berber, et al. 1966; Che, et al. 2000). CNT arrays, for example, have been grown to function as an interfacial material capable of improving the thermal resistance between chips and heat sink surfaces (Xu and Fisher 2006). The thermal resistance of these arrays was reported to be comparable to conventional phase change materials, but when used in combination with these conventional materials to form a composite, the thermal resistivity was greatly reduced by nearly four times (Xu and Fisher 2006). Research in the microelectronics field has also been conducted to investigate the use of CNTs as cooling fins in micro-scale heat exchangers that enhance heat transfer through convection. Micro-fins laser etched from aligned CNTs have recently been fabricated and demonstrated to increase heat transfer in chips by 11% under free convection and 19% under forced (Kordás, et al. 2007). Similar work has also shown a 10-15% increase in performance over silicon fins (Wang, et al. 2006). In these efforts, performance was limited because the carbon nanotubes were not in direct contact with the heated surface since they were grown on a separate substrate. With good thermal contact, however, improvements of 2-3 times greater heat transfer have been estimated for CNT cooling arrays when compared to conventional heat sinks (Bhattacharya, et al. 2006).

This section extends the concept of using aligned CNTs to produce micro-fin

architectures for SMA wires to increase actuation frequency without introducing potential complications due to a change in cooling medium. The DC plasma enhanced chemical vapor deposition (PECVD) procedure used to successfully grow the CNTs on the surface SMA is detailed along with preliminary analysis of the results. This analysis includes a discussion of the resulting microstructure, and physical experimentation designed to determine overall heat transfer improvements. A simple lumped parameter heat transfer model is described and applied to the results to quantify the distinct and repeatable improvement in convective heat transfer due to the growth of CNTs. In this section, a preliminary proof-of-concept is investigated and validated for the cooling of the SMA wires. With further improvements to this method, the frequency response of SMA actuators can be improved without the introduction of complex or expensive cooling media. This method can be employed in many applications including the class of lightweight hand-held active tremor cancellation systems enabled by this dissertation.

3.2.1 CNT Growth

The critical component to producing the micro-scale cooling fins for the SMA wire's surface was the growth process. This was achieved through the use of the DC plasma enhanced chemical vapor deposition (PECVD) process used to grow aligned CNTs (AuBuchon, et al. 2004; AuBuchon, et al. 2005). In this PECVD process, catalyst particles are initially deposited on a substrate (e.g. silicon), and a carbon-rich gas is introduced in the ambient environment. This gas decomposes on the surface of the catalyst particle, and the carbon diffuses through the particle under an activity gradient and precipitates to the opposite side, increasing the height of the growing nanotube (Chhowalla, et al. 2001). The direction of growth in general follows the direction of the applied electrical field.

The specific CNT growth on the 15 mil, 70º C Flexinol SMA wires (see Figure 3.7 for schematic) was conducted in an environment of ammonia (NH_3) and acetylene (C_2H_2) with the SMA wires fixed to an electric-field-concentrating metal (molybdenum) stage. After heating to 700 °C in a low-pressure hydrogen atmosphere, the atmosphere was changed to NH_3 with a pressure of 3 torr and flow rate of 150 sccm. A DC bias of 650 V was applied between an anode above the sample and the cathode stage just below the sample. Under the applied voltage, a DC glow discharge formed and the NH_3 plasma was allowed to treat the surface of the wires for 2 minutes. This plasma was used to break the surface into small islands, typically done for thin Ni films (AuBuchon, et al. 2004), that act as catalyst particles for CNT growth. After the surface treatment, the applied bias was decreased to 550 V and C_2H_2 was added to the chamber flowing at 30 sccm with the total NH_3 and C_2H_2 pressure held at 3 Torr.

The CNTs grew under a tip growth mechanism (Figure 3.8) where the decomposition of the atmospheric hydrocarbon causes carbon to be absorbed into the catalyst particle. Carbon diffuses into the particle until super-saturation is reached at which point carbon precipitates in tubular form lifting the catalyst away from the SMA surface. At the end of this process, the catalyst particles remain at the tips of each CNT.

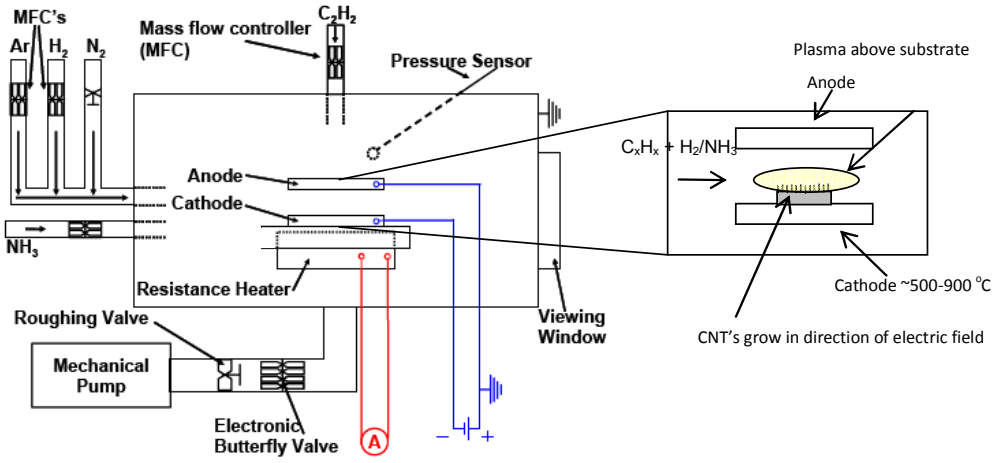

Figure 3.7. PECVD System. CNTs grow from carbon-rich plasma in the direction of the field lines created by a DC Bias applied between the anode and cathode.

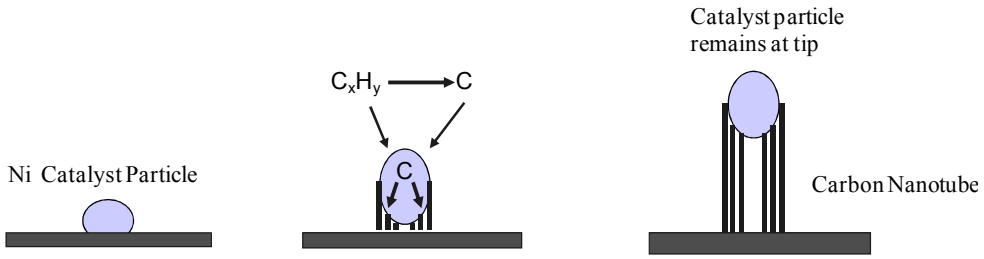

Figure 3.8. CNT Tip Growth Mechanism. At super-saturation, carbon precipitates in tubular form lifting the catalyst particle from the substrate.

Since the electric field in the cathode plasma sheath was perpendicular to the stage, the SMA wires were surface treated on only half of their surface and it was on this half that the CNTs were grown. Following the process, the SMA wire was tested to verify that the Shape Memory Effect remained since the 700 °C processing temperature was higher than the annealing temperature. The sample was physically deformed and upon resistive heating was visually observed to recover and return to its original shape.

For microstructural analysis, field emission scanning electron microscopy (SEM) was performed using a Phillips ESEM operated at 30 kV. From the SEM images (Figure 3.9), the surface growth of the aligned CNTs was visually observed to be relatively uniform along the surface. From the images, the nanotubes were observed to have average diameters of 30 nm, lengths of 2-5 μm, and a density of approximately 2 CNTs/μm^2. Assuming an average nanotube length of 3.5 μm, the growth of the nanotubes was estimated to have increased overall surface area of the wire by 33% from 12 mm^2 to 16 mm^2 (with the nanotubes estimated as ideal fins). This ideal fin assumption was made because of the high thermal conductivity of the carbon nanotubes, upwards of 6600 W/mK (Berber, et al. 1966), and their microscopic lengths. Due to these features, the temperature along the carbon nanotube was expected be nearly equal to its base temperature – the SMA surface temperature – thus effectively increasing the wire surface area at its surface temperature.

3.2.2 Experimental Setup and Procedure

To measure the increase in cooling performance from the CNT surface treatment, an experiment was developed (Figure 3.10) to measure the temperature profiles obtained under free-cooling. Both regular and carbon nanotube treated wires approximately 0.4 inches long were clamped by their ends with two machined aluminum clamps that were bolted to a PVC surface to ensure that the only electrical conduit was through the wire sample. Electrical connections were made on each aluminum clamp to heat the sample to a set temperature under constant current. Because the carbon nanotubes were grown on only one side of the wire, the sample was oriented such that the treated side faced away from the camera. This ensured that the

(a) 2000x

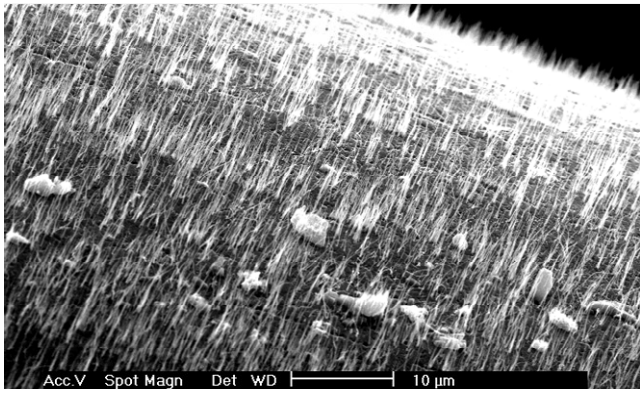

(b) 10000 x

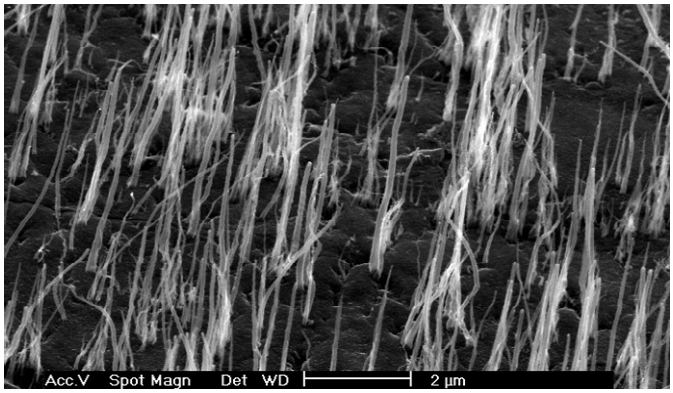

Figure 3.9. SEM images of CNTs. Vertically aligned CNTs were grown on the surface of a 15 mil. diameter SMA wire (70 °C Flexinol fabricated by Dynalloy, Inc.)

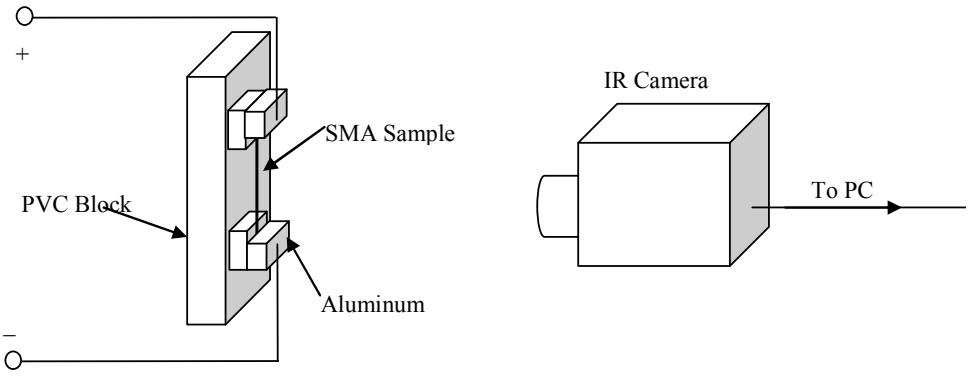

Figure 3.10. Fabricated fixture used to hold samples during testing. Electrical connections were made on top and bottom screws of the fixture (for resistive heating) which were insulated using a PVC block.

surface emissivity recorded by the camera was identical to that of a regular wire providing an accurate temperature measurement. Stray air currents were isolated from the experiment, by shrouding the entire sample in a box (Figure 3.11).

During each run, the wire sample was electro-resistively heated to an initial temperature of approximately 75 °C. An IR camera was focused on the center of the wire's length which was sufficiently far from the wire clamps ensuring that the thermal gradients in the axial direction were small and that the primary mechanism of heat transfer was through radial convection. As with the validation experiments for the midpoint transformation method (Section 3.1.2) emissivity for the 70 °C Flexinol wire was calibrated to 0.76 for an accurate surface temperature measurement. After monitoring a 75 °C steady-state surface temperature with the calibrated IR camera, heating was removed by shutting off the current and the surface temperature of the wires under free cooling was recorded in real-time by an IR camera at 10 frames per second (sent to a PC computer). The wire temperature with respect to time was later recorded by analyzing the captured IR images. The experiment was repeated for three separate pieces of regular wire, and three trials of the nanotube treated wire. Between each trial, the sample tested was physically removed from the fixture and a new sample

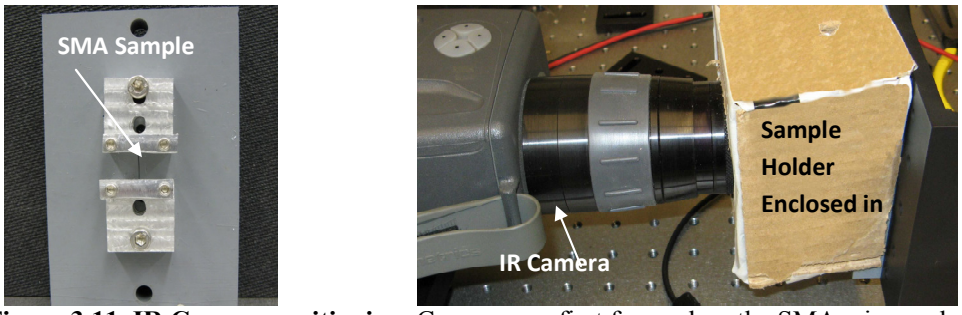

Figure 3.11. IR Camera positioning. Camera was first focused on the SMA wire, and then shrouded with a box to isolate the system from any stray air currents. The wire was fixed in place with an aluminum block.

was installed. This was done to account for any possible error that could be produced due to installation.

3.2.3 Results and Discussion

The collected cooling profiles (Figure 3.12) show the cooling profiles for the regular and CNT treated SMA wires. The wires began cooling at an initial normalized temperature ($T-T_{amb}$) of approximately 53 °C which decayed exponentially with time. In general, the regular wires took longer to cool to a given temperature – for example, the time interval at 20 °C (indicated by the bracket in Figure 3.12) is distinct between the two wire types, measuring approximately 0.6 seconds. Figure 3.12 also shows that

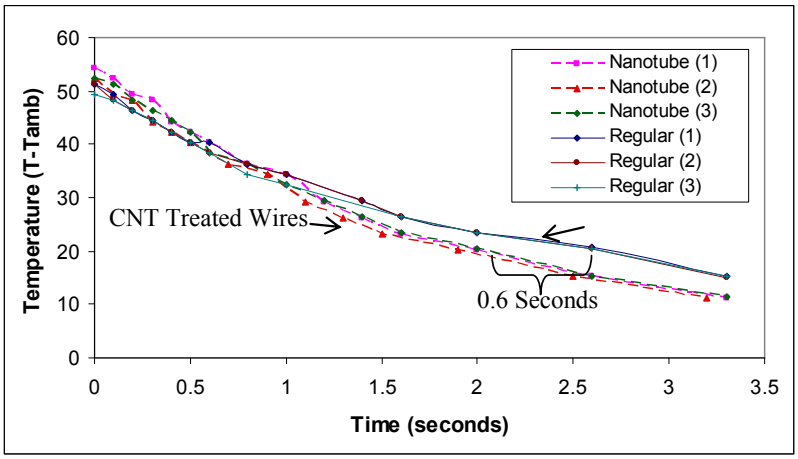

Figure 3.12. Cooling Profiles for Regular and CNT Coated Wires. Regular wire and nanotube treated wires tended to group together with a 0.6 difference in cooling time to reach 53 °C.

the difference in cooling speeds was repeatable for the series of experiments as the different experimental runs for the regular wires and the CNT treated wires grouped into two separate curves.

While the direct temperature measurements in Figure 3.12 show differences in cooling times, they can also be used to quantify the cooling rate differences. These rate differences can be extracted by analyzing the overall shape of the cooling curves and extracting their decay constants, which area directly related to the effective convective heat transfer coefficient *h*. To quantify the temperature decay constants for the two wire types, and to relate these constants to the convective heat transfer coefficient, a heat transfer model was applied to the system under free Newtonian cooling. For the nanotube treated wire, the convective heat transfer coefficient in the model, *h,* was specified to account for both the heat transfer from the SMA surface, and through the nanotube fins.

3.2.3.1 Cooling Model

The cooling model was derived assuming that the wires cooled freely in air, and that the dominant mechanism of heat transfer occurred through natural convection as justified in Section 3.1.2. Temperature variations in the radial direction were also assumed to be small. This assumption was arrived through the calculation of the Biot number for the SMA wire, which is defined as,

$$B_i = \frac{hL_C}{k}, \tag{3.10}$$

where h is the convective heat transfer coefficient, L_C is the characteristic length of the wire (volume to surface area ratio), and k is the thermal conductivity. If the Biot number is small (<<1), the heat conduction process offers little resistance (in comparison to convection) to the overall heat transfer, and thus the temperature gradients in the material are small. Using a thermal conductivity of 18 (W/mK) (Dynalloy 2009),

characteristic length of 9.52 E-5 meters, and a convective heat transfer constant of 50 W/m^2K (lower bound to the data in Figure 3.4), the Biot number was calculated to be 2.64 E-4 (<<1), indicating that thermal variants in the radial direction are indeed negligible. With these reductions, the heat transfer equation for the wire is derived through an energy balance assuming lumped parameters,

$$\rho CV \frac{DT}{dt} + hA(T - T_{amb}) = 0\,, \tag{3.11}$$

where ρ is the density of the SMA, C is the heat capacity, V is the total volume, T is the surface temperature (assumed to be uniform in the radial direction), h is the effective convective coefficient, A is the surface area of the SMA wire, and T_{amb} is the ambient temperature measured at 23 °C. By scaling the temperature in Equation 3.11,

$$\rho CV \frac{D\theta}{dt} + hA(\theta) = 0\,, \tag{3.12}$$

where $\theta = T - T_{amb}$. The solution to Equation 3.12 is exponential, and the time dependent temperature profile is

$$\theta(t) = \theta_o e^{-\left(\frac{hA}{\rho Cv}\right)t}\,, \tag{3.13}$$

where θ_o is the scaled temperature of the wire at time t=0. Taking the natural log of both sides gives

$$\log\theta(t) = \log(\theta_0) - \frac{hA}{\rho CV}t\,. \tag{3.14}$$

Equation 3.14 represents an equation for a line, with the slope depending on: 1) the bulk properties of the wire (ρ and C) and dimensional properties (A and V) assumed to have not changed from the wire treatment, and 2) the surface convective property h theorized to increase with the nanotubes added to the wire surface.

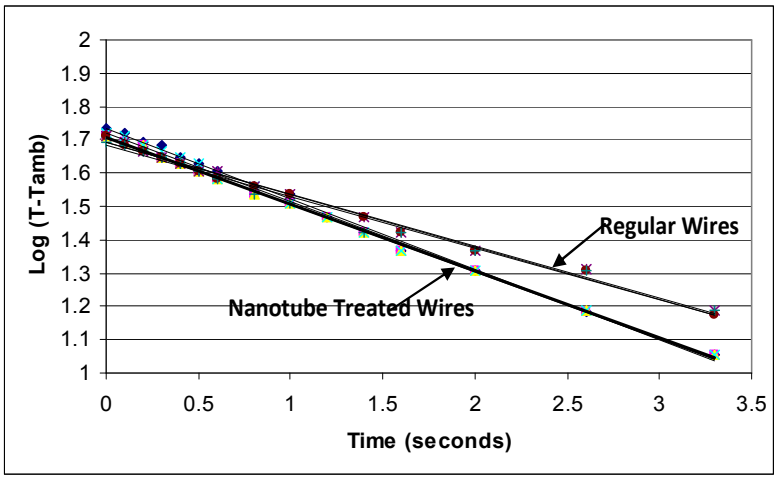

Figure 3.13. Log of Temperature vs. Time. A comparison of the cooling rates for the nanotube coated and regular SMA wires show a clear difference. Three trials for each are plotted with linear fits.

3.2.3.2 Cooling Comparison

Figure 3.13 shows the log of the temperatures graphed in Figure 3.12. The transformed data now shows a linear trend indicating that the assumptions made in deriving Equation 3.14 (particularly neglecting the nonlinear term for radiation) were valid. Linear fits were applied to the data in Figure 3.13, and their equations are listed in Table 3.6. Two important facts emerge from the fits: first there is no significant variation in slope between trials of the same type of wire, and second that there is indeed a variation between the CNT treated wire and the regular wires. Taking an average for the three trials gives an average slope of approximately -0.20 s^{-1} for the nanotube treated wire, and -0.16 s^{-1} for the regular wires. Using a density of 6.5 E6 kg/m^3 , specific heat of 0.5 J/kg K (Chang, et al. 2006), and diameter of 0.381 mm an estimate of the effective h (using the SMA surface area as the value for A) was calculated to be ~62 W/m^2K for the carbon nanotube treated wire and ~50 W/m^2K for the regular SMA wire, which is a 19% increase. Assuming that identical growth was covered on the entire wire (thus doubling the increase in the effective h value) and using the lumped heat transfer model, the cooling time to an estimated Martensite finish

Table 3.6. Linear fits to the transformed cooling data. The slope of the fits are directly proportional to the wire cooling rate constants.

Nanotube Coated SMA Wire	Regular SMA Wire
y=-0.21x+1.73	y=-0.16x+1.69
y=-0.20x+1.71	y=-0.16x+1.69
y=-0.20x+1.71	y=-0.15x+1.68

temperature of 40 °C would decrease from 2.9 seconds to 1.96 seconds. This would increase frequency performance by 48% with no additional weight or added bulk.

The increase in cooling performance is significant, yet less than the estimated 33% increase in effective cooling surface area observed from the SEM images (Figure 3.9). This difference may be due to imperfect fin efficiency or a potential non-uniformity in the deposited nanotubes. Further increases in nanotube length in the SMA sample would likely increase the cooling effect, and may produce improvements closer to the 2-3 times increase calculated in (Bhattacharya, et al. 2006), which was based on much longer fin lengths. Additionally, increasing the density of the nanotubes (number of cooling fins) may further aid improvements in heat transfer. On a Si substrate densities as high as ~20 CNTs/μm^2 have been reported (AuBuchon, et al. 2004), suggesting that density improvements of up to ten times are theoretically possible. With these further improvements, combined with alterations in the PECVD process to efficiently cover the entire wire surface, SMA wires with significantly higher cooling properties can be produced. These wires will be capable of functioning in actuators with simpler cooling media allowing for further improvements in the already lightweight, compact stabilization systems made possible by the work in this dissertation.

3.3 Conclusions

To improve the frequency of SMA actuators and minimize their power consumption, this chapter investigated methods to evaluate conventional cooling

techniques and an unconventional cooling approach utilizing carbon nanotubes. For conventional cooling methods, an experimental method was developed that overcomes current shortcomings in measuring the surface temperature of SMA wire, which is needed to calculate the convective coefficient, h. By measuring the midpoint transformation strain as a function of temperature, predictions of surface temperature in various environmental conditions were made. These predictions enabled Newton's cooling law to be employed to calculate h when the wire was supplied with a known power under steady-state conditions. Unlike traditional techniques, this method was based on a strain measurement allowing calculations of the convective coefficient to be made for any size wire in any ambient medium. This was demonstrated by measuring h in a wide range of conditions that can be employed for various applications. These conditions included wire diameters ranging from 6 to 20 mils in air (free and flowing), mineral oil, thermally conductive grease, and water. For validation, separate thermal imaging tests were also conducted for the only two allowable cases, 15 and 20 mil diameters in air. Close agreement between these two separate procedures was shown, demonstrating that the new transformation strain method is a robust procedure that overcomes measurement issues experienced by traditional techniques (i.e. the invasive properties of thermocouples on thin wires and problems with IR cameras viewing thin wires and used in media other than air). Additionally, the transformation strain method is completely general and applicable to any SMA actuator where motion can be measured.

Using the general form of correlations in literature for the convection from a smooth cylinder in still air and a cross-flow, empirical correlations were generated for each of the ambient media tested. Because the all-encompassing fits found in literature typically provided only general estimates of the collected data and did not apply well to

wires of small diameter, the fit parameters were adjusted for each test condition using a GRG optimization algorithm. The resulting continuous equations closely followed the collected data in relating the power dissipation from the SMA wire to the wire diameter, flow rate, and fluid properties (as close as 1.2% average error for water). They also offer improvements over conventional correlations (such as Hilpert of Morgan) by 8% for water, 36% for mineral oil, and 33% for convection in air. Because these correlations are continuous functions, they may be readily used in optimization algorithms to ensure that the cooling requirements are properly chosen to improve frequency performance while minimizing power consumption. In addition, SMA material models will benefit from the correlations allowing for interpolation across discrete points to fully map and understand an actuator's design space.

For situations where conventional cooing methodologies are not acceptable (e.g. where weight constraints prohibit a heat exchanger, and force requirements limit the wire diameter) the effects of improving the cooling rate of SMA wires through the surface growth of vertically aligned CNTs were also presented in this chapter. Due to their high thermal conductivity, the CNTs were intended to act as cooling fins capable of increasing the effective cooling area of the heated wire surface. Using a DC plasma enhanced chemical vapor deposition (PECVD) process, vertically aligned nanotubes were grown directly on half of the wire's surface (lengthwise). Their presence and direct attachment to the wire surface was confirmed in SEM imaging. The observed nanotubes had average diameters of 30 nm, lengths of 2-5 μm, and had an overall density of approximately 2 CNTs/μm^2. The shape memory effect was observed to have remained after the CNT growth process.

Because the CNTs were grown from the surface of the SMA wire, thermal contact resistance was assumed to be small thus benefiting overall cooling performance. These

improvements in overall convective heat transfer verified from direct measurements of cooling profiles under free cooling in air for both CNT treated and untreated SMA wires. A clear difference in cooling speed was noted after fitting the data to a lumped model, where the average *h* value was calculated to have increased by 19% from 50 W/m^2K to 62 W/m^2K. The results of these preliminary tests show a distinct improvement in cooling due to the CNT growth, an effect that can be used to improve the cyclic performance for many small SMA systems (e.g. MEMS) without the addition of unwanted bulk or power consumption. Cooling performance from the CNT growth is expected to further improve with full wire coverage. Assuming that identical growth can occur on the entire wire (thus doubling the increase in the effective *h* value), the cooling time to an estimated Martensite finish temperature of 40 °C using the lumped model would decrease from 2.9 seconds to 1.96 seconds. This would increase frequency performance by 48% with no additional weight or added bulk. The concept and methodology of growing CNTs on a metal NiTi substrate may also benefit the cooling of micro-electronics. Since it is currently difficult to grow CNTs directly on a metal substrate, the developed method that utilizes the Ni in the alloy as catalyst particles may prove useful in enhancing heat transfer due to its superior thermal conductivity over traditional silicon substrates.

The previously non-existent cooling data collected both from the midpoint transformation study and the CNT surface treatment analysis represents invaluable information that can be used to predict the behavior of SMA actuators to ensure that frequency requirements are met and that power consumption is minimized. The measured convective coefficients, for example, can be used in thermodynamic SMA models, where useful predictions can be made in the output motion response (i.e. frequency and amplitude) to an arbitrary input heating power signal. These models can

be directly used to select the appropriate cooling medium that minimizes the amplitude of this power signal, given set of actuation specifications. For this purpose, the following chapter develops a transient thermodynamic model for antagonistic SMA that utilizes the cooling data measured by the midpoint transformation method developed in this chapter. To provide design insight and understand the antagonistic SMA actuator, the model is exercised in a series of simulation-based design studies that explore the various design tradeoffs affecting frequency and power draw. In Chapter 5, this general antagonistic model is applied to a proof-of-concept case-study where it is shown to be instrumental in advancing a new class of hand-held active tremor cancellation systems. This is accomplished by using the cooling properties measured in this chapter, and conducting detailed simulations for a range of design scenarios ensuring that the resulting actuation system produces a required amount cancellation at an identified frequency range in the most power-efficient manner.

Chapter 4: Transient Thermodynamic Modeling and Experimental Validation of an Antagonistic SMA Actuation Architecture

While the actuation frequency of SMA can be dramatically improved through changes in its convective environment (as studied in Chapter 3), improvements in cancellation accuracy can be obtained through the use of actuation architectures such as antagonistic configurations. Higher cyclic rates over single-wire actuators, for example, are possible since one wire can be activated before the other is cooled to initiate motion reversal (Featherstone and Teh 2006). In addition, more precise control is possible since an antagonistic wire can reduce the effects of hysteresis (Moallem and Tabrizi 2009; Teh and Featherstone 2008). For a similar reason, lower power draw can result during precise positioning since the wires may not need to be activated repeatedly.

Due to these benefits, antagonistic SMA actuators have been used successfully in a variety of applications including human assistance (De Laurentis and Mavroidis 2002; Pathak, et al. 2007; Pfeiffer, et al. 1999), micromanipulation (Bellouard, et al. 1998; Kohl, et al. 2002; Zhang, et al. 2001), and position control (Maclean, et al. 1997; Williams and Elahinia 2006), which typically uses ad-hoc (typically PID) and heuristic control approaches. While most of these methods have been shown to produce accurate, precise, and relatively high-speed response (Moallem and Tabrizi 2009; Teh and Featherstone 2008), they often result in unwanted complexity. For example, these systems generally involve costly electronics and require extensive tuning and

adjustments based on the antagonistic actuator's operating conditions. During the product's life, these systems also have a risk of losing controller accuracy as most do not account for changing conditions such as ambient temperature or battery charge.

Efficient design of the antagonistic actuator is another challenge since there are many variables that are difficult to predict the effects of (e.g. wire diameter, length, convective coefficient, ambient temperature, and electric heating input), presenting several non-intuitive design tradeoffs. Increasing the convective coefficient (as studied in Chapter 3), for example, increases the actuator's frequency capabilities but also increases power draw. Wire diameter and length affect the output force and displacement, but they also significantly impact the power consumption and packaging. Due to the competing effects of these different variables, the overall antagonistic actuator design is difficult to balance, often leading to sub-optimal motion behavior (i.e. frequency and amplitude), power-draw, and packaging. Thus, there is a strong need for a simple yet accurate, predictive model of the antagonistic system that can solve these issues and guide the designer to produce more educated designs capable of meeting motion and packaging requirements while minimizing power draw. A model would also be useful in easing or eliminating the need for on-line controller tuning, by allowing the process to be accomplished in simulation.

For these reasons, this chapter develops a thermodynamic model of antagonistic SMA architecture to improve overall predictability and understand the various design tradeoffs affecting frequency and power draw. While the SMA model is derived from a reduced form of a thermodynamic material model, it includes compatibility terms to account for antagonistic connectivity. It also encompasses additional model conditions including inertial dynamics, static friction, slack conditions (where the wires cannot support compressive load), empirical fits for the convective heat transfer, and a model

for local boiling effects. To characterize the improvement in accuracy for each of these conditions, experimental data over frequencies of 0.3-10 Hz is used to quantify model tracking in both the transient and steady-state regions. Comparisons to further experimental tests are presented to validate the full model (with all conditions present) for various input duty cycles, heading amplitudes, and SMA wire diameters. With the model experimentally validated, design studies are investigated through model simulations under a variety of operating conditions. These studies focus on characterizing the key requirements (e.g. mechanical advantage, cooling medium, ambient temperature, duty cycle, power draw and wire diameter) to produce motion at a desired amplitude and frequency. The results of these investigations are highly useful in generating engineering insight that serves to facilitate the design of antagonistic SMA actuators for hand-held tremor cancellation applications.

4.1 Model of SMA Wire in Antagonistic Architecture

The transient thermodynamic model (nomenclature given in Table 4.1) is developed for a general antagonistic architecture, which is defined in Figure 4.1 to consist of two opposing wires that are connected to a shared output stage of mass m. Movement towards the right is achieved by electro-resistively heating the right SMA wire while the left wire cools. This causes the right wire to transform to an Austenite phase, contract, and move the stage while simultaneously elongating the left wire in its Martensite phase. Motion in the left direction is similarly achieved by heating the left wire while the right wire cools. In Figure 4.1, two compression springs are fitted between the ground and stage, with stiffness k and free length equal to the neutral length of the wire. This free length configuration is equivalent to a single spring compressed to a neutral position by an external load such as a weight since the resultant force is zero at neutral and is positive or negative with linear slope k away from the

Table 4.1. Nomenclature and values for the antagonistic model solution.

Symbol	Name	Value	Units
P_s	Prestrain	1	%
k	Spring Stiffness	4.0	kN/m
d	Wire Diameter	0.254-0.508	mm
l	Length	0.178	m
β	Max. SMA Strain	5	%
ρ	Density	6.5	Mg/m^3
μ_c	Critical Driving Force	1.01	J/g
ΔS	Entropy Change	-67	mJ/gK
T_R	Reference Temperature	323	K
T_a	Ambient Temperature	296	K
v_o	Kinetic Stiffness	50	g/Js
E	Young's Modulus	70	GPa
H	Convective Coefficient	1.8-5.8	kW/m^2K
R	Wire Resistivity	18.8	Ω/m
m	Mass of Stage	220	g

neutral position. If a device were made such that the free length of the compression springs were more than the neutral length (if the springs were compressed to be fitted in the device and always remained in contact with the output stage), or if the springs worked both in compression and extension, same model would be used with the effective stiffness changed to $2k$.

From these stated assumptions, this section develops a general modeling framework for the antagonistic system. This framework consists of three sets of coupled time-dependent equations: 1) a group of differential equations describing the material's thermodynamic phase transformation, 2) a collection of compatibility equations specific to the antagonistic configuration, 3) and a set of energy balance and convective heat transfer equations. Additional conditions are derived to account for the antagonistic wires becoming slack, friction, convective heat transfer, and localized boiling in the coolant.

4.1.1 SMA Modeling Background

To develop a full model for a generic antagonistic SMA actuator, a suitable constitutive modeling foundation was selected from the literature that describes the

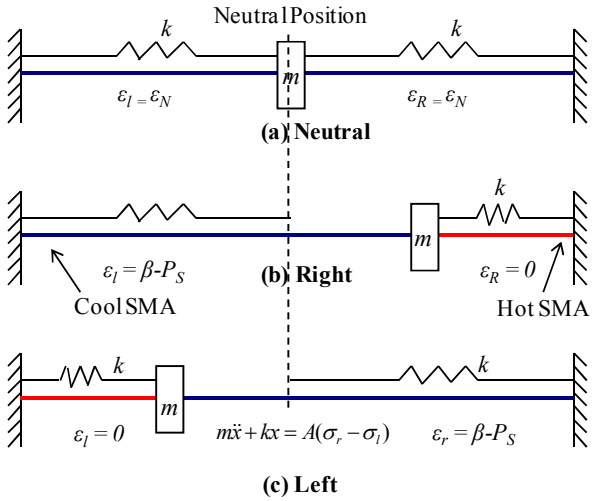

Figure 4.1. Schematic of a generic antagonistic system. Operating strains are labeled in the figure according to model nomenclature.

material's basic behavior with respect to temperature and stress. While numerous material models exist in this active area of research, most can be classified into three categories, each with its own benefit and drawback: a) Empirical, b) Microstructure, and c) Thermomechanical Modeling. Each of these categories is evaluated in further detail, and the most suitable approach is selected as a basis for the model derived in this chapter.

4.1.1.1 Empirical Modeling

The first SMA models were of the empirical form where in 1986 Tanaka (Tanaka 1986), developed an exponential description for the phase fraction of Martensite, as an internal variable. While Liang and Rogers 1990 modified the Tanaka model's phase transformation law with a cosine relationship, both models were limited to the high temperature case and were not capable of describing the de-twinning of Martensite. Brinson 1993 offered a solution to this problem by decomposing the Martensite phase fraction into two variants (twinned and detwinned), yet still retained the empirical cosine relationship for their evolution. While empirical approaches are useful due to their simplicity and are still used in many engineering applications, they do not lead to

physical insight in the underlying physics of phase transformation. In certain cases, these models can violate the second law of thermodynamics unless specific initial conditions or specific stress-temperature histories are provided (Chung, et al. 2007). While this incongruity can be corrected, through a modification of the empirical relationship (Chung, et al. 2007) it is desirable to use a physically based model for the material that is thermodynamically admissible.

4.1.1.2 Microstructure Modeling

To provide such a physically-based understanding, recent work has focused on producing models in the second main category, microstructure evolution, to examine the material's behavior with regard to its crystal structure. These models consist of a mechanical component governing stress-strain behavior that is coupled to a chemical component determined by entropies of the material's Austenite and Martensite phases. Bo and Lagoudas 1999, for example, developed a polycrystalline model that uses back and drag stress to simulate two-way shape memory effect and material shakedown. Other examples of recently developed models focusing on microstructure include those developed by Gao et al, 2000, who base a model on habit planes and transformation directions, Goo and Lexcellent 1997, who focuses on two-way effects, and Vivet and Lexcellent 1998 who characterize the differences between tension and compression in super-elasticity. While the models focusing on the microstructure of SMA provide significant physical insight and accuracy, they typically require finite-element implementations, and are difficult to use in simulating engineering applications that mainly require 1-D modeling (Seelecke and Müller 2004).

4.1.1.3 Thermomechanical Modeling

As a result, a third category of thermomechanical modeling is being revisited for simplification in 1-D applications. Ivshin and Pence 1994, for example, detailed a

model based on equilibrium thermodynamics, though material hysteresis is modeled with assumed envelope functions that must be fit with additional parameters. Another model using concepts of statistical thermodynamics was developed by Achenbach and Müller 1985 and extended by Seelecke and Müller 2004 showing use in design, feedback control, and optimal control. Recent thermodynamic modeling developed by Shaw 2002 has also shown promise in understanding SMA device physics due to its phenomenological nature, and its ability for model-reduction. For example, Shaw and Churchill 2009 have recently demonstrated its reduction by neglecting individual terms that describe detailed phenomena such as propagating phase transformation fronts to produce a lumped analytical solution in terms of the *Lambert* function. This solution eliminates the need for any PDE solution, yet captures most of the behavior useful for engineers working in design and optimization. The model is also thermodynamically consistent, and does not experience the incongruities of traditional empirical models revealed by Chung, et al. 2007. In fact, through model reduction or selecting an appropriate kinetic relationship, the phase transformation can be made implicit (Shaw and Churchill 2009) eliminating the need for empirical kinetic descriptions. Due to this ease of simplification, the modeling foundation from Shaw and Churchill 2009 was selected, and a similar reduction approach taken with an important difference occurring in necessity of retaining the two internal martensitic state variables to account for twinned and de-twinned Martensite (to describe slack conditions in antagonistic actuators). In this section, this reduction process is detailed where the original Helmholtz free energy given by Chang et al. 2006 is modified to a reduced form. The modeling contribution made in this chapter is based on this reduced form, where two instances (one for each antagonistic wire) are coupled through compatibility equations to form a generic antagonistic model. Additional contributions including the addition of

dynamics, slack, friction, boiling, and convective heat transfer conditions are also developed and applied to the antagonistic modeling methodology.

4.1.2 Model Formulation

The full Helmholtz Free Energy function used by Chang, et al. 2006 is given as,

$$\begin{aligned}\phi(\varepsilon,\xi,T) = {} & \frac{E_A + (\xi_1+\xi_2)\Delta E}{2\rho}\left[\varepsilon - (\xi_1-\xi_2)\beta\right]^2 + \frac{\gamma}{2\rho}\left(\frac{\partial\varepsilon}{\partial x}\right)^2 \\ & -(T-T_R)(\xi_1+\xi_2)\Delta S \\ & +c_1(1-\xi_1-\xi_2)(\xi_1+\xi_2) \\ & +(c_o - s_o)(T-T_R) - c_o T\ln\left(\frac{T}{T_R}\right)\end{aligned} \quad . \qquad \textbf{(4.1)}$$

The first line of the full Helmholtz free energy function represents the elastic energy contribution were ε is the strain the wire, β is the maximum recoverable strain under zero stress, ρ is the mass density, γ is the strain gradient parameter, E_A is the Young's modulus of Austenite, and ΔE is the change in young's modulus between Austenite and Martensite. The tensile and compressive phase fractions for Martensite are expressed as ξ_1 and ξ_2 with the Austenite phase fraction ξ_3, being implicit (the Martensite and Austenite phase fractions sum to one). The second line of the Helmholtz free energy function represents an energy contribution due to phase-dependent entropy where T_r is the reference transformation temperature, and ΔS is the change of entropy due to phase transformation, which is related to the latent heat of transformation. The energy of mixing is accounted in the third line where the constant c_1 affects the slope of the pseudoelastic transformation path. The last line in the Helmholtz free energy function (Equation 4.1) represents the phase-independent thermal energy where c_o or s_o are the specific heat and specific entropy. For the transient antagonistic model developed in this chapter, reductions of the full Helmholtz free energy function (Equation 4.1) are performed through the assumption that the change in Young's modulus between

Austenite and Martensite ΔE is negligible, there is no free energy of mixing (c_1), and there are no gradients along the material (in any direction) for temperature, strain, and phase fraction, eliminating the need for a PDE solution. Churchill and Shaw 2009 demonstrate that these assumptions give satisfying results compared to a finite element approach in terms of the actuator's gross behavior. The resulting reduced free energy is

$$\begin{aligned}\phi(\varepsilon,\xi,T) = \frac{E}{2\rho}\left[\varepsilon-(\xi_1-\xi_2)\beta\right]^2-(T-T_R)(\xi_1-\xi_2)\Delta S \\ +(c_o-s_o)(T-T_R)-c_oT\ln\left(\frac{T}{T_R}\right)\end{aligned} \quad . \tag{4.2}$$

The tensile and compressive Martensite phase fractions are defined such that when the SMA wire is cool but fully stretched in tension under load (there is assumed to be no two-way effect), ξ_1 is equal to one while ξ_2 is zero (this is also known as de-twinned Martensite). When the wire is heated, it contracts and transforms to Austenite, and both ξ_1 and ξ_2 are zero (Figure 4.2). Cooling the wire again, but applying no load produces both tensile and compressive Martensite variants and both ξ_1 and ξ_2 are 0.5 (this state is also known as twinned Martensite).

The stress in each wire is defined as the partial derivative of the Helmholtz free energy with respect to strain (holding the other states constant). For each wire (with subscript x replaced with l or r for the left or right wire of the antagonistic pair),

$$\sigma_x = \rho\frac{\partial\phi_x}{\partial\varepsilon_x} = E\left[\varepsilon_x-(\xi_{1,x}-\xi_{2,x})\beta\right], \tag{4.3}$$

where, for example, ε_l is the strain in the left wire. The partial derivative of the Helmholtz free energy with respect to the tensile or compressive Martensite phase fraction (ξ_1 or ξ_2) is equal to the thermodynamic driving force vector $\boldsymbol{\mu}$ dictating the magnitude and direction of phase transformation. For each wire,

$$\boldsymbol{\mu}_x = \begin{bmatrix} \mu_{1,x} \\ \mu_{2,x} \end{bmatrix} = \begin{bmatrix} \dfrac{\beta E}{\rho}\left[\varepsilon_x - \left(\xi_{1,x} - \xi_{2,x}\right)\beta\right] + \left(T_x - T_R\right)\Delta s \\ -\dfrac{\beta E}{\rho}\left[\varepsilon_x - \left(\xi_{1,x} - \xi_{2,x}\right)\beta\right] + \left(T_x - T_R\right)\Delta s \end{bmatrix}. \tag{4.4}$$

To account for hysteresis, phase evolution only occurs if the thermodynamic driving force is greater than a critical value, μ_c by the relation given in (Chang, et al. 2006). For the time derivative of the phase fraction vector $\boldsymbol{\xi}$,

$$\dot{\boldsymbol{\xi}}_x = \begin{cases} 0 & : \text{ if } \boldsymbol{\mu}_x \cdot \mathbf{m}_x < \mu_c \\ v_o\left(\boldsymbol{\mu}_x \cdot \mathbf{m}_x - \mu_c\right)\mathbf{m}_x & : \text{ if } \boldsymbol{\mu}_x \cdot \mathbf{m}_x > \mu_c \end{cases}. \tag{4.5}$$

Since the phase fractions must be non-negative and sum to one, an "admissible space" is defined as shown in Figure 4.2. The driving force cannot bring the phase fractions outside of this admissible space. Therefore, Equation 4.5 employs a unit vector ***m*** defined depending on the state of the material. The unit vector ***m*** is defined as the unit vector of ***μ*** if the phase fractions are either within the interior of the admissible space and not on any boundaries, or if the phase fractions lie on any of the edges, and ***μ*** is pointing inwards. Otherwise, if ***μ*** points outwards, ***m*** is the unit vector of its projection along the boundary. If the phase fractions reside on one of the corners, ***m*** is zero if ***μ*** points directly outward (Chang, et al. 2006).

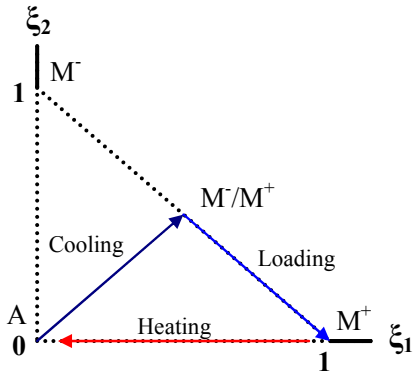

Figure 4.2. Admissible Space. Martensite phase fractions must reside within the triangle, adapted from (Chang, et al. 2006).

4.1.3 Antagonistic Compatibility Relations

Unique to modeling antagonistic systems is the coupling between the left and right wires, which had to be derived. Because many devices are designed to strain the opposing wire to some fraction of the maximum strain β (conservatively this can be half) to ensure operation over many cycles, an amount of pre-strain (P_s) is incorporated in the strain compatibility equation,

$$\varepsilon_r + \varepsilon_l = (\beta - P_s), \tag{4.6}$$

which is shown in Figure 4.1. These strains are also directly related to the position x of the stage through,

$$\varepsilon_r = \left(\frac{\beta - P_s}{2} - \frac{x}{l} \right), \tag{4.7}$$

and

$$\varepsilon_l = \left(\frac{\beta - P_s}{2} + \frac{x}{l} \right), \tag{4.8}$$

which is consistent with Equation 4.6. Stress coupling is found by applying a force balance on the stage, which is assumed to have a mass m

$$m\ddot{x} + kx = A(\sigma_r - \sigma_l) + F_f, \tag{4.9}$$

where F_f is used to account for static friction. Depending on the actuator speed relative to its cooling environment, it is possible that one of the antagonistic wires can become slack near the end of the actuation stroke. Figure 4.3 illustrates this scenario, where at a low duty cycle the power to the heated wire is turned off before the opposing antagonistic wire is heated. During this time, the heated wire cools and is stretched (from Austenite to de-twinned Martensite) by the system spring while the opposing cool wire becomes slack from the resulting motion. Since the SMA wires are thin and cannot support compressive loads care must be taken in identifying and distinguishing two operating regimes: taught and slack.

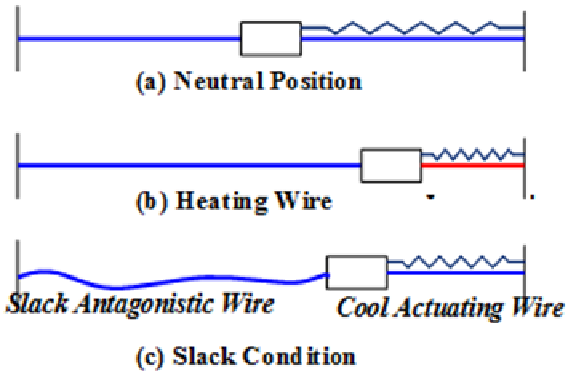

Figure 4.3. Slack Conditions. Antagonistic wire can become slack if actuating wire is cooled before heating antagonistic wire.

4.1.3.1 Antagonistic Wire Taught

Taught operation is defined when the stress in both wires is positive (tensile). If the stage is assumed to have a mass, the strain in the SMA wires must be determining by twice integrating the acceleration in Equation 4.9 to give position, x, and substituting the resulting value in the strain equations (Equations 4.8 and 4.9). For a stage with negligible mass (m=0), however, direct equations for the strains in the left and right wires (as functions of phase fraction) can be obtained. By setting m to zero in the force balance (Equation 4.9), and substituting the equations for stress (Equation 4.3) and position as a function of strain (reformulating Equations 4.7 and 4.8) wire strains are expressed as,

$$\varepsilon_l = -\frac{1}{2E+\tilde{k}l}\left[E\beta\left[\left(\xi_{1,r}-\xi_{2,r}\right)-\left(\xi_{1,l}-\xi_{2,l}\right)\right]+\left(E+\frac{\tilde{k}l}{2}\right)\left(P_s-\beta\right)\right], \qquad \textbf{(4.10)}$$

for the left wire (where $\tilde{k}$ is the spring stiffness divided by the wire cross sectional area A) and

$$\varepsilon_r = \beta+\frac{1}{2E+\tilde{k}l}\left[E\beta\left[\left(\xi_{1,r}-\xi_{2,r}\right)-\left(\xi_{1,l}-\xi_{2,l}\right)\right]+\left(E+\frac{\tilde{k}l}{2}\right)\left(P_s-\beta\right)\right]-P_s. \qquad \textbf{(4.11)}$$

for the right wire.

4.1.3.2 Antagonistic Wire Slack

If an antagonistic wire goes into compression, its stress is negative in value. Since small diameter wires cannot support this type of compressive loading they buckle (become slack). To account for this, whenever stress is detected to be negative it is instead set to zero. For example, if the left wire were to become slack,

$$\sigma_l = 0, \tag{4.12}$$

and from the force balance, Equation 4.9

$$\sigma_r = \frac{m\ddot{x} + kx - F_f}{A} \tag{4.13}$$

As with the taught conditions, the position x must be integrated from acceleration before expressions for the wire strains can be obtained using the wire length. However, for a stage of zero mass, the integration of position can be avoided and the strains can be expressed directly. Using the same substitution process used to derive Equations 4.10 and 4.11, and following the substitution procedure using Equations 4.12 and 4.13,

$$\varepsilon_l = \left(\xi_{1,l} - \xi_{2,l}\right)\beta \tag{4.14}$$

and (with m=0),

$$\varepsilon_r = \frac{1}{1 + \frac{\tilde{k}l}{E}}\left[\left(\xi_{1,r} - \xi_{2,r}\right)B + \frac{\tilde{k}L}{E}\left(\frac{\beta - P_s}{2}\right)\right] \tag{4.15}$$

.

Analogous stress and strain equations for system are used should the right wire go slack, with the l and r subscripts switched.

4.1.4 Energy Balance and Convective Heat Transfer

With the transformation kinetics and mechanics of the antagonistic SMA wires defined, a final equation is needed to predict the actuator's thermal response to heating inputs and convective losses to the environment. The evolution of temperature over

time is described by a traditional lumped heat equation with an additional latent heat term, derived from a general form given in (Chang, et al. 2006). In these equations, power is assumed to be input through electric heating (by an applied current *I*) and heat is lost via convective cooling to the environment. Two separate equations are used for each wire where, as before, the general subscript *x* is replaced by *r* or *l*:

$$\rho A l c_o \dot{T}_x = \rho A l \left(\mu_x - \begin{bmatrix} T\Delta S \\ T\Delta S \end{bmatrix} \right) \cdot \dot{\xi}_x - h\pi d l \left(T_x - T_{amb} \right) + I_x{}^2 R_x l \,. \qquad \textbf{(4.20)}$$

In the heat equation (Equation 4.20) *I* is the input current, *R* is the wire resistivity (resistance per unit length), and *L* is the length of wire, *h* is the convective heat transfer coefficient, and T_{amb} is the temperature of the surrounding environment. Because the wire resistivity depends on material phase (Churchill and Shaw 2008; Ikuta, et al. 1988), the final input term for power of the heat equation (Equation 4.20) can be replaced with *IV*, where the input voltage *V* is often more convenient to measure.

The heat equation (Equation 4.20) shows that the heat transfer coefficient *h* affects the overall power consumption and cooling time (and thus frequency) of the actuator in the tradeoff studied in Chapter 3. While increasing the convective coefficient *h* improves the cooling speed it also increases energy dissipation during heating, raising power requirements for the actuator. This effect requires special consideration since the convective coefficient *h* is difficult to measure for thin wires, yet changes significantly depending on wire geometry and cooling medium. To address this issue, Chapter 3 had developed a method using low-power, steady-state tests to measure *h* at the SMA's midpoint transformation temperature of 60 °C for a range of diameters (6 to 20 mils) and cooling media (air, mineral oil, thermal grease, and water). Of these tested media, water cooling was selected for this chapter's experimental validation studies due to its higher cooling properties and ease of use that enabled many tests at a variety of

different frequencies. Because traditional empirical correlations (such as the Hilpert correlation) were known to deviate by as much as 20% from experimental data, Chapter 3 focused on experimentally measuring the convective coefficient for SMA under a variety of conditions. However, due to the nature of the measurement technique used in Chapter 3, the collected data was only gathered at a fixed transformation temperature of 60 °C. For media such as water, the convective coefficient h is known to vary with temperature. Thus, of the several existing empirical correlations a suitable equation by Kuehn and Goldstein was found to not only intersect with Chapter 3's measured data point for water, but also provide estimates for temperatures above and below 60 °C. The correlation takes the form of,

$$\mathrm{Nu}_D = \frac{hD}{k} = 0.518\left[1+\left(\frac{0.599}{\mathrm{Pr}}\right)^{3/5}\right]^{-5/12} \mathrm{Ra}_{\mathrm{D}}^{1/4} \quad \text{for } \mathrm{Ra}_{\mathrm{D}} \le 10^9, \qquad \textbf{(4.21)}$$

where the Nusselt number Nu_D is related to the heat transfer coefficient h through the wire diameter D and the fluid's thermal conductivity k. The Prandtl number Pr is a fluid property and the Rayleigh number, Ra_{D}, is defined for a cylindrical shape as

$$\mathrm{Ra}_D = \frac{g\alpha(T_s - T_a)D^3}{\upsilon\kappa}, \qquad \textbf{(4.22)}$$

In Equation 4.22, g is the acceleration due to gravity, α is the thermal expansion coefficient of the fluid (K^{-1}), T_s is the wire's surface temperature, T_a is the fluid's ambient temperature (K), D is the wire diameter, v is the fluid's kinematic viscosity (m^2/s), and κ is the thermal diffusivity (m^2/s). Values of the fluid properties for water as a function of temperature were calculated from (McQuillan, et al. 1984; McQuillan 2009). Another approach to modeling the convective coefficient is to lump the temperature variation into a single average value. This value was allowed to vary between heating and cooling cycles as suggested by Bhattacharyya, et al. 2002, and was adjusted from the values obtained in Chapter 3. Because the lumped value for h

encapsulates effects due to temperature variations or fluid motion they were expected to vary from the values obtained under steady-state and constant temperature in Chapter 3. However, the data in Chapter 3 is still highly useful as a general estimate and is useful for design since values are given for a variety of cooling media using a relatively simple experimental method.

In addition to the convective coefficient h, necessary considerations were made for boiling in water. While several general empirical correlations exist for nucleate pool boiling of liquids, they are rather complex and are useful when the input power is increased by several orders of magnitude (Incropera and DeWitt 2001). For the model's purposes, these power levels were not anticipated, and thus a binary approximation was selected for simplicity to approximate the latent heat effects when the SMA surface temperature reaches boiling. These effects were lumped into the h-value, which was increased by a factor of 2000 when the wire was above boiling temperatures. For temperatures below boiling, h was left unaffected.

4.1.5 Solution Procedure for Transient Model

To predict motions of the antagonistic actuation system, the heat, compatibility, and material equations must be solved simultaneously. Simulating numerically, the heat equation (Equation 4.20) is integrated for the left and right wire through a forward time-step scheme to obtain the temperature of the wires over time. The time derivative of ξ is obtained by substituting the thermodynamic driving force (Equation 4.4) into the kinetic equations (Equation 4.5). The acceleration of the stage solved in the force balance equation (Equation 4.9) and is twice integrated to produce position. In the examples in this chapter, the initial condition is selected to be the neutral position. Both wires are set to the cool ambient temperature, and tension in the wires is assumed to be zero about the equilibrium. Strain in each wire is set to the neutral strain (Equation 4.9).

Because there is no Austenite phase in either wire in the initial state, the tensile and compressive Martensite phase fractions in both wires sum to one,

$$\begin{aligned} \xi_{1,r} + \xi_{2,r} &= 1 \\ \xi_{1,l} + \xi_{2,l} &= 1 \end{aligned} . \tag{4.22}$$

Combining these relations with Equation 4.3 for each wire and setting the stress to zero results in the initial phase fraction at time t=0,

$$\xi_{1,l} = \xi_{1,r} = \frac{\beta - P_s}{4\beta} - \frac{1}{2} \tag{4.23}$$

and

$$\xi_{2,l} = \xi_{2,r} = \frac{1}{2} - \frac{\beta - P_s}{4\beta} . \tag{4.24}$$

With these initial conditions, the transient thermodynamic model's coupled ordinary differential equations are integrated with respect to time to produce actuation response to a defined input heating signal.

4.2 Experimental Validation of the Transient Thermodynamic Model

While the developed model can simulate a motion response for a generic antagonistic actuator, its correlation to a physical system had to be validated. Thus, an experimental setup and test procedure was created. An initial series of tuning studies was first conducted to study the effect of various conditions in the model, including the slack and boiling conditions, static friction, inertia of the output stage, and convective

coefficient *h* for the wires. Further tests were performed to validate the full antagonistic model under changing conditions. These tests included validation studies over a range of actuating amplitudes, frequencies, duty cycles, and wire diameters. Through these experiments, the model's predictive utility is established, and valid regions are identified for the model's use in actuator simulation for design and controller tuning.

4.2.1 Experimental Setup and Procedure

The model validation was accomplished through the use of an experimental setup (Figure 4.4, Figure 4.5) that was designed to apply varying electric heating inputs to an antagonistic SMA system immersed in a liquid bath of distilled water at room temperature. The antagonistic actuator consisted of two lengths of 70 °C Flexinol wire (approximately 4.5 inches in length each, strained to 1.5% at the neutral position) that were fixed to a wall at one end, and at the other end crimped to a common movable stage (Figure 4.4) that had a measured mass *m* of 220 grams. The stage was fitted with linear ball bearings on a hardened steel shaft such that friction in the direction of motion was negligible. To give the actuator an internal stiffness, a compression spring was installed in the setup with a measured stiffness of 4.0 kN/mm. Electricity was supplied to either SMA wire from a Samlex adjustable DC power supply through one of two

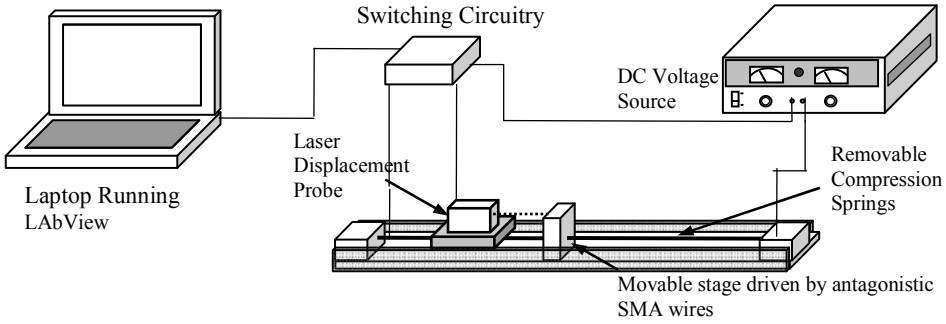

Figure 4.4. Schematic of the experimental test apparatus. Antagonistic wires move a low-friction output stage, with its motion measured with a Laser displacement sensor.

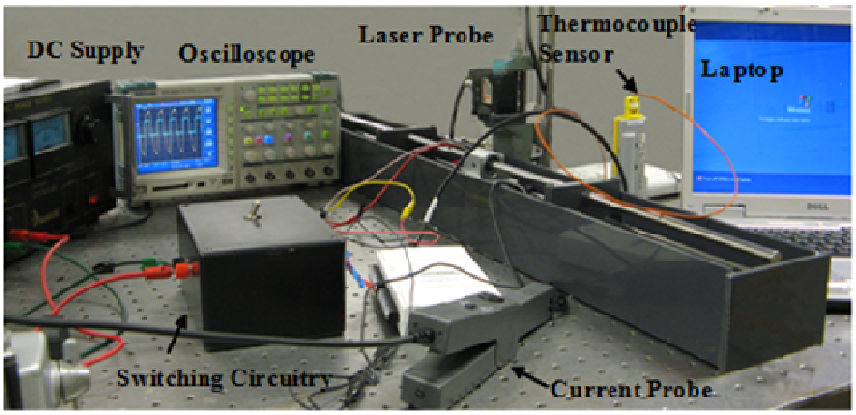

Figure 4.5. Photograph of the experimental setup for an antagonistically configured device. Motion and input power were monitored and recorded in software.

external MOSFET transistors controlled by a PC running LabVIEW (Figure 4.5). The resulting output motion was measured with a MicroTrak Laser displacement sensor, and the input current and voltage were measured with oscilloscope probes.

The antagonistic device was tested under a variety of conditions to validate the model's predictive capabilities. For each experimental condition tested, the model was solved using the parameters listed in Table 4.1. The geometric, spring, and environmental variables were adjusted according to the experimental conditions. Material properties were taken from (Chang, et al. 2006), while the reference temperature T_R was estimated from differential scanning calorimetry data (Chang, et al. 2006).

Using these parameters, several experiments on the antagonistic actuator were conducted. Changes in the amount of input current (heat delivery) were investigated to correlate theoretical amplitude under partial transformation to experimental data. Actuation frequency was studied to characterize the model's limitations, while duty cycle and wire diameter effects were compared to examine the model's ability to predict output motion profiles.

4.2.2 Model Analysis

The antagonistic model developed in Section 4.1.2 consisted of several additional conditions including convection, slack, boiling, friction and inertia. The overall effect of each condition, however, was unknown, and in some cases their addition introduced more complexity. For example, accounting for the mass of the movable stage creates a second order differential equation that must be solved numerically (increasing solution time). The slack and boiling conditions also introduce binary effects in the model that can add numeric complexity. Thus, studies were conducted to quantify the overall tracking improvement for each of the conditions: convective coefficient, slack/boiling, friction, and inertia. In this section the effects of each condition are studied in comparison to experimental data for a variety of frequencies ranging from 0.3 Hz (quasi-static) to 10 Hz. The tracking accuracy is quantified with respect to four key metrics (illustrated in Figure 4.6): 90% rise time, 90% fall time, amplitude, and cooling offset errors. The rise and fall time metrics account for transient behavior and are most

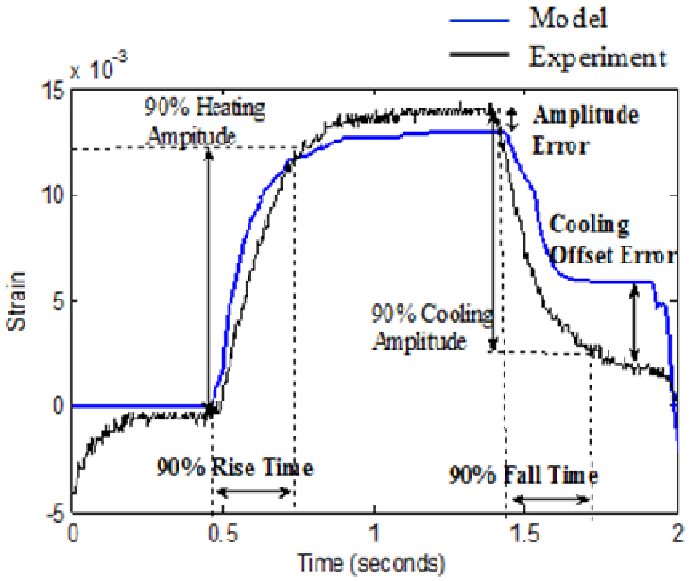

Figure 4.6. Key metrics for analyzing model fit. Rise and fall times measure transient errors, while amplitude and cooling offset measure steady-state errors due to friction, slack conditions, or insufficient heating.

closely affected by the heat transfer coefficient and inertial dynamics. The cooling offset is an error that arises due the antagonistic wire going into compression (producing negative stress). It can also result from unaccounted friction in the experiment.

4.2.2.1 Convective Coefficient

When analyzing the data, it was found that the lumped convective coefficient with fixed but different coefficients on the heating and cooling cycle produced more accurate tracking results than the temperature varying model, *h(T)*. This could be due to boiling effects occurring on the heating cycle, which may cause the lumped convective coefficient to be higher. In Table 4.2, a summary of the resulting lumped convective coefficients is provided in the quasi-static regime (0.3 Hz). Tests were also conducted in the dynamic regime (greater than 0.3 Hz), and it was found that the increasing convective coefficient in the antagonistic model improved the tracking performance on the cooling cycle due to the moving stage disturbing the liquid bath. This motion likely caused local flow near the wires that increased at higher operating frequencies causing the rising trend in the h-value (Table 4.3). Due to the greater accuracy, data from both Table 4.2 and Table 4.3 were utilized in the "full model" for each of the following comparison studies.

The greatest factor affecting the antagonistic model's tracking performance is the convective coefficient, which influences the transient response (heating rise time and

Table 4.2. *h*-values for SMA wire of various diameter for 0.3 Hz. Heating values based on (Pathak, et al. 2008), cooling values were determined from model fit.

Wire Diameter (mil)	**Heating *h*-value** ($kWm^{-1} K^{-1}$)	**Cooling *h*-value** ($kWm^{-1} K^{-1}$)
8	5	2.6
10	4.5	2.3
15	3.5	1
20	3	0.8

Table 4.3. *h*-values for SMA wire of 10 mil diameter for varying frequency. Heating values determined from model fit on experimental tests.

Frequency (Hz)	Cooling *h*-value ($kWm^{-1} K^{-1}$)
0.3	2.3
1	2.6
2	4.8
3	5.2
4	6.2
5	5.8
6	6.2
10	7.8

cooling fall time) by affecting the heating and cooling speeds. Amplitude is also manipulated, as the convective coefficient influences whether partial or full transformation will occur for a given input power. If insufficient cooling is predicted, a cooling offset error will occur especially at higher frequencies. In Figure 4.7 two different models for the convective coefficient are used and compared to experimental tests for frequencies ranging from 0.3-10 Hz.

The first model utilizes the temperature-dependent Kuehn and Goldstein correlation that was selected based on the measurements conducted in Chapter 3. This correlation allows the *h*-value to vary with temperature from 1.8 $KWm^{-1}K^{-1}$ at 23 ºC to 5.8 $KWm^{-1}K^{-1}$ at 99 ºC (the boiling condition occurs at 100 ºC). The second model for *h* allows the convective coefficient to vary between heating and cooling, and was incorporated in the full model due to its greater accuracy. On the heating cycle the convective coefficient was fixed to the upper value of the Kuehn and Goldstein correlation (5.8 $KWm^{-1}K^{-1}$), while on the cooling cycle the value varied according to actuation frequency, which was due to fluid movement induced by the actuating stage.

As shown in Figure 4.7, the full model provides significantly greater tracking accuracies than the temperature dependent, *h(T)*, correlation, especially on the cooling cycle. This is especially apparent at 3 Hz, where the *h(T)* correlation under-predicts the

cooling of the wires, causing both a fall time and cooling offset error of 44% and 370%.

By allowing the convective coefficient to vary with frequency, these errors are reduced to only 12% and 20% (Figure 4.8). The rise-time error is also affected by the

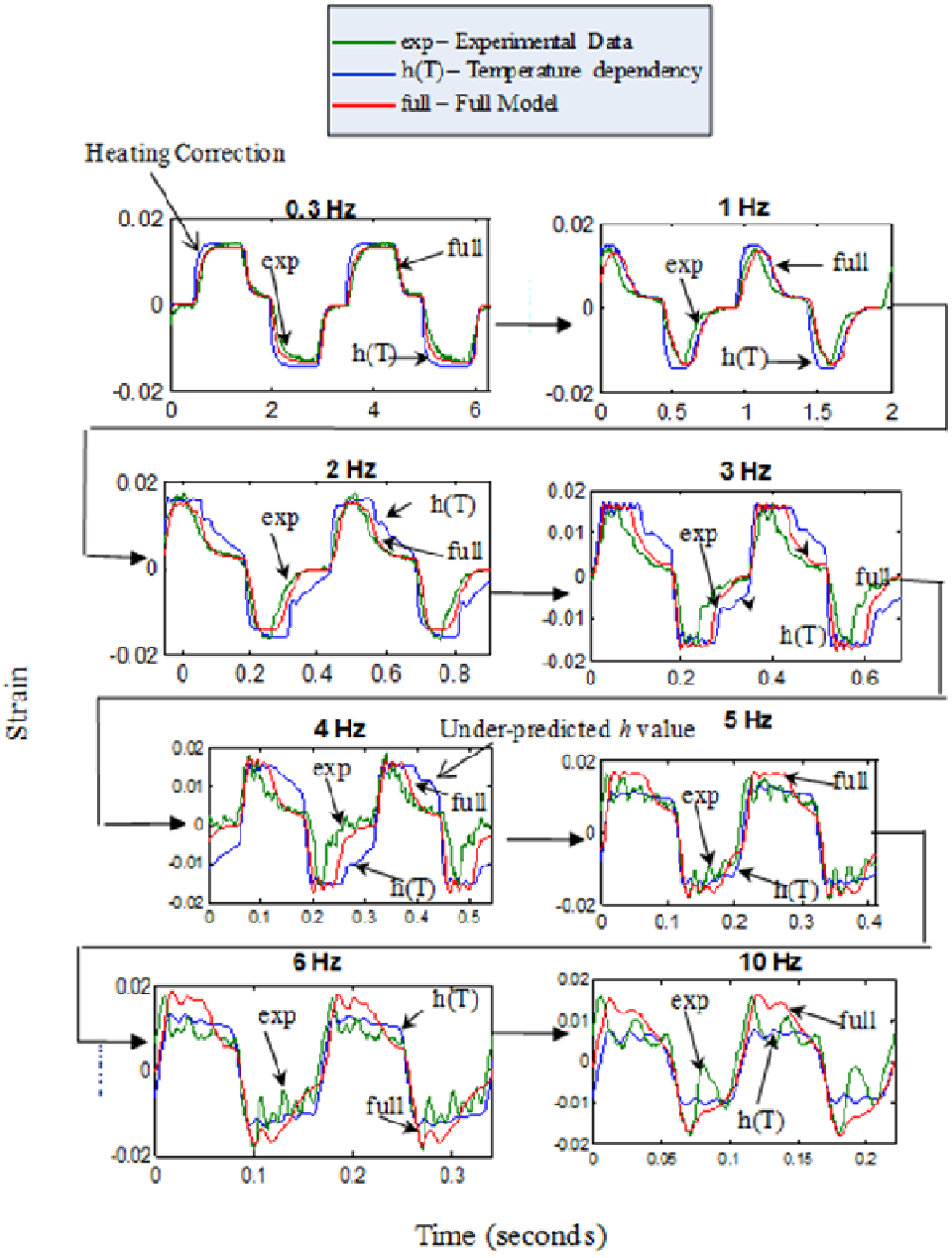

Figure 4.7. Effects of Convective Coefficient in the Antagonistic Model for Various Frequencies. Increasing the convective coefficient to account for fluid disturbance, and having higher *h* values for heating were found to produce accurate tracking over the simpler temperature dependent version, *h(T)*.

selected *h*-value. For example, at 3 Hz an error of 63% occurs with *h*(T) model due to an under-prediction in heating time. By using the full model, this under-prediction is corrected and the rise-time error is reduced to 30%. As shown in Figure 4.8, this reduction is consistent for all frequencies up to 10 Hz (where errors for both models drop to only 3%). In Figure 4.8, the amplitude error is also plotted and is shown, for the h(T) model, to increase as frequency is increased (up to 42% for 10 Hz). This is due to the fact that the wires are being under-cooled in the model at higher frequencies and cannot produce full motion. By allowing the *h*-value to vary with frequency, the full antagonistic model corrects this error, and at 10 Hz it is reduced to only 9%.

4.2.2.2 Slack

To ensure that the SMA wires did not support compressive loads in the model, the slack conditions (Equations 4.12-4.19) were formulated and included in the antagonistic model. In Figure 4.9 and Figure 4.10, the effects of the slack conditions are

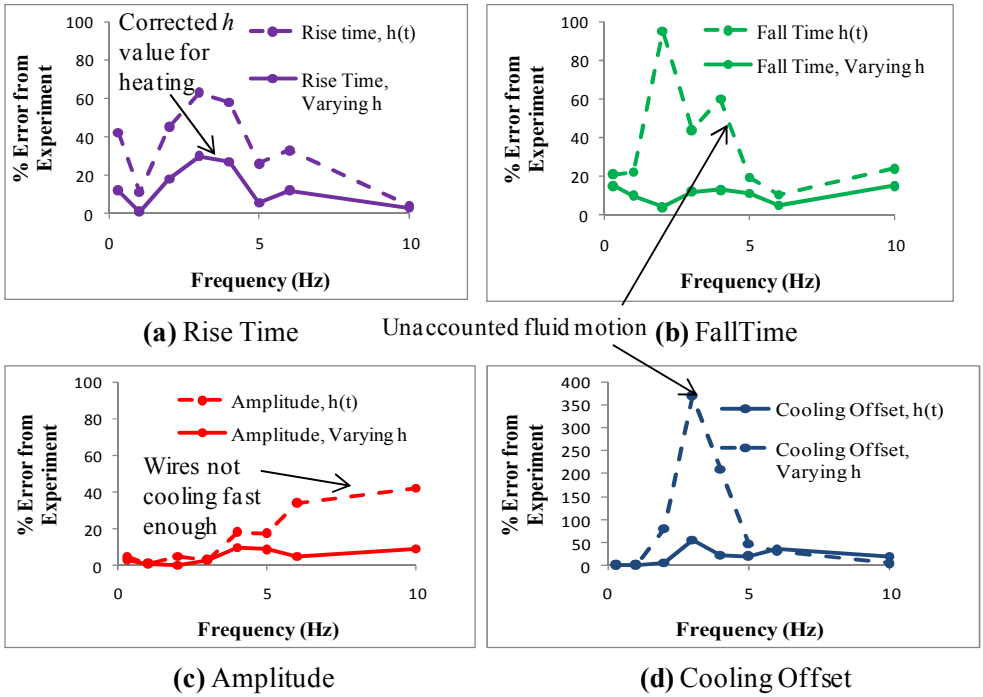

Figure 4.8. Errors Corrected by Varying Convective Coefficient. Transient (rise/fall time), amplitude, and cooling offset errors are all significantly reduced.

studied with respect to the full model's response. Figure 4.9 shows the details of an experimental test at a relatively slow speed (0.33 Hz) for 10 mil wire, where current is alternately supplied to each antagonistic wire at a 33% duty cycle. In this figure, a plot of the input power shows that the power initially begins at a lower value of 13.5 watts but then increases 20% during wire transformation as the resistivity and length of the wire change under the constant heating voltage. When the wire is fully transformed the power is constant at 16.5 watts.

Under these phase transformations, the measured motion profile shows corresponding rises under heating (to 1.3% max strain from neutral). Immediately after the power is stopped, the recorded motion falls back towards the neutral position. In this region where power is removed from the SMA wire, the slack conditions become crucial, since without them the predicted motion profile remains at an offset (e.g. 0.6%

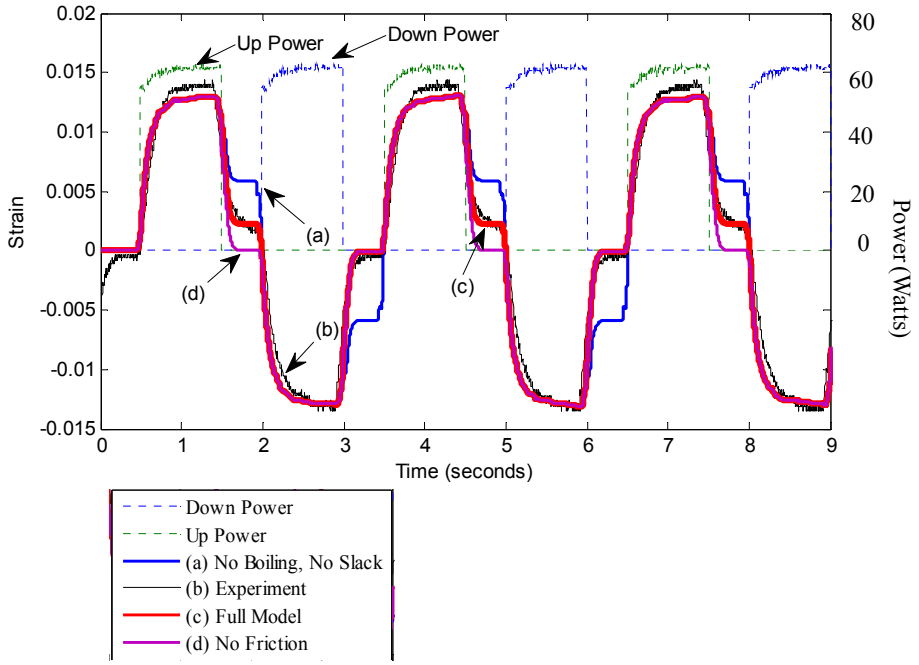

Figure 4.9. Comparison of experimental motion with slack and boiling conditions. Including both of these conditions was deemed necessary as they significantly reduce tracking error.

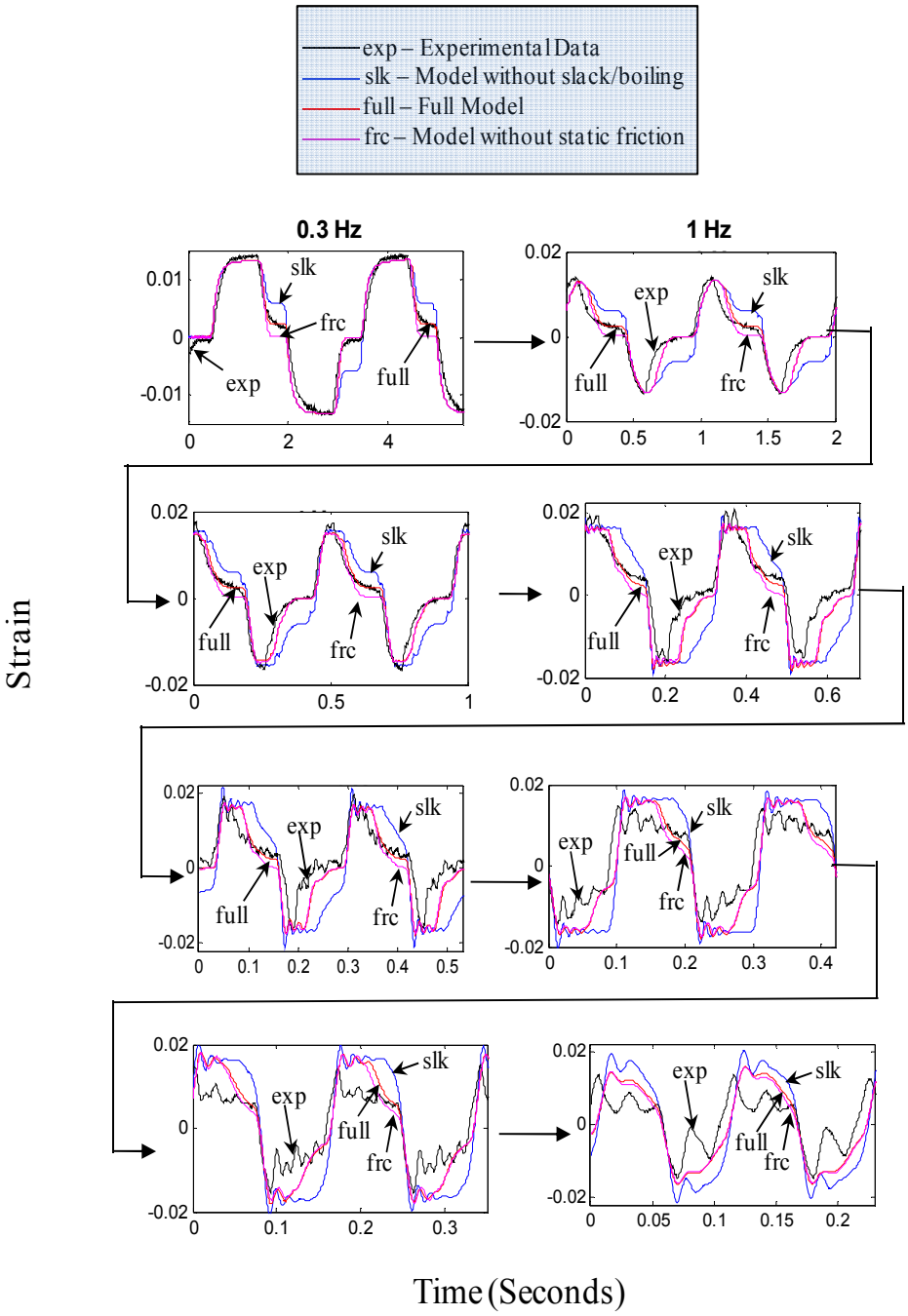

Figure 4.10. Slack, Boiling, and Friction Conditions for Various Frequencies. The full model is compared to instances with slack/boiling and friction conditions neglected. Cooling offset and amplitude errors are corrected the inclusion of all three conditions.

strain in Figure 4.9), and creates a significant cooling offset error (187%).

This error is caused by the simulated antagonistic wire incorrectly going into compression, thus preventing the stage from returning to the neutral position. At higher

frequencies (Figure 4.10) the offset error remains high at 100% for 4-10 Hz (Figure 4.11). However, entering the slack condition in the model solves this problem, significantly reducing the cooling offset error below a bound of 20% for the full tested frequency range (Figure 4.11). While the slack conditions had a significant impact on the cooling offset error, the accuracy in transient performance (i.e. rise and fall times) was not affected.

4.2.2.3 Boiling

In the experimental tests it was observed that the SMA wires could induce local boiling at high levels of input power. To account for this behavior, the antagonistic model was modified, where the wire temperature was kept from exceeding 100 °C through a binary increase in the convective coefficient *h*. In the experimental tests (Figure 4.10), the model configuration without boiling follows the experimental data though there is an amplitude mismatch that arises at frequencies greater than 3 Hz. This mismatch increases at higher frequencies (Figure 4.11), reaching 28% at 10 Hz (compared to 6% for the full model), and occurs from the wires being heated beyond boiling temperatures in simulation and transforming more than in the experiment. At higher frequencies the error is amplified due to the fast, high-power heating cycles that quickly transform the wires by raising the temperature to boiling. However, by correcting the antagonistic model with the boiling conditions, the over-prediction in amplitude is resolved as shown in Figure 4.11.

4.2.2.4 Friction

In the experimental data (Figure 4.10), an additional feature is present that takes the form of an asymmetry between the cooling return cycles. While the downward stroke fully returns to the neutral position, the upward stroke cools to a position that is offset from neutral (see point c in Figure 4.9). This phenomenon is likely due to static friction

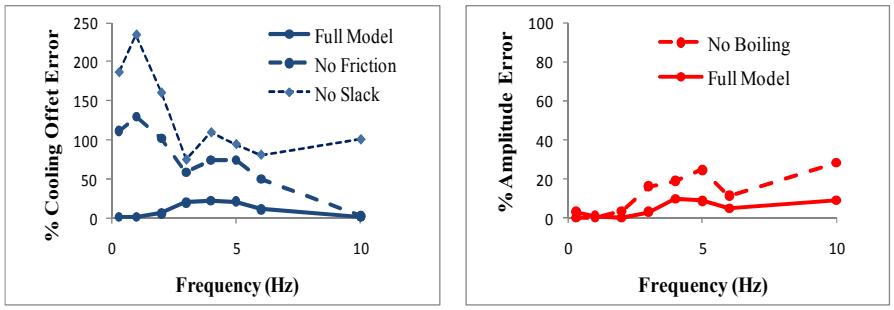

(a) Cooling Offset Error **(b) Amplitude Error**

Figure 4.11. Model Improvements from Slack, Boiling, and Friction Conditions. Significant errors in cooling offset and amplitude are corrected by the inclusion of these conditions. Rise time and fall time are not affected.

present in the experimental rig (e.g. due to localized contaminants in the bearing surface), which the antagonistic model with no modeled friction is unable to predict, creating a 110% error at 0.3 Hz. However, by setting the friction term F_f to 1.8 N for the right wire (Equation 4.13) the offset is eliminated as shown in Figure 4.9. The friction term is most important for lower frequencies where the stage fully returns to the neutral position (Figure 4.10). At higher frequencies, the cooling time is reduced, causing the stage to remain in the upward or downward positions. Thus, the error associated with the friction term reduces from 110% at 0.3 Hz to only 2% at 10 Hz (Figure 4.11).

4.2.2.5 Inertia

At frequencies higher than 3 Hz, effects of the output stage‘s inertia begin to influence overall motion (Figure 4.12). In the experimental trace, these effects are noticeable at the top and bottom strokes where oscillations are present. At 6 Hz and 10 Hz (Figure 4.12), these oscillations are clearly illustrated, where the natural frequency is found to be 70 Hz. Plots of the model with and without inertia are also shown in Figure 4.12, and at the higher frequencies (above 3 Hz) oscillations arise that are absent in the version of the model with no inertial effects. These oscillations have a natural frequency of 67 Hz, which matches closely to the experimental result, deviating by only 4%.

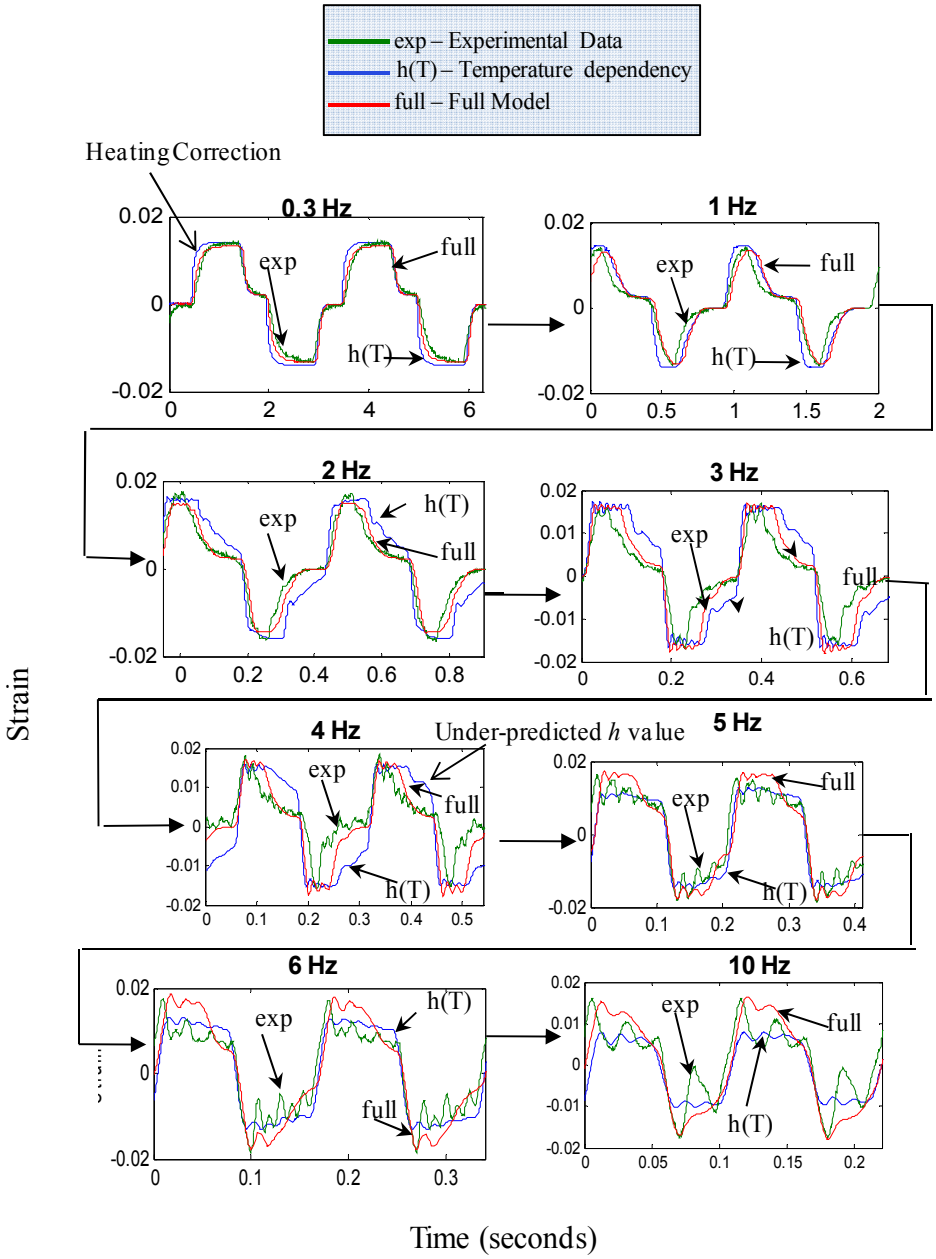

Figure 4.12. Effects of Inertia in the Antagonistic Model for Various Frequencies. After 3 Hz, inertial effects begin to effect rise time, fall time, and output amplitude.

In both the model and experiment, the natural frequency of the oscillation is lower than the square root of the spring stiffness over the mass of the stage, which predicts a natural frequency of 21.5 Hz. This reduction is likely due to the effects of the heated SMA wire, which adds to the system stiffness. In fact, using the value for Young's modulus and wire length in Table 4.1 and knowing the cross sectional area, the stiffness

due to the heated wire can be incorporated, which raises the estimated natural frequency to 52 Hz. This estimate is in the same range (within 25%) of value measured in the model and experiment, indicating that the stiffness of the heated wire is a contributor to the overall system stiffness.

As seen in Figure 4.12, the addition of inertia also changes the predicted transient behavior. For example, at frequencies above 3 Hz the inertia of the stage causes a large initial peak (due to momentum) in the experiment that is matched by the full SMA model and is absent when inertia is neglected. At frequencies above 3 Hz, the under-prediction in amplitude caused by the negligence of inertia causes an error of up to 24% at 4 Hz and remains at 15% at 10 Hz. Including inertia in the model reduces this error to a maximum of 9.7% at 4 Hz, and the source of error shifts from under-prediction to over-prediction (Figure 4.12). In addition to amplitude, the rise and fall times are affected by inertial dynamics, and as shown in Figure 4.13. When neglecting the mass of the stage, the antagonistic model predicts significantly slower rise-times at higher frequencies due to a delay in the peak of the upward and downward stroke. By including the mass of the stage in the model, this error is corrected at higher frequencies, and at 5 Hz, for example, it is reduced from 42%to 6% (Figure 4.13). Due to the corrected peak in output motion, the fall-time error is also corrected at frequencies above 3 Hz, where the greatest reduction in error occurs at 6 Hz from 22% to 5%. While the inclusion of inertial dynamics affects the transients, it does not affect the cooling offset, which is primarily affected by the slack and friction conditions.

4.2.2.6 Summary

Table 4.4 summarizes the contributions that each of the model condition makes in the four key fit metrics. The percent error is averaged over all of the tested frequencies, and Table 4.4 shows that the model for the convective coefficient, h, makes the most

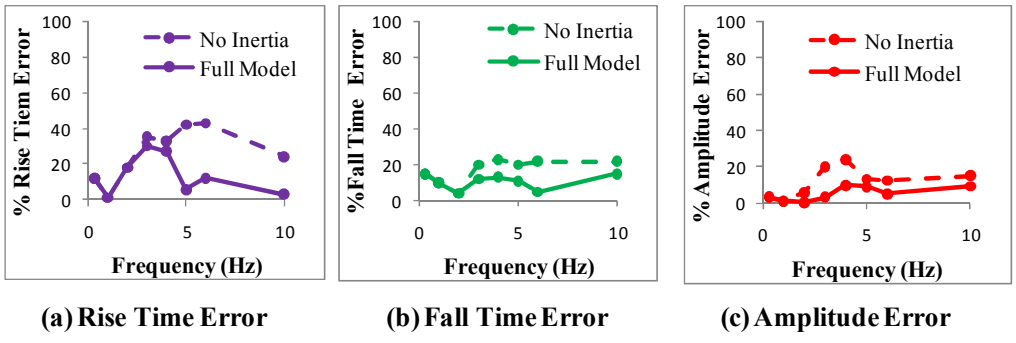

(a) Rise Time Error **(b) Fall Time Error** **(c) Amplitude Error**

Figure 4.13. Rise Time, Fall Time, and Amplitude Error Reduction. Including inertial effects in the model significantly reduce errors at frequencies above 3 Hz.

significant contribution in both the transient (rise/fall time) and steady-state response (amplitude and cooling offset). The addition of inertia also improves the average amplitude error and transient response, but not as greatly (i.e. rise/fall time errors are only improved by 12% and 6.4%). Thus, some tracking accuracy may be sacrificed to improve solution time with a 1st order model, as opposed to the 2nd order differential equation required when including inertia. For the experiments tested, friction was important to include, as it corrected the asymmetric steady-state offset error (by 65% on average). The slack conditions also corrected the cooling offset error in both directions by an average of 120%.

Lastly, at the higher frequencies where the wires were quickly heated under high power the boiling condition was crucial to correct amplitude error. At lower frequencies, the wires were not heated to boiling temperatures and the condition had no effect, which is why the average improvement was relatively low (6%) compared to the other conditions. However, its inclusion is crucial as it simulates the power losses encountered when overheating the SMA wires beyond boiling temperatures.

4.2.3 Varying Experimental Conditions

After building the full model and characterizing the effect of the primary conditions (Table 4.4), further tests were conducted to characterize the full antagonistic model's

Table 4.4. Effect of Each of the Model Conditions. Average improvement in % error over the frequency range of 0.3-10 Hz are computed and listed.

Condition	Rise Time Error (%)	Fall Time Error (%)	Amplitude Error (%)	Cooling Offset Error (%)
Slack	none	none	none	120
Boiling	none	none	9	none
Friction	none	None	none	65
Inertia	12	6.4	7	none
h-value	22	26	11	83

tracking performance under a variety of experimental test conditions. The effects of frequency were studied on the full model to understand the effects of heating and cooling time with respect to motion response and power consumption. Amplitude tracking was tested with a series of partial transformation tests, and output shaping was studied with respect to the applied duty cycle. Finally, wire diameter was varied to characterize the model's capability of predicting the transient and steady-state response dictated by the wire's heating/cooling times and stress generated against the system spring.

4.2.3.1 Frequency Tests

Because many antagonistic actuators are created for relatively high-frequency operation (such as applications in human tremor cancellation), the overall effects of frequency were studied. In the model analysis (Section 4.2.2) the full model is shown to track well over the four key fit metrics (Figure 4.8) with an average error of only 5% in amplitude and 10% in cooling offset. The transients also match well, with an average error of 13% and 11% for the 90% rise and fall times. The overall shape is tracked in the full series of tests (Figure 4.7) where the motion profiles in both experiment and simulation significantly change when the driving frequency is increased. This is primarily due to the decrease in effective cooling time at higher cycle speeds, where for example a doubling in driving frequency would halve the available cooling time for the SMA wires. At a specific point (3 Hz in the case of Figure 4.7) the platform no longer

fully returns to the neutral position since the SMA wires are not being completely cooled. At this frequency the platform only cools to 0.2% strain from neutral (14% of the total motion amplitude), and at higher frequencies (approximately 5 Hz) this effect is further amplified since the wires have even less time to cool and can only relax to 0.7% strain from neutral (50% of total motion). Since the model tracks these effects and is capable of predicting the point where the wires do not fully cool, it can be used to enhance actuator design. For example the model can be used to predict and avoid operation above the upper frequency bound for a given wire diameter and cooling medium (operating above this level may result in the wires pulling against one another, developing potentially damaging stress levels).

While conducting the cyclic tests, power was additionally monitored, and the total energy required for each phase transformation was calculated for each frequency level. Figure 4.14 shows that the energy exponentially decays to a steady-state as the frequency increases, with a time constant of 6.25 seconds. This decay is due to the fact that the wire is heated over a shorter time so less energy is lost to natural convection. At lower frequencies, the wire is heated over a long period so there is a lot more energy loss to the environment. Figure 4.14 also shows that the heating energy approaches a theoretical limit of 3 J, which is the latent heat and specific heat of transformation for the wire (Table 4.1). This is the energy required to heat the wire and transform its phase assuming no losses to the environment. Note that since the actual applied power was fed to the model, the energy results are the same between model and experiment.

4.2.3.2 Partial Transformation Tests

While the frequency tests showed the antagonistic model's correlation and limitations over a variety of conditions, the tests were fixed for full phase transformation. However, in many cases SMA wires operate under partial

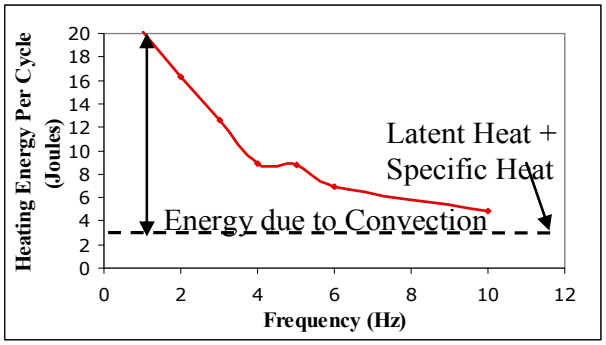

Figure 4.14. Heating energy per cycle with respect to frequency. As frequency increases, heating energy converges to a theoretical asymptote.

transformation. Thus, further experiments were performed to characterize the model's correlation under these varying conditions. In these tests the driving frequency and duty cycle were fixed at 0.33 Hz and 33%, but the input current was varied from 3.5, 3.9, and 4.5 Amps for low, medium, and full transformation levels. The full transformation level was observed by slowly increasing the applied power until no further increase in displacement amplitude was measured.

From the resulting profiles in Figure 4.15, the predicted amplitude of motion matches the experiment at the high current level with of only 4.5% error. At the medium and low input current levels, however, this error is larger (19% and 25%) since the model under-estimates the motion produced. It is possible that this error is caused by inaccuracies in the selected lumped convection model, which may over-estimate the cooling rate at lower temperatures.

The transient tracking performance is illustrated in the low input current level where similar 90% rise times are demonstrated for the experiment and model (difference of only 0.035 seconds, 7% error). At the medium and high current levels, this accuracy diminishes and the rise time errors increase to 33% and 13% seconds (Figure 4.16). This increase is caused by a slowing of the experimental response near boiling temperatures, which may also be under-estimated by the model for the

temperature dependency of *h*.

In the cooling transient response, the antagonistic model follows the experimental motion profile with similar accuracy for the three input amplitudes. The low amplitude, for example, predicts a 90% cooling time of 0.13 seconds, which is 35% from the experimentally measured time of 0.2 seconds. The medium current level has a similar 90% experimental cooling time of 0.21 seconds which the model deviates 30% from at 0.14 seconds. Lastly, the antagonistic model deviates 25% from the experiment at the high current amplitude (0.15 seconds for the experiment vs. 0.12 seconds for the model). From Figure 4.15 it can be seen that the deviation between experiment and theory primarily occurs near the end of the cooling cycle, and there is good correlation for the bulk of the profile. An explanation for this observation is that the lumped model for free convection under cooling may not fully capture the actual convection from the

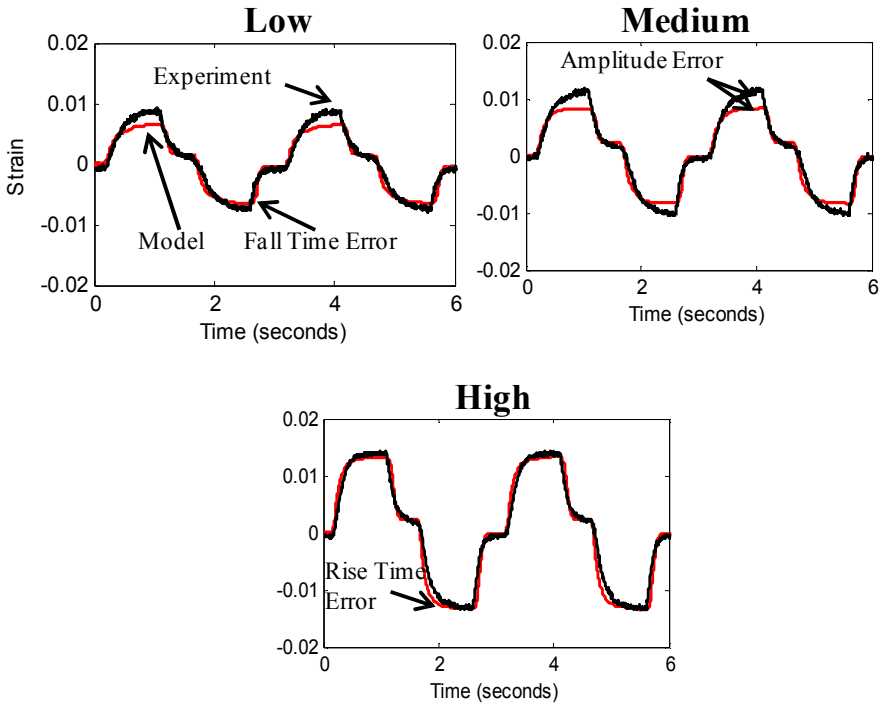

Figure 4.15. Partial transformation tracking at three different power input levels. The antagonistic model was capable of reproducing the unique shapes and amplitudes, with the transient heating and cooling responses being the most accurate at low power.

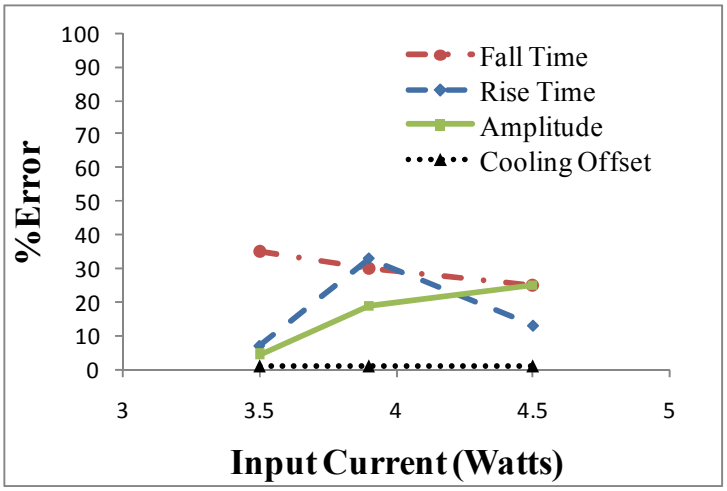

Figure 4.16. Steady State and Transient Errors from Partial transformation tracking at three different power input levels. Amplitude error increases with current while cooling offset and fall time errors decrease.

wire, which may be affected by local effects such as temperature and flow conditions that are difficult to accurately predict.

4.2.3.3 Duty Cycle Tests

While changing the input current level directly affects the output motion amplitude, the overall shape can be adjusted through changes in the heating duty cycle (Figure 4.17). This effect occurs because the duty cycle directly affects the amount of heating and cooling time allotted for each wire, which in turn affects the shape of the output motion profiles that similarly varied in the frequency studies (Figure 4.7). Understanding these changes is particularly useful when adjusting an actuator to produce a certain motion profile (either for actuation or cancellation) in open loop. Thus, to fully characterize the duty cycle effects, tests were conducted for 10-mil wire with the frequency fixed at 1 Hz, where the square wave duty cycle was varied from 15% to 45% in 5% increments.

The resulting profiles measured from these experiments (Figure 4.17) demonstrate the evident change in shape from a low to high duty cycle. At the lower duty cycles (15%-20%) sharp peaks are produced in the experiment and simulation because the

wires are quickly heated and then allowed to fully cool under the spring load, thus allowing the motion platform to return to the neutral position. At higher duty cycles (above 35%), the wires are heated over a longer period of time, and the cooling times are limited. This produces a more smooth motion, and at a 45% duty cycle a nearly sinusoidal output motion is produced.

In Figure 4.18 the error plots show that the experiments match the model's prediction, especially in amplitude where the maximum error is only 11%, occurring at the 35% driving signal. The transients are also captured by the model, for example at a 45% duty cycle the 90% rise time is predicted to be within 0.1 seconds (16%) of the experiment's rise time of 1.15 seconds. At the lower duty cycles, the model performs with similar accuracy, where for example the rise time of the 20% duty cycle response is predicted within 19%. The cooling fall time varies more among the different duty cycles tested. The greatest error occurs on the relaxation from the stroke of the 20% duty cycle experiment (Figure 4.17) where the model under predicts the experiment's

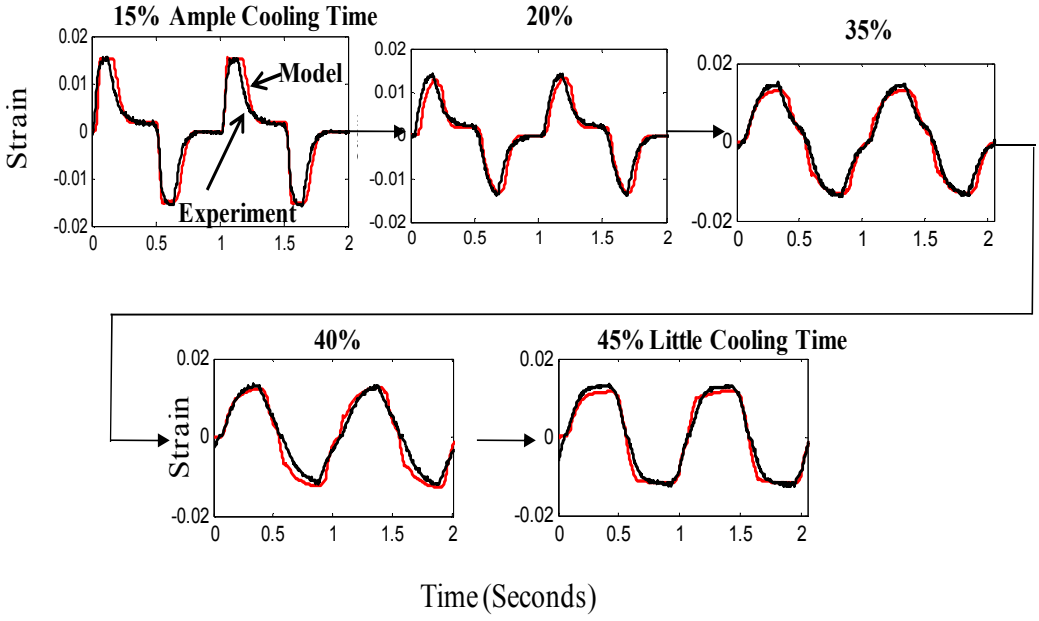

Figure 4.17. Duty cycle effects for both experiment and simulation. Unique shapes reproduced by the model for each trial, with an increasing transient accuracy at higher duty cycles.

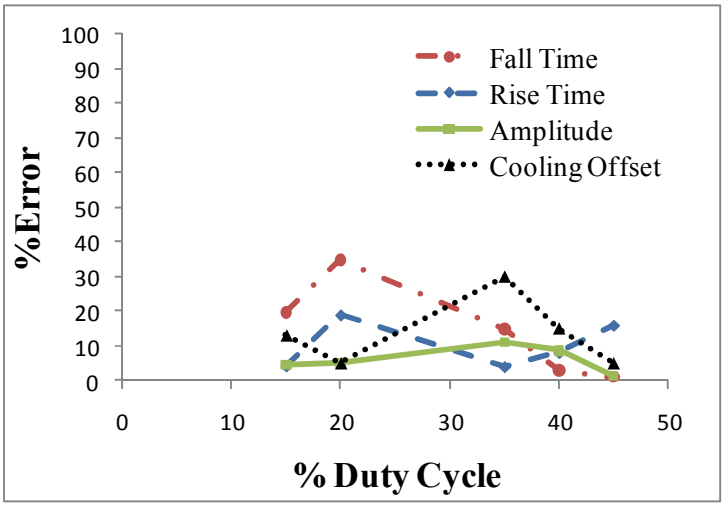

Figure 4.18. Tracking Error for Duty Cycle Variations. Fall time error decreases with increasing duty cycle, while rise time has no clear trend. Cooling offset has a peak at 35% duty cycle.

0.15 second fall time by 35%. The greatest accuracy in model correlation for the cooling time occurs at the highest duty cycle of 45% where the model predicts the 0.1 second fall time within 1%. This greater accuracy is likely due to the fact that, in this case, the opposing wire begins to actuate only 0.1 seconds into the opposing wire's cooling cycle. In this operating mode, the fall time is not only dictated by free-convection, but also by the opposing wire that is being heated.

4.2.3.4 Wire Diameter Tests

The SMA wire diameter is another variable that plays a role in the output produced by a given input power signal. By increasing or decreasing the wire diameter, several physical properties are altered including the surface area to volume ratio, bulk mass, overall resistance, and the amount of stress encountered by the material. In general, increasing the wire diameter produces more actuating force at the expense of slower response, both in heating and cooling, for a given power input. Decreasing the diameter allows for higher cyclic speeds, but limits the output force. To demonstrate the effects of the wire diameter, four commonly available sizes of Flexinol 70 °C were chosen: 8, 10, 15, and 20 mils. Each of these wires was cycled in distilled water at 0.33 Hz.

The results in Figure 4.19 demonstrate the great effect the wire diameter has on the motion profiles. At the lower wire diameters (8 and 10 mil), ample cooling time allows the wires to fully return to the neutral position under the same given spring stiffness after heating. As the wire diameter is increased, this no longer remains the case and for the 15 mil diameter the wire takes more time to cool and falls just short of the neutral position at 0.2% strain before the opposing wire is heated. For the 20 mil wire diameter, the convective heat transfer can no longer fully extract heat from the larger bulk material. As a result, the wires only partially cool and there is not enough force from the system springs to return the motion platform to the neutral position. As a result, the motion platform stops at 0.5% strain from neutral before being forced in the opposite direction.

The model correlates well to the experiment in amplitude of motion, with a less than 5% error in all cases (Figure 4.20). As diameter increases, amplitudes both from the

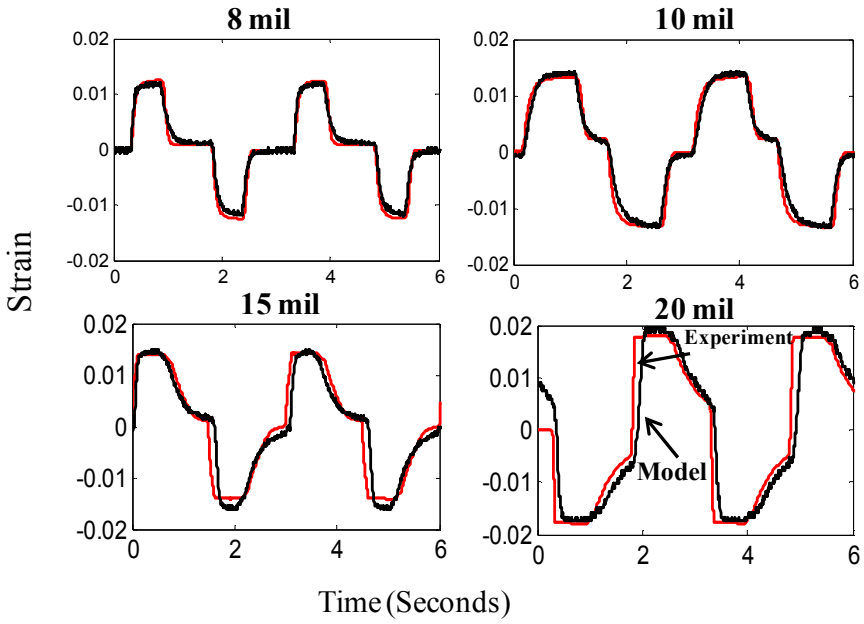

Figure 4.19. Experimental and simulation results for various wire diameters cycled at 0.3 Hz, 20% duty cycle. An overall smoothing effect occurs as the wire diameter is increased, reducing the cooling time but increasing the accuracy of the transient regions estimated by the model.

experiment and model increase (from 0.012 to 0.018 strain) since the thicker wires produce more force against the same spring. The transient tracking error for the larger wire diameters is also reduced except for the rise-time error which increases to a maximum at 40% for 20 mil. This is due to an under-prediction in heating time. However, the model closely matches the 90% cooling time with only an 8% error. At the other extreme in wire diameter, the transient tracking is compromised. For example the 8 mil case shows that the 90% rise time predicted by the model is 36% faster (by 0.1 seconds from the 0.26 experimental rise time), and the fall time error is 32% faster (by 0.06 seconds from the 0.12 seconds fall time). As before, this increase in cooling time error is likely due to a lower than predicted heat transfer coefficient at lower cooling temperatures, which increases the experimental cooling time near the neutral position.

4.3 Design Studies

The experimental studies of frequency, duty cycle, amplitude, and wire diameter showed that the transient thermodynamic model was capable of following a wide range of conditions, replicating the unique output shapes created by the changing driving or

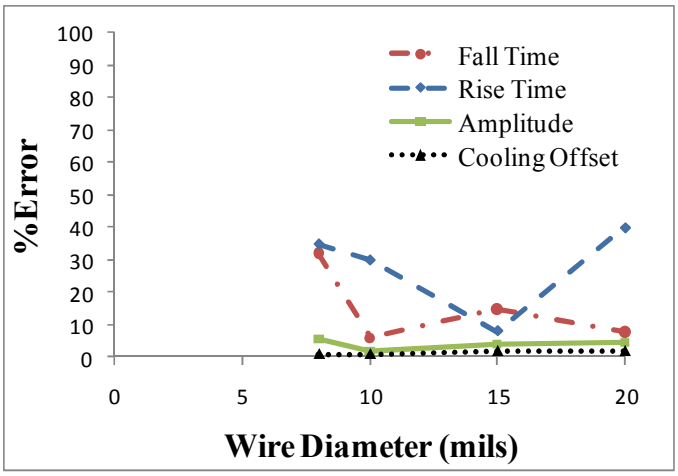

Figure 4.20. Error Tracking for Changing Wire Diameter. The rise time error significantly increases for 20 mil, while the rest of the tracking errors have a general decreasing trend with increasing diameter.

geometric variables. Limitations in the model did occur in some areas of operation such as when the convective model under predicted cooling times and transformation amplitude. Overall, however, the model was capable of matching changing behavior of the output amplitude and transient response, providing a basis for detailed simulation studies.

In this section, studies are performed to gather additional information on the behavior of antagonistic systems through a high number of simulation trials that would have been extremely difficult to accomplish experimentally. To improve simulation time for the high volume of trials, inertia was neglected in the model though all other conditions (described in Section 4.2.3) were retained. The results of the studies are presented to characterize the mechanical advantage, environmental conditions (cooling medium and ambient temperature), heating signal form, and power amplitude needed to provide a desired frequency and amplitude output from the antagonistic actuator. These characterizations provide indispensible design insight that can be used to improve frequency operation and minimize power consumption for antagonistic actuators in hand-held tremor cancellation systems.

4.3.1 Mechanical Advantage

In many situations a tradeoff must be made between force and displacement. For example, certain applications may require large amounts of motion at low levels of force. In these situations, long, thin SMA wires are typically used since thicker wires require significantly more energy to heat. Another possible solution, however, would be to introduce a lever with a low mechanical advantage (defined as the actuator's output force divided by the force from the SMA). This lever would require a large diameter SMA wire operating with a higher force level. In exchange for this force, the output displacement would be amplified thus requiring much smaller wire lengths.

Since the effect of mechanical advantage is not well-understood in the context of frequency and power consumption, simulations were conducted using the antagonistic model with a small modification in the compatibility equation.

The modification for a mechanical advantage is achieved by changing the equation for the spring's force (neglecting mass *m*). Assuming that each antagonistic wire acts through a form of lever before connecting to the common platform, the stress balance (Equation 4.7) is modified to include a lever ratio *r* that when increased decreases the mechanical advantage. Thus, with negligible mass, the new stress balance equation is written as

$$kx_i = Ar(\sigma_r - \sigma_l). \tag{4.25}$$

where x_i is the input displacement to the lever. The output displacement is expressed as

$$x_o = \frac{x_i}{r}. \tag{4.28}$$

Using the modified equations, the antagonistic model was simulated with a spring stiffness *k* of 4 kN/m in a water-cooled environment over frequencies of 1 and 4 Hz. For each tested frequency, the wire diameter was incrementally increased from 6 to 35 mils and the lever ratio *r* was adjusted for each test condition to maximize the output motion while keeping the wire stress below 200 MPa, which was selected as an upper bound from manufacturer's guidelines (Dynalloy 2009) ensuring operation without any material shakedown. At the adjusted lever ratio, the required wire diameter and length to produce 2 mm of motion was recorded along with the power consumption (Figure 4.21, Figure 4.22).

The results of the simulation study indicate that increasing the wire diameter of the actuator (and increasing the lever ratio *r*) reduces the amount of power required for its operation. At 1 Hz, for example, the power consumption drops by as much as 25% when switching from a long, thin wire (6 mils, 1.1 m) to a short thick wire (35 mils,

0.06 m). The reason for this decrease in power consumption is due to the fact that the surface area is reduced when using shorter wires, which reduces the amount of heat lost to the environment during the actuation cycle. An additional benefit of introducing a mechanical advantage is the potential to increase packaging capabilities as the wire length is significantly reduced (Figure 4.22) – for the 1 Hz case by as much as 18 times.

In Figure 4.21, the relationship between wire diameter and power consumption follows different paths depending on the operating frequency, and in general higher frequencies require more power. For example, a 10 mil wire requires only 22 W at 1 Hz, but at 4 Hz increases in power draw by 59% to 35 W. This is due to the fact that the wire is going through phase changes more frequently at higher cycle rates. Figure 4.21 also shows the limitations in wire diameter due to frequency in the form of the stress limit (dashed line), which is inversely proportional to frequency. It is at this stress limit where the SMA wire diameters are too large for the operating frequency and cannot sufficiently cool, developing internal stresses beyond the 200 MPa limit. It is important to realize that this stress limit signifies the optimal actuation curve, since it intersects

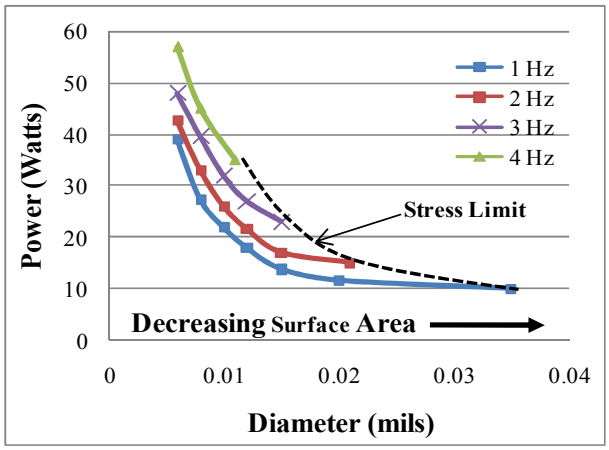

Figure 4.21. Diameter Effects on Power Through Mechanical Advantage. Decreasing the mechanical advantage increases the required wire diameter reducing power losses.

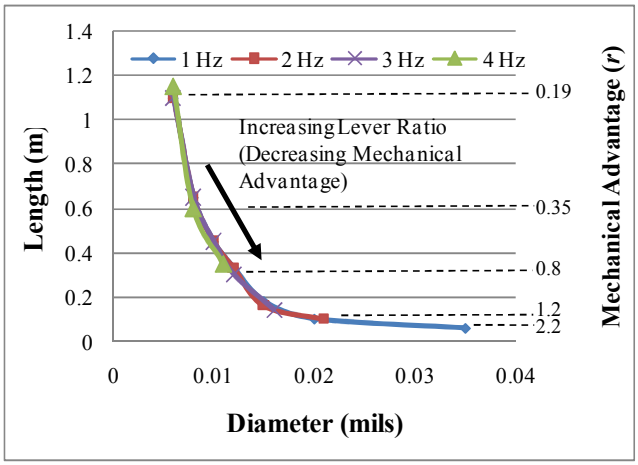

Figure 4.22. Wire Length and Mechanical Advantage Needed for Increasing Diameter. Increasing the wire diameter decreases the required mechanical advantage and also decreases the necessary wire length.

with the maximum wire diameter (and lowest power draw) for each operating frequency.

4.3.2 Environmental Effects

In Chapter 3, studies were detailed to accurately quantify the convective heat transfer coefficient from SMA for a variety of wire diameters and cooling media. This was accomplished to provide the necessary data to understand of the cooling of SMA, which affects both frequency and power consumption. To understand this tradeoff, it is necessary to use the measured data in a predictive model. Thus, this section focuses on coupling the derived thermodynamic model for the antagonistic SMA actuator to the measured cooling data to provide insight into the complex interaction between frequency and power consumption. Simulations are performed for a variety of cooling media and ambient temperatures (which increase SMA cooling with decreasing values). The SMA wire diameter is another variable that is studied to characterize the geometric effect of the wire's surface area to volume ratio.

4.3.2.1 Convective Coefficient

For operating frequencies of 1-16 Hz, the antagonistic model was used to calculate the required convective coefficient for various wire diameters (6-20 mils). For these studies the ambient temperature was set to 23 °C (room temperature) and spring stiffness k set to a value of 40 N/m. For each test condition, a bisection method algorithm was used to search for the convective coefficient allowing stable operation at full motion. As with the mechanical advantage studies, this stable operation was defined for operating stress below 200 MPa.

The simulation results for the convective coefficients (Figure 4.23a) show a mapping of cooling medium with respect to frequency for different wire diameters. This plot is valuable for design work, as it serves as a guide for the type of cooling environment necessary to produce a given frequency at a selected wire diameter. As expected, increasing the actuation frequency greatly affects the necessary convective coefficient, ranging by roughly an order of magnitude over the 1-16 Hz range. For example, 6 mil SMA wire operating at 1 Hz requires 440 W/m^2K (air cooling), while at 16 Hz the requirement increases to 8057 W/m^2K (water cooling). Figure 4.23a also demonstrates the effect of wire diameter on cooling speed. For a given cooling medium, for example thermal grease at 2000 W/m^2K, a 6 mil diameter wire can operate at 4.5 Hz, while a 20 mil wire can only produce 1.4 Hz, which is a 69% decrease. Thus, if a reduction in wire diameter is possible, it can benefit an application by producing significantly higher frequency capabilities.

While changing the passively cooled environment can significantly affect actuation frequency, care must be taken to understand the resulting increase in power draw. Figure 4.23b shows the simulated results, where power consumption (normalized with wire length) increases with increasing frequency. This occurs because convection is increased to improve cooling which also has the negative effect of dissipating energy

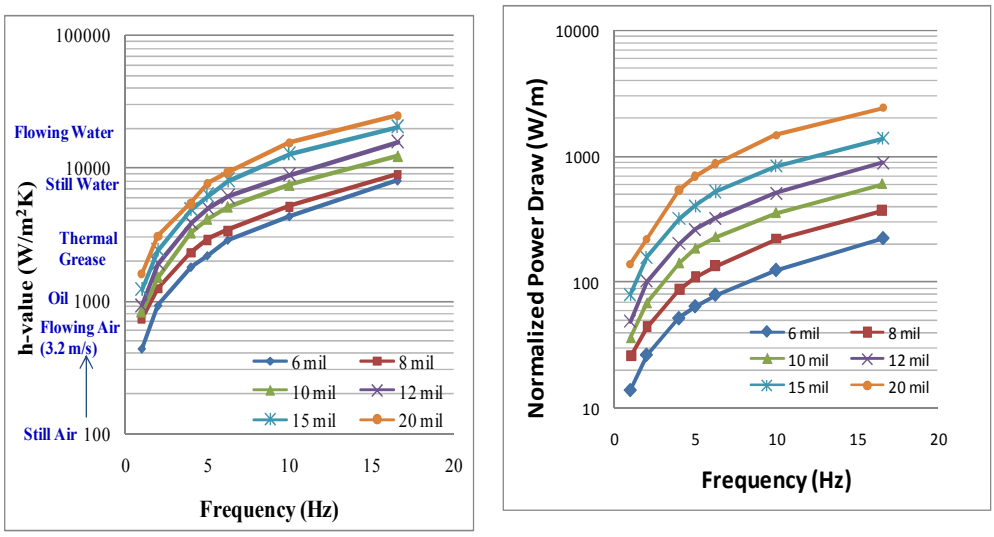

(a) Required Convective Coefficient **(b) Normalized Power Requirements**

Figure 4.23. Convective Coefficient and Power Requirements for Increasing Frequencies. Increasing cyclic speed of SMA actuator increases h-value and power consumption requirements over several orders of magnitude.

during heating, reducing actuator efficiency. In addition, at higher frequencies the material is undergoing more phase transformations per second, further increasing power consumption. The total increase in power use is significant, ranging over an order of magnitude from 1-16 Hz for all wire diameters simulated. The 6 mil wire, for example increases 16 times from 13.75 W/m at 1 Hz to 221 W/m at 16 Hz. Larger wire diameters draw even more power since more material must be heated. The 20 mil wire, for example, requires nearly 11 times more power than the 6 mil wire for all simulated frequencies. This is primarily due to the increase in volume (by a factor of 11 due to the diameter increase), which requires a corresponding increase in latent heat.

4.3.2.2 Ambient Temperature

Another key variable that drives the convective heat transfer from SMA, and thus frequency capability, is the ambient temperature. In many situations the actuator must perform under changing temperature conditions, or a self-contained actuator may exhibit self-heating where the waste heat from the SMA raises the temperature of its

cooling environment. To understand this issue, the effects of ambient temperature were characterized using model simulations that were performed as with the convection studies under the same conditions but with the cooling medium held constant (still water, using Equation 4.21). Wire diameter was varied between 6 and 20 mils, and the necessary ambient temperature to produce full motion without exceeding 200 MPa was solved using the bisection method for a given operating frequency. For each data point, the driving power was recorded and normalized with wire length.

The results of the study (Figure 4.24) show a linear relationship between ambient temperature and operating frequency, with a changing slope for different wire diameters. For example, increasing the operating frequency for the smallest wire diameter decreases the required ambient temperature at a rate of approximately 2°C/Hz. The largest wire diameter of 20 mil, on the other hand, decreases at a rate of 12.5 °C/Hz indicating a lower temperature sensitivity (84% difference). This effect is crucial to recognize when designing small-diameter actuators in environments of changing ambient temperature, since the self-heating effect is amplified for smaller

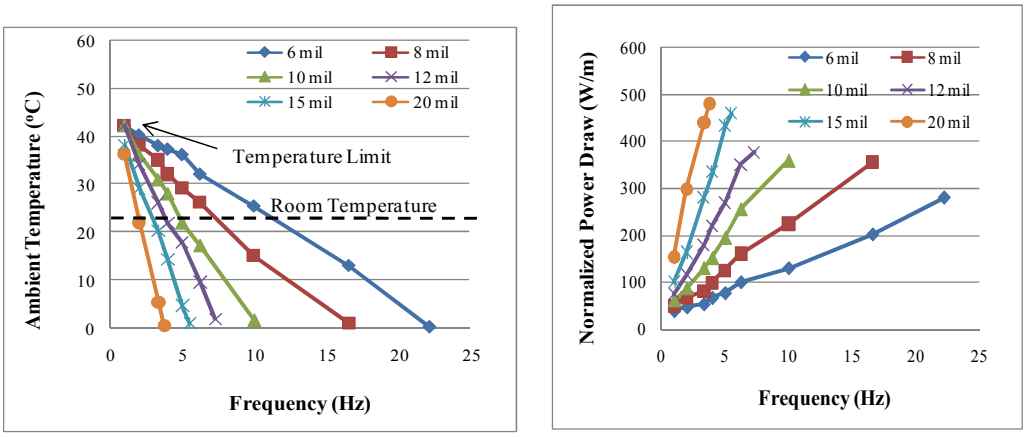

(a) Ambient Temperature Effects **(b) Power Draw**

Figure 4.24. Ambient Temperature and Power Requirements for Increasing Frequencies. Higher frequencies can be achieved by decreasing the ambient temperature, though this increases power draw.

geometries. Another important feature to recognize in Figure 4.24a is the temperature limit that all lines approach at the y-intersection. This limit of approximately 44 °C equals the Martensite finish temperature for the simulated SMA wire. If the ambient temperature reaches or exceeds this value the actuator wires will never fully cool and the antagonistic actuator would begin to generate potentially damaging stress levels.

As with increasing convective properties, decreasing the ambient temperature also increases the power consumption. Figure 4.24b shows this effect for the various wire diameters, and linear relationship is also present with power draw increasing with respect to frequency for all simulated wire diameters. Because a greater amount of material must be heated, and a lower ambient temperature is required for the same frequency levels, larger diameters require more power (e.g. 20 mil requires 3.8 times more power at 1 Hz than 6 mil). Additionally, increasing the operating frequency for larger wire diameter wires increases the power requirements at a greater rate than thinner wires. For example, a 20 mil wire has a normalized power draw that increases linearly at a rate of 119 W/(Hz m) while the rate for a 6 mile wire is 11 times less at 10.8 W/(Hz m). This difference is mainly due to change in volumetric ratio (increasing the latent heat of transformation). This causes significant energy losses during the heating cycle, and thus increases the power draw at a greater rate.

4.3.3 Duty Cycle

Another property affecting actuation performance is the actual signal used to electro-resistively heat the SMA wire. In many applications the simplest and most practical heating signal is a square wave, which as demonstrated in section 3.5, is capable of producing unique output motion waveforms depending on the duty cycle used. Because a smaller duty cycle allows more time for cooling, it was hypothesized that this would also affect frequency response and power consumption. To study these

effects in detail, the model was run for a variety of scenarios in simulation. The degree of motion loss for driving frequencies over the range of 1-14 Hz was investigated for duty cycles of 5-40 % with a fixed wire diameter of 15 mil and spring stiffness k of 40 N/m under water cooling (at 23 °C). To illustrate the overall benefits of using antagonistic wires, these results were compared to a single wire operating against a reset spring. Because removing a wire from the system is the same as treating it as consistently slack, the slack compatibility equations (Equations 4.12-4.15) were used to simulate a single wire using the antagonistic simulation code. Power consumption for the actuator was also tested under varying duty cycles for frequencies of 0.5 to 3 Hz. Using a bisection method algorithm, the power draw required to produce full motion was solved and recorded for each data point.

When increasing the driving frequency in a given medium, the wires reach a point where they cannot be fully cooled and begin to actuate against one another resulting in a degradation in output motion. Figure 4.25 shows this effect where for a 20% duty cycle, motion loss begins to occur after 3 Hz, and by 6.7 Hz approximately 50% of the full motion is lost. While this effect can be exploited (accepting motion loss to improve driving frequencies) care must be taken to ensure that the operating stresses are below the material's shakedown limit. While this limit is often pre-set by the manufacturer, it can be raised to higher levels through additional processing (Sun, et al. 2008). In Figure 4.25 decreasing the duty cycle of the driving signal has the overall effect of shifting the motion loss curve to the right, where for a 5% duty cycle a 50% motion loss occurs at 7 Hz (a 4% increase over the result for the 20% duty cycle). Increasing the duty cycle has the opposite effect, shifting the curve to the left and decreasing frequency capabilities. For example at a 40% duty cycle a 50% reduction in motion occurs at 5.6 Hz, which is a 16% decrease from the motion produced for the 20% duty cycle. In Figure 4.25a, a

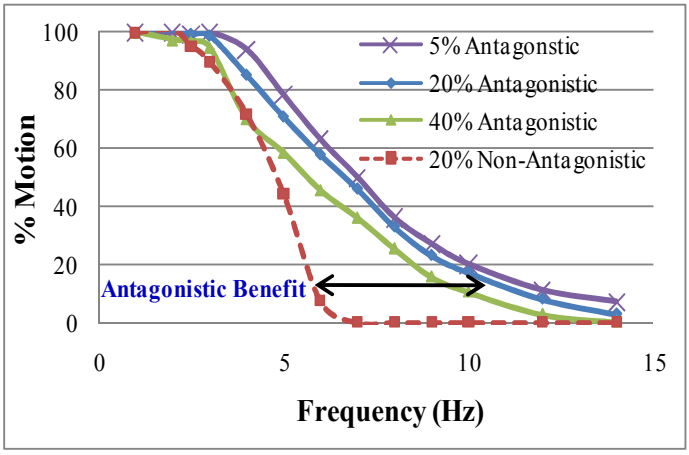

Figure 4.25. Effects of duty cycle on output motion. Decreasing the duty cycle increases the achievable frequencies. Antagonistic wires offer frequency significant benefit over single wires.

fourth curve is plotted for a single wire driven by a 20% duty cycle that demonstrates the benefit of using an antagonistic actuator. This curve drops in output motion earlier than the antagonistic system driven at the same duty cycle. For example, a 50% motion loss for the single wire occurs at 4.8 Hz, which is a 28% decrease from the 6.7 Hz achievable by the antagonistic system. The reason for this effect lies in the fact that the antagonistic actuator can force a reciprocal motion before the opposing wire fully cools.

In addition to affecting the output motion, an increase in duty cycle for the antagonistic system significantly affects the overall power draw. At a slow operating frequency of 0.5 Hz, this effect is the most pronounced as the normalized power consumption (Figure 4.26) increases in a nearly linear fashion from 52 to 216 W/m when the duty cycle is increased from 5 to 45%. This increase occurs because the SMA wire spends more time being heated at larger duty cycles thus increasing convective heat losses. In fact, at the highest duty cycle of 45%, the normalized power draw (216 W/m) is 95% of the value for a single wire electrically heated under steady-state at the transformation temperature of 70 °C (228 W/m), where all heat losses are through

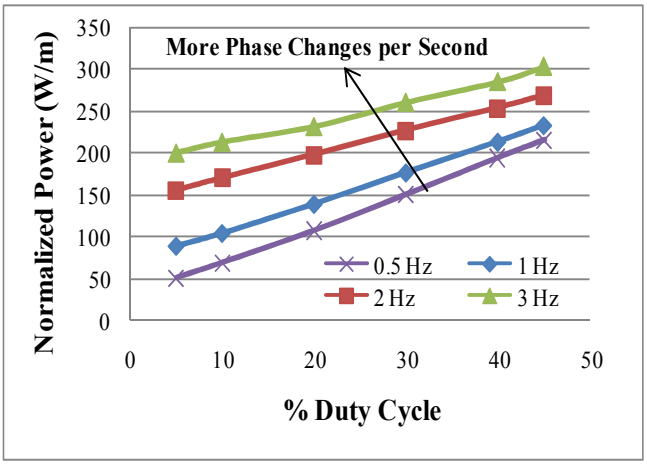

Figure 4.26 Effects of duty cycle power draw. Decreasing the duty cycle lowers heat losses and thus reduces power consumption.

convection. At higher frequencies the normalized power draw increases beyond this level, by as much as 25% at 3 Hz, which is caused by the higher number of phase transformations per second that the material must undergo. However, at these higher frequencies the rate of increase in normalized power draw for increasing duty cycles decreases. For example at 0.5 Hz, the normalized power consumption increases with a slope of 4.1 W/m per % duty cycle while at 3 Hz the slope is reduced by 37% to 2.6 W/m per % duty cycle. This difference is directly related to the wire temperature, where at slow frequencies the wire spends more time fully heated (thus experiencing greater convective losses) than wires driven at faster frequencies.

Overall, these results demonstrate an important tradeoff when increasing the antagonistic actuator's duty cycle. While smooth motion is achieved (Figure 4.17) the simulation results in Figure 4.25 demonstrate that motion degradation can occur and that power consumption can significantly increase, especially for slow driving frequencies. However, with proper care, these effects can be mitigated and even exploited as demonstrated in Figure 4.25 where significantly higher frequency operation is achievable under partial transformation.

4.3.4 Summary and Design Implications

In the design study, each variable for the antagonistic actuator was studied in the context of output speed, amplitude, and power consumption. While these variables were studied over a wide range, Table 4.5 shows a summary of their key effects when varied around a mid-operating point of 12 mil diameter actuating at 3 Hz in a water cooled environment. In this section, each design variable is summarized in further detail, and the tradeoffs and interactions on the general system (in terms of impact on frequency, amplitude, and power consumption) are discussed. While some effects such as mechanical advantage and convective coefficient are non-linear near the extremes of operation, the results in Table 4.5 linearizes their effects at the mid-operating point to provide a general understanding of their interactions on the system for the majority of expected operating conditions.

The results in Table 4.5 show that the heat transfer coefficient h and the ambient temperature T_a, have competing yet approximately equal impacts on the frequency and power draw of the actuator. For instance, increasing h by 10% improves the actuator's frequency by approximately 8%, though as discussed in Section 4.3.2.1 its increases raises the power draw (in this case by 5%) due to an increase in convective losses during heating. Similar effects can be produced by decreasing the ambient temperature. Since the convective coefficient can change by orders of magnitude depending on the medium used, significant impacts on frequency and power draw can be made that are unachievable by varying the ambient temperature, which changes in value over a much more narrow range. However, to produce small changes in frequency or power draw, the ambient temperature can be adjusted instead of changing cooling media.

The duty cycle D_c affects all three performance metrics, though its overall influence is comparatively weak. For example, a 10% increase in duty cycle reduces the

Table 4.5. Summary of Parameter Effects on Actuator Design. Each variable was perturbed 10% for an antagonistic actuator operating with 12 mil wire between 3 and 4 Hz.

Input Variable			Output Result (% Change)		
Symbol	**Name**	**%Variation**	**Frequency**	**Amplitude**	**Power Draw**
h	Convective Coefficient	+10	+8	no effect	+5
T_a	Ambient Temperature	+10	-9	no effect	-5
D_c	Duty Cycle	+10	-2	-1.4	+2
d	Diameter	+10	-8	no effect	+10
l	Length	+10	no effect	+10	+10
r	Mechanical Advantage	+10 (Implies d +4, l -5)	-4	no effect	-5

frequency capability by 2% due to a shorter cooling time, and increases the power draw by 2% due to greater convective losses during the heating cycle. Amplitude also decreases by 1.4% under partial transformation, due to cooling limitations. Increasing the wire diameter *d,* however, creates a strong relationship on frequency and power draw. Increasing *d* by 10%, for example to increase the amount of output force, produces an 8% decrease in frequency due to slower cooling, and a 10% increase in power draw caused by the greater volume of material that must be heated.

While the decrease in frequency can be offset by a 10% increase in *h* or 10% decrease in T_a (Table 4.5), the power draw would be further increased by 5% in each case. Table 4.5 further shows that the wire length *l* has the greatest impact on the actuation amplitude, assuming that the antagonistic actuator operates at a constant strain. Thus, increasing the length by a given amount increases the output amplitude by the same (in the case of Table 4.5 10%). This increase in amplitude, however, comes with the cost of a corresponding increase in power consumption due to the greater amount of surface area and material volume. As studied in Section 4.3.1, the SMA length and diameter can be interrelated through the use of leverage in the actuator. For a 12 mil wire, increasing the mechanical advantage *r* by 10% increases the required wire diameter by 6% and decreases the length by 5%. This has the overall benefit of

decreasing the power draw by 5%, though reduces the operating frequency by 4%. Again, this frequency reduction can be corrected by increasing h or decreasing T_a, though this will come with a penalty of increased power expenditure.

Overall, the results of the design studies have produced useful information on the effects of the key parameters involved in creating antagonistic SMA actuators. Most of the design variables were found to affect frequency and power consumption, and can be adjusted to compensate for penalties introduced by certain design requirements. Changes in operating conditions can also be compensated for – for example, if the ambient temperature were anticipated to increase under self-heating, the penalty in frequency can be estimated and compensated for by increasing the convective properties of the coolant or reducing the wire diameter. Through this improved understanding, engineers can anticipate the gross performance of various actuators without conducting detailed calculations and thus produce tuned actuators capable of meeting performance requirements with relative ease.

4.4 Conclusions

Through a thermodynamic approach, a transient model for an antagonistic SMA actuator has been developed, bringing forward a physical understanding that can be used to improve the predictability and design insight of actuation systems needed in hand-held tremor cancellation systems. To accurately model the behavior of SMA, conditions were formulated to account for inertia, friction, slack wires, boiling of the coolant, and local convection. The inclusion of these conditions was demonstrated to be essential, as a comparison study showed a reduction in tracking error over the transient (rise and fall times) and steady-state (amplitude and cooling offset) regions for a range of frequencies of 0.3 to 10 Hz. The introduction of slack conditions in the model, for example, reduced the cooling amplitude offset error by an average of 120%, and the

addition of friction in the model reduced the cooling offset error by 65%. Modifications in the assumed convective heat transfer coefficient improved average rise and fall time errors by 22% and 26%, and improvements in the cooling offset error were made at higher frequencies (resulting in an average improvement of 83%). Further experimental validation of the antagonistic model was accomplished using input frequencies ranging from 0-10 Hz, duty cycles from 10-45% and wire diameters from 8-20 mil. Overall, very good agreement was demonstrated for frequencies below 5 Hz where inertial effects of the test apparatus were low. At these frequencies, amplitude prediction matched within 8% with better results in those cases where full transformation occurred. Error existed in the transient prediction for many cases, but for those cases exhibiting partial transformation, slow heating, and reduced cooling time (i.e. cases where the wire was not simply heated or cooled suddenly) the transient prediction were more accurate. This was the case for increasing duty cycle, where the 45% duty cycle case matched with the greatest accuracy in heating and cooling times (producing only 1% errors). Additionally, increasing the wire diameter allowed for greater accuracies due to gradual transitions, and at 20-mil diameters only 2% and 8% transient errors were observed during heating and cooling.

To provide design insight on the various tradeoffs present in antagonistic actuators, the validated model was utilized to simulate a number of design configurations. These studies focused on the key design choices (e.g. mechanical advantage, cooling medium, ambient temperature, duty cycle, power draw and wire diameter) necessary to produce motion at a desired amplitude and frequency. By varying the mechanical advantage, studies showed that the most compact antagonistic systems employing the shortest, largest diameter wire allowable for a given operating frequency consume the least amount of power. This is due to the smaller amount of surface area exposed by the

shorter wires, which lowers the amount of heat losses due to convection. Further investigations regarding the effects of convective heat transfer were accomplished through a study that mapped the required cooling media for various operating frequencies and wire diameters. Normalized power consumption was calculated for these mappings, and it was found that power draw can significantly increase when increasing actuation speed (6 mil wire increased 16 times from 1 Hz to 16 Hz) showing that proper care must be taken to consider power when specifying frequency. The ambient temperature was also studied and it was found that a linear relationship between required temperature and frequency existed. The slope of this relationship was found to be dependent on wire diameter (84% difference between 6 and 20 mil) showing that small-diameter wires are much more sensitive to changing ambient temperature. Power consumption also increased for increasing speed/decreasing ambient temperature, and increased in a linear fashion with respect to frequency for all wire diameters. A final study investigated the effect of duty cycle, which was found to produce less motion degradation for decreasing values, due the longer cooling times. In these studies, a single wire actuator was compared to the antagonistic system, and it was found that at 20% duty cycle the single wire began to degrade in motion at lower frequencies. In fact, a 50% motion loss for the single wire occurred at 4.8 Hz, which is a 28% lower than the 6.7 Hz achievable by the antagonistic system. This was due to the fact that the antagonistic actuator was able to force a reciprocal motion before the opposing wire fully cooled.

Using the model, a series of design studies were conducted to produce useful information on the effects of the key parameters involved in creating antagonistic SMA actuators. Most variables were found to affect frequency and power consumption, and can be adjusted to compensate for penalties introduced by certain design requirements.

Changes in operating conditions can also be compensated. For example, if the ambient temperature were anticipated to increase under self-heating, the penalty in frequency can be estimated and compensated for by increasing the convective properties of the coolant or reducing the wire diameter. Through this improved understanding, engineers can anticipate the gross performance of various actuators without conducting detailed calculations and thus produce tuned actuators capable of meeting performance requirements with relative ease.

The experimental validation and design studies demonstrate the antagonistic model's significant utility in predicting output performance for a variety of potential actuator configurations. The positive experimental correlations indicate that the model can be used as the basis for tuning or designing motion control systems for antagonistic SMA wires, capable of providing tremor cancellation at a minimal power draw. These capabilities are instrumental in enabling a new class of tremor cancellation devices, a fact that is demonstrated in Chapter 5, in the context of a medical case-study. In this study the antagonistic model is adopted and used in a parameter analysis to guide the optimal selection of key design variables (diameter, length, mechanical advantage, cooling medium, and controller gain) in a closed-loop tremor cancellation system. To demonstrate technological feasibility a prototype of this stabilization system was fabricated, and its cancellation performance is detailed showing significant promise for commercial use.

Chapter 5: Dynamic Case-Study: The Active Cancellation of Tremor (ACT) System

By developing a model and experimental based understanding of antagonistic SMA, this dissertation develops a technological basis that is capable of solving current actuation limitations to enable a new class of hand-held tremor cancellation devices. As demonstration, this chapter develops a proof-of-concept case-study that has potential of aiding individuals suffering from Essential Tremor. As discussed in Chapter 1, this is a pervasive condition affecting over 10 million people in the US alone. The Active Cancellation of Tremor (ACT) concept provides assistance through a compact SMA motion generating platform that acts as an interface between the user's hand and an object requiring stabilization. To enable the ACT system's functionality, specific focus is placed on the antagonistic SMA actuator, which through application of this dissertation's work, is designed for predictable and controllable operation over a specified frequency range with minimal power draw. These design goals are achieved by applying the thermodynamic antagonistic SMA model developed in Chapter 4 to a detailed parametric study. This study investigates the ACT system's design tradeoffs and constraints with respect to power consumption for varying SMA wire diameter, length, wire angle, controller gain, and coolant type. Measurements from the cooling research conducted in Chapter 3 are utilized in the parameter study and are key to the model's accurate prediction of frequency and power draw. The results of the parameter study are used to aid the design of a proof-of-concept prototype of the ACT system that

avoids material shakedown (Chapter 2) through predictive design to produce stable output amplitude. The prototype is tested under closed-loop control for a variety of disturbance signals, showing significant tremor cancellation. The functionality of the ACT prototype serves not only to validate its purpose as an assistive device, but also to demonstrate the general class of hand-held active cancellation that is capacitated by this dissertation.

5.1 Handheld Tremor Cancellation Device

As discussed in Chapter 1, the fundamental challenge to the successful implementation of a hand-held tremor cancellation system is the actuator since the entire device must be compact and lightweight, yet still meet the motion requirements (at least 1 mm peak to peak, Slack and Ma 2007, at 1-5 Hz, Findley 1995, Fox and Randall 1970). The device must also be capable of meeting the 50% RMS requirement described in Chapter 1 to significantly improve the quality of life for individuals suffering from tremor. The SMA actuator must therefore be carefully designed to provide this necessary frequency and amplitude while consuming a minimal amount of power. In this section, this is made possible through a modeling framework that is developed by applying the antagonistic model to the ACT system's unique kinematics. In section 5.2, this system model is instrumental in studying the cancellation system's design space, which is used to minimize overall power consumption while allowing for stable cancellation performance under closed-loop control.

5.1.1 ACT System Architecture and Operation

The entire ACT system (Figure 5.1) can be separated into four major components: the base, attachment, motion-generating platform, power-supply, and controller/sensor. The user attaches the desired implement they wish to use (e.g. spoon, make-up applicator, etc.) into the attachment by pushing it into a compliant gripper. During

operation, the user holds the base of the device which houses the electronics, power, and SMA coolant. Tremor from the user is transmitted to the base, which if the cancellation device were off, would pass to the attached implement. However, with the device activated, the embedded controller uses the motion sensor to detect the user's disturbance in plane, orthogonal to the axis of the implement (x and y direction in Figure 5.1) and signals the cancellation platform to move in the opposing direction to cancel the tremor's net effect.

The key to the stabilizing effect of the cancellation device is the motion generating platform which consists of two decoupled platform sliders (Figure 5.2) – one producing motion in the x-direction and the other in the y-direction. Both platforms operate in the same manner through an angled packaging architecture (Figure 5.3), where to amplify displacement the SMA wire is placed in the antagonistic configuration studied in Chapter 4, but pulling from an angle θ from horizontal. The output of the antagonistic

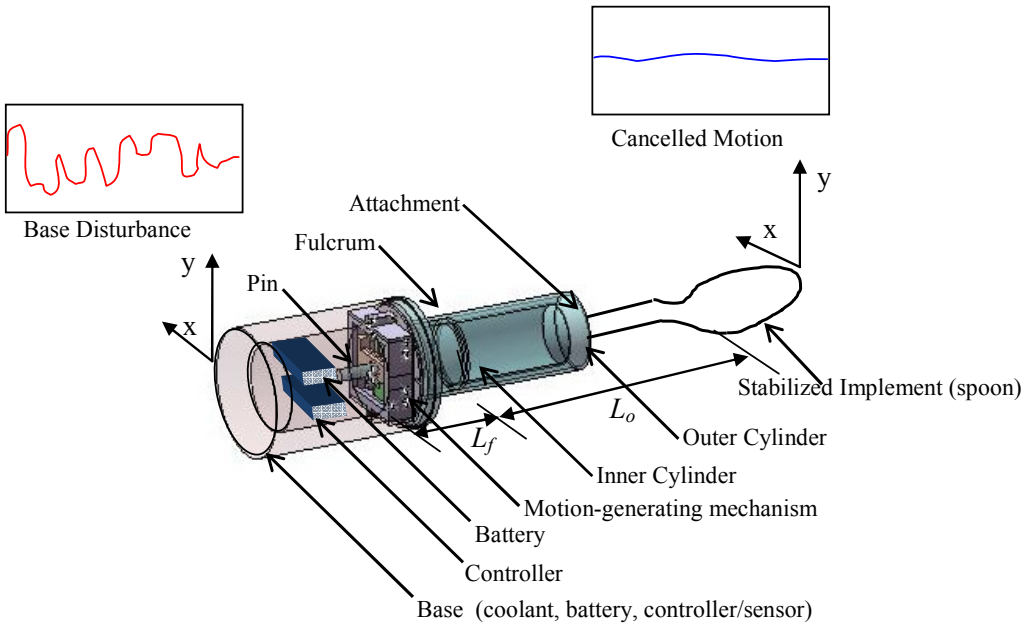

Figure 5.1. Schematic of the ACT architecture. The base of the cancellation platform is subject to a disturbance, which is cancelled by the motion-generating platform.

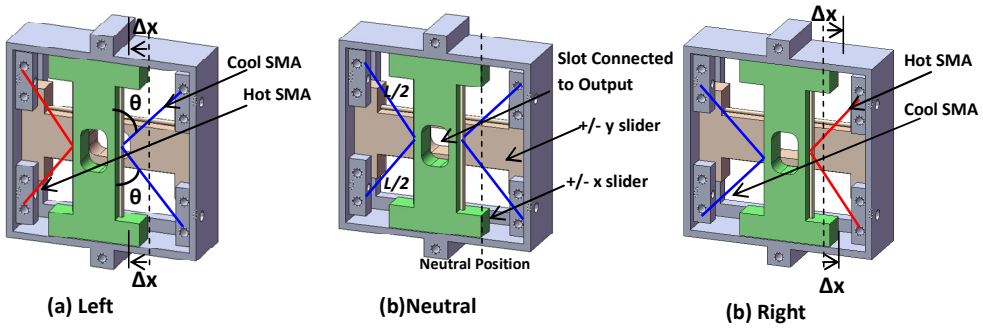

Figure 5.2. Schematic of the ACT architecture. Operation of the ACT system's motion generating platform. Heating the appropriate SMA wire causes it to contract forcing the output slider in the desired direction while resetting the opposing cool antagonistic partner.

actuator in (Figure 5.2) connects to an output pin, which is attached to an inner cylinder that houses the stabilized object, and pivots about a fulcrum. The fulcrum has a built-in compliance to return the inner cylinder to the neutral position under zero power. Because each direction of motion in the platform is isolated from one another, there is no coupling in stress or displacement allowing their kinematics to be described individually. These kinematic relationships are developed and coupled to a general model for antagonistic SMA developed in Chapter 4. This model was selected due to its simplicity, physical basis, and the fact that it is thermodynamically admissible. In addition, the model was tuned and experimentally validated in Chapter 4 (with good correlation) for the operating conditions anticipated for human tremor cancellation providing greater reliability over existing models. This model is therefore highly useful in understanding the effects and tradeoffs of the various design variables to ensure that the ACT system is capable of functioning at the necessary frequency and amplitude to cancel human tremor with minimal power requirements.

5.1.2 Motion Generating Platform Kinematics

Because the ACT device's motion generating platform contains a unique angled antagonistic SMA architecture, equations for each slider's kinematics have to be developed to ensure compatibility with the thermodynamic model derived in Chapter 4.

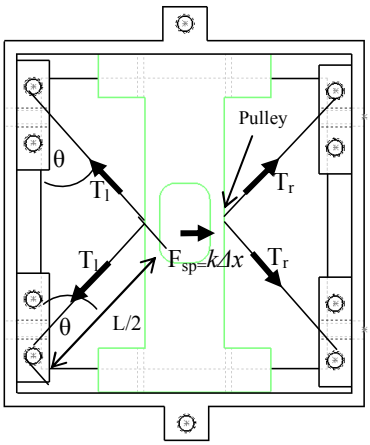

Figure 5.3. Force balance for the motion generation platform. SMA wires pass through a pulley, pulling at an angle θ that amplifies the force to the system spring F_{sp}.

Unlike straight wires, the angled architecture in the ACT system causes the input stress, σ, and strain, ε, from the SMA to be related to the fulcrum compliance force F_{sp} and displacement Δx through the wire angle θ (inertial effects are assumed to be low). In Figure 5.3, a continuous segment of SMA is used for each direction, where the wire is passed through a pulley that is attached to the platform slider. In this configuration the wires form a V shape, with an angle θ from horizontal. The fulcrum stiffness of k functions to restore the platform slider to its neutral position under zero power and provides the force F_{sp} proportional to the output displacement, Δx. From a simple quasi-static force balance a relationship the wire tensions can be related through,

$$2T_r \sin\theta + F_{sp} = 2T_l \sin\theta \,, \tag{5.1}$$

where T_l and T_r are tensions in the left and right wires. This can be related to the SMA wire strain through an energy balance as,

$$T_l L \Delta\varepsilon = 2T_l \sin\theta \Delta x \,. \tag{5.2}$$

where Δx is the output displacement. Rearranging the energy balance (Equation 5.2) and cancelling terms yields a relationship between the change in strain of the SMA ($\Delta\varepsilon$) and the output displacement of the motion platform (Δx),

$$\Delta x = \frac{L\Delta\varepsilon}{2\sin\theta}, \tag{5.3}$$

where from Figure 5.1, the motion of the stabilized object Δx_o is expressed as,

$$\Delta x_o = \frac{L_o}{L_f}\Delta x \cdot \tag{5.4}$$

It is crucial to recognize that the form of the motion platform equation is identical to the displacement equation (Equation 4.28) with the lever ratio

$$r = 2\sin\theta . \tag{5.4}$$

Thus, by substituting this ratio *r* directly into the already derived kinematic equations for motion (Equation 4.28) and effective spring stress (Equation 4.27) the antagonistic model in Chapter 4 is directly applicable.

5.1.3 ACT System Model Solution

To predict the ACT system's capability for tremor cancellation, the equations for the motion-generating platform behavior were combined with a simple controller in simulation (Figure 5.4). Because the assumed combined mass of the platform and stabilized implement was low (20g) compared to the experimental stage in Chapter 4 (220g), inertia was neglected in the model to allow for fast solution times. To produce the ACT system model, the output motion of the antagonistic model from Chapter 4 was added to an external tremor disturbance (modeled as a sinusoid), and subtracted from a zero (stable) reference to produce a net error signal. Input power to the ACT system was calculated from this error signal through the application of a proportional gain. If the resulting command signal were positive, current was sent to the antagonistic wire responsible for moving the platform in the negative direction. A negative command signal actuated the wire for positive motion, thus cancelling the disturbance. The operating stress and the net power consumption (obtained by multiplying current and voltage) of the ACT system was calculated and recorded to a file, and the entire

system (Figure 5.4) was simulated in a forward time-stepping algorithm. Due to symmetry of the ACT system, only the up/down direction was necessary to solve since the results were identical for the left/right direction.

5.2 Parameter Analyses

To gain insight and quantify the its design tradeoffs, the ACT system model was exercised across the design variables (wire diameter d, length l, convective coefficient h, angle θ, gain p) to investigate their impact on power consumption, disturbance cancellation, and operating stress. Minimizing the power consumption of the device (final term in heat equation, Equation 4.20) was selected as the design objective since it would minimize the required battery size and its weight needed for a given run-time. In addition, lowering the power draw would reduce the amount of energy required to be dissipated from the SMA wires, effectively lowering the device's steady-state operating temperature. Unfortunately, reducing the power consumption while maintaining cancellation performance is not straightforward due to the complicated system behavior. Increasing the controller gain and convective coefficient, for example, can improve cancellation performance, yet both have the negative effect of increasing the power draw, as the gain increases the controller activity while the convective coefficient increases energy losses during heating. Lowering the wire diameter and length can reduce power consumption due to the smaller amount of SMA material, yet this raises the operating stresses and decreases the actuator's overall response.

5.2.1 Assumptions

For the parameter analysis several assumptions were made to produce practical solution times and produce a realistic design space mapping. These assumptions focused on defining the primary system variables and their discretized ranges. Design

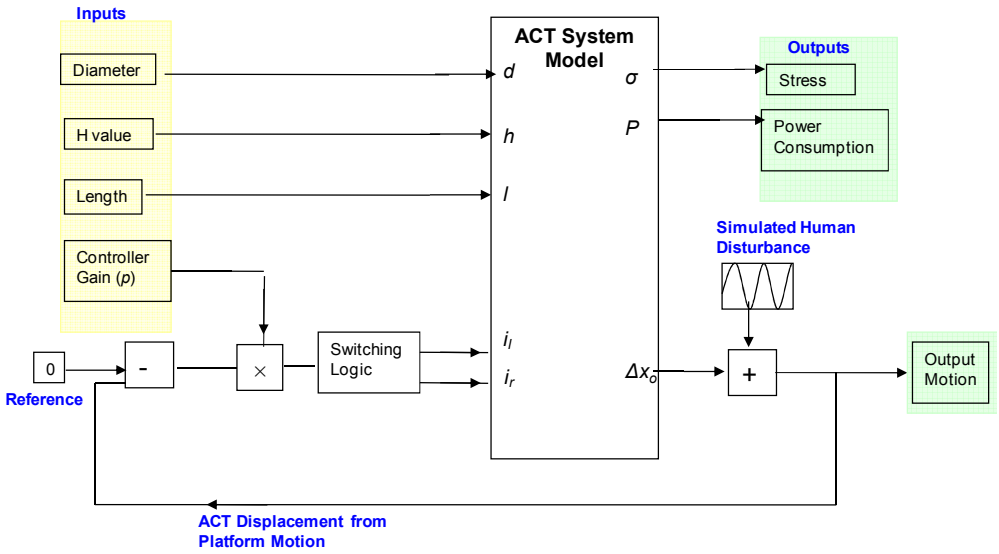

Figure 5.4. Simulation block diagram of the ACT system. Inputs are diameter, h-value, and length, while outputs are the wire stress/strains, power consumption, and tracking error.

constraints were also defined and enforced to ensure stable closed-loop cancellation with operating stresses below the manufacturer's shakedown stress level to safeguard against amplitude degradation (as studied in Chapter 2).

5.2.1.1 Variables

For the study, it is assumed that the material is a commercial SMA 70 °C Flexinol wire from Dynalloy, Inc. whose material properties (Table 4.2) were obtained from the manufacturer (Dynalloy 2009) and experiments performed by Chang, et al. 2006. In the parameter study, discrete sizes in wire diameter, between 6 and 20 mil as available by the manufacturer (Dynalloy 2009), are studied along with the wire angle θ, which is varied between 25 and 65 degrees in increments of 10. Similarly to assist in simulation speed the other design parameters are discretized across ten increments from 0-3 in. and 0-55 for the length l, and gain p (Table 5.1). By experimentally measuring the force-deflection of the ACT device's compliant fulcrum (Figure 5.1) a value of 14 kN/m was selected for the stiffness k. In the parameter study, the convective medium is also limited to correspond to practical fluids in which the wires can be immersed: air

Table 5.1. System variables and their feasible ranges. Ranges are dictated by practical limitations in packaging, simulation speed, and materials availability.

Symbol	Description	Range	Units
d	Wire Diameter	6-20	Mils
l	Wire Length	0-3	Inches
p	Proportional Gain	0-55	N/A
θ	Wire Angle	25-65	Degrees
h	Convective Coefficient	65-5000	W/m^2K

flowing from 0-625 ft/min, oil, thermal grease, and water. Values for these convective coefficients are utilized from experimental measurements detailed in Chapter 3.

In Figure 5.4, the simulated tremor is assumed to take the form of a sinusoid with a single dominant frequency (Rocon 2004). The amplitude of the sinusoid is selected to be 1 mm and the frequency is chosen as 3 Hz (the middle of the identified 1-5 Hz tremor range). The simulated voltage source is fixed at 12 volts as this is a common voltage output from off-the-shelf batteries. While heating under fixed voltage, current is varied through a fast-switching duty cycle that is modulated by the proportional controller. The electrical resistance of the SMA wire segments is known to vary with wire diameter, and the values are based from curve fits of data provided by the wire manufacturer (Dynalloy 2009).

5.2.1.2 Constraints

While solving for a minimum power draw, several constraints on the ACT system (Table 5.2) were implemented to produce tremor cancellation while satisfying packaging requirements and ensuring stable amplitude from the SMA actuator. The stress in the SMA wire, for example, was constrained to be below a safe operating level of 200 MPa, according to the manufacturer's guidelines (Dynalloy 2009) to ensure that the wires are not subjected to cyclic shakedown (Sun, et al. 2008). Another constraint placed a minimum RMS stabilization error (1%) from the assumed 3 Hz frequency, 1 mm amplitude sinusoidal nominal tremor disturbance (Paul S. Slack and Ma 2007).

Table 5.2. Physical Constraints and descriptions. Identified constraints ensure a feasible design capable of producing sufficient cancellation without experiencing any degradation in motion due to shakedown.

Name (description)	Equation
Stress (Must be below Mfg. Recommendation)	$\sigma \leq 200MPA$
Motion (RMS stabilization error must be less than 1%)	$RMS(error\_out) < 1\%$
Packaging (Wire length must be less than 3 in)	$L \leq 3in$
Wire Lower Bound	$L \geq 0in$
Proportional Constant Upper Bound	$P \leq 55$
Proportional Constant Lower Bound	$P \geq 0$

The 3 in. upper bound on the SMA length is a dimensional constraint relating to the overall device size, which is bounded to be below 2 inches in diameter. The proportional constant's upper bound is a result of numerical trials where it was found that values above this level significantly increased simulation time and power consumption due to excessive controller activity. In the following sections, these constraints are applied to the system design space to gain an overall understanding of the ACT system and guide its final design.

5.2.2 Convective Coefficient

The convective coefficient *h* is a crucial variable to consider when designing the ACT system since, as studied in Chapter 3, it directly relates to the cooling medium type, frequency capabilities, and power consumption. For example, the design study in Chapter 4 demonstrates that an increase in the convective coefficient improves the convective heat flux during cooling, which increases the frequency capabilities of the actuator (see Figure 4.14a). However, this increase in heat convection also occurs during the heating cycle resulting in a negative effect of increased power draw (see 4.14b). Lowering the convective coefficient can be done to reduce power draw, though a limit (dependant on medium type and wire diameter) is eventually reached where the wires do not fully cool and begin to actuate against one another, resulting in an increased operating stress.

To study the effects of the convective coefficient on the ACT system's operation, a parameter study was conducted for various wire diameters and *h*-values (utilizing the coupled diameter/*h*-value correlations given in Chapter 3). To ease numerical computation the wire length and angle (both assumed not to affect cooling time) were fixed at 1.6 inches and 45 degrees, respectively. After running the simulation and applying the physical constraints in Table 5.2, the actuator designs resulting in the minimum operating stress for each cooling medium were filtered and recorded.

The results (Table 5.3) show that only water and thermal grease operate at stresses below 200 MPa. Due to the higher cooling properties of water (Chapter 3), the operating stress in this medium is also 14% lower than the stress in thermal grease. For the other cooling media, the lower convective coefficients do not allow the wires to fully cool, causing them to force against one another. Under these conditions the lowest stress occurs at the highest wire diameters of 20 mil (due to the larger cross-sectional area), though this minimum stress is well beyond the 200 MPa limit. Overall, these results indicate that air and mineral oil are not feasible for use in the ACT system due to their cooling limitations. Therefore, further parameter studies focus only on water and thermal grease, since feasible design solutions can only be found in these two media.

Table 5.3. Minimum feasible operating stress conditions for various cooling media. Only water and thermal grease operated at feasible stress, with the lowest stress occurring at 8 mil. diameters.

Medium	*h* value (Pathak, et al. 2008) (w/m^{2}K)	Controller Gain *p*	Diameter *d* (mils)	Stress σ (MPa)	
Water	3200-5580	4	8	132	Feasible
Thermal Grease	1950-4320	4	8	151	Stress
Oil	511-1000	16	20	315	Infeasible
Air 625 ft/min	400-644	12	20	309	Stress
Air 460 ft/min	325-569	12	20	311	
Air 250 ft/min	270-487	8	20	312	
Air 150 ft/min	227-416	8	20	312	
Air 0 ft/min	20-153	6	20	315	

5.2.3 Diameter

In addition to the cooling medium, as demonstrated in Section 4.3 the wire diameter can significantly affect actuation frequency, operating stress, power consumption, and output stroke. Thin wires, for instance, have a higher surface area to volume ratio and can cool more quickly than large diameter wires (as shown in Figure 4.12). Because of their smaller diameter, thin wires also contain less material and therefore require a lower amount of energy to heat. Wires that are too thin, however, may not be capable of producing sufficient force and can develop infeasible stress levels (Dynalloy 2009). To quantify these effects, the ACT system model was simulated over a range of discrete wire diameters and lengths for a fixed controller gain of 4 and wire angle of 45 degrees. The results (Figure 5.5) show that the power draw in both cooling media decreases for decreasing wire diameters (at longer wire lengths). For example, at a fixed wire length of 2.7 inches, decreasing the wire diameter from 15 to 6 mil decreases the power draw by 48% in water and 54% in thermal grease. This effect exists since there is less bulk material to heat.

At the extreme cases (smallest and largest wire diameters of 6 and 20 mils) there are spikes in the power consumption for the water cooled actuation. At 6 mil, a peak of 46 watts occurs, while a much larger peak of 108 watts occurs for 20 mil, which is primarily due to the wire's larger size. These peaks occur because the wires are not producing enough motion, which the controller interprets as a lack of response and increases power delivery. For the 20 mil wires, this lack of response is due to insufficient cooling, while for the 6 mil wires it is because there is insufficient force to overcome the internal system stiffness. For thermal grease, a peak of 125 watts for the 20 mil diameter wire (Figure 5.5b) also occurs due to insufficient cooling. A power spike for the 6 mil wire, however, is absent since the lower cooling rate offered by

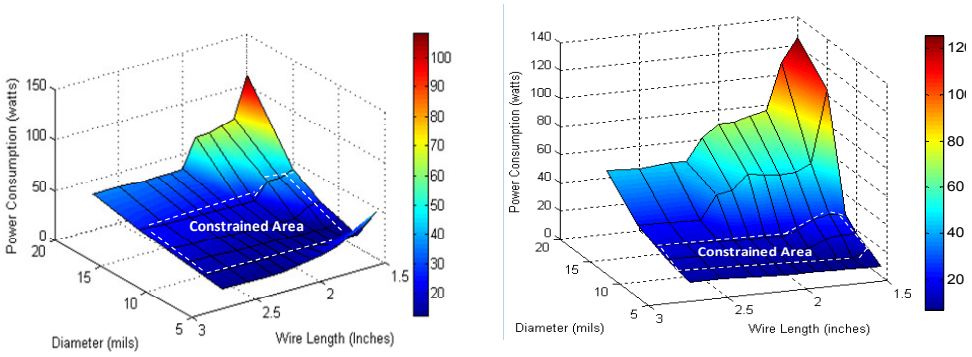

(a) Water **(b) Thermal Grease**

Figure 5.5. Unconstrained design spaces for varying diameter and length. A near-monotonic decrease in power occurs with decreasing diameter. Proportional gain is fixed to 4 and wire angle of 45 degrees for this plot.

thermal grease allows the wire to be heated to higher temperatures and produce a greater motion response for the same controller gain.

After applying the design constraints (Table 5.2) to the simulated space, a sub-space was created in Figure 5.6 in the form of contour plots. In this topographical mapping, the wire diameter follows the decreasing trend to the active stress constraint of 8 mil diameter for both cooling media. The 6 mil wire is eliminated in both water and thermal grease because it is unable to support the operating forces, which causes the development of infeasible stresses. Both 15 and 20 mil wire diameters are also eliminated in thermal grease due to insufficient cooling. In water cooling, only the 20 mil diameter wire is eliminated allowing feasibility for 15 mil wire because of the water's higher convective coefficient (which as measured in Chapter 3, for a 15 mil wire is 43% greater than the *h*-value for thermal grease).

5.2.4 Length

As seen in Figure 5.5 and Figure 5.6, the wire length also plays a significant role in the motion performance and power consumption of the ACT system. Since the transformation strain of the SMA is relatively constant, an increase in length is directly

proportional to the output displacement as expressed in Equation 5.3. However, this comes with the cost of greater power draw and cooling loads since additional material must be heated and cooled. In addition, wire lengths that are too small produce insufficient motion causing the controller to increase energy delivery. In thermal grease, for example, the power increases by 51% (from 8.6 to 13 Watts) when decreasing the wire length from the 1.8 inch optimum to the lower bound of 1.5 inches. The topographical mapping of the design space (Figure 5.6) demonstrates that this tradeoff is indeed genuine since none of the constraints for wire length are active at the optimal points, which for 8 mil diameter in water lies at approximately 1.7 inches, (1.8 inches for thermal grease). Figure 5.6 also shows that the optimal length shifts to larger values for increasing wire diameters. At 12 mil, for example, the optimal length increases by 23% to 2.1 inches for water and by 6% to 1.9 inches for thermal grease. The greater shift in the water coolant can be explained by the lower operating stress (due to greater cooling). This facilitates the use of longer wires working under partial transformation. In Figure 5.6 the water also has a lower sensitivity to wire length than thermal grease when the length is decreased from its optimal point. Reducing the wire length in water from 1.8 to 1.5 inches causes the power to increase by 13%, from 15 to 17 Watts, which is less than the 51% increase experienced with thermal grease. This again is likely due to the greater cooling that water provides, which increases the overall response of the actuator.

5.2.5 Controller Gain

While a simple proportional controller was found to stabilize the ACT system in simulation, its gain must still be carefully selected since it can significantly affect overall performance. For instance, increasing the gain raises error sensitivity and thus improves stabilization performance, though this can considerably raise the controller's

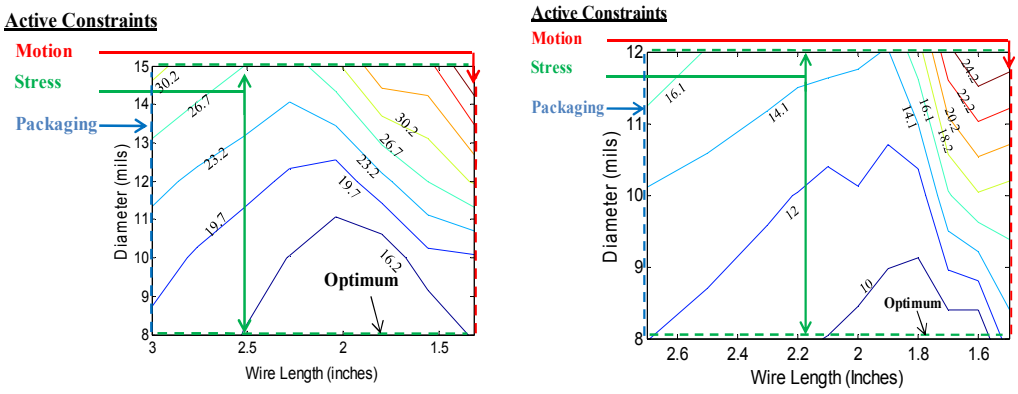

(a) Water **(b) Thermal Grease**

Figure 5.6. Constrained design spaces for varying diameter and length. The length produces a valley with the optimal point occurring near 1.8 inches. Proportional constant is fixed at 4, and the wire diameter is fixed at 45 degrees.

power draw. Decreasing the gain will lower the power consumption though cancellation performance will begin to degrade.

To quantify the points where these effects occur, a design space was created (Figure 5.7) where a set of simulated gains are plotted with varying wire length. In this particular plot, the wire diameter and angle are fixed at 8 mils and 45 degrees. The results in Figure 5.7 show that increasing the proportional gain consistently increases the power demands in media – for example at a wire length of 2.7 inches, power draw increases by 258% from 9.1 to 23.6 watts for water and 213% from 8.5 to 18.2 watts for thermal grease. This amplification of power draw again is due to the controller's increase in sensitivity over small errors, which causes it to expend more power to correct them. At high gains and low wire diameters, a spike in power draw occurs (59 watts for water and 38 watts for thermal grease) because the small wire lengths produce insufficient motion response. At the low gains the least amount of power is consumed, though at the lowest levels (less than 4) cancellation performance is degraded.

By applying the design constraints (Table 5.2) the points providing insufficient cancellation are eliminated along with regions of high operating stresses where high

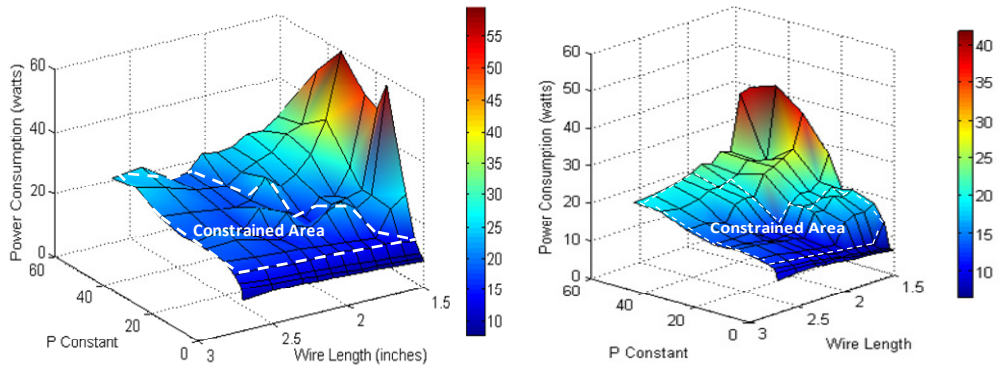

(a) Unconstrained Area **(b) Constrained Area**

Figure 5.7. Unconstrained design spaces for water and thermal grease for varying gain and length. A decrease in power occurs with decreasing gains. Diameter and angle are fixed at 8 mil and 45 degrees.

controller activity causes the antagonistic wires to insufficiently cool. In Figure 5.8 a topographical mapping of the constrained space shows a length dependency on the stress constraint (the boundary forms an angle with the x-y axes). This is due to the fact that the shorter wires are easier to heat, and thus their operating stresses more sensitive to the gain than the longer wires. The topologies in Figure 5.8 also show that a most efficient operating regime exists for both the water and thermal grease coolants at a gain of 4 (lowest feasible value, motion constraint is active) and a wire length close to 1.8 inches. For water, the power consumption at this optimal value is equal to 13.75 watts, while for thermal grease it is 32% lower at 9.3 watts due to the lower convective coefficient. While this power reduction is favorable in terms of battery size and weight, the cost and practical considerations must be made before selecting thermal grease, which is typically expensive in large quantities and can be difficult to apply to the wires.

5.2.6 Wire Angle

Because it introduces a form of mechanical advantage (as studied in section 4.3.1), the angle θ from horizontal (Figure 5.3), also affects power consumption, packaging,

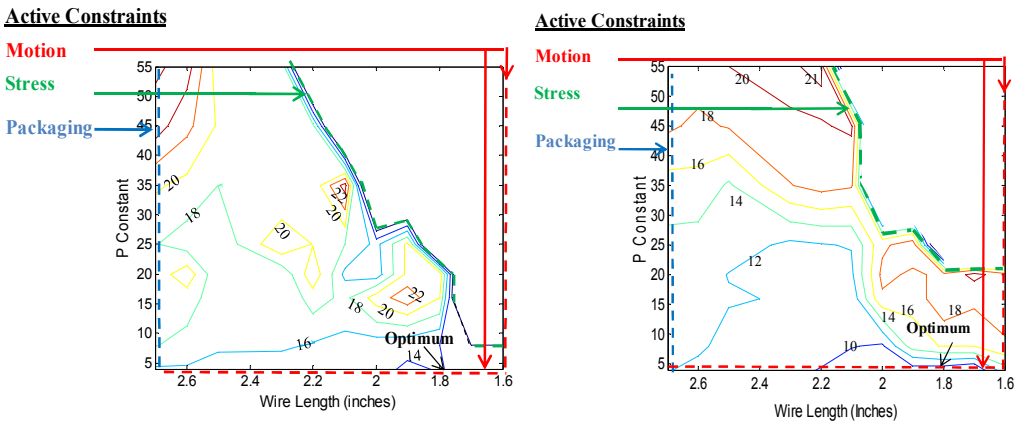

(a) Water **(b) Thermal Grease**

Figure 5.8. Constrained design spaces for varying gain and length. The optimal gain is the lowest feasible value for the fixed diameter of 8 mil and wire angle of 45 degrees.

and the frequency capabilities of the ACT system's motion generating platform. As described by the kinematic modeling in Section 5.1.2, the wire angle effectively functions as a lever, where if θ were decreased the output displacement per unit strain would be increased. Another effect of decreasing θ occurs in the effective lever's force amplification, which decreases through the effective spring stiffness (Equation 4.27). Increasing θ produces the opposite effect. To study the consequence that a variable leverage has on the ACT system's optimal power draw, five design scenarios were simulated for water and thermal grease with wire angles ranging from 25 to 65 degrees in increments of 10.

To explore the different design scenarios, a constrained optimization algorithm was used on the model. The Simulink model was modified to interact with the trust-region reflective optimization algorithm *fmincon* in Matlab and the algorithm was run with an initial point near the observed minima for both water and thermal grease. The optimization results (Table 5.4), show that in both water and thermal grease a smaller wire angle produces a more favorable design in terms of power consumption. For example, decreasing the angle from 65 to 25 degrees in water reduces the power draw by 4.9 watts in water and 4.3 watts in thermal grease (both are 42% reductions). As

discussed in Section 4.3.1, this power reduction occurs because the mechanical advantage reduces the required displacement from the SMA wire (increasing the required force). Thus, shorter wire segments (62% decreases from 65 to 25 degree wire angles) at larger diameters (increased from 6 to 10 mils) are utilized that have an overall reduced surface area over the longer thinner wires.

Another effect of decreasing the wire angle involves the planar area of the stack package, which significantly decreases (by as much as 7 times from 65 degrees to 25 degrees) due to the smaller wire lengths. Increasing the wire angle reduces the required force allowing for thinner wires, though the lengths must be greater to produce sufficient motion. However, this may be necessary as thin wires are capable of producing higher frequency responses. For the optimal solution in thermal grease it is noted that the minimal power consumption is consistently lower than water 5.9 watts, by as much as 30%. This is due to the fact that the superior cooling properties are actually not needed and result in causing unnecessary power consumption during the heating cycle. However, in an actual design, practical limitations often necessitate a simpler, cheaper, and more readily-available coolant such as water at the expense the increase in power draw.

Table 5.4. Optimization Results for water. Several wire angles were run for water cooling showing that a decrease in mechanical advantage decreases the objective function.

Cooling Medium	Wire Angle (Degrees)	Wire Diameter (mils)	Wire Length (inches)	P Constant	Package Size (in^2)	Objective Function (watts)
Water	25	10	0.87	1.9	1.12	6.8
	35	10	1.23	2.9	2.84	9.3
	45	8	1.49	4.9	4.44	10.8
	55	6	2.06	6.0	7.97	11.4
	65	6	2.32	7.3	8.20	11.7
Thermal Grease	25	10	0.92	2.0	1.30	5.9
	35	10	1.2	2.5	2.70	7.3
	45	8	1.5	3.05	4.50	7.6
	55	6	1.9	5.9	6.78	9.1
	65	6	2.3	6.5	8.10	10.2

5.3 Tremor Cancellation Device and Experiments

To demonstrate an instance in the general class of hand-held cancellation that this dissertation enables, a simplified version of the ACT system was built using the results of the parameter study and was experimentally validated. This was accomplished through cancellation tests for a variety of single-frequency disturbances of up to 1 mm peak-peak amplitude at 1-5 Hz, which is within the frequency range of large-amplitude unintentional tremor of the elbow and forearm (Elble 1986; Elble 1995; Fox and Randall 1970; NSAC 2007). An actual human tremor signal consisting of multiple components in the 1-5 Hz frequency range was also tested to show viability for human interaction. Power consumption during this cancellation process was recorded, compared to the ACT system model's prediction, and used to estimate packaged battery solutions for an entirely self-contained assistive device.

5.3.1 ACT Prototype

The experimental prototype of the ACT system was built according to the design parameters summarized in Table 5.5. In this table the diameter and length were chosen based on the parameter studies, which indicated the optimal points in the constrained space. The liquid coolant and wire angle were guided by the parameter study, but the globally optimal points (25 degree angle in thermal grease, Table 5.4) were not selected due to practical considerations in the laboratory environment. The thermal grease, for example, is expensive in large quantities, and is difficult to apply uniformly especially when working with small parts that continuously need to be disassembled and reassembled. Therefore despite its higher power requirements, water coolant in the proof-of-concept. The wire angle was also increased from 25 to 45 degrees to facilitate the small part fabrication. Therefore, from Table 5.4, 8 mil diameter, 1.5 inch long wires were used for the 45 degree wire angle in distilled water.

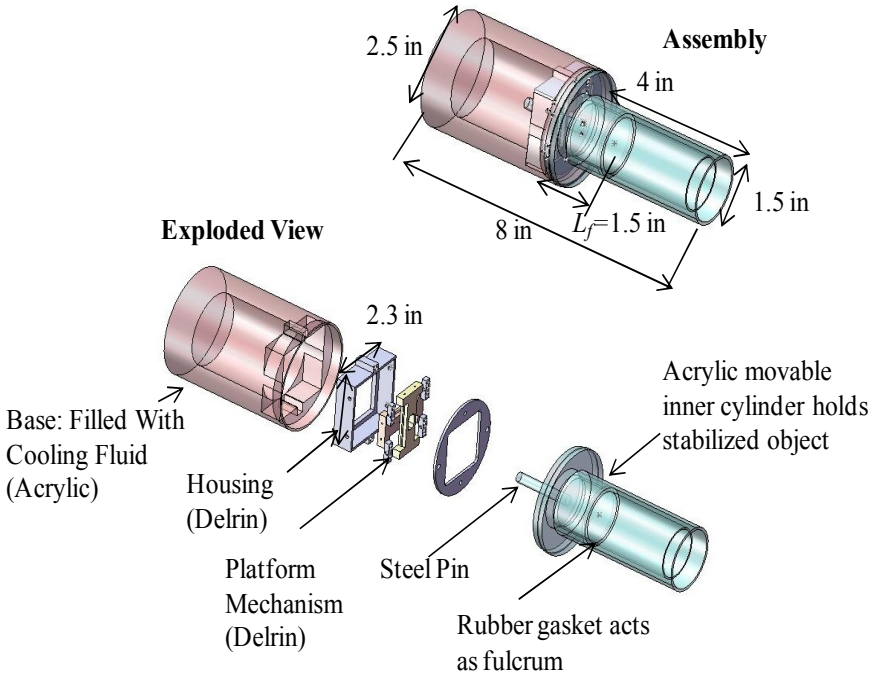

Figure 5.9. Prototype of the ACT system. A CAD design was generated based on the selected design, and a prototype was fabricated for experimental testing.

In the motion generating platform, all of the moving parts conceptualized in Figure 5.2 (housing and both sliders) were designed to fit inside an outer casing (Figure 5.9). The motion generating platform parts were machined from Delrin due to its low-friction properties, and the SMA wires were attached with a set screw to adjustable crimp blocks (Figure 5.10a). By adjusting the set screws, these blocks were positioned to ensure that the wires experienced a maximum of 3% strain during operation. To heat the wires, electrical connections to the aluminum blocks were made mechanically through the use of set-screws. The water coolant surrounded the SMA wires in an

Table 5.5. Design specifications for the ACT prototype. The wire angle and water cooled environment were selected to aid in assembly repeated experimental testing.

Variable	Name (description)	Value	Units
d	Wire Diameter	8	Mils
l	Wire Length	1.5	inches
p	Proportional Gain	5.5	N/A
h	Cooling Medium	4280 (water)	W/m^2K (fluid)
θ	Wire Angle	45	Degrees

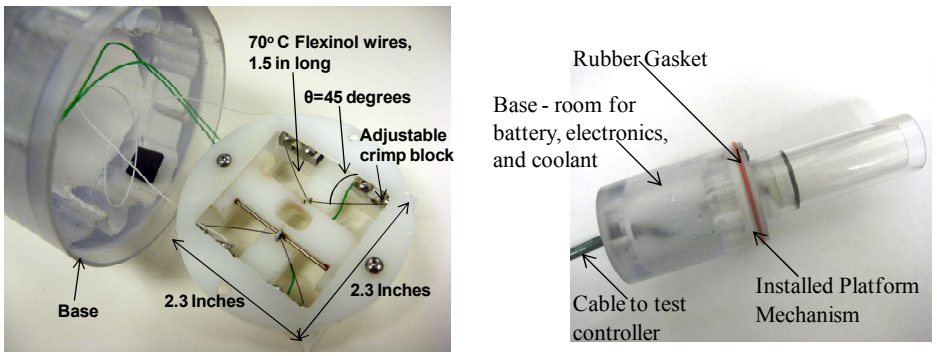

(a) Motion Generating Platform **(b) ACT Device**

Figure 5.10. Fabricated motion generating platform and ACT device. SMA wires are electro-resistively heated to produce necessary motion.

acrylic chamber bored from cylindrical stock (Figure 5.10b). To electrically power the SMA through this air/water interface, a water-sealed rubber grommet was used. Output from the SMA motion platform was transmitted through a steel pin to an inner movable cylinder that was held in place with a rubber o-ring. This ring sealed the coolant and provided stiffness of approximately 14 kN/m to allow the output cylinder to return to a neutral position under zero-load.

To control the SMA actuator, a sensor/controller package was designed and implemented in two separate configurations: position and velocity feedback control. Position feedback was used to validate the model-based design of the ACT prototype (which assumed position control), while velocity control was implemented to test a fully embedded solution that is inherently capable of filtering (low-pass) slow tracking motions from tremor. For the position feedback, a Laser displacement sensor was used to output inertial position to an ATMEGA16 digital microcontroller which returned a command to the actuator based on proportional control.

Velocity feedback was achieved through the use of an IDG300 dual axis MEMS gyro sensor that sent an analog signal to the ATMEGA16 that returned actuator commands through a proportional gain. The second velocity feedback control strategy

not only demonstrated the potential for an embedded sensor/controller solution, but also provided an allowance for slow intended tracking motions due to the inherent low-pass filtering properties of the rate-feedback control. In each series of tests, the a/d converter of the microcontroller sampled the feedback signals at 5 KHz. Depending on whether the input to the microcontroller was above or below a reference signal, the microcontroller output a duty cycle signal of 60 Hz to a MOSFET transistor that was responsible for switching 12 volts to the appropriate SMA wire.

5.3.2 Cancellation Test Procedure

The experimental set up, illustrated in Figure 5.11, was used for all the cancellation experiments. During tests, the ACT system was suspended by a wire from its center of mass and pivoted in the vertical degree of freedom. The bottom of the tremor cancellation device was attached to a LabWorks 139-40 Electrodynamic Shaker System, controlled by a laptop running LabView. During each trial the Laser displacement sensor was used to record the disturbance with the tremor cancellation device off and with the device powered on, and this recorded data was stored to the PC. Because human tremor is often characterized as being sinusoidal in nature with a dominant frequency (Rocon 2004), initial cancellation tests focused on demonstrating closed-loop control of single-frequency sinusoidal disturbances (Figure 5.13). Three frequency levels were chosen (1, 3, and 5 Hz) to test the device through the 1-5Hz tremor frequency range. Further experiments were conducted on a real human tremor signal, demonstrating successful cancellation and feasibility for clinical development.

5.3.3 Single Frequency Testing

In the single-frequency domain, the experimental setup illustrated in Figure 5.11 was utilized to test the ACT prototype under several sinusoidal motion disturbances. The proportional controller of the ACT system was tuned by adjusting the feedback

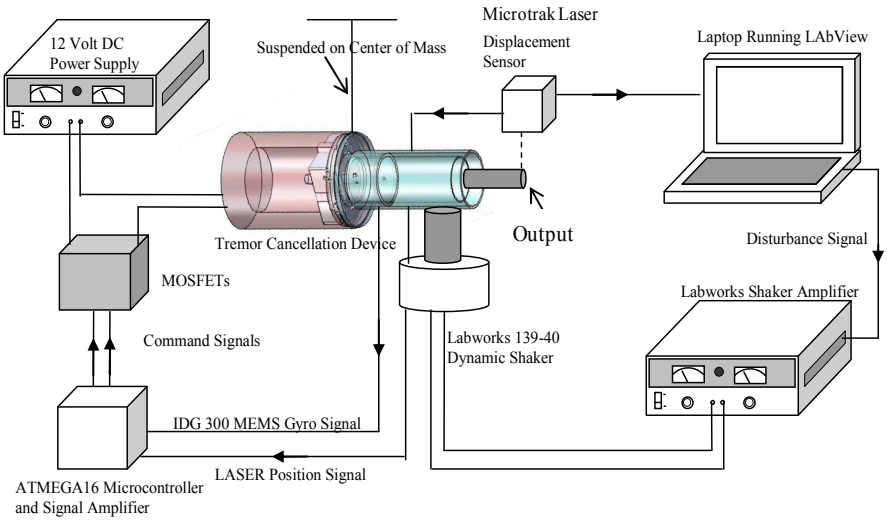

Figure 5.11. Schematic the ACT experimental setup. The device is excited by a shaker, and stabilizes an output Laser pointer under closed-loop control.

gain until the smallest amplitude of resultant motion was observed under an assumed dominant 3 Hz tremor disturbance. In Figure 5.12, this process is illustrated, where the degree of cancellation improves with increasing gain up to a limit of approximately 5.5. Gains higher than this level produce unstable oscillations that cause a degradation in performance. It should be noted that the experimentally selected gain of 5.5 is only 10% of that obtained in the design optimization (4.9 for 45 degrees wire angle, Table 5.4) showing the utility of the model-based design process for controller tuning. In addition, the stable cancellation observed under simple proportional control in the experimental trials validates the model's general prediction that this form of control is appropriate.

The specific cancellation results using this gain are shown in Figure 5.13. At 1 Hz significant motion cancelation was achieved with 82% peak-peak and 80% RMS signal reductions. At 3 Hz, some performance degradation was recorded. At this frequency, 61% RMS cancellation was produced with a peak-peak reduction of 72%, which still is significant for being near the upper limit of the tremor specification. At the upper frequency bound of 5 Hz, degradation in performance was observed and only 44% RMS cancellation was produced with a peak-peak reduction of 53%. Overall, all of the

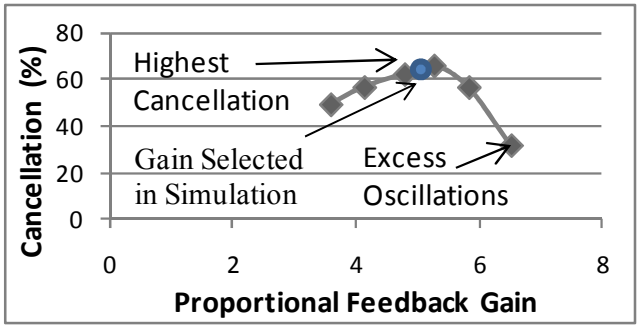

Figure 5.12 Degree of Cancellation for Increasing Gain. Cancellation performance increases to a peak at a gain of approximately 5 times, after which performance decreases.

cancellation trials demonstrated significant disturbance rejection, though the model simulations all had the criteria that the RMS cancellation would be below 5E-4 mm (near-zero). The greater errors seen in the experiment are likely due to dynamics (causing the observed high-frequency 25-30 Hz components) that were not accounted for in simulation, which also explains why the error increases for increasing frequencies.

Additional tests were completed using position feedback to characterize the ACT system's response to various disturbance amplitudes. In these experiments, the shaker output was varied over a range of 0.5 to 1.8 mm (peak-peak), for 1, 3, and 5 Hz. Figure 5.14 shows the results of these tests, and it is clear that the device is most effective over tremor amplitudes of 1-1.5 mm, which is what the system was designed for. For amplitudes greater than 1.5 mm, the SMA wires begin to overheat since they were physically unable to produce the required amount of motion, causing a overall reduction in stabilization (by up to 16% for 3 Hz). For the small-amplitude disturbances lower than 1 mm, the simple proportional controller is unable to actuate the wires through their hysteresis in time, thus resulting in lower cancellation performance (for 3 Hz, this reduction is 15% lower than peak cancellation performance at 1.5 mm).

Experiments using a MEMS gyro rate sensor were also conducted to demonstrate feasibility for a completely embedded solution. By implementing this gyro sensor, the

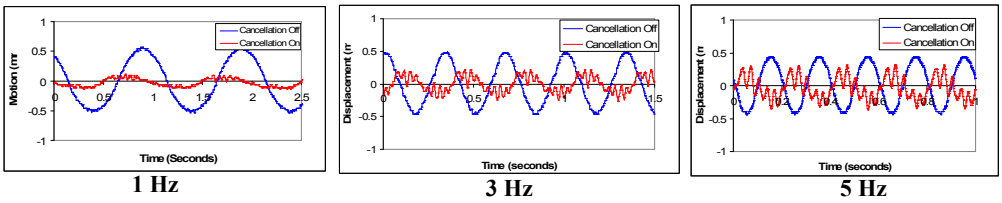

Figure 5.13. Stabilization results using Laser Displacement Sensor. Results show cancellation performance for position feedback control for 1, 3, and 5 Hz.

ACT system was capable of differentiating between relatively high-frequency tremor and slow intended motions, acting as a low-pass filter. Because the derivative control was different from position control, gains were not calculated and instead manually tuned until a maximum cancellation was observed with little oscillation.

Figure 5.15 shows the cancellation performance at each of the tested frequencies, demonstrating once again considerable disturbance cancellation. For example, at 1 Hz a reduction of 67% peak-peak amplitude is achieved along with an RMS cancellation of 78%, which is only slightly lower than that obtained using the Laser displacement sensor. At 3 Hz, substantial cancellation was also observed as the peak-peak amplitude was reduced by 70% along with an RMS cancellation of 75%. This performance is noticeably better than the Laser displacement sensor tests (which experienced 61% RMS cancellation at 3 Hz) indicating that the rate control may be more suitable for higher frequencies, as the rate feedback amplitude increases with frequency. At the

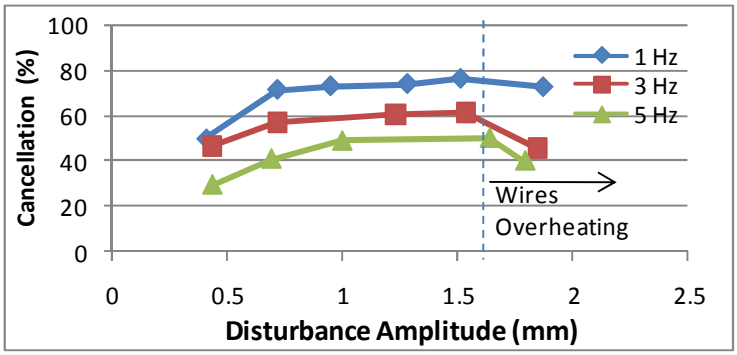

Figure 5.14. Cancellation performance for increasing disturbance amplitudes. Performance increases until 1.5 mm disturbances after which degradation in performance begins.

upper frequency bound of 5 Hz, however, difficulties in cancellation do arise which are likely due to dynamic effects. The cancelled signal in Figure 5.15, for example, shows a peak-peak cancellation of 53%, which is 17% less than that observed for 3 Hz. The RMS cancellation of 69%, which is also 6% lower than the cancellation calculated for 3 Hz. Overall, however, the single-frequency tests demonstrate appreciable cancellation for the 1-5 Hz frequency range, up to 80% RMS for 1 Hz. Because the identified tremor resides in this same frequency range, considerable stabilization of a human tremor signal should also be expected.

5.3.4 Human Tremor Cancellation

To validate this hypothesis and demonstrate the ACT's prototype's potential for human assistance, an actual tremor signal was acquired (consisting of multiple frequency components) and used as a disturbance profile. The tremor motion signal was obtained from a healthy volunteer who was instructed to hold the ACT system (in its off state) as steady as possible. During this time, the tip displacement of the device was recorded with the Laser displacement sensor and its output was displayed on an oscilloscope to give the volunteer visual feedback. The recorded motion, shown in Figure 5.16, displays the oscillatory nature of the recorded tremor, which exhibits a peak-peak amplitude of approximately 1.5 mm. The frequency decomposition shown in the FFT transform (Figure 5.17a) indicates that the dominant frequencies in the

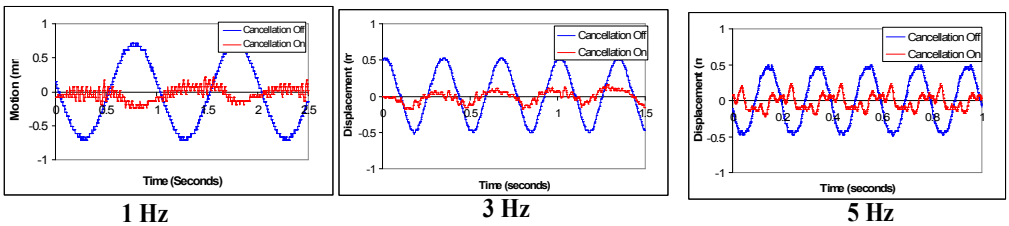

Figure 5.15. Stabilization results under angular rate control. MEMS gyro sensor is used for disturbances of 1, 3, and 5 Hz

recorded tremor signal (for the healthy individual) are mainly below 3 Hz. This result is consistent with assumed dominant frequency when designing the ACT system. The amplitude of the frequency components above 3 Hz are very small (less than 20% of the amplitude at 1 Hz), indicating that the performance degradation demonstrated by the single-frequency tests at 5 Hz is not a significant issue. Tests on the tremor cancellation device were conducted using the same experimental setup shown in Figure 5.11, where the recorded tremor signal was output from the laptop running LabView. This signal was fed into the shaker amplifier, causing the shaker to replicate the five seconds of recorded tremor repeating in a loop.

In Figure 5.16 the resulting tip displacement is plotted with the tremor cancellation device on (using the MEMS gyro for velocity feed-back control) and off. The resultant plot with the tremor cancellation device activated shows that most of the sharp peaks are cancelled, and the output motion remains low (0.1 mm RMS), proving the active tremor cancellation concept. It is noted that after the 3-second mark in Figure 5.16 the cancelled motion does begin to drift from this zero position to 0.3 mm, though this is due to the fact that the tremor disturbance signal drifts in its neutral position as well.

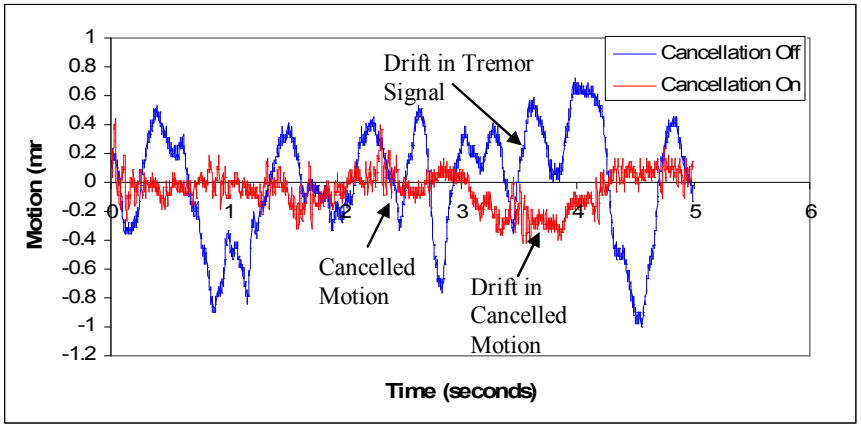

Figure 5.16. Stabilization of human tremor signal. Human tremor disturbance loop plotted with the cancellation device turned off and on.

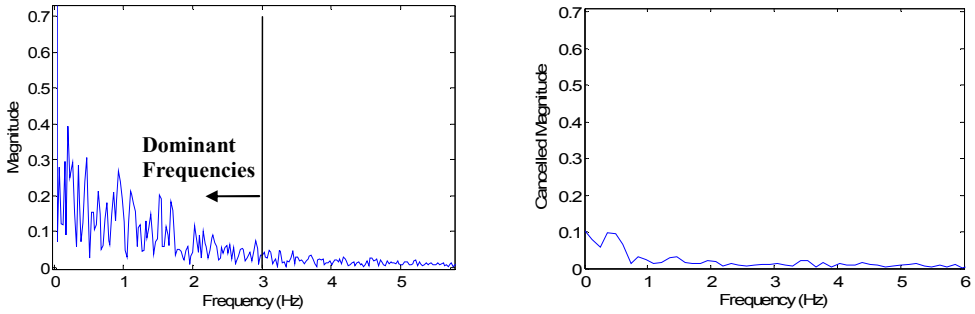

Figure 5.17. Human Tremor Measurements. Dominant frequencies are all below 3 Hz, and are mainly below 2 Hz.

Neglecting this drift, the overall cancellation is 71% RMS, which is only 7% lower than the cancellation produced during the 1 Hz single-frequency disturbance test. This result exceeds the 50% RMS cancellation goal specified in Section 1.2.4, showing the technology's potential for use in systems that can significantly improve the quality of life of many individuals. The FFT of the cancelled signal (Figure 5.17b) also reflects the significant reduction, where only low-frequencies (below 0.5 Hz) that are in the same range as tracking motions are preserved due to the low-pass filtering properties of the gyro sensor.

5.3.5 Power Consumption

In addition to cancellation performance, power consumption is a significant metric affecting actuator design, and was studied by comparing the actual power draw to that predicted by the ACT system model. During the tremor cancellation experiments, the input power was monitored at 3 Hz, and the average consumption was calculated to be 11.20 Watts, which is only 7% lower than the power draw of 12.07 Watts that was predicted during simulation. The small deviation may be due to a combination of manufacturing/installation error, or numerical error during simulation. Because the error is small, however, the excellent agreement demonstrates the significant utility of the design model and validates its use for predictive design. Assuming a NiMH battery

is used to power the cancellation device in two degrees of freedom (thus twice the measured power consumption), and that an approximate energy density for NiMH is 70 Wh/Kg (Zhan, et al. 1999), approximately 160 grams battery weight would be needed for 30 minutes of operation. If weight were a significant issue, more expensive lithium ion batteries could be employed that weigh only 70 grams for the same 30 minutes of operation, assuming energy densities of 160 Wh/Kg (Vincent 2000). Additionally, from the results of the wire angle study (Table 5.4), employing a smaller wire angle of 25 degrees in a medium of thermal grease could reduce the power consumed by 55%. Thus, the battery weight could potentially be reduce this same amount, or the run-time could double to over one hour for the same 70 grams of weight.

5.4 Conclusions

Through the model-based design, parameter analysis, fabrication, and testing of the ACT system, the general antagonistic SMA technology developed in this dissertation has been successfully proven to enable a new class of tremor cancellation. The ACT system is shown to provide stabilization assistance through a highly compact motion generating platform that is capable of reducing disturbances in the 1-5 Hz range. To achieve this, a motion platform was designed and fabricated utilizing SMA actuators operating at a tailorable angle. To predict transient motion performance and power consumption, kinematic equations for the platform mechanism were coupled to the thermodynamic model developed in Chapter 4, and a parameter study was conducted for a closed-loop tremor cancellation system. The study investigated the effects of changing cooling medium, wire diameter, length, controller gain, and wire angle with respect to the essential performance metrics including the degree of cancellation and power consumption. From these studies, it was found that only water and thermal grease were capable of providing the cooling required for the system to function under

the shakedown stress specified by the manufacturer. The SMA wire diameter and the controller's proportional gain were observed to have a decreasing relationship with power consumption and thus the optimal solutions were the smallest constrained values of 8 mil. Wire length, on the other hand, had a non-monotonic relationship since lengths that were too long required excess power consumption, and lengths that were too short produced insufficient response, which the controller reacted to by increasing the power delivery (by up to 51% for thermal grease). When varying the mechanical advantage of the motion generating platform, model-based optimization studies showed that a decreasing wire angle produced optimal designs of higher wire diameter and lower wire lengths. Power consumption decreased with decreasing wire angle (by 42% from 65 to 25 degrees), indicating that it is advantageous to use a low mechanical advantage for antagonistic SMA actuators.

Using the results obtained during simulation, a proof-of-concept ACT prototype was fabricated and tested for cancellation under several disturbances. As a first order approximation to human tremor, single-frequency sinusoids (at 1, 3, and 5 Hz) were tested. These experiments were extended to a further test that was conducted using a recorded human tremor disturbance, which was shown to consist of multiple frequency components in the 1-3 Hz range. Prior to testing under these conditions the ACT system's controller was tuned to provide the greatest cancellation performance for a 3 Hz disturbance. Using the selected controller gain, tests were conducted on the ACT system demonstrating significant cancellation. Using position feedback, the 1 and 3 Hz disturbances were shown to be cancelled by 80 and 61% RMS. The gyro rate sensor similarly produced cancellations of 78% and 75% RMS, for the same frequencies. At the higher frequency of 5 Hz, the gyro sensor outperformed the position feedback (25% greater at 69% RMS), which was likely due to the fact that the controller signal using

the gyro rate sensor is amplified at higher frequencies due to the first derivative term. To test the ACT device under a real human tremor signal, the motion was recorded from a healthy volunteer and was characterized using a FFT analysis. Results of this analysis showed that the frequency components of the individual's forearm tremor was upper-bounded by 3 Hz, and had the greatest amplitude in the 1 Hz range. These results confirmed the initial design assumptions that the tremor would exist in the 1-5 Hz range. Using the recorded tremor as a disturbance signal, the ACT device was shown to produce a 71% RMS cancellation, demonstrating the device's potential for practical use, and exceeding the 50% RMS cancellation goal defined in Section 1.2.4. The power draw while operating the tremor cancellation device was also in close agreement with the system model's prediction (within 7%), demonstrating the model's predictive capabilities. In addition, the recorded power showed significant viability for a battery-operated device with potential run-times of 1 hr with just 70 grams of battery weight.

The overall success of the ACT prototype serves to demonstrate the active cancellation technology enabled by this dissertation. By utilizing the model and experimental basis for antagonistic SMA actuation, a highly compact actuator was implemented that is capable of functioning in a desired frequency range at a minimal power draw. Controllability was also demonstrated both in simulation and experiment, where a simple proportional controller was tuned to cancel motion disturbances. The ACT system illustrates just one successful instance of an entire range of tremor cancellation devices that has significant potential to provide assistance to a diverse and very large population in a variety of market sectors including biomedical, military, and manufacturing.

Chapter 6: Conclusion

The goal of this dissertation is to establish an experimental and model based scientific understanding of antagonistic SMA actuation to enable a new class of hand-held active tremor cancellation. This was specifically accomplished through the construction of a model and body of empirical support that provides the necessary design insight and predictive power for an antagonistic actuator that ensures stable amplitude and high frequency motion with low power draw. The first objective in meeting this goal was accomplished through the study of the shakedown process of SMA. In this study, a quasi-static design method was developed that was demonstrated to allow for stable, high output amplitude under high operating stress (300 MPA). The second objective to resolve speed and power issues was achieved through basic studies of the convective heat transfer from SMA wires. Part of these investigations resulted in the study of the antagonistic architecture and its increased frequency capabilities. Studies also focused on understanding the balance of frequency and power through the development of a new experimental method capable of collecting data for the convective heat transfer coefficient for a variety of SMA wire diameters in any medium. The second objective was also satisfied through the development of a novel cooling technique using carbon nanotubes (CNTs). The CNTs were shown to improve cooling times due to an effective increase in the wire's surface area. To enhance the antagonistic actuator's predictability, the third objective of this dissertation required the development a thermodynamic model. This was accomplished through the model's

derivation and the inclusion of several unique conditions including the effects of wires becoming slack, inertia, friction, boiling, and variations in the local heat transfer coefficient. Each of these conditions was studied in detail, and the antagonistic model was validated for a variety of operating conditions showing favorable correlation. The fourth objective of this dissertation required a demonstration of the developed antagonistic actuation technology in enabling human tremor cancellation. This was accomplished through the detailed study of a hand-held active cancellation case-study. The Active Cancellation of Tremor (ACT) device was designed using the thermodynamic model and cooling data, and was built to assist individuals suffering from essential tremor. In this study, an actual prototype was fabricated illustrating potential for lightweight, compact actuation. The prototype was tested to show significant cancellation under closed-loop control, exceeding the 50% RMS cancellation goal and meeting this dissertation's fourth objective. This success marks the first steps in transforming antagonistic SMA actuation into a viable technology that can offer a hand-held, compact, and power-efficient solution capable of meeting the challenging actuation and frequency requirements required for a new class of hand-held active tremor cancellation systems.

6.1 Contributions

The research performed in this dissertation has brought forward several contributions in a number of key steps. These include the investigation of a material shakedown, the study of SMA wire cooling, the development of a thermodynamic system model, and a design case-study of a practical tremor cancellation application.

6.1.1 Quasi-Static Design Accounting for Shakedown

To ensure stable amplitude output of an antagonistic SMA actuator while operating at high stress, an empirical understanding of shakedown was developed and applied to a

graphical design process for an antagonistic SMA actuator. During the shake down process, an empirically obtained double-exponential function was found to fit the recorded motion loss with high accuracy (0.99 R-value). This important discovery allows for prediction of wire performance during shakedown under known loading conditions. This allows for greater control in stabilizing the material before installation, and allows for the design of actuators functioning at higher operating stresses, which are currently set by conservative design rules (Dynalloy 2009). The double exponential form of the empirical fit is also suggestive of a physical process dictated by a rate constant (as is typically found when modeling diffusion or chemical reactions). This work overall gives a greater understanding SMA shakedown that can be used in a variety of applications (particularly industrial) where accurate, repeatable motion is required.

The results of the shakedown study were used to develop a graphical design process that was applied to an SMA Stabilizing Handgrip (SMASH) to ensure stability in output amplitude. For this process, the required operating forces and displacements were calculated through the derivation of a dynamic model that developed and applied to the M16 rifle. From this model it was found that the quasi-static requirements for both the force and displacement (8 N and 2 mm) were shown to dominate the dynamic tremor range of 0-3 Hz, and were therefore used to specify the antagonistic actuator's design. By developing a graphical model of the actuator's loading path, the amount of force required to overcome the opposing wire, friction, and internal stiffness was taken into account. The wires were shaken down in an experimental apparatus under a load of 40 N, which was a safety factor above the estimated wire loading requirements of 25 N. Using the empirical shakedown model, only 2% decay in motion over the lifetime of the installed post-shakedown wires was predicted. Test results with the shaken down

wires proved that quasi-static specifications of 4mm in the azimuth and elevation directions were met and produced repeatable motion. Overall, these results demonstrate that by using the shakedown process for SMA, stable, predictable output motion can be produced at relatively high operating stresses. By stabilizing the SMA wires through the tested shakedown process, high-amplitude motion can be retained over the actuator's lifetime. This ensures the reliable function of not only the SMASH but also any SMA actuation system.

Further studies on the SMASH demonstrated cancellation in open-loop, revealing that the SMA actuated cancellation system was linear – cancelled motion was simply a sum of the SMASH actuation motion and the disturbance motion. This result shows that a perfect inverse of the known disturbance (i.e. the dominant sinusoidal decomposition of a human tremor signal) would theoretically produce zero net motion, providing implications for simple open-loop or feed-forward control. The three empirically derived heating profiles (square, ramp, and preheat) were tested to approximate the inverse of a 1 Hz 2 mm peak-peak sinusoidal disturbance, and almost total stabilization (97% RMS) was demonstrated. In these studies, the power consumption and cooling medium were not optimized though these preliminary results demonstrate a first hand-held SMA actuated tremor cancellation system. With further improvements in power consumption and the implementation of a closed-loop control system, the SMASH has significant potential to be fielded. Such a system could significantly reduce soldier and civilian casualties in the ever increasingly urban battlefield.

6.1.2 Investigation of Convective Heat Transfer

To balance the trade-off between frequency response and power efficiency of SMA actuators, studies further studies were conducted to understand and improve the

convective heat transfer from the material. The midpoint transformation method was developed as a novel technique to measure the convective coefficient with an accuracy that is at present extremely difficult to achieve using conventional means (e.g. using IR cameras or thermocouples). The midpoint transformation method is completely general and can be applied to any geometry SMA or any size (macro or micro scale) as long as motion recovery can be observed under a known heating power. In addition, the technique can be applied in situ, where local effects (e.g. flow obstructions), changing surface properties over time, and heating effects are difficult to accurately replicate in an outside experiment. By measuring these local convective effects, accurate measurements can be utilized in system models to ensure frequency specifications are met and power consumption is minimized in actuator design. In this dissertation, the midpoint transformation method was applied to Flexinol wire from Dynalloy, Inc., and used to measure wires ranging from 6 to 20 mils in diameter in various media (free/flowing air, mineral oil, thermal grease, and water). Using the general form of proposed correlations in literature for the convection coefficient of a cylinder in still air and a cross-flow, empirical correlations were generated for each of the ambient media tested. Because the all-encompassing fits found in literature typically provided only general estimates of the collected data and did not apply well to wires of small diameter, the fit parameters were adjusted for each test condition using a GRG optimization algorithm. The resulting continuous equations closely followed the collected data in relating the power dissipation from the SMA wire to diameter, flow rate, and fluid properties (as close as 1.2% average error for water). They also offer improvements over conventional correlations (such as Hilpert of Morgan) by 8% for water, 36% for mineral oil, and 33% for convection in air. These correlations are highly useful in SMA material models where predictions of power draw and actuating

frequency can be made. Using the convective data and such models, predictions can be made to design actuators operating in optimally chosen cooling media to meet frequency specifications yet also function with a minimal power draw. For tremor cancellation systems, this would help guarantee cancellation functionality while minimizing battery weight (and thus overall system weight) to lead to a highly versatile and portable system.

Further cooling investigations focused on the research and development of a treatment to increase the SMA material's effective surface area and thus cooling performance. This treatment consisted of growing carbon nanotubes (CNTs) on the wire surface to create vertically aligned microfins of unusually high thermal conductivity. Using a DC plasma enhanced chemical vapor deposition (PECVD) process, vertically aligned nanotubes were grown directly on one half of the wire's surface (lengthwise). The CNT presence and direct attachment to the wire surface was confirmed in SEM imaging. The observed nanotubes had average diameters of 30 nm, lengths of 2-5 μm, and had an overall density of approximately 2 CNTs/μm^2, and the shape memory effect was observed to have remained after the CNT growth process. To the author's knowledge this is the first time carbon nanotubes have successfully been grown on the surface of NiTi wire (where the Ni particles were used as a catalyst). To test the convective performance enhancement, a series of free-cooling tests were conducted that showed an increase in the average h value of 19% from 50 W/m^2K to 62 W/m^2K over untreated wires. By extending this work, cooling improvements can be made without changing the cooling medium or flow rate. This has potential to reduce system power consumption (the use of an external fan may be eliminated), and also potentially allow for the use of lighter or more cost-effective coolants.

6.1.3 Thermodynamic Modeling

Using the data and empirical correlations gathered from the cooling studies, actuation predictability was enhanced through the derivation and validation of a thermodynamic model for antagonistic SMA. Because of the selected basis of the antagonistic model, incongruities (namely violations of the 2nd law) that traditional empirical models can experience (Chung, et al. 2007) were avoided allowing for thermodynamically admissible operation. The model also accounted for several physical conditions unique to antagonistic actuation. In separate tuning studies, the effect of each condition (slack wires, friction, boiling, inertial dynamics, and variations in the convective coefficient) were investigated and compared to experimental tests ranging from 0.3-10 Hz, encompassing the human tremor frequency range. The additional conditions that made the derived model unique were shown to significantly heighten tracking performance both in the transient and steady-state responses. This improved the model's overall prediction and utility for design. To further validate the model's accuracy, experimental tests were accomplished using input frequencies ranging from 0-10 Hz, duty cycles from 10-45% and wire diameters from 8-20 mil. Overall, very good agreement was demonstrated for frequencies below 5 Hz. At these frequencies, amplitude prediction matched within 8% with better results in those cases where full transformation occurred. Error existed in the transient prediction, but for those cases exhibiting partial transformation, slow heating, and reduced cooling time (i.e. cases where the wire was not heated or cooled suddenly) the transient prediction was more accurate. This was the case for increasing duty cycle, where at 45% the greatest accuracy occurred in heating and cooling times (producing only 1% errors). These tracking capabilities demonstrate the model's viability for use in the simulation, design optimization, and off-line controller tuning of any antagonistic system operating either in open or closed-loop.

With the model experimentally validated, actuation design studies were conducted in simulation demonstrating the model's capability to study a wide variety of conditions that would have been an enormous undertaking to conduct using experimental methods alone. The studies focused on the key design choices (e.g. mechanical advantage, cooling medium, ambient temperature, duty cycle, power draw and wire diameter) of an antagonistic system that are necessary to produce motion at a desired amplitude and frequency. By varying the mechanical advantage, studies showed that an antagonistic system employing the shortest, largest diameter wire allowable for the given operating frequency is most the desirable configuration in terms of power consumption. This result can be used in many future actuation systems requiring a small package size and low power draw. For example, a leveraging architecture can be designed to significantly increase portability of hand-held systems. This would simultaneously reduce the power requirements enabling a significantly smaller battery. Further studies in convection were accomplished through an additional study that mapped the required cooling media and power draw for various operating frequencies and wire diameters. This valuable mapping can be utilized as a reference that can guide design choices regarding wire diameter and operating environmental conditions. The ambient temperature was also studied and it was found that a linear relationship between required temperature and frequency existed, allowing an engineer to predict the expected frequency losses of an actuator undergoing self-heating. A final study compared the cyclic response of a single wire actuator to an antagonistic system, and it was found that the single wire began to degrade in motion at lower frequencies by as much as 28%. This result validates the frequency benefit of antagonistic SMA, showing that its use can provide higher cyclic speeds since reciprocal motion can occur while the opposing wire is still cooling.

6.1.4 ACT Case Study

Using the antagonistic SMA model and the results of the cooling studies, an Active Tremor Cancellation (ACT) device was investigated as part of the general class of hand-held tremor cancellation systems enabled by this dissertation. The ACT device is demonstrated to provide tremor stabilization through a highly compact motion generating platform that is capable of reducing disturbances in the 1-5 Hz range to assist individuals suffering from essential tremor. The device was designed through a detailed parameter analysis based on the cooling studies in Chapter 3 and antagonistic model derived in Chapter 4. This analysis was capable of specifying the SMA actuator (i.e. its actuating angle, wire diameter, length, and cooling medium) and its controller. Using a suitable set of design parameters form the parameter analysis, a proof-of-concept prototype of the ACT system was created. The ACT prototype was tested for cancellation under a variety of disturbances including single-frequency sinusoids (at 1, 3, and 5 Hz) and a recorded human tremor disturbance, which was shown to consist of multiple frequency components in the 1-3 Hz range. The device was tested to produce 71% RMS cancellation of the human tremor under simple proportional control. This result exceeds the 50% RMS cancellation goal specified in Section 1.2.4. It also verifies the model's predictions for stable operation, and validates the use of a proportional controller. This is highly useful in mass-produced systems because a simple proportional controller typically requires fewer components, which is desirable since it drives production costs downward. In addition, the power draw of the tremor cancellation device was measured and found to be close to estimates (within 7%) produced during simulation, again demonstrating the predictive capabilities and accuracy of the model-based design. The recorded power draw showed significant viability for a battery-operated device with potential run-times of 1 hr with just 70 grams of battery weight. The demonstrated size and weight of the motion-generating

actuator was also shown to be significantly more compact than traditional actuation systems. Overall volume could be reduced to 0.5 in^3 for 2 DOF. This is 64% of the volume required for two conventional voice-coil actuators capable of producing the same motion (H2WTechnologies 2009).

While in the past technological solutions to human tremor have suffered from weight, comfort, and cost issues, the ACT system overall demonstrates a new active cancellation technology that uses antagonistic SMA actuators to provide motion in a compact, lightweight solution. In general, the ACT system has served to exemplify the work of this dissertation by demonstrating the first steps towards a generic technology that can be applied to a practical hand-held device, capable of providing assistance of the multitudes of individuals currently afflicted by tremor disorders.

6.1.5 Antagonistic SMA Actuator Characteristics and Design Strategies

Throughout this dissertation, a large amount of information was presented to guide the designer in creating antagonistic actuators; the following discussion reviews and compiles these findings into three main categories: environmental conditions, geometric properties, and electric heating input. Environmental conditions such as ambient temperature and the convective properties of the cooling medium were studied in detail both experimentally and in simulation through the use of the antagonistic model. Geometric properties including diameter, length, and mechanical advantage were all characterized by simulating a general antagonistic system and studying the specific application of the ACT device. Lastly, the effects of the electric heating input on the SMA wires acting in both open and closed loop were also characterized. The overall impact of key design variables in each of these three categories is summarized with respect to the performance of the antagonistic actuator for tremor cancellation. In

light of these aggregated findings, design strategies are suggested to minimize power consumption while maintaining frequency, amplitude, and cancellation performance.

6.1.5.1 Environmental Conditions

As studied in Chapters 3 and 4, the convective heat transfer coefficient h has significant impact on the performance of the antagonistic SMA actuator. Table 6.1 shows that a 10% increase in the convective coefficient increases the actuation frequency by 8% and power consumption by 5%. The ambient temperature is shown to have a similar effect, where a 10% increase decreases the operating frequency by 9% and power consumption by 5%. Though these effects are similar, it was shown in Section 3.1.2 that the convective coefficient can vary over several orders of magnitude, from 70 $Wm^{-1}K^{-1}$ (for air) to 5.5 $kWm^{-1}K^{-1}$ (for water), while in most applications the ambient temperature only varies from -40º C to 60º C. Furthermore in Section 4.3.2 it was shown that an ambient temperature above 43º C will not allow the 70º C Flexinol wires to cool beyond the Martensite finish temperature, thus developing unacceptable levels of stress (above shakedown limit) in the wires. Thus, in comparison to changes in ambient temperature, changing the convective coefficient more significantly affects frequency and power draw. The convective coefficient is also typically easier to control

Table 6.1. Effects of Key Design Variables. Each variable is increased by 10% for an operating condition of 12 mil diameter, 2 in wire length, and 3-4 Hz frequency range.

Input Variable			Output Result (% Change)			
Var.	**Name**	**%Variation**	**Frequency**	**Amplitude**	**Power Draw**	**RMS Cancellation**
h	Convective Coefficient	+10	+8	no effect	+5	no effect
T_a	Ambient Temp.	+10	-9	no effect	-5	no effect
D_c	Duty Cycle	+10	-2	-1.4	+2	no effect
d	Diameter	+10	-6.7	no effect	+11	no effect
l	Length	+10	no effect	+10	+10	+7
r	Mechanical Advantage	+10 (d +4, l -5)	-4	no effect	-5	no effect
p	Feedback Gain	+10	no effect	+7	+2	+7

(e.g. through variations in flow) and can be used to compensate for changes in ambient temperature. For example, a reduction in operating frequency caused by self-heating (e.g. through the increase in temperature of a liquid bath) may be compensated for by an increase in local flow. If the convective coefficient is raised by the same percent as the increase in ambient temperature, the frequency reduction will be eliminated and the power draw will be unaffected (Table 6.1). This strategy can be very useful in a variety of applications and can easily be implemented under closed-loop control.

Besides convective coefficient there are several additional design considerations, discussed in Chapter 3, that must be made when selecting a cooling medium for SMA wires. For example, even though water coolants provide the highest convective heat transfer (~5 $kWm^{-1}K^{-1}$) they also possess a high heat capacity, reducing the effect of self-heating. However, water coolants are difficult to manage in practical applications due to the need for improved sealing and special care for parts to resist corrosion. On the other hand, thermally conductive grease could be used to circumvent these issues but it is significantly more expensive, has a greater density (increased weight), and is difficult to spread evenly throughout a device. Despite these limitations, thermal grease does possess one key advantage over the other cooling media, that is, its high thermal conductivity (which is up to 115 times greater than air). This allows thermal grease to facilitate heat transfer to the environment, reducing the possibility of self-heating. Unlike water and thermal grease, oil provided an intermediate level of *h*-value, (between 512 and 997 $Wm^{-1}K^{-1}$). Oil is inexpensive and does not promote corrosion, but like water it does require careful sealing. Ambient air (with zero flow) provided the lowest *h*-value of the media tested in this dissertation, though it is much easier and cheaper to use in application, requiring no additional parts or installation. Due to its low heat capacity, air should be continuously exchanged to prevent temperature build-up.

This can be done through the introduction of forced air where *h*-values are improved by up to 5.6 times, though this benefit comes with the cost of an external fan or other means to move the air. An extra advantage gained by using forced convection is the ability to make live adjustments of the *h*-value over a large range (by a factor of 1.7 in these tests), such that the balance between cyclic performance and power consumption can be adjusted in real-time. Such adjustments may also be used to compensate for any losses in frequency performance due to changes in ambient temperature.

6.1.5.2 Geometric Properties

Another essential set of variables affecting system performance are the geometric properties of the SMA actuator, including the wire diameter, length, and mechanical advantage. The SMA diameter not only affects the amount of stress the material experiences for a given load, but also impacts its frequency capabilities. Increasing the wire diameter by 10%, for example, can reduce operating stress by 18% to prevent shakedown (Chapter 2), though this comes with a tradeoff of a 6.7% decreased operating frequency (Table 6.1) and 11% increased power consumption. While the frequency limitation can be averted through an increase in the convective coefficient or decrease in ambient temperature, this would result in even more of a penalty in power consumption (see Table 6.1). Thus, it is crucial to consider power draw when selecting larger diameter wires to reduce operating stress.

In addition to diameter, the SMA wire length was shown to significantly affect the performance of the antagonistic actuator. For example as shown in Table 6.1, a 10% increase in length increases the overall power draw and actuation stroke equally. This is due to an increase in material and in surface area associated with the longer length, which heightens convective losses to the environment during heating. In the closed-loop cancellation studies of the ACT, it was shown that an optimal solution

existed for the wire length. Lengths that were too short, for instance, produced insufficient motion causing the controller to increase energy delivery. In the case of the thermal grease medium, power consumption increased by 51% (from 8.6 to 13 Watts) when decreasing the wire length from the 1.8 inch optimum to the lower bound of 1.5 inches. Lengths that were too long, on the other hand, caused an increase in power requirement that was proportional to the increase in length beyond the optimal point (which is consistent with Table 6.1). However, this same increase in length did produce an equal return in improved cancellation. A 10% increase, for example, increased the RMS cancellation by 7%. Although cancellation performance can be improved in this way, it is crucial to realize the associated penalty in power consumption. Thus the general strategy should be to set an RMS cancellation goal as a constraint, within which power consumption can then be minimized.

In the antagonistic design studies, mechanical advantage (Section 4.3.1) was shown to couple wire length and diameter through an additional system parameter *r* that can be varied to achieve increased packaging and decreased power draw. The ACT system used this mechanical advantage in the form of an angled wire architecture that was studied in Section 5.2.6. In these cases, it was shown that using mechanical advantage to amplify motion through a greater input force was a favorable approach in terms of power consumption and packaging. Table 6.1 illustrates this fact, where a 10% increase in the lever ratio *r* requires a 4% increase in wire diameter *d* and a 5% reduction in wire length. Overall, this produces a 5% decrease in power consumption, indicating that a decrease in mechanical advantage (output force over input force) decreases power consumption. Packaging is also improved, as was demonstrated in the ACT design where a decrease in wire angle from 65 to 25 degrees reduced the planar surface area by as much as 7 times (see Section 5.2.6). The only penalty that arises when using a low

mechanical advantage is a decrease in frequency performance (Table 6.1). Thus, as discussed in Section 4.3.1, the mechanical advantage should be chosen such that the wire diameter performs just above the application's required frequency so as to avoid the build-up stress levels that can induce material shakedown.

6.1.5.3 Electric Heating Input

In addition to the environmental and geometric properties of the actuator, it was found in this dissertation that the driving conditions can significantly impact performance both in open and closed loop control. Under open-loop operation, studies in Chapter 4 demonstrated that for a given wire diameter and cooling medium, higher duty cycles heated the SMA wires over longer periods of time, producing smooth motion (nearing a sinusoid at the upper limit). However, the increase in duty cycle presented a drawback in the form of energy losses. For example, a 10% increase in duty cycle produces a 2% increase in power consumption (Table 6.1). While this effect seems small, it is important to recognize that the duty cycle can be varied by 450% (Section 4.3.3). Near the actuator's cooling limit, increases in the duty cycle decrease the available cooling time, producing amplitude degradation. In the same conditions, a 10% increase in duty cycle produces a 1.4% decrease in amplitude at a constant frequency. At constant amplitude the 10% increase in duty cycle produces a 2% decrease in frequency. Table 6.1 shows how these effects can be counteracted by changing some of the other system variables. For instance, the cooling medium can be adjusted to a higher h value or the ambient temperature T_a can be decreased. However, this would come with the cost of a further increase in power consumption.

Under closed-loop proportional control, the design studies of the ACT system showed that increasing gain p produced greater cancellation at the expense of an increase in power consumption due to higher controller activity. For example,

increasing the gain by 10% (from p =10 to p =11) had the effect of increasing the actuator's output amplitude by 7%, which in turn increased the RMS cancellation of the actuator by the same amount (see Table 6.1). However, due to the resulting increase in controller activity, power draw also increased by 2%. As shown in Section 5.2.5, this increase in power consumption can be significant, raising the energy requirements by 258%, from a gain of 5 to 55. Thus, a conservative controller gain should be selected to satisfy RMS cancellation goals (in simulation this was chosen to be less than 1%) while meeting the overall design objective of minimizing power consumption.

6.2 Limitations and Future Work

While this dissertation has developed several key innovations regarding antagonistic SMA for tremor cancellation, it is important to recognize some of the current technological limitations and identify directions of further research.

6.2.1 SMA Material

While several key issues of SMA have been addressed in this dissertation (namely speed, power, and predictability), there are a number of important areas that must be addressed to enable its commercial viability. One important matter is the number of cycles the wire can withstand before failing (fatigue). It has been reported that the stress levels in the SMA wire directly affect the fatigue life for full transformation (Bertacchini, et al. 2003). In addition, partial transformation was reported to significantly affect the number of cycles to failure. Strain amplitudes between 4.4% and 8.3% caused failures after 10^4 and 10^5, though reports of reducing the actuation amplitude below 3% prevented failure beyond 10^7 and 10^8 cycles (McNichols, et al. 1981). This is due to a superficial layer that exhibits brittleness during cooling and has a higher risk of developing cracks (Bertacchini, et al. 2003). These effects are complications that must be addressed if the material were to be run at high cyclic speeds

for long lifetime requirements. For a typical device being used at 3 Hz for one hour a day for two years, this amounts to 190E6 cycles. Further methods to characterize the number of cycles to failure should therefore be investigated, and studies can focus on modeling the relationship between fatigue life and operating stress, temperature, and percent transformation to aid in actuator design.

Material shakedown is another area requiring further attention. Through the work of this dissertation an empirical relationship was derived that fit the motion degradation of NiTi wire undergoing shakedown with high accuracy (0.99 R-value). This double exponential fit is suggestive of two physical processes may be modeled with a rate equation. The rate for each of these processes may be dependent on temperature, stress, and percent transformation during each cycle and can be modeled through a physically derived relationship. By understanding the physical mechanisms of the shakedown process, motion degradation can be avoided in future designs with greater ease. In addition, using a physical model the design process of a new class of actuators can be developed that operate at higher loads yet can react to a predictable motion loss by adjusting the wire's operating tensions.

6.2.2 Cooling Techniques

To improve and understand the cooling of SMA wires the midpoint transformation methodology was developed as a powerful technique capable of measuring the convective properties of any wire geometry in any cooling medium. However, the method, as presented, is only valid in the low temperature regimes where conventional SMA's operate. At higher temperatures (e.g. operating regimes of high-transformation temperature SMA's) radiation effects must be accounted for when measuring the heat dissipation, which is complicated since the wire emissivity must be known. Additionally, the measurement methodology is only able to reliably calculate a

convective coefficient at the wire's mid-point transformation temperature. For fluids where convection is dependent on the wire's surface temperature, a series of measurements is required to be taken over a range of SMA surface temperatures. Currently the only solution for this problem is to either approximate the relationship with existing empirical correlations, or to use a different material that changes resistivity with temperature. Both solutions, however, can only serve as estimates since existing correlations are known to be approximate and other materials likely have different surface features than particular SMA wire of interest.

Investigations on the use of Carbon Nanotubes (CNTs) to improve the cooling of SMA wires also had several key limitations that can be addressed in future work. In these experiments much lower nanotube densities were observed on the SMA wire than what can be obtained on silicon substrates. Additionally, the nanotubes were shorter than those grown on silicon. It is likely that with modifications of the PECVD process used, greater densities and lengths can be achieved, which would likely improve the heat transfer from the wire surface. Additionally, due to the nature of the PECVD process only half of the SMA wires were coated with the carbon nanotubes, limiting the enhanced cooling effect. Future work can investigate methods to change the orientation of the wire and geometry of the cathode to cover the entire wire surface in one deposition process.

6.2.3 Modeling

The antagonistic model was shown to predict the motion profiles of a generic actuator that is representative of a wide variety of systems. It was found that by selecting different empirical descriptions for the convective coefficient, more accurate fits were produced at each of the tested frequencies. However, it is desirable to have a physical description for convection and future work should focus on deriving a

relationship based on actuation frequency (inducing local flow) and ambient temperature. While this may be difficult to analytically model, dedicated experiments can be performed to obtain these relationships.

For many engineering applications a simple closed-form analytical solution is required to provide an estimate of output performance that is easy to solve. While the antagonistic model was indeed reduced from a much more general form (requiring a PDE solution), the compressive Martensite variable was retained to model slack in the system. The retention of this variable, however, reduced the model to a series of coupled ODE's still must be solved numerically, and depending on the simulation conditions the solution time very long. For these reasons, and for designs not requiring high precision, further model reduction should also be investigated in future work to determine a closed-form analytical solution such as the one proposed by (Shaw and Churchill 2009) for single wires.

6.2.4 Active Tremor Cancellation

To show feasibility of this dissertation's research the ACT system was successfully designed and tested, though several key improvements are still necessary to ensure the success and commercial viability. For instance, the ACT system's output motion amplitude was limited to a nominal level of 1 mm, which is not sufficient to stabilize large amplitude tremor present in many patients. The assistive device in its current form, however, can be used in conjunction with pharmacological treatments, which can bring a patient's level of tremor in the 1 mm range. Additionally, further work can focus on increasing the cancellation amplitude without significantly affecting the system's power requirements.

For the proof-of-concept device a sub-optimal solution was also chosen for ease of assembly and testing. Future work should extend on this prototype to create an actuator

operating at a smaller wire angle where shorter, larger diameter wires can be used in a thermal grease cooling medium. According to the parameter study in this dissertation, selecting this type of design would significantly reduce the power consumption and reduce the size and weight of a packaged battery (by nearly half). Additional work is also recommended test the ACT device in 2 DOF. Since the two DOF's are currently designed to be decoupled, the process is a relatively easy task as the design and control of the first DOF would simply be replicated. It is crucial, however, that the DOF's designed in a future prototype operate in the required directions for patient tremor stabilization. To accomplish this, characterizations of a patient's tremor should be performed to identify the dominant directions of movement. Trials should also be accomplished to characterize the physiological response of the patient's tremor with respect to visual feedback (i.e. stabilized vs. non-stabilized) and to investigate the ACT device's role in rehabilitation. These efforts would be instrumental in extending the hand-held ACT device into the marketplace where it will serve as a competitive, cost-effective solution.

6.3 Future Applications and Spinoffs

While direct uses of the tremor cancellation technology have been illustrated in the military and medical case-studies, the fundamental research conducted in this thesis can benefit many additional areas. For example, the midpoint transformation methodology and growth of carbon nanotubes on SMA has many potential applications in the microscale. The use of the Nickel in the NiTi alloy as catalyst particles has allowed the growth of CNTs on a metal substrate, which is currently very difficult to achieve yet highly desirable due to the direct thermal contact of the cooling fins. Thus certain structures requiring a large amount of heat dissipation in a small scale can be built with the NiTi alloy. Microscale shape memory alloy actuators can also be built and treated

with CNTs to improve their frequency response, which would allow for a class of microstructures capable of producing large-amplitude and large-force cyclic motion.

This dissertation's antagonistic modeling, combined with the convective cooling measurements has also enabled the predictive design of many potential applications that require stable, cyclic operation at the upper frequency bounds of SMA. Examples of these applications include new types of lightweight and compact pumps, electric/mechanical switches, and optical controls. The antagonistic modeling can also be used to predict the SMA material's reaction to changing environments. By knowing a changing ambient temperature, for example, and treating it as an input to the model, an SMA actuator can be designed to produce a specified motion profile over a temperature range. This can enable passively responding structures such as windows, vents, safety latches, and automatic shut-off valves where the control, temperature sensing, and actuation can all be designed into the SMA material and actuation mechanism.

The general technology developed in the ACT and SMASH case-studies can also be extended to several different applications. For example, additional cases of human-tool interaction can be addressed including the development of new precision instruments for surgeons and manufacturing tools. The vibration cancellation technology can also be extended beyond human interaction where disturbances must be reduced in a small and compact manner. For instance, antagonistic actuators could be embedded in various built structures where they can provide cyclic motion to stabilize vibrations caused by seismic events, improving overall earthquake safety. These actuators can be cost-effective and in some cases may provide an attractive solution to an expensive seismic retrofit. Active cancellation using antagonistic SMA actuators can additionally be used in moving vehicle settings where, for example, various

electronics and displays can be stabilized to enhance visualization when traveling over rough terrain. Overall, the work of this dissertation has developed a base technology that has been shown to have significant promise in human tremor cancellation, yet can also be extended to introduce new and useful technologies in several market sectors. These technologies will not only inspire future research but also and introduce novel products in the world marketplace.

References

Allum, J. H., V. Dietz, and H. J. Freund
1978 Neuronal mechanisms underlying physiological tremor. Journal of Neurophysiology 41(3):557-571.

Ang, W. T.
2004 Active tremor compensation in handheld instrument for microsurgery. Robotics Institute, Carnegie Mellon University, Ph. D. Dissertation CMU-RI-TR-04-28.

Ang, W. T., P. K. Khosla, and C. N. Riviere
2005 Kalman filtering for real-time orientation tracking of handheld microsurgical instrument, 2005. Vol. 3.

Anouti, A., and W. C. Koller
1995 Tremor disorders. Diagnosis and management. Western Journal of Medicine 162(6):510.

Army, US
1994 FM 23-10 sniper training. .

—
2003 FM3-22.9, rifle marksmanship M16A1, M16A2/3, M16A4 and M4 CARBINE chapter 7-29.

Arnau, A.
2008 Piezoelectric transducers and applications: Springer Verlag.

AuBuchon, J. F., L. H. Chen, A. I. Gapin, D. W. Kim, C. Daraio, and S. Jin
2004 Multiple sharp bendings of carbon nanotubes during growth to produce zigzag morphology. Nano Letters 4(9):1781-1784.

AuBuchon, J. F., L. H. Chen, and S. Jin
2005 Control of carbon capping for regrowth of aligned carbon nanotubes. J. Phys. Chem. B 109(13):6044-6048.

Ay, H., J. Y. Jang, and J. N. Yeh
2002 Local heat transfer measurements of plate finned-tube heat exchangers by infrared thermography. International Journal of Heat and Mass Transfer 45(20):4069-4078.

Ballantyne, G. H., and F. Moll
2003 The da Vinci telerobotic surgical system: the virtual operative field and telepresence surgery. Surgical Clinics of North America 83(6):1293-1304.

Banks, H. T., R. C. Smith, and Y. Wang
1997 Smart material structures: modeling, estimation, and control: John Wiley & Son Ltd.

Barnes, B., D. Brei, J. Luntz, and C. Lavigna
2005 Development of an Antagonistic SMA Actuator for INSTAR Rifle stabilization System. Proceedings of IMECE2005 ASME International Mechanical Engineering Congress and Exposition, 2005.

Bellouard, Y., R. Clavel, R. Gotthardt, J. E. Bidaux, and T. Sidler
1998 A new concept of monolithic shape memory alloy micro-devices used in micro-robotics, 1998. Vol. 98, pp. 499-502.

Bengi, H., and J. G. Thomas

1973 Studies on human ocular tremor. Perspectives in biomedical engineering:281–292.

Berber, S., Y. K. Kwon, and D. Tomanek
1966 Unusually high thermal conductivity of carbon nanotubes. J. Phys. Chem. Solids Phys Rev Lett 84:4613.

Bertacchini, O. W., D. C. Lagoudas, and E. Patoor
2003 Fatigue life characterization of shape memory alloys undergoing thermomechanical cyclic loading. Smart Structures and Materials 2003 5053:612-624.

Bharti, S., and M. I. Frecker
2004 Optimal design and experimental characterization of a compliant mechanism piezoelectric actuator for inertially stabilized rifle. Journal of Intelligent Material Systems and Structures 15(2):93.

Bhattacharya, K.
2003 Microstructure of martensite: Why it forms and how it gives rise to the shape-memory effect: Oxford University Press, USA.

Bhattacharya, P., Y. Joshi, A. Fedorov, N. Bajwa, and P. Ajayan
2006 Carbon Nanotube (CNT) Fins for Forced Convection Cooling of High Power Microprocessors, 2006, pp. 146-146.

Bhattacharyya, A., D. C. Lagoudas, Y. P. Wang, and V. K. Kinra
1995 Thermoelectric cooling of shape memory alloy actuators: theoretical modeling and experiment, 1995. Vol. 2427, pp. 198.

Bhattacharyya, A., L. Sweeney, and M. G. Faulkner
2002 Experimental characterization of free convection during thermal phase transformations in shape memory alloy wires. Smart Materials and Structures 11(3):411-422.

Brei, D. E., J. Vendlinski, D. K. Lindner, H. Zhu, and C. LaVigna
2003 Development and demonstration of INSTAR: inertially stabilized rifle. Proceedings of the SPIE, Smart Structures and Materials, 2003. Vol. 5056, pp. 255.

Brinson, L. C.
1993 One-dimensional constitutive behavior of shape memory alloys: thermomechanical derivation with non-constant material functions and redefined martensite internal variable. Journal of Intelligent Material Systems and Structures 4(2):229.

Browne, A., N. L. Johnson, J. Aase, and J. Brown
2008 Active Material Actuated Louver System.

Buehler, W. J., and F. E. Wang
1968 A summary of recent research on the nitinol alloys and their potential application in ocean engineering. Ocean Eng 1(1):105-120.

Busch, J. D., W. E. Purdy, and A. D. Johnson
1992 Development of a non-explosive release device for aerospace applications. The 26th Aerospace Mechanisms Symposium, 1992. Vol. 1992.

Calzetti, S., M. Baratti, M. Gresty, and L. Findley
1987 Frequency/amplitude characteristics of postural tremor of the hands in a population of patients with bilateral essential tremor: implications for the classification and mechanism of essential tremor. British Medical Journal 50(5):561-567.

Cao, C., and G. Rogers
2007 Robotics in healthcare: HF issues in surgery: Online paper. http://ase. tufts. edu/mechanical/EREL/Publ ications/D-4. pdf.

Chang, B. C., J. A. Shaw, and M. A. Iadicola
2006 Thermodynamics of Shape Memory Alloy Wire: Modeling, Experiments, and Application. Continuum Mechanics and Thermodynamics 18(1):83-118.

Chang, L. C., and T. A. Read
1951 Plastic deformation and diffusionless phase changes in metals—the gold–cadmium beta phase. Am. Inst. Min. Metall. Eng.—J. Met 191(1):47–52.

Che, J., T. Cagin, and W. A. Goddard Iii

2000 Thermal conductivity of carbon nanotubes. Nanotechnology 11:65-69.

Chhowalla, M., K. B. K. Teo, C. Ducati, N. L. Rupesinghe, G. A. J. Amaratunga, A. C. Ferrari, D. Roy, J. Robertson, and W. I. Milne

2001 Growth process conditions of vertically aligned carbon nanotubes using plasma enhanced chemical vapor deposition. Journal of Applied Physics 90:5308.

Choi, D. Y., and C. N. Riviere

2005 Flexure-based manipulator for active handheld microsurgical instrument. Engineering in Medicine and Biology Society, 2005. IEEE-EMBS 2005., 2005, pp. 2325-2328.

Chopra, I.

2002 Review of State of Art of Smart Structures and Integrated Systems. AIAA Journal 40(11):2145-2187.

Chung, J. H., J. S. Heo, and J. J. Lee

2007 Implementation strategy for the dual transformation region in the Brinson SMA constitutive model. Smart Materials and Structures 16:N1-N5.

Churchill, C. B., and J. A. Shaw

2008 Shakedown response of conditioned shape memory alloy wire, 2008. Vol. 6929, pp. 69291F.

Churchill, C. B., J. A. Shaw, and M. A. Iadicola

2009 Tips and Tricks for Characterizing Shape Memory Alloy Wire: Part 2 — Fundamental Isothermal Responses. Experimental Techniques 33(1):51-62.

Clark, A. E.

1980 Ferromagnetic materials. Vol 1:533.

Cleary, K., and C. Nguyen

2002 State of the art in surgical robotics: clinical applications and technology challenges. Journal of Image Guided Surgery 6(6):312-328.

Congalton, D.

1999 Shape memory alloys for use in thermally activated clothing, protection against flame and heat. Fire and materials 23(5):223-226.

Cullity, B. D., and C. D. Graham

2008 Introduction to magnetic materials: IEEE.

Dapino, M. J., R. C. Smith, L. A. E. Faidley, and A. B. Flatau

2000 A coupled structural-magnetic strain and stress model for magnetostrictive transducers. Journal of Intelligent Material Systems and Structures 11(2):135.

De Laurentis, K. J., and C. Mavroidis

2002 Mechanical design of a shape memory alloy actuated prosthetic hand. Technology and Health Care 10(2):91-106.

Dietz, V., E. Bischofberger, C. Wita, and H. J. Freund

1976 Correlation between the dischanges of two simultaneously recorded motor units and physiological tremor. Electroencephalography and clinical neurophysiology 40(1):97.

Ditman, J. B., L. A. Bergman, and T. C. Tsao

1996 The design of extended bandwidth shape memory alloy actuators. Journal of Intelligent Material Systems and Structures 7(6):635-645.

Duerig, T., A. Pelton, and D. Stöckel

1999 An overview of nitinol medical applications. Materials Science and Engineering A 273(275):1-2.

Dye, T. E.

1990 An experimental investigation of the behavior of nitinol Masters, Virginia Tech.

Dynalloy

2009 Introduction to Flexinol.

Elble, R. J.

1986 Physiologic and essential tremor. Neurology 36(2):225-231.

—

1995 Mechanisms of Physiological Tremor and Relationship to Essential Tremor. Handbook of Tremor Disorders.

Elble, R. J., M. Brilliant, K. Leffler, and C. Higgins
1996 Quantification of essential tremor in writing and drawing. Movement Disorders 11(1):70-78.

Elble, R. J., and J. E. Randall
1978 Mechanistic components of normal hand tremor. Electroencephalography and clinical neurophysiology 44(1):72.

Electrophysics
2008 Electrophysics Corp.

EngineeringToolBox
2009 The Engineering Toolbox, Vol. 2009.

Erbstoeszer, B., B. Armstrong, M. Taya, and K. Inoue
2000 Stabilization of the shape memory effect in NiTi: an experimental investigation. Scripta Materialia 42(12):1145-1150.

Evidente, V. G. H.
2000 Understanding essential tremor. Postgrad Med 108:138-49.

Falcioni, J. G.
1992 Shape memory alloys. Mechanical Engineering-CIME v114 4:114.

Featherstone, R., and Y. H. Teh
2006 Improving the speed of shape memory alloy actuators by faster electrical heating, 2006, pp. 67. Springer.

Forssberg, H., P. E. Ingvarsson, N. Iwasaki, R. S. Johansson, and A. M. Gordon
2000 Action tremor during object manipulation in Parkinson's disease. Movement Disorders 15(2).

Fox, J. R., and J. E. Randall
1970 Relationship between forearm tremor and the biceps electromyogram. Journal of Applied Physiology 29(1):103-108.

Godard, O. J., M. Z. Lagoudas, and D. C. Lagoudas
2003 Design of space systems using shape memory alloys. Proceedings of the SPIE, Smart Structures and Materials, 2003. Vol. 5056, pp. 545.

Grant, D., and V. Hayward
2000 Constrained force control of shape memory alloy actuators. Proc. of the IEEE Int. Conf. on Robotics and Automation, 2000. Vol. 2, pp. 1314-1320. Citeseer.

Grant, Danny
1999 Accurate and Rapid Control of Shape Memory Alloy Actuators, Department of Electrical and Computer Engineering, McGill University.

H2WTechnologies
2009 Voce Coil Linear Actuators (Non Commutated DC Linear Actuators).

Hartl, D. J., and D. C. Lagoudas
2007 Aerospace applications of shape memory alloys. Proceedings of the Institution of Mechanical Engineers, Part G: Journal of Aerospace Engineering 221(4):535-552.

Heath, Mark, Mike Topping, Richard Huxley, and Paul Hawkins
2003 Design Considerations in Active Orthoses for Tremor Suppression: Ergonomic Aspects and Integration of Enabling Technologies. Assistive Technology -- Shaping the Future AAATE.

Hemsel, T., and J. Wallaschek
2000 Survey of the present state of the art of piezoelectric linear motors. Ultrasonics 38(1-8):37-40.

Hendriks, J., M. Rosen, N. L. J. Berube, and M. L. Aisen
1991 A second-generation joystick for people disable by tremor. Proc. 14th Annual RESNA Conference, 1991, pp. 21-26.

Higgins, G. C., and K. F. Stultz
1953 Frequency and amplitude of ocular tremor. Journal of the Optical Society of America 43(12):1136-1140.

Hilpert, R.
1933 Correlations for Laminar Forced Convection in Flow Over an Isothermal Flat Plate and in Developing and Fully Developed Flow in an Isothermal Tube. Forsch Gebiete Ingenieurwes 4.
Hu, M., H. Du, S. F. Ling, Z. Zhou, and Y. Li
2004 Motion control of an electrostrictive actuator. Mechatronics 14(2):153-161.
Huang, W.
2002 On the selection of shape memory alloys for actuators. Materials and Design 23(1):11-19.
Huber, J. E., N. A. Fleck, and M. F. Ashby
1997 The selection of mechanical actuators based on performance indices. Proceedings: Mathematical, Physical and Engineering Sciences:2185-2205.
Iadicola, M. A., and J. A. Shaw
2002 The effect of uniaxial cyclic deformation on the evolution of phase transformation fronts in pseudoelastic NiTi wire. JOURNAL OF INTELLIGENT MATERIAL SYSTEMS AND STRUCTURES 13(2-3):143.
—
2004 Rate and thermal sensitivities of unstable transformation behavior in a shape memory alloy. International Journal of Plasticity 20(4-5):577-605.
Ikuta, K.
1990 Micro/miniature shape memory alloy actuator, 1990, pp. 2156-2161.
Ikuta, K., M. Tsukamoto, and S. Hirose
1988 Shape memory alloy servo actuator system with electric resistancefeedback and application for active endoscope, 1988, pp. 427-430.
Incropera, F. P., and D. P. DeWitt
2001 Heat and mass transfer. John Wiley & Sons, Inc.
IntelligentAutomation
2009 Army SBIR Awards.
Joyce, G. C., and P. M. Rack
1974 The effects of load and force on tremor at the normal human elbow joint. The Journal of Physiology 240(2):375-396.
Kallmayer, C., D. Lin, J. Kloeser, H. Oppermann, E. Zakel, and H. Reichl
1995 Fluxless flip-chip attachment techniques using the Au/Sn metallurgy, 1995, pp. 20-28.
Kallmayer, C., H. Oppermann, G. Eugelmann, E. Zakel, and H. Reichl
1996 Self-aligning flip-chip assembly using eutectic gold/tin solder indifferent atmospheres, 1996, pp. 18-25.
Kandlikar, S. G., S. Joshi, and S. Tian
2003 Effect of channel roughness on heat transfer and fluid flow characteristics at low Reynolds numbers in small diameter tubes. Atmosphere 4(6):7.
Kauffman, G. B., and I. Mayo
1997 The story of nitinol: the serendipitous discovery of the memory metal and its applications. The Chemical Educator 2(2):1-21.
Kohl, M., B. Krevet, and E. Just
2002 SMA microgripper system. Sensors & Actuators: A. Physical 97:646-652.
Koo, J., and C. Kleinstreuer
2005 Analysis of surface roughness effects on heat transfer in micro-conduits. International Journal of Heat and Mass Transfer 48(13):2625-2634.
Kordás, K., G. Tóth, P. Moilanen, M. Kumpumäki, J. Vähäkangas, A. Uusimäki, R. Vajtai, and P. M. Ajayan
2007 Chip cooling with integrated carbon nanotube microfin architectures. Applied Physics Letters 90:123105.
Kromann, G. B.
1995 Thermal Modeling and Experimental Characterization of the C4/Surface-Mount-Array Interconnect Technologies. IEEE Transactions on

Components Packaging and Manufacturing Technology Part A 18:87-87.
Krulevitch, P., A. P. Lee, P. B. Ramsey, J. C. Trevino, J. Hamilton, and M. A. Northrup
1996 Thin film shape memory alloy microactuators. Microelectromechanical Systems, Journal of 5(4):270-282.
Lagoudas, D. C.
2008 Shape Memory Alloys: Modeling and Engineering Applications: Springer Verlag.
Lagoudas, D. C., P. B. Entchev, and P. K. Kumar
2003 Thermomechanical characterization SMA actuators under cyclic loading, 2003. Vol. 3, pp. 15–21.
Lagoudas, D. C., C. Li, D. A. Miller, and L. Rong
2000 Thermomechanical transformation fatigue of SMA actuators, 2000. Vol. 3992, pp. 420.
Levine, J. L., and M. A. Schappert
2005 A mouse adapter for people with hand tremor. IBM Systems Journal 44(3):622.
Liang, C., and C. A. Rogers
1990 One-dimensional thermomechanical constitutive relations for shape memory materials. Journal of Intelligent Material Systems and Structures 1(2):207.
Lindner, D. K., H. Zhu, D. Brei, J. Vindlinski, C. LaVigna, and I. TechnoSciences
2002 Intertially Stabilized Rifle Using Recurve Actuators. Proceedings of IMECE, 2002. Vol. 1001, pp. 48109-2125.
Mabe, J. H., F. Calkins, and G. Butler
2006 Boeing's variable geometry chevron, morphing aerostructure for jet noise reduction, 2006, pp. 1–19.
Maclean, B. J., B. F. Carpenter, and M. S. Misra
1997 Adaptive control surface using antagonistic shape memory alloy tendons: Google Patents.
Manto, M., M. Topping, M. Soede, J. Sanchez-Lacuesta, W. Harwin, J. Pons, J. Williams, S. Skaarup, and L. Normie
2003 Dynamically responsive intervention for tremor suppression. Engineering in Medicine and Biology Magazine, IEEE 22(3):120-132.
Marshall, J., and E. G. Walsh
1956 Physiological tremor. British Medical Journal 19(4):260.
McKnight, G. P., A. L. Browne, and N. L. Johnson
2009 A reversibly deployable air dam: a bending approach based on embedded shape memory alloy actuators, Part II: technology demonstration. Industrial and Commercial Applications of Smart Structures Technologies. 7290:72900C-72900C.
McNichols, J. L., P. C. Brookes, and J. S. Cory
1981 NiTi fatigue behavior. Journal of Applied Physics 52(12):7442-7444.
McQuillan, F.J., J.R. Culham, and M.M. Yovanovich
1984 Properties of Some Gases and Liquids at One Atmosphere. University of Waterloo.
McQuillan, Frank
2009 Thermal Fluid Properties Calculator. Waterloo, Ontario.
Meinders, E. R., T. H. Van Der Meer, and K. Hanjalic
1998 Local convective heat transfer from an array of wall-mounted cubes. International Journal of Heat and Mass Transfer 41(2):335-346.
MemryCorporation
2009.
Michaelis, J.
1988 Introducing the neat eater. Action Res 6(1):2-3.
Miyazaki, S., T. Imai, Y. Igo, and K. Otsuka
1986 Effect of cyclic deformation on the pseudoelasticity characteristics of Ti-Ni alloys. Metallurgical and Materials Transactions A 17(1):115-120.

Miyazaki, S., K. Mizukoshi, T. Ueki, T. Sakuma, and Y. Liu
1998 Fatigue life of Ti-50 at.% Ni and Ti-40 Ni-10 Cu(at.%) shape memory alloy wires. Materials Science and Engineering A(Switzerland) 273:658-663.
Moallem, M., and V. A. Tabrizi
2009 Tracking Control of an Antagonistic Shape Memory Alloy Actuator Pair. IEEE Transactions on Control Systems Technology 17(1):184-190.
Morgan, V. T.
1975 The overall convective heat transfer from smooth circular cylinders. Advances in heat transfer. 11:199-264.
Nam, T. H., J. P. Noh, D. W. Jung, Y. W. Kim, H. J. Im, J. S. Ahn, and T. Mitani
2002 The R phase transformation in Ti-49Ni (at.%) shape memory alloy ribbons fabricated by melt spinning. Journal of Materials Science Letters 21(1):11-13.
NeaterSolutions
2009 Neater Solutions.
Nersessian, Nersesse
2001 Personal Conversation with B. Galeazzi, US Army ARDEC.
NPF
2009 Treatment Options, National Parkinson Foundation.
NSAC
2007 Advanced fire control technology RPP.
Ölander, A.
1932 An electrochemical investigation of solid cadmium-gold alloys. Journal of the American Chemical Society 54(10):3819-3833.
Omega
2009 Omega Engineering, Inc.
Otsuka, K., and X. Ren
2005 Physical metallurgy of Ti–Ni-based shape memory alloys. Progress in Materials Science 50(5):511-678.
Pathak, A., D. Brei, and J. Luntz
2008 Experimental Characterization of the Convective Heat Transfer from Shape Memory Alloy (SMA) Wire to Various Ambient Environments. ICAST, Ascona, Switzerland, 2008.
Pathak, A., D. Brei, J. Luntz, C. LaVigna, and H. Kwatny
2007 Design and quasi-static characterization of SMASH: SMA stabilizing handgrip, 2007. Vol. 6523, pp. 652304.
Patkin, M.
1977 Ergonomics Applied to the Practice of Microsurgery. ANZ Journal of Surgery 47(3):320-329.
Paul S. Slack, and Xianghong Ma
2007 Tremor amplitude determination for use in clinical applications. Measurement Science and Technology (11):3471.
Pfeiffer, C., K. DeLaurentis, and C. Mavroidis
1999 Shape memory alloy actuated robot prostheses: initial experiments, 1999, pp. 2385-2391. Citeseer.
Piezomechanick
2009 Technical Specifications 1000/16/200.
Pitt, D. M., J. P. Dunne, E. V. White, and E. Garcia
2001 SAMPSON smart inlet SMA powered adaptive lip design and static test, 2001, pp. 16–20.
Pohl, M., C. Heßing, and J. Frenzel
2004 Electrolytic processing of NiTi shape memory alloys. Materials Science & Engineering A 378(1-2):191-199.
Potapov, P. L., and E. P. Da Silva
2000 Time response of shape memory alloy actuators. Journal of Intelligent Material Systems and Structures 11(2):125.

Putzke, J. D., Jr R. E. Wharen, A. A. Obwegeser, Z. K. Wszolek, J. A. Lucas, M. F. Turk, and R. J. Uitti
2004 Thalamic Deep Brain Stimulation Essential Tremor: Recommendations Long-Term Outcome Analysis. The Canadian Journal of Neurological Sciences 31(3):333-342.
Qiu, J., J. Tani, D. Osanai, Y. Urushiyama, and D. Lewinnek
2000 High-speed response of SMA actuators. International Journal of Applied Electromagnetics and Mechanics 12(1):87-100.
Redmond, J. A., D. Brei, J. Luntz, A. L. Browne, and N. L. Johnson
2008 Behavioral model and experimental validation for a spool-packaged shape memory alloy actuator. Proceedings of SPIE, the International Society for Optical Engineering, San Diego, CA, 2008. Vol. 6930, pp. 693004.
—
2009 Effect of bending on the performance of spool-packaged shape memory alloy actuators. Proceedings of the SPIE, San Diego, 2009. Vol. 7290, pp. 729007.
Reynaerts, D., and H. V. Brussel
1998 Design aspects of shape memory actuators. Mechatronics 8(6):635-656.
Reynolds, D. D., and R. H. Keith
1977 Hand arm vibration. Part I: Analytical model of the vibration response characteristics of the hand. Journal of Sound and Vibration 51(2):237-253.
Reynolds, D. D., and W. Soedel
1972 Dynamic response of the hand-arm system to a sinusoidal input. Journal of Sound and Vibration 21(3):339-353.
Riviere, C. N., W. T. Ang, and P. K. Khosla
2003 Toward active tremor canceling in handheld microsurgical instruments. IEEE Transactions on Robotics and Automation 19(5):793-800.
Rocon, E.
2004 Pathological tremor management: Modelling, compensatory technology and evaluation. Technology and Disability 16(1):3-18.
Rocon, E., M. Manto, J. Pons, S. Camut, and J. M. Belda
2007 Mechanical suppression of essential tremor. The Cerebellum 6(1):73-78.
Rocon, E., A. F. Ruiz, and J. Pons
2003 Theoretical control discussion on tremor suppression via biomechanical loading, 2003, pp. 832–836.
Rocon, E., A. F. Ruiz, J. L. Pons, J. M. Belda-Lois, and J. J. Sanchez-Lacuesta
2005 Rehabilitation robotics: a wearable exo-skeleton for tremor assessment and suppression. Robotics and Automation, 2005. ICRA 2005. Proceedings of the 2005 IEEE International Conference, 2005, pp. 2271-2276.
Rondelli, G.
1996 Corrosion resistance tests on NiTi shape memory alloy. Biomaterials 17(20):2003-2008.
Rosen, M. J., A. S. Arnold, I. J. Baiges, M. L. Aisen, and S. R. Eglowstein
1995 Design of a controlled-energy-dissipation orthosis (CEDO) for functional suppression of intention tremors. J Rehabil Res Dev 32(1):1-16.
Sagma, S.
2003 Tremor. American family physician(1970) 68(8):1545-1552.
Salzbrenner, R.
1984 Shape memory heat engines. Journal of Materials Science 19(6):1827-1835.
Sanders, B., D. Cowan, and L. Scherer
2004 Aerodynamic performance of the smart wing control effectors. Journal of Intelligent Material Systems and Structures 15(4):293.
Sanitjai, S., and R. J. Goldstein
2004 Forced convection heat transfer from a circular cylinder in crossflow to air and liquids. International Journal of Heat and Mass Transfer 47(22):4795-4805.
Saraf, S.

2006 Role of robot assisted microsurgery in Plastic Surgery. Indian Journal of Plastic Surgery 39(1):57.

Schäfer, E. A.
1886 On the rhythm of muscular response to volitional impulses in man. The Journal of Physiology 7(2):111.

Seelecke, S., and I. Müller
2004 Shape memory alloy actuators in smart structures: Modeling and simulation. Applied Mechanics Reviews 57:23.

Shabalovskaya, S. A.
1996 On the nature of the biocompatibility and on medical applications of NiTi shape memory and superelastic alloys. Bio-medical materials and engineering 6(4):267.

Shahani, B. T., and R. R. Young
1976 Physiological and pharmacological aids in the differential diagnosis of tremor. British Medical Journal 39(8):772.

Shahin, A. R., P. H. Meckl, J. D. Jones, and M. A. Thrasher
1994 Enhanced cooling of shape memory alloy wires using semiconductor" heat pump" modules. Journal of Intelligent Material Systems and Structures 5(1):95.

Sharoky, C.
2005 Time spent under anesthesia could up risk. Retrieved January 4:2008.

Shaw, J. A.
2002 A thermomechanical model for a 1-D shape memory alloy wire with propagating instabilities. International Journal of Solids and Structures 39(5):1275-1305.

Shaw, J. A., and C. B. Churchill
2009 A reduced-order thermomechanical model and analytical solution for uniaxial shape memory alloy wire actuators. Smart Materials and Structures 18(6):065001.

Sidman, A. D.
2006 HANDHELD PLATFORM STABILIZATION SYSTEM EMPLOYING DISTRIBUTED ROTATION SENSORS: Google Patents.

Singh, K., J. Sirohi, and I. Chopra
2003 An improved shape memory alloy actuator for rotor blade tracking. Journal of Intelligent Material Systems and Structures 14(12):767.

Song, G., V. Chaudhry, and C. Batur
2003 Precision tracking control of shape memory alloy actuators using neural networks and a sliding-mode based robust controller. Smart Materials and Structures 12:223-231.

Stephens, J. A., and A. Taylor
1974 The effect of visual feedback on physiological muscle tremor. Electroencephalography and clinical neurophysiology 36:457-464.

Sun, H., A. Pathak, J. Luntz, D. Brei, P. W. Alexander, and N. L. Johnson
2008 Stabilizing shape memory alloy actuator performance through cyclic shakedown: an empirical study. Proceedings of the SPIE, Smart Structures and Materials, San Diego, CA, 2008. Vol. 6930, pp. 69300Q.

Sundar, V., and R. E. Newnham
1992 Electrostriction and polarization. Ferroelectrics 135(1):431-446.

Sung, G. T., and I. S. Gill
2001 Robotic laparoscopic surgery: a comparison of the da Vinci and Zeus systems. Urology 58(6):893-898.

Sutton, G. G., and K. Sykes
1967 The effect of withdrawal of visual presentation of errors upon the frequency spectrum of tremor in a manual task. The Journal of Physiology 190(2):281-293.

Talamini, M. A., and E. J. Hanly
2005 Technology in the operating suite. Pp. 863-866, Vol. 293: Am Med Assoc.

Tan, X., and J. S. Baras

2004 Modeling and control of hysteresis in magnetostrictive actuators. Automatica 40(9):1469-1480.

Tanaka, K.
1986 A thermomechanical sketch of shape memory effect: one-dimensional tensile behavior. Res Mech. 18(3):251-263.

Taylor, R., P. Jensen, L. Whitcomb, A. Barnes, R. Kumar, D. Stoianovici, P. Gupta, Z. X. Wang, E. Dejuan, and L. Kavoussi
1999 A steady-hand robotic system for microsurgical augmentation. The International Journal of Robotics Research 18(12):1201.

Teh, Y. H., and R. Featherstone
2008 An Architecture for Fast and Accurate Control of Shape Memory Alloy Actuators. The International Journal of Robotics Research 27(5):595.

Teravainen, H., and D. B. Calne
1980 Action tremor in Parkinson's disease. British Medical Journal 43(3):257-263.

Thanvi, B., N. Lo, and T. Robinson
2006 Essential tremor-the most common movement disorder in older people. Age and ageing 35(4):344-349.

Tolbert, M. A.
2002 Expertise in nano-alignment aids photonics manufacturing. Laser focus world 38(1):161-169.

Tsugawa, C., E. Nishijima, T. Muraji, M. Yoshimura, N. Tsubota, and H. Asano
1997 A shape memory airway stent for tracheobronchomalacia in children: an experimental and clinical study. Journal of pediatric surgery 32(1):50-53.

Uchino, K.
1992 Electrostrictive actuators: materials and applications. Piezoelectricity:331.

Vincent, C. A.
2000 Lithium batteries: a 50-year perspective, 1959–2009. Solid State Ionics 134(1-2):159-167.

Volpe, B. T., M. Ferraro, H. I. Krebs, and N. Hogan
2002 Robotics in the rehabilitation treatment of patients with stroke. Current Atherosclerosis Reports 4(4):270-276.

Von Wahlde, R., M. Kregel, T. Haug, and T. Brosseau
1996 Application of an Inertial Reticle System to an Objective Personal Weapon: ARMY RESEARCH LAB ABERDEEN PROVING GROUND MD.

Voyles, R. M., and S. Hulst
2005 Micro/macro force-servoed gripper for precision photonics assembly and analysis. Robotica 23(04):401-408.

Wang, F. E., W. J. Buehler, and S. J. Pickart
1965 Crystal Structure and a Unique``Martensitic"Transition of TiNi. Journal of Applied Physics 36:3232.

Wang, T., M. Jonsson, E. Nystrom, Z. Mo, E. E. B. Campbell, and J. Liu
2006 Development and characterization of microcoolers using carbon nanotubes, 2006. Vol. 2.

Weaver, J. M.
1990 System Error Budgets, Target Distributions and Hitting Performance Estimates for General-Purpose Rifles and Sniper Rifles of 7.62 x 51 mm and Larger Calibers: Army Material Systems Analysis Activity Aberdeen Proving Ground.

Wellman, P. S., W. J. Peine, G. Favalora, and R. D. Howe
1998 Mechanical Design and Control of a High-Bandwidth Shape Memory Alloy Tactile Displays. Lecture Notes in Control and information Sciences:56-66.

Williams, E. A., and M. H. Elahinia
2006 Design of a two degree of freedom shape memory alloy actuator for mirror positioning, 2006. Vol. 6173, pp. 617304.

Wu, X. D., Y. Z. Fan, and J. S. Wu
2000 A study on the variations of the electrical resistance for NiTi shape memory

alloy wires during the thermo-mechanical loading. Materials and Design 21(6):511-515.

Xu, J., and T. S. Fisher

2006 Enhancement of thermal interface materials with carbon nanotube arrays. International Journal of Heat and Mass Transfer 49(9-10):1658-1666.

Zesiewicz, T. A., and R. A. Hauser

2001 Phenomenology and treatment of tremor disorders. Neurologic Clinics 19(3):651-680.

Zhan, F., L. J. Jiang, B. R. Wu, Z. H. Xia, X. Y. Wei, and G. R. Qin

1999 Characteristics of Ni/MH power batteries and its application to electric vehicles. Journal of Alloys and Compounds 293:804-808.

Zhang, H., Y. Bellouard, T. C. Sidler, E. Burdet, A. N. Poo, and R. Clavel

2001 Monolithic Shape Memory Alloy microgripper for 3D assembly of tissue engineering scaffolds, 2001. Vol. 4568, pp. 50.

Zukauskas, A., J. Ziugzda, and G. F. Hewitt

1985 Heat transfer of a cylinder in crossflow: Hemisphere Washington, DC.